# Design and Implementation of a High-Contrast, Millijoule-Level Ultrafast Optical Parametric Amplifier for High-Intensity Lasers

**PhD Thesis by Yannik Zobus**
Zur Erlangung des Grades eines Doktors der Naturwissenschaften (Dr. rer. nat.)
Genehmigte Dissertation von Yannik Zobus aus Rüdesheim am Rhein
Tag der Einreichung: 05.04.2023, Tag der Prüfung: 15.05.2023

1. Gutachten: Prof. Dr. Vincent Bagnoud
2. Gutachten: Prof. Dr. Markus Roth
Darmstadt, Technische Universität Darmstadt

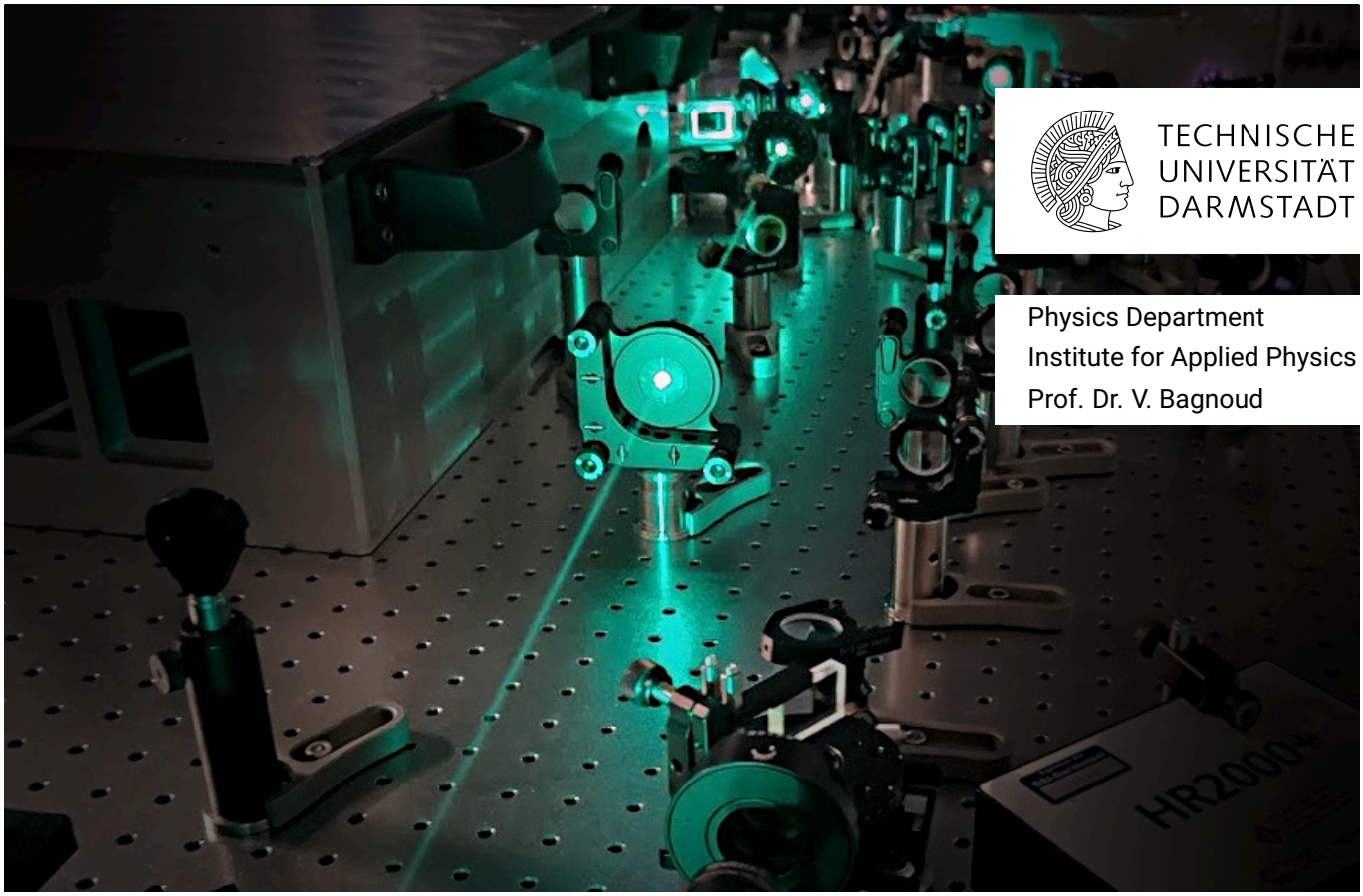

Design and Implementation of a High-Contrast, Millijoule-Level Ultrafast Optical Parametric Amplifier for High-Intensity Lasers
PhD Thesis by Yannik Zobus

Accepted doctoral thesis by Yannik Zobus

Date of submission: 05.04.2023
Date of thesis defense: 15.05.2023

Darmstadt, Technische Universität Darmstadt

## Erklärungen laut Promotionsordnung

### § 8 Abs. 1 lit. c PromO

Ich versichere hiermit, dass die elektronische Version meiner Dissertation mit der schriftlichen Version übereinstimmt.

### § 8 Abs. 1 lit. d PromO

Ich versichere hiermit, dass zu einem vorherigen Zeitpunkt noch keine Promotion versucht wurde. In diesem Fall sind nähere Angaben über Zeitpunkt, Hochschule, Dissertationsthema und Ergebnis dieses Versuchs mitzuteilen.

### § 9 Abs. 1 PromO

Ich versichere hiermit, dass die vorliegende Dissertation selbstständig und nur unter Verwendung der angegebenen Quellen verfasst wurde.

### § 9 Abs. 2 PromO

Die Arbeit hat bisher noch nicht zu Prüfungszwecken gedient.

Darmstadt, 05.04.2023

Y. Zobus

# Kurzfassung

Das Ziel der hier vorliegenden wissenschaftlichen Ausarbeitung war die Entwicklung eines Lasermoduls zur Verbesserung des zeitlichen Kontrastes an Hochintensitätslasersystemen und dessen Implementierung am Hochleistungslaser PHELIX an der GSI Helmholtzzentrum für Schwerionenforschung GmbH in Darmstadt. Durch die Verbesserung des zeitlichen Kontrastes sollen Experimente mit Laser-Plasma-Wechselwirkung unter extremen Spitzenintensitäten ermöglicht werden, ohne das Target bereits vor dem Eintreffen des Hauptpulses zu modulieren oder zu zerstören.

Im Rahmen dieser Arbeit habe ich deshalb einen ultraschnellen optisch-parametrischen Verstärker (engl. ultrafast optical parametric amplifier, uOPA) entwickelt, welcher eine Verstärkung mit hohem zeitlichen Kontrast von kurzen Laserpulsen bis in den Millijoulebereich ermöglicht und somit nachfolgende, kontrastverschlechternde Verstärkersysteme ersetzen kann. Dadurch kann neben der Reduktion der verstärkten Spontanemission auch das Auftreten von Vorpulsen verhindert werden.

Dafür habe ich zusätzlich ein Pumpmodul für diesen Verstärker entwickelt, welches sich in einem breiten Bereich um die zentrale Wellenlänge von 1 µm einsetzen lässt und somit an verschiedenen Lasersystemen als Pumplaser für uOPA Systeme eingesetzt werden kann.

So habe ich neben dem Hochkontrastverstärker für das Nd:Glas Lasersystem PHELIX ein zweites uOPA Modul für den Einsatz am diodengepumpten Yb:$CaF_2$ Lasersystem PENELOPE aufgebaut. Die Implementierung des Moduls am Hochleistungslaser PHELIX habe ich im Rahmen dieser Arbeit umgesetzt, wodurch ein Verstärker, welcher intensive Vorpulse erzeugte, erfolgreich aus der Verstärkungskette entfernt werden konnte. Damit habe ich den Vorpulskontrast am PHELIX um nahezu drei Größenordnungen auf ein Kontrastlevel von $6{,}2{\cdot}10^{-11}$ abgesenkt, wodurch die Vorpulsintensität, selbst für die höchstmögliche Intensität am PHELIX, unter 100 GW/$cm^2$ gehalten werden kann.

Die Ergebnisse dieser Arbeit habe ich in einer Publikation veröffentlicht [1] und in einer weiteren Publikation, welche kürzlich zur Veröffentlichung akzeptiert wurde, eingereicht [2].

# Abstract

The objective of this work was the development of a laser module to improve the temporal contrast of high-intensity laser systems and its implementation at the high-power laser PHELIX at the GSI Helmholtzzentrum für Schwerionenforschung GmbH in Darmstadt. By improving the temporal contrast, experiments with laser-plasma interaction under extreme peak intensities should be made possible without disturbing or destroying the target before the arrival of the main pulse.

In the frame of this work, I have therefore developed an ultrafast optical parametric amplifier (uOPA), which enables high-temporal-contrast amplification of short laser pulses up to the millijoule range and can thus replace subsequent contrast-degrading amplifier systems. In addition to reducing amplified spontaneous emission, the occurrence of pre-pulses can also be prevented.

I have additionally developed a dedicated pump module for this amplifier, which can be used in a wide spectral range around the central wavelength of 1 µm and thereby can be implemented on various laser systems as a pump laser for uOPA systems.

Thus, in addition to the high-contrast amplifier for the Nd:glass laser system PHELIX, I have built a second uOPA module for use in the diode-pumped Yb:$CaF_2$ laser system PENELOPE. I implemented the module on the high-power PHELIX laser as part of this work, which successfully replaced an amplifier, which generated intense pre-pulses, in the amplification chain. This allowed me to lower the pre-pulse contrast at PHELIX by nearly three orders of magnitude to a contrast level of $6.2 \cdot 10^{-11}$, keeping the pre-pulse intensity, even for the highest possible intensity at PHELIX, below 100 GW/cm$^2$.

I have written two papers about the results of my work, of which one is already published [1] and the other one has been accepted for publication recently [2].

# Education

### Master of Science (Physics)

*09.03.2016 - 29.11.2018*

**Technical University of Darmstadt**
Karolinenplatz 5
64289 Darmstadt
Germany

**Thesis:** Construction of a double-staged fiber amplifier for an uOPA pump stage
Grade: 1.0 (very good)
Final grade: 1.11 (very good)

### Bachelor of Science (Physics)

*01.10.2012 - 08.03.2016*

**Technical University of Darmstadt**
Karolinenplatz 5
64289 Darmstadt
Germany

**Thesis:** Conversion of the high-energy laser system nhelix with subsequent beam characterization
Grade: 1.3 (very good)
Final grade: 2.35 (good)

### General University Entrance Qualification

*01.08.2003 - 31.07.2012*

**St. Ursula-Schule**
Rüdesheimer Straße 30
65366 Geisenheim
Germany

**Specialized courses:**
- Physics (written exam), 14 pt (very good)
- Mathematics (written exam), 13 pt (very good)

Final grade: 2.1 (good)

# Contents

*In Gedenken an Margot und Hans Zobus*
**18.03.1936; †10.08.2019*
**20.10.1931; †20.12.2019*

# 1. Introduction

Ever since the invention of the laser by T. Maiman in 1960 [3], which already allowed to step into the field of nonlinear optics [4], researchers tried to increase the field strength of the laser as it enabled the investigation of a plethora of other novel phenomena that were inaccessible in the laboratory before. As a consequence, several technological innovations have been developed over time, which allowed for increasing the laser peak power.

The first milestone shortly after Maiman's invention of the laser was reached with the invention of Q-switching in 1962 [5]. This enabled the creation of laser pulses at similar energy levels but shorter duration. Like this, pulse durations of about 120 ns could be achieved, compressing the energy in time to reach a peak power of about 300 kW [5]. This significantly surpassed the peak power of previously demonstrated "spontaneous" pulsing [6]. Following the path of pulse-duration reduction, another groundbreaking development emerged in form of the mode-locking of lasers [7–9]. This technique unlocked the creation of pico- and sub-picosecond long pulses [10], which however only featured pulse energies around the nanojoule level at creation. Consequently, the pulse energy had to be increased again to reach higher peak powers than before. This could, however, quickly damage the laser system, which required either increasing the beam size or the pulse duration to mitigate nonlinear self-focusing and to stay below the damage thresholds.

The required increase of the beam size was realized with the implementation of the **M**aster **O**scillator **P**ower **A**mplifier (MOPA) architecture in the frame of fusion-relevant research laser facilities [11, 12]. The larger beam diameter, paired with maximized energy extraction from the laser medium, increased the available peak power to the multi-terawatt level, even though the pulses were significantly longer than the ones achieved using the mode-locking scheme (0.2 ns to 10 ns) [12]. These newly available peak powers brought the attention of the community to the importance of the temporal contrast for the first time. The scale of the amplifiers generated high levels of incoherent noise, such as **A**mplified **S**pontaneous **E**mission (ASE), pre-pulses or even flash-lamp light which was able to disturb the main laser-target interaction. This was a challenge for experiments where the available intensities in excess of $10^{17}$ W/cm$^2$ should be used [11]. Here, an absolute value for a good contrast was defined as intensities below $10^{10}$ W/cm$^2$ before the main pulse, corresponding to seven orders of magnitude relative to the peak intensity.

However, with the invention of the **C**hirped **P**ulse **A**mplification (CPA) architecture [13], the development of **Ti**tanium-doped **Sa**pphire (Ti:Sa), a new extremely broadband laser material [14, 15], and technology-developments to temporally stretch and compress laser pulses [16, 17], the way was paved for even more extreme laser power and intensity. Shortly after, intensities exceeding $10^{18}$ W/cm$^2$ [18] and estimations for intensities of $10^{19}$ W/cm$^2$ - $10^{20}$ W/cm$^2$ were generated [19]. Eventually, the first petawatt-surpassing laser was built from a single beam line of the Nova facility [20] and reached a peak intensity of $7{\cdot}10^{20}$ W/cm$^2$, which was groundbreaking at that time.

As the CPA architecture made intensities from $10^{14}$ W/cm$^2$ to $10^{19}$ W/cm$^2$ even at less powerful facilities routinely available, the challenge of high-field laser physics began to drift drastically. While previously, new phenomena like **H**igh-**H**armonic **G**eneration (HHG) [21], multiphoton ionization [22], relativistic self-focusing [23], and electron- [24] or even ion acceleration [25] were not accessible in

the laboratory, the research field experienced a surge of corresponding investigations. In this context, the steadily increasing intensities shifted the issue of the temporal contrast back into focus once more, as even small pre-pulses or ASE could disrupt the main-pulse interaction by igniting a pre-plasma or alter precisely defined pre-plasma properties. Concerning the interaction of the laser with solid targets, these disturbances started to get problematic [26]. Depending on the peak intensity and the process to investigate, the need for a temporal contrast of up to 10-11 orders of magnitude arose for solid-target interactions if no pre-plasma should be created.

Fast forwarding to the present, we find that the trend of increasing the laser intensity still continues. By now, the number of petawatt-class laser facilities worldwide in operation or going to be built is around 50 [27] and peak powers above 10 PW [28] and intensities above $10^{23}$ W/cm$^2$ [29] have been realized lately. Simultaneously, the investigation, understanding and application of high-intensity laser-plasma interaction advanced. However, this did not relax the demands on the temporal contrast but strengthened it.

Re-considering the idea of an undisturbed target for a peak intensity of $10^{23}$ W/cm$^2$, a contrast of about 13 orders of magnitude would be necessary. However, we find the state of the art (assuming no post-compressor cleaning) to be around >10 to >12 orders of magnitude concerning the incoherent-noise pedestal and only 8-10 orders of magnitude concerning pre-pulses [30–38].

## 1.1. Thesis goals and structure

This work was carried out within the LOEWE research cluster "Nuclear Photonics" at the Institute of Nuclear Physics of the Technical University of Darmstadt and within the framework of the research platform "ATHENA - Accelerator Technology Helmholtz Infrastructure". The aim of the LOEWE research cluster "Nuclear Photonics" is the usage and optimization of novel radiation sources, such as laser-generated particle sources and intense gamma rays, to investigate the field of nuclear photonics, which combines the fields of nuclear- and high-energy-density physics. Similar efforts are ongoing within the ATHENA development platform, which is driving the development of plasma-based particle accelerators to cover applications ranging from medical uses to new possibilities in nuclear and particle physics. Within this context, the generation of laser pulses with high temporal contrast takes an important role.

The main objective of the work at hand was therefore to develop a module based on **u**ltrafast **O**ptical **P**arametric **A**mplification (uOPA), which is used to generate a contrast-enhanced seed for high-intensity lasers. Specifically, the goals were the implementation of that module at the **P**etawatt **H**igh-**E**nergy **L**aser for heavy **I**on e**X**periments (PHELIX) at GSI Helmholtzzentrum für Schwerionenforschung GmbH in Darmstadt and the construction of a module for the **P**etawatt **EN**ergy-**E**fficient **L**aser for **O**ptical **P**lasma **E**xperiments (PE**N**ELOPE) at Helmholtzzentrum Dresden - Rossendorf e.V..

PHELIX can deliver pulses with energies up to 200 J and a pulse duration of about 500 fs, which, when focused down to a micrometer-sized spot, reach intensities above $10^{21}$ W/cm$^2$ [5]. Although the temporal contrast already was a topic of research at PHELIX and previous work [36] was done to mitigate the problematic nature of ASE, pre-pulses still degrade the temporal contrast. With a pre-pulse contrast above $10^{-8}$, corresponding to intensities above $10^{13}$ W/cm$^2$ at worst, these pre-pulses are problematic for high-contrast-demanding experiments and must be removed.

The most problematic pre-pulses are generated in the first regenerative amplifier of the PHELIX front-end. Therefore, the main goal for the developed module was to generate high-quality pulses with sufficient energy to bypass this amplifier and by this, remove the pre-pulses.

This thesis is divided into three major segments. In chapter 2, I will detail the features of the temporal contrast, which are found in modern high-intensity laser systems. This covers the origin and generation

processes of these features within the laser chain. Afterwards, I will define the requirements for the temporal contrast, discuss the difficulties of contrast metrology and present some possibilities to still retrieve a measurement of the temporal contrast. Lastly, I will give an overview of contrast-enhancement strategies, which are applied in high-intensity laser systems.

Within chapter 3, the design of the contrast-enhancement strategy of this work, a millijoule-level uOPA, is described. Here, I will first give a theoretical description of OPA and discuss the parameters which are most important for the amplification of short laser pulses within this process. After this, I will define the output objectives for the uOPA that should be developed. Since this requires the use of numerical simulations, I will give a brief overview of existing simulation software for nonlinear optics and then proceed to use the simulations to define the required parameters of the uOPA and its pump laser.

In chapter 4, I will present the development of the uOPA system and its implementation at PHELIX. I will start with the setup of the pump laser, followed by its characterization. Details on the setup and the results of this characterization were also published in the journal *Optics Express* [1]. In the subsequent sections, I will discuss the setup of the uOPA stage and evaluate its performance with regard to the target parameters. Furthermore, I will discuss aspects of the system, which can be optimized to increase its performance or applicability in high-intensity laser systems. Lastly, I will describe the implementation of the uOPA at PHELIX and how it has impacted the temporal contrast at PHELIX.
A manuscript on the design and performance evaluation of the uOPA as well as its impact on the temporal contrast at PHELIX has been submitted to *High Power Laser Science and Engineering* and was recently accepted for publication [2].

In chapter 5, I will summarize the work at hand and give a brief outlook.

# 2. Temporal contrast in the context of high-intensity laser systems

Nowadays, the research community demands to use highest intensities in the range of $10^{21}$ W/cm$^2$ and above. To reach such intensity levels, the pulse energy must be maximized while the pulse duration and focal-spot diameters must be minimized. The origin of the intense pulses is typically a short-pulse oscillator, which already delivers pulses with high temporal and spatial quality. Yet, with pulse energies in the nanojoule range, significant amplification is necessary to boost the pulse energy up to the joule or even the kilojoule range. Fortunately, such amplification factors became feasible with the introduction of **C**hirped **P**ulse **A**mplification (CPA).

However, to maintain the spectral bandwidth to produce short pulses and spatial quality to create small foci, high-fidelity amplification is necessary. While this alone poses major challenges, even higher standards must be met for high-intensity laser-plasma experiments, which require defined pre-plasma properties or an intact, non-ionized target before the main pulse arrives. This imposes further challenges on the amplification fidelity, as at intensity levels of $10^{21}$ W/cm$^2$, even the slightest distortions may alter the interaction of the main pulse with the target. Regarding the temporal aspect of the amplified pulses, a measure for the amplification fidelity is found in the temporal contrast, which is defined as the ratio between the peak intensity of the laser pulse and the intensity of the laser pulse at an arbitrary point in time before the peak intensity.

To get a deeper understanding of this parameter, I will define the temporal laser contrast and which contrast-degrading features can be found, especially in CPA lasers. I will explain where different temporal-contrast imperfections originate in high-intensity laser facilities and what the formation processes of these imperfections are. After that, I will shortly discuss, what the contrast requirements for high-intensity lasers are and how to measure if the requirements are met. Lastly, I will present several technologies that are used to reduce/clean these imperfections or avoid them in order to increase the temporal contrast and regain high-fidelity amplification.

## 2.1. Temporal-contrast in CPA lasers

With CPA as fundamental architecture for modern high-intensity laser systems, a detailed look at an exemplary temporal pulse profile, generated in such a system is useful to determine what kind of features degrade the temporal contrast of the pulse. In CPA lasers, the relevant timescales for the degradation of the temporal contrast typically range from below one picosecond up to multiple nanoseconds. Figure 2.1 shows an exemplary simulated temporal pulse profile (blue curve) showing all prominent contrast features of a short-pulse CPA laser system.

In a pulse profile with imperfect contrast, as seen in the example in Fig. 2.1, several contrast-degrading features are present, which may be classified into coherent and incoherent features.

Within the group of incoherent features, there is a few nanosecond-long noise pedestal that rises slowly until it reaches a plateau, which in Fig. 2.1 is at $10^{-11}$. Belonging to the group of coherent contrast features, we find pre-pulses at various positions prior to the main pulse on top of the incoherent

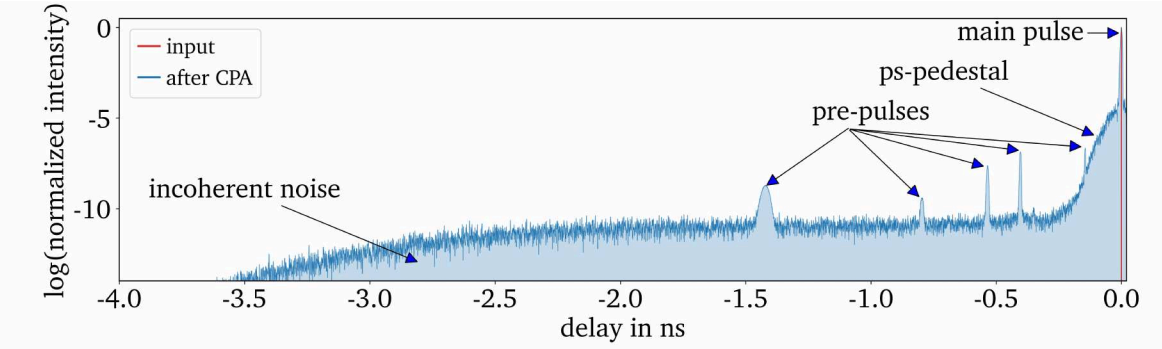


Figure 2.1.: Exemplary, simulated pulse profile (blue) of a CPA laser, which exhibits several contrast degrading features and the input pulse profile (red). The plot is normalized to the peak intensity of the main pulse at t = 0 ns.

noise, a few-hundred picosecond-long rise in intensity directly prior to the main pulse (referred to as ps-pedestal, rising edge, rising slope, etc.), and the elongation of the main pulse compared to its input pulse shape (red curve).

All these contrast features can or will generally be found in modern CPA-based laser systems, but may vary in amplitude, shape, and temporal positioning. In order to better understand the formation processes and origins of the contrast features in CPA lasers, I will describe the basic architecture of a CPA laser in the next section.

### 2.1.1. Basic setup of a CPA laser

Figure 2.2 shows an exemplary setup of a high-intensity laser facility. It must be noted that the exact setup of a high-intensity laser, for example, the number of amplifiers, energy output and pulse duration of the system, may substantially differ compared to existing systems. This section will only provide a basic, generalized view of modern laser systems.

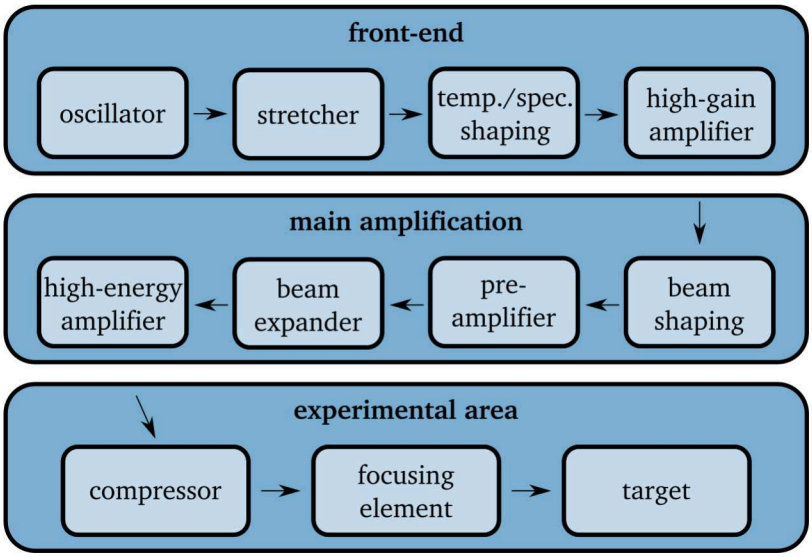


Figure 2.2.: Schematic, generalized setup of a high-intensity, CPA-based laser facility.

Beginning at the front-end, the starting point of the CPA laser, a short-pulse oscillator generates pulses in the duration of a few femtoseconds up to picoseconds. Since the output pulse energy of short-pulse oscillators is in the range of nano- to microjoule, the pulses must pass several amplification stages to increase their energy and reach the intensity that is required for experimental campaigns. However, as a rule of thumb, intensities should not exceed $10^{10}\,\mathrm{W/cm^2}$ [18] during amplification, but rather stay beneath this value to mitigate the influence of nonlinear effects and also decrease the risk of laser-induced damage, for example, via small-scale self-focusing [40]. To limit the intensity, high-intensity laser facilities employ the technique of CPA, which reduces the pulse intensity during the amplification by temporally stretching the pulses from the femtosecond up to the nanosecond scale. A common way to do this is the implementation of a diffraction-grating-based pulse stretcher [16, 41].

After stretching, it is not uncommon to spectrally and temporally shape the pulses to precompensate gain narrowing or dispersion in the system. This can be done via an **A**cousto-**O**ptic **P**rogrammable **D**ispersive **F**ilter (AOPDF) [42], which allows to actively manipulate the spectrum and phase and therefore the duration of the pulse. After that, one or multiple amplifiers boost the pulse from the nanojoule- up to the low millijoule level, corresponding to a gain of $10^6$ or more. Established amplifiers to reach such gain levels are regenerative amplifiers [43], multi-pass amplifiers [44], fiber amplifiers [45, 46], **O**ptical **P**arametric **C**hirped **P**ulse **A**mplification (OPCPA) [47] or a combination of them. Because of the low output energy in the millijoule range, these amplifiers can be built compactly, as the beam size can remain small during amplification. However, further amplification to higher energies requires reducing the intensity first, as the intensity of pulses with beam radii below 1 mm and energies up to tens of millijoules already approaches the low $\mathrm{GW/cm^2}$ range, even for stretched pulses as long as 2 ns.

Since pulse-stretcher setups are complex, cost-intensive, large and further stretching will result in a space-consuming setup for the temporal compression, the intensity reduction is done via beam expansion. Furthermore, beam shaping to flat-top distributions to maximize the energy extraction in the amplifiers is commonly applied. Before the injection into the pre- and main amplifier stages, the beams are magnified from the sub-mm to the few-centimeter scale for energies in the joule range or even to the meter scale for energies in the kJ range. The established amplifier types here differ from the front-end amplifiers, as not the gain but the total amount of energy must be maximized. Amplifier types that are used for this are again multi-pass amplifiers [48–50], OPCPA [51, 52] and rod or slab amplifiers [53, 54].

Propagating to the experimental area of the facility, the pulses are first temporally compressed in a diffraction-grating-based compressor to maximize their peak power. Finally, to reach the highest intensities to be used in experiments, the fluence is also maximized by focusing the large beam to spot sizes with diameters of a few micrometers. Following this scheme of gradually ramping up the energy while keeping the intensity at moderate levels during amplification and increasing the intensity after amplification via temporal compression and spatial focusing, modern laser systems can reach intensities of $10^{23}\,\mathrm{W/cm^2}$ [29]. At these intensities, even pre-pulses and the incoherent noise plateau as shown in Fig. 2.1 impose difficulties for some experiments. Consequently, the intensity of these features must be reduced or their formation avoided, which in turn requires the knowledge of their origins in the laser system, as well as their formation processes.

In the following sections, I will therefore address the generation processes of these features and the intensity requirements that arise for these features. Also, I will give a brief overview of how to measure their presence and how to reduce or avoid their influence.

### 2.1.2. Main-pulse elongation

The elongation of the main pulse is generally related to additional dispersion or a misalignment of the stretcher and compressor of the system. This means the different frequency components of the pulse may cover different optical pathways while propagating through the system, which translates to a phase difference between the frequency components. A common representation of the phase difference is its expansion into a Taylor series in the spectral domain:

$$\varphi(\omega) = \sum_{n=0}^{\infty} \frac{\varphi^{(n)}(\omega = \omega_0)}{n!} \cdot (\omega - \omega_0)^n. \tag{2.1}$$

Here, $\omega$ is the angular frequency, $\omega_0$ the central frequency and $\varphi^{(n)}(\omega = \omega_0)$ the n-th derivative of $\varphi$ with respect to $\omega$, evaluated at $\omega_0$. $\varphi(\omega)$ is commonly referred to as the spectral phase. Each of its constituents will influence the temporal shape of the pulse differently. For example, the zeroth order corresponds to an absolute phase offset, commonly referred to as the carrier-envelope offset phase, the first order to a temporal shift, the group delay of the pulse, and the higher orders correspond to dispersive effects, which impact the temporal shape of the pulse. Consequently, since only orders starting from the second one change the temporal pulse shape, the sum of all accumulated phases must result in a form that can be described by a linear phase plus an offset to achieve the shortest pulse duration. For a CPA laser this can be written as:

$$\varphi_{stretcher}(\omega) + \varphi_{compressor}(\omega) + \varphi_{add.dispersion}(\omega) = \varphi^{(0)} + \varphi^{(1)} \cdot (\omega - \omega_0). \tag{2.2}$$

Here $\varphi_{stretcher}(\omega)$ is the phase of the stretcher, $\varphi_{compressor}(\omega)$ the phase of the compressor and $\varphi_{add.dispersion}(\omega)$ accounts for every additional dispersion in the system. If this equation is fulfilled, the pulse is called bandwidth limited or is referred to as **F**ourier-**T**ransform **L**imit (FTL). However, if eq. 2.2 is not fulfilled, a deformation of the pulse can be observed. This is depicted in Fig. 2.3 for the spectral-phase orders of two to four.

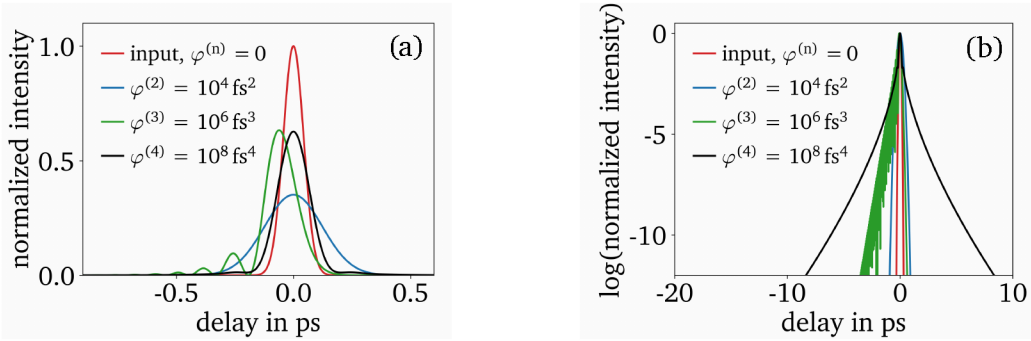


Figure 2.3.: Impact of different spectral phase components on the pulse shape in linear (a) and log-scale (b). The plots show a pulse with Gaussian spectrum centered at 1053 nm with 16 nm **F**ull **W**idth **H**alf **M**aximum (FWHM) bandwidth for different values of the spectral-phase orders, described in the plot legend. The pulse distributions in (a) are normalized to their integral and in (b) normalized to their peak intensity.

The second-order phase distributes the frequency components linearly in time, effectively stretching the pulse. Such a pulse is also called linearly chirped. As the spectrum is now distributed in time, the pulse shape in time will inherit the spectral shape, if stretched sufficiently.

Compared to the former, the third- and the fourth-order phase (Fig. 2.3 green and black) influence the temporal shape in a more distorting way, by creating a set of trailing or leading pulses or plateau-like structures, respectively. While the second-order phase can rapidly reduce the peak intensity, higher spectral-phase orders can significantly reduce the temporal contrast of the pulse as shown in the log-scale plot in Fig. 2.3(b). Generally, all the induced spectral-phase orders should be compensated. Methods to do this are described in section 2.4.

### 2.1.3. Incoherent noise

The noise shown in Fig. 2.1 is a common feature in all laser systems as it is directly connected to pulse amplification. In CPA lasers, the duration of this noise plateau is approximately equal to the stretched pulse duration. Due to the incoherent nature of the noise, the duration will not change significantly during compression and will therefore feature a much longer duration than the compressed main pulse. In principle, we find two potential origins for this noise: the amplification of spontaneously emitted radiation, commonly referred to as **A**mplified **S**pontaneous **E**mission (ASE), or spontaneous parametric down-conversion, resulting in **P**arametric **S**uper**F**luorescence (PSF).

#### 2.1.3.1. Amplified spontaneous emission

Spontaneous emission is an unavoidable effect in laser amplifiers that rely on population inversion in active media and emits with a rate that is an intrinsic property of the active medium [55]. As this is a statistical process, the emitted photons are distributed over the emission bandwidth of the medium and do not possess a fixed phase relation, creating incoherent noise. To determine the contrast degradation through the amplification of this noise, its power must be calculated and compared to the power of the amplified signal. A detailed derivation for the ASE power is carried out in appendix A.2. In multi-pass amplifiers, for example regenerative amplifiers, with $n$ passes, the power of the ASE can be approximated by [56, 57]:

$$P_{ASE} \approx {\bar{g}_0}^n \cdot \frac{P_{fl}^{(1)}}{\bar{g}_0 - 1}. \tag{2.3}$$

Here, $\bar{g}_0$ is the small-signal gain, averaged over the amplification bandwidth of the amplifier and $P_{fl}^{(1)}$ the power of the spontaneously emitted fluorescence after the first pass of the amplifier. Dividing eq 2.4 by $P_{sig}$, the power of the signal after amplification with seed energy $E_{sig,in}$ and compressed pulse duration of $\Delta t_{sig}$, the temporal-contrast $TC$ after degradation via ASE can be defined as:

$$TC = \frac{P_{ASE}}{P_{sig}} \approx \frac{\Delta t_{sig}}{{\bar{g}_0}^n \cdot E_{sig,in}} \cdot {\bar{g}_0}^n \frac{P_{fl}^{(1)}}{\bar{g}_0 - 1} = \frac{\Delta t_{sig}}{E_{sig,in}} \cdot \frac{P_{fl}^{(1)}}{\bar{g}_0 - 1}. \tag{2.4}$$

For unsaturated amplification, the gain can be estimated as equal for the signal and the fluorescence. This makes it evident that the temporal contrast gets enhanced if a larger seed energy is used. To estimate the theoretical temporal contrast, the effective fluorescence $P_{fl}^{(1)}$ must be estimated, which can be done by [57]:

$$P_{fl}^{(1)} = \bar{I}_{sat} A \ln\left(\frac{\bar{g}_0}{1 - \bar{L}}\right) \cdot K_{\Delta\omega} K_p K_{\Delta\Omega}, \tag{2.5}$$

where $\bar{I}_{sat}$ and $\bar{L}$ are the amplification-bandwidth-averaged values for the saturation intensity, the small-signal gain and the losses, respectively. $K_{\Delta\omega}$, $K_p$ and $K_{\Delta\Omega}$, describe the spectral, polarization

and angular acceptance of the amplifier and $A$ is the pump area. Following the description and using the supplied parameters in reference [57] for a pulse with 350 fs FTL, an amplification from 1 nJ to 1 mJ within 50 passes in an **N**eo**d**ymium (Nd)-phosphate glass amplifier would result in a temporal contrast of approximately $8.3{\cdot}10^{-10}$.

#### 2.1.3.2. Parametric superfluorescence

For OPCPA lasers, similar incoherent noise levels are found, despite exploiting a completely different mechanism and avoiding the storage of light in a medium via population inversion. The origin for this is the spontaneous parametric down-conversion of a pump-photon due to the presence of quantum fluctuations [58].

Again, to define the temporal-contrast degradation, the input noise, which starts the PSF, must be determined. In reference [59], this is done in analogy to the process of spontaneous Raman scattering, which also builds up from quantum noise [60, 61]. There, the input noise intensity for an OPA is defined as two times the Raman input-noise intensity, as both signal and idler can initiate the down-conversion [59]:

$$I_{noise,OPA} = 2 \cdot I_{noise,Raman} = 2 \cdot \frac{\hbar\omega^3 n^3}{8\pi^3 c_0^2} \Delta\Omega\Delta\omega. \tag{2.6}$$

Here, $\omega$ is the signal center frequency, $n$ the ordinary refractive index, $c_0$ the vacuum speed of light, $\Delta\Omega$ the solid angle of the emitted radiation and $\Delta\omega$ the detectable spectral bandwidth. Contrary to eq. 2.5 there is no scaling with the gain, hence by calculating the input noise power from eq. 2.6, the temporal contrast can be calculated by dividing the input noise power by the compressed input seed power. To do this, we can assume that only the noise photons, which match the solid angle and the frequency bandwidth of the signal, contribute to the effective noise input. For a Gaussian mode with waist $w_0$ and wavelength $\lambda$, the solid angle can be approximated by

$$\Delta\Omega \approx \pi\theta^2 \approx \pi \left(\frac{\lambda}{\pi w_0}\right)^2. \tag{2.7}$$

To compare the contrast to that of the previous section, a 350 fs long, bandwidth-limited pulse, centered at 1053 nm with an energy of 1 nJ is used for the calculation. With a refractive index of 1.654 as in a common nonlinear crystal $\beta$-**B**arium **BO**rate (BBO), this yields a temporal contrast of $7.5{\cdot}10^{-10}$.

#### Conclusion

Both ASE and PSF show similar levels of theoretical temporal-contrast degradation. In reality, degraded contrast values may be achieved due to coupling losses into regenerative multi-pass amplifiers or non-optimized pump-spot sizes in relay-imaged multi-pass amplifiers, which may even degrade the spatial contrast in the focal spot [57]. In OPCPA systems, the achievable contrast values may be lower because of larger pump-to-signal beam ratios, imperfect phase-matching configurations or non-ideal pump-to-signal delay [62].

Depending on the mechanism and the optical setup, in which the incoherent noise is generated, the duration of this incoherent-noise plateau differs. While for OPCPA lasers, this timescale is bound to the duration of the pump pulse, the ASE-plateau duration is, e.g., in a regenerative amplifier limited to the cavity-roundtrip time or in an imaging multi-pass amplifier to the lifetime of the excited state. When optical switches are used to remove excessive noise, the duration of the noise-plateau is typically as long as the stretched signal pulse plus the rise- and fall time of the switch.

Furthermore, both ASE and PSF contrast depend on the seed energy and compressed pulse duration of the signal. This in turn implies that it is useful to compress the pulses to their shortest possible pulse duration and to maximize the seed energy without decreasing the contrast of the seed. Available amplification methods to apply such pre-amplification of the signal will be described in section 2.4.

### 2.1.4. Pre-pulses

Other clearly observable features in Fig. 2.1 are pulse replicas of the main pulse. These may originate as leakage light from subsequent or preceding pulses in the short-pulse oscillator or be generated due to multiple reflections on imperfect **A**nti-**R**eflection (AR) coatings. The principle of their generation is seemingly straightforward and depicted in Fig. 2.4.

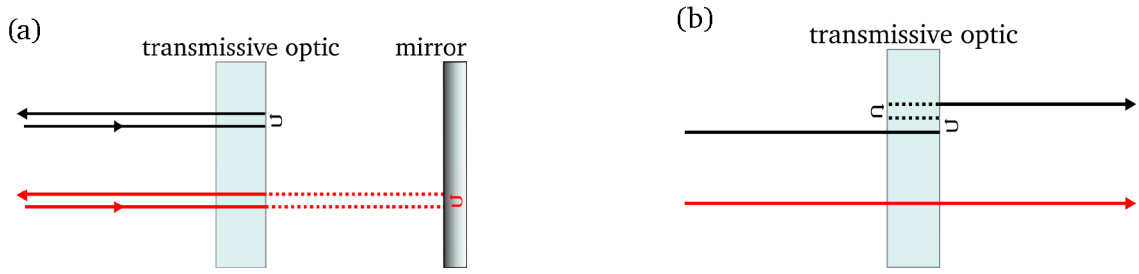


Figure 2.4.: Schematic generation of pulse replicas. (a) Pre-pulse generation by single, partial reflection before a 0° mirror. (b) Post-pulse generation by double reflection inside a transmissive optic. The intended pathway is shown in red and the unintended in black. The dotted line represents the additional pathway.

Figure 2.4(a) shows the principle of pre-pulse generation. The incoming pulse (red path) propagates through a transmissive optic, e.g., a **W**ave **P**late (WP), reflects on a 0° mirror and is again transmitted through the WP. Due to the non-zero reflectivity, a small part of the pulse (black path) reflects on the rear- or front side of the transmissive optic. Since the intended pathway is longer by a certain amount (dotted red line), a pre-pulse is generated. Analogous to this principle, post-pulses can also be created. This is shown in Fig. 2.4(b), in which the post-pulse is generated by a double reflection within a transmissive optic and delayed by a time corresponding to twice the optical length of the material.

At first glance, post-pulses do not impact the contrast of high-intensity laser on a relevant timescale, as they arrive after the main interaction. However, it was shown theoretically [63] and experimentally [64,65] that pre-pulses are generated from post-pulses by Kerr-based nonlinear-coupling of the stretched pulses with their pulse replicas. Figure 2.5 and Figure 2.6 depict the principle of this pre-pulse-generating mechanism.

Figure 2.5(a) shows the intensity of a short, Gaussian-shaped pulse, trailed by a pulse replica at 15.8 ps and a contrast of $10^{-6}$. Such a pulse replica may be generated in a thin optic, like a WP, with an AR coating that exhibits a reflectivity of 0.1 %. Transforming this electric field into the spectral domain (Fig. 2.5(b)) we can see a modulation on top of the Gaussian spectrum, whose frequency and amplitude depend on the post-pulse delay and relative amplitude compared to the main pulse. As described in section 2.1.2, stretching of the pulse will distribute the frequency components of the pulse over time and therefore, the sinusoidal modulation transfers to the temporal domain as shown in Fig. 2.5(c).

Up to this point, no pre-pulse is generated, and the original temporal shape of the pulse can be restored. However, during the amplification process in a CPA laser, the pulse propagates through media, which will cause not only linear refraction but also nonlinear refraction due to a third-order nonlinear

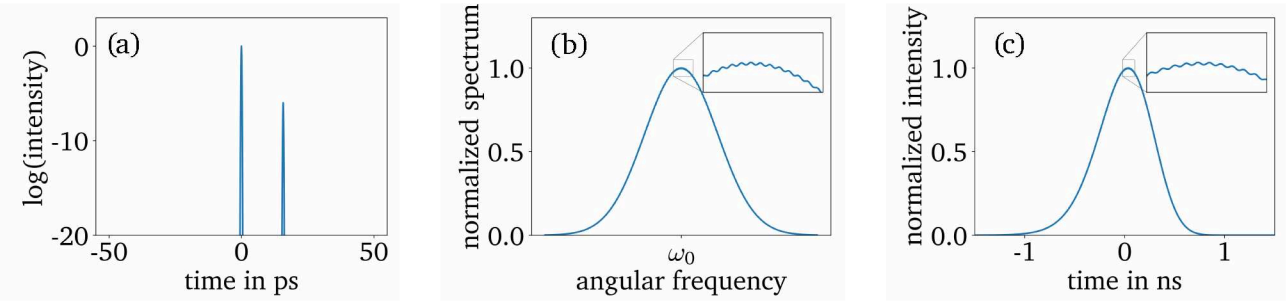


Figure 2.5.: Impact of a post-pulse on the temporal contrast in CPA lasers. (a) The main pulse is trailed by a pulse replica at 15.8 ps with a contrast of $10^{-6}$. (b) The spectrum of the main pulse with post-pulse. (c) Temporal profile after stretching. The inlets show a zoom to emphasize the modulation.

effect, which changes the effective refractive index to [66]:

$$n(t) = n_{lin} + n_{nonlin}(t) = n_{lin} + n_2 \cdot I(t). \tag{2.8}$$

Here, $n_{lin}$ is the linear and $n_{nonlin}$ the nonlinear contribution to the refractive index, $n_2$ the nonlinear refractive index and $I(t)$ the temporally dependent pulse intensity. Accordingly, the accumulated temporal phase $\Phi_{acc}(z,t)$ of a pulse at position z, with a wavelength $\lambda$ after propagation through a medium of length $l$ can be calculated as:

$$\Phi_{acc}(z = l, t) = \frac{2\pi}{\lambda}\left(n_{lin}l + \int_0^l n_2 I(z,t)dz\right). \tag{2.9}$$

Here, the first part accounts for the linear response of the medium, while the second accounts for the nonlinear contribution and is also referred to as break-up or B-integral and is a measure of the accumulated nonlinear phase shift. Equation 2.9 shows, that the intensity-dependence and therefore time-dependence of the nonlinear refractive index directly translates to an intensity-dependent phase-shift. Accordingly, the phase shift of temporal slices with higher pulse intensity is greater than that of that with lower intensity.

This effectively imprints the temporal-intensity profile into the phase of the pulse, as shown in Fig. 2.6(a). It is evident, that the sinusoidal intensity modulation in the temporal domain was transferred to the spectral phase of the pulse when comparing the additional nonlinear phases for a single pulse (inlet in Fig. 2.6(a), orange) with that of a pulse followed by a pulse replica (Fig. 2.6(a), blue). Recompression of these pulses eventually reveals the impact of the nonlinear coupling.

This is shown in Fig. 2.6(b), in which a comb of pulse replicas can now be observed. Here, it is also highlighted that the amount of accumulated nonlinear phase shift directly correlates with the intensity of the newly created pre-pulses and scales with the square of the B-integral value [63]. Furthermore, Fig. 2.6 implies, that even a B-integral as little as 0.01 rad creates a pre-pulse at a contrast level of $3.4{\cdot}10^{-11}$ from a post pulse with a contrast level of $10^{-6}$. This is especially relevant during amplification in large-area amplifiers of high-intensity lasers, in which the energy density is maximized, and therefore the highest intensity is reached. For example, assuming amplification at PHELIX whose Nd:glass main amplifier features a nonlinear refractive index of $2.28{\cdot}10^{-16}$ cm$^2$/W at best and $3.47{\cdot}10^{-16}$ cm$^2$/W at worst [67]. With a pulse energy of 100 J, a beam diameter of 28 cm and a pulse duration of 1 ns, a B-integral of 0.01 rad accumulates already after a propagation distance of approximately 3 cm to 4.5 cm.

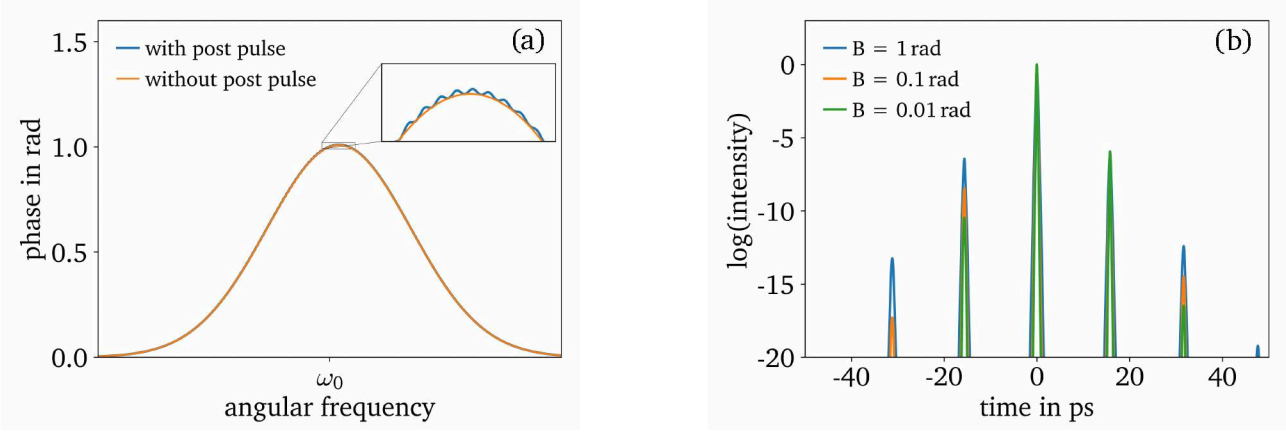


Figure 2.6.: (a) Phase introduced by nonlinear interaction with a medium for a single pulse (orange) and a pulse followed by a post-pulse (blue) as defined in Fig. 2.5. (b) Intensity of the re-compressed pulse after obtaining a maximum peak nonlinear phase shift of 1 rad (blue), 0.1 rad (orange) and 0.01 rad (green).

As this mechanism also applies in the presence of multiple post-pulses, the overall contrast trace can rapidly become complicated. Consequently, all kinds of pulse replicas should ideally be avoided.

### 2.1.5. Picosecond-pedestal / rising edge

The last contrast feature I would like to briefly discuss is the ps-pedestal/rising edge, directly prior to the main pulse as shown in Fig. 2.1. This ps-pedestal is also a CPA-specific feature, which is found to degrade the temporal contrast on a timescale of a few tens up to a few hundred picoseconds [30, 32]. In recent years, it has become apparent that the origin of this feature lies in the key components of a CPA laser: the stretcher and compressor [68–70]. These components utilize the spatio-spectral dispersion of the beam to introduce a large amount of spectral phase to stretch the pulse to a long duration or reverse this process and compress the stretched pulse to the shortest duration. However, it is precisely this spatio-spectral mapping which renders the pulse susceptible to surface defects of the optics on which it is spectrally dispersed. Spatially dependent phase distortions then directly translate to the spectral phase, which creates the ps-pedestal. The exact phase and therefore the amplitude and width of the ps-pedestal relates to the power spectral density of the surface, the injected beam size and the stretcher configuration [68, 70].

### Conclusion

In this chapter, I presented the origins and generation processes of the temporal-contrast features, which include ASE and PSF, pre-pulses, the ps-pedestal and basic pulse elongation through low-order dispersion. All these features are typically found in CPA laser and pose challenges to the plasma-physics community since the existence of these features may disturb the interaction between the main pulse and a target. In the next section, I will therefore discuss the temporal-contrast limits that should not be crossed by these features.

## 2.2. Contrast requirements for the creation of intense laser pulses

From the experimentalist's point of view, the laser intensity is an important parameter that, when increased sufficiently, can reveal a lot of physical phenomena during the interaction of the laser with matter. However, with a nowadays achievable intensity of $10^{23}\,\mathrm{W/cm^2}$, even little temporal-contrast features may impact the interaction of the pulse at its peak intensity with the target. For example, in the field of laser-ion acceleration, advanced acceleration mechanisms that promise the generation of high energetic ions, utilize intensities beyond $10^{21}\,\mathrm{W/cm^2}$, but simultaneously require a defined plasma pre-expansion or no plasma expansion at all [71–74]. This consequently sets requirements on the temporal contrast in order to meet the initial plasma/target conditions on the arrival of the peak intensity. Ideally, the temporal contrast is sufficiently high to completely avoid ionization prior to the arrival of the peak intensity. If still a pre-plasma is needed, it can be created via a designated pre-pulse.

However, as shown in the previous sections, there are numerous sources of temporal-contrast degradation, which might cause premature ionization of the target. Therefore, I will discuss laser-induced ionization mechanisms and their respective threshold intensities in more detail in the next section.

### 2.2.1. Laser-induced ionization

In general, laser-induced ionization of materials is associated with the absorption of the incoming light. However, there are a number of absorption mechanisms, and depending on the illuminated material, the influence of each absorption mechanism varies. Accordingly, a distinction between different types of materials must be made when regarding their damage threshold and therefore the contrast requirements for laser-plasma experiments. For solids, an essential distinction is made between absorbing materials like metals and transparent materials such as dielectrics.

Metals provide quasi-free electrons in the conduction band, which can directly oscillate in the electric field of the laser. Collisions of the oscillating electrons with the lattice of the material will then transfer energy and heat the material. At this point, the timescale of the heating process becomes relevant, since it determines whether the heat, introduced by the colliding electrons, can diffuse within the lattice or not [75]. If the heat-deposition rate exceeds the diffusion rate, the lattice starts to heat up to the melting point. For longer time scales with a pulse duration above 1 ns, this results in a damage-fluence scaling with the square root of the pulse duration [76, 77]. Accordingly, the damage-threshold intensity starts to scale with the inverse square root of the pulse duration. However, for time scales below 1 ns, the thermal diffusion slowly becomes negligible and the damage fluence becomes nearly pulse-duration-independent [75]. Consequently, the damage-threshold intensity scales with the inverse of the pulse duration. For gold, damage-threshold intensities of slightly above $10^9\,\mathrm{W/cm^2}$ at 900 ps were shown, while for sub-ps pulses a threshold intensity close to $10^{12}\,\mathrm{W/cm^2}$ was demonstrated [77].

Even though dielectrics are insulators, the damage-threshold intensity also shows an inverse square root pulse-duration dependency, similar to that of metals, for a pulse duration of approximately 10 ps and upwards [78], implying thermally induced damage [79]. Here, the material is heated via collisional ionization of background carriers in the conduction band, which creates an electron avalanche, followed by increased laser absorption [78]. Below a pulse duration of 10 ps, the scaling does not follow a simple law anymore and the ionization consists of multiple processes, including collisional-, multiphoton- and tunnel ionization [78, 79]. As the observed damage-threshold intensities are too low to be fully explainable by these mechanisms alone, it is assumed that impurities or defects such as color centers in the material lower the band-gap energy [80], which facilitates the onset of the damage process via tunnel- and multiphoton ionization. Using fused silica, damage-threshold intensities surpass $10^{10}\,\mathrm{W/cm^2}$ for 1 ns long pulses and are slightly above $10^{12}\,\mathrm{W/cm^2}$ for 1 ps long pulses [79].

For pure atomic gases, the ionization process is described well by the mechanisms of multiphoton-, tunnel- and barrier-suppression ionization [81] alone and also holds well experimentally [82–84]. These mechanisms are depicted schematically in Fig. 2.7(a), (b) and (c), respectively.

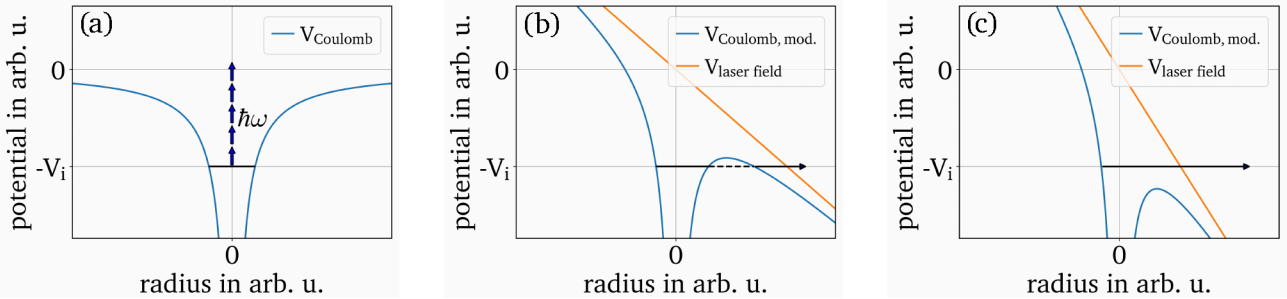


Figure 2.7.: Schematic of multiphoton ionization (a), tunnel ionization (b) and barrier-suppression ionization (c), where $V_i$ is the ionization potential, $V_{Coulomb}$ the Coulomb potential, $V_{Coulomb,mod.}$ the modified Coulomb potential and $V_{laser\ field}$ the potential of the laser field.

The mechanism of multiphoton ionization requires a quasi-simultaneous absorption of multiple photons (arrows in Fig. 2.7(a)) whose total energy $N \cdot \hbar\omega$ exceeds the binding energy of the electron to overcome the Coulomb-potential $V_{Coulomb}$ for ionization. For very high laser intensity, for which the electric-field strength is in the range of the atomic field strength, the Coulomb potential is strongly modified by the instantaneous potential of the laser [81]. As a result, the effective potential ($V_{Coulomb,mod.}$) may be lowered enough such that the electron can tunnel through the potential barrier (Fig. 2.7(b)) or, if the potential is lowered sufficiently, the electron can escape over the potential (Fig. 2.7(c)). The needed laser intensity for these mechanisms to become relevant are above $10^{12}$ W/cm$^2$ [81, 85].

For the sake of completeness, I want to mention another cause of ionization, which is direct ionization via the absorption of a photon whose energy is higher than the electron binding energy. Yet, even for the first ionization energy of caesium, which features the lowest ionization energy [86] with 3.894 eV [87], this corresponds to a wavelength of about 318 nm. However, most high-intensity laser facilities use Ti:Sa-, Nd- or **Y**tter**b**ium (Yb)-based systems with center wavelengths around 800 nm, 1053 nm or 1030 nm, respectively. Therefore, this ionization mechanism is not the driving force of laser-induced ionization in modern high-intensity laser systems, since their bandwidth does not cover the necessary wavelength range.

## Conclusion

Depending on the choice of target material, ionization occurs at different intensities. Atomic gases feature the highest threshold values above $10^{12}$ W/cm$^2$. Lower thresholds and a dependency on the pulse duration are found for dielectrics and metals. This is especially relevant in the context of temporal contrast. As the damage-threshold intensity decreases with longer interaction duration, higher contrast levels are needed for ns-long contrast features like ASE or PSF compared to pre-pulses whose duration is similar to the compressed main pulse. Table 2.1 summarizes approximate contrast requirements for pre-pulses, incoherent-noise plateaus and the ps-pedestal for a peak intensity of $10^{21}$ W/cm$^2$.

Table 2.1.: Approximate maximum intensity (I) and contrast requirements (CR) for pre-pulses, the ps-pedestal and incoherent-noise plateaus for a peak intensity of $I_{peak}$ = $10^{21}$ W/cm$^2$ and a center wavelength of 1 µm. The values for metals and dielectrics correspond to gold and fused silica [77]. For gases, hydrogen, with an ionization intensity of >$10^{13}$ W/cm$^2$ to produce reasonable ionization [84], is assumed.

| | **Pre-pulses (≈ 1 ps)** | | **ps-pedestal (≈ 100 ps)** | | **ASE/PSF (≈ 1 ns)** | |
|---|---|---|---|---|---|---|
| **Target material** | **I in W/cm$^2$** | **CR** | **I in W/cm$^2$** | **CR** | **I in W/cm$^2$** | **CR** |
| **Atomic gas** | $10^{13}$ | $10^{-8}$ | $10^{13}$ | $10^{-8}$ | $10^{13}$ | $10^{-8}$ |
| **Metals** | $6{\cdot}10^{11}$ | $6{\cdot}10^{-10}$ | $7{\cdot}10^{9}$ | $7{\cdot}10^{-12}$ | $2{\cdot}10^{9}$ | $2{\cdot}10^{-12}$ |
| **Dielectrics** | $2{\cdot}10^{12}$ | $2{\cdot}10^{-9}$ | $10^{11}$ | $10^{-10}$ | $4{\cdot}10^{10}$ | $4{\cdot}10^{-11}$ |

## 2.3. Contrast metrology

To avoid pre-ionization of a target or receive reasonable estimations for the plasma creation via simulations, it is mandatory to determine the temporal contrast of a laser system in the first place. This requires to detect and resolve all the temporal-contrast features mentioned in section 2.1, which are above the ionization threshold. A single device that would allow us to conduct this characterization of the temporal contrast is very challenging, as it would have to combine all the following capabilities:

- A **large dynamic measurement range** is needed to include all features that might be able to ignite a pre-plasma on a solid-density target. The temporal contrast values in table 2.1 imply that a dynamic range of more than twelve orders of magnitude is necessary to characterize the temporal contrast in the range which still might cause ionization at a pulse intensity of $10^{21}$ W/cm$^2$. The required dynamic range even increases to 14 orders of magnitude for the currently highest achievable intensity of $10^{23}$ W/cm$^2$ [29].
- The **temporal window** of the measurement must be large enough to capture the extent of the incoherent noise plateau and ideally all pre- and post-pulses. Assuming the use of optical switches to temporally filter out the noise plateau and the pulse replica outside the stretched pulse duration, the total width of the temporal measurement window must be at least as wide as the stretched pulse duration. For most high-intensity lasers this pulse duration is in the lower nanosecond range [30, 51, 53].
- A **high temporal resolution** is mandatory if not only the more outlying contrast features are to be measured, but also simultaneously the temporal pulse profile of the main peak. With achievable pulse durations (FWHM) of about 20 fs to 30 fs [29, 30, 88], a reasonable requirement for the resolution would be in the order of 2 fs or less.
- **Retrieving the spectral phase** is an upgrade to the high temporal resolution and also a needed step to compress the pulse close to its FTL.
- **Single-pulse measurement** allows characterizing the pulse-to-pulse fluctuations in the temporal contrast or the peak intensity and speeds up the measurement process.

Unfortunately, there is currently no device that covers all the mentioned parameters, but there are devices that cover individual parameters very well. Concerning the high temporal resolution, a direct

measurement would require tools with response times shorter than the pulse duration. However, there are no electronics with sufficient bandwidth to create such response times. Nonetheless, there are a variety of devices using techniques such as intensity autocorrelation [89], **F**requency-**R**esolved **O**ptical **G**ating (FROG) [90], **S**pectral **P**hase **I**nterferometry for **D**irect **E**lectric-field **R**econstruction (SPIDER) [91] and **S**elf-**R**eferenced **S**pectral **I**nterferometry (SRSI) [92], which all are capable of resolving sub-10 fs pulses [93–95] in a single-shot operation, by using the pulse itself as a measurement tool.

Aside from intensity autocorrelation, all the other techniques are also capable of retrieving the complete electric field, including the phase of the pulse. This facilitates a precise manipulation of the spectral phase to compress the pulse and create the highest possible intensity. However, due to their single-shot capabilities and very high temporal resolution, these devices lack in size of the total temporal window, which is typically below 2 ps to 3 ps. Also, the dynamic range of these devices is in the order of four to six orders of magnitude and thus, not sufficient to measure all contrast features, such as the incoherent noise plateau, low-intensity pre- or post-pulses and the full extent of the ps-pedestal.

Complementary to the previous methods, there are scanning cross-correlators available. Generally, these devices do not impress with temporal resolution (order of 10 fs), but with their extraordinarily high dynamic range and comparatively large temporal measurement window. Since these parameters enable to scan the complete temporal domain of CPA lasers on currently all relevant intensity levels, it has become an indispensable tool to characterize the temporal contrast of high-intensity laser systems. In the following, I will briefly describe the setup and functionality of such a system. Figure 2.8 shows a schematic of the setup.

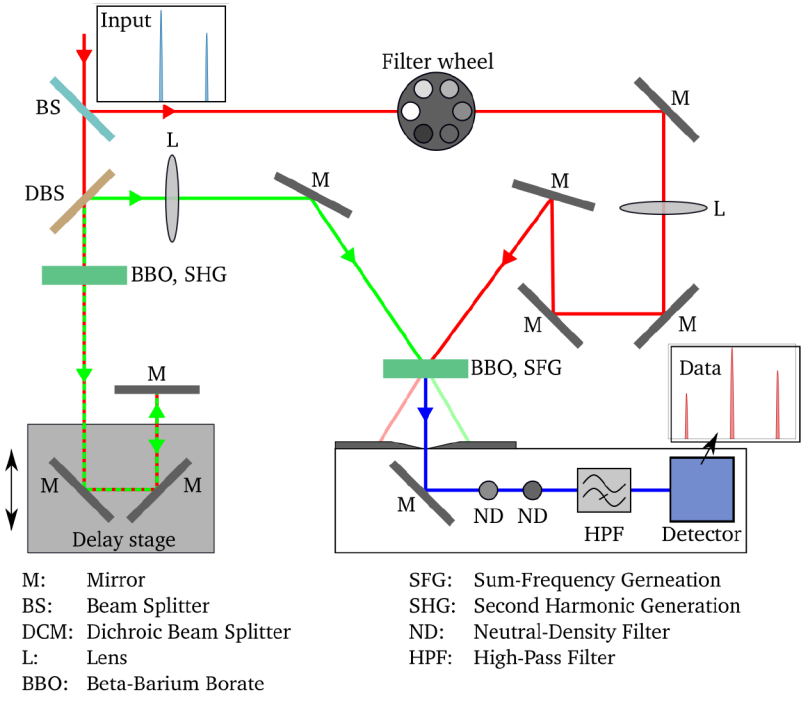


Figure 2.8.: Schematic setup of a third-order cross-correlator, based on reference [96].

The incoming pulse is split by means of a beam splitter (BS). The transmitted part of it passes a dichroic beam splitter (DBS), is frequency doubled in a BBO crystal (BBO, SHG), and undergoes a variable delay, which is adjusted for every measurement point. Reflected at a 0° mirror (M), the pulse is

sent back to the dichroic beam splitter and is separated from the residual, non-frequency-doubled pulse. Afterwards, the pulse is focused with a lens (L) on another BBO crystal (BBO, SFG). The portion that is reflected at the beam splitter passes through a filter wheel and is then also focused on the second BBO. The resulting sum frequency signal can be separated due to the non-collinearity of the fundamental beams and passes two neutral-density filters (ND), which can be used variably. Before the signal reaches the detector, which is a photon multiplier with adjustable amplification, it is additionally filtered by a high-pass filter (HPF) to remove potential stray light. The combination of all these variable filters and a noise reduction by a wider non-collinear angle of the **S**um-**F**requency **G**eneration (SFG) [96], a dynamic range of 14 orders of magnitude over a time window of 4 ns can be achieved [97].

Although this suffices to characterize the most relevant range of a CPA contrast trace, the biggest drawback of these devices is their time-consuming measurement. Since every step in time must be measured separately, the measurement, e.g., for a 10 Hz laser, can take several hours for a complete scan and cannot be used to measure pulse-to-pulse fluctuations. Furthermore, as the principle of this measurement is a correlation of the pulse with its frequency-doubled copy, artificial pre- or post-pulses will be generated from post- or pre-pulses in the measured contrast trace (compare Fig 2.8: "Data" and "Input"). However, the use of the frequency-doubled pulse for the correlation enables identifying the artificially created pulses, as the intensity of the artifact is reduced quadratically.

Lastly, I want to emphasize that the development of measurement devices for the characterization of the temporal field and intensity distribution is still an active field of research and new methods, ideas or devices are constantly investigated. For example, the technique of SRSI was further exploited to increase the dynamic range up to nine orders of magnitude and the temporal window up to 20 ps [98] while still providing single-shot performance and retrieval of the phase. Additionally, scaling to even higher dynamic ranges and longer time windows seems possible, making it a good candidate for intermediate time-window measurements.

## 2.4. Contrast-enhancement strategies - an overview

In this section, I cover the most relevant strategies and techniques, which are used to avoid temporal contrast features or reduce their intensity. This includes optical switching, phase manipulation, nonlinear-cleaning techniques, clean-amplification techniques or dedicated optical designs which are applied before the main amplification. Yet, also techniques such as plasma mirrors, which are applied after full amplification and compression, are discussed.

### 2.4.1. Fast optical switches

A simple, yet powerful strategy is the implementation of fast optical switches, such as a **P**ockels **C**ell (PC). Their functionality is based on the rotation of polarization by manipulating the birefringence of an optical medium. In combination with polarizers, these switches, with rise times as short as 100 ps, can suppress incoherent noise and pre- or post-pulses. However, after stretching the pulse, their influence only reaches as far as the stretched pulse duration, since otherwise the pulse energy and spectral bandwidth of the stretched pulse will be reduced. Furthermore, using these devices after compression is typically not possible since first, they rely on transmissive optics, which are to be avoided due to strong nonlinear effects and second, the beam size is typically too large for commercially available devices. Depending on the quality of the used polarizers, these devices can suppress contrast features with an extinction ratio of three to five orders of magnitude before stretching and outside the stretched-pulse duration.

### 2.4.2. Spectral-phase manipulation

The aim of this strategy is to minimize the residual spectral phase. This benefits the contrast in two ways. First, the contrast-degrading influence of higher spectral-phase orders, as shown in Fig 2.3(b), is reduced. Second, the pulse intensity is increased, which is a general aim in a high-intensity laser facility and also increases the contrast of the incoherent noise since its temporal incoherence renders it insensitive to small spectral-phase changes.

To minimize the residual spectral phase, the first step consists in adjusting the stretcher- and compressor alignment. However, since only second- and third-order spectral phases can be minimized by this alignment, other methods to remove the residual phase are necessary, especially for ultra-short pulses in the range of a few tens of femtoseconds. The most widespread solution to reduce this residual phase is the implementation of an AOPDF [42, 99] or a **S**patial **L**ight **M**odulator (SLM) [100, 101]. Both solutions enable direct manipulation and adaptive control of the spectral phase and amplitude and thus enable a fast and reactive optimization of the pulse duration. As these methods are commonly applied in the front-end of laser systems due to maximum energy- and beam-size limitations, they effectively pre-compensate the spectral phase which is generated later in the system.

### 2.4.3. Nonlinear pulse cleaning in a double-CPA setup

Targeting contrast features, such as pre-pulses, post-pulses and incoherent noise, a solution is given by nonlinear pulse cleaning. This method follows a pre-amplification and is applied in a double CPA setup as shown in Fig. 2.9.

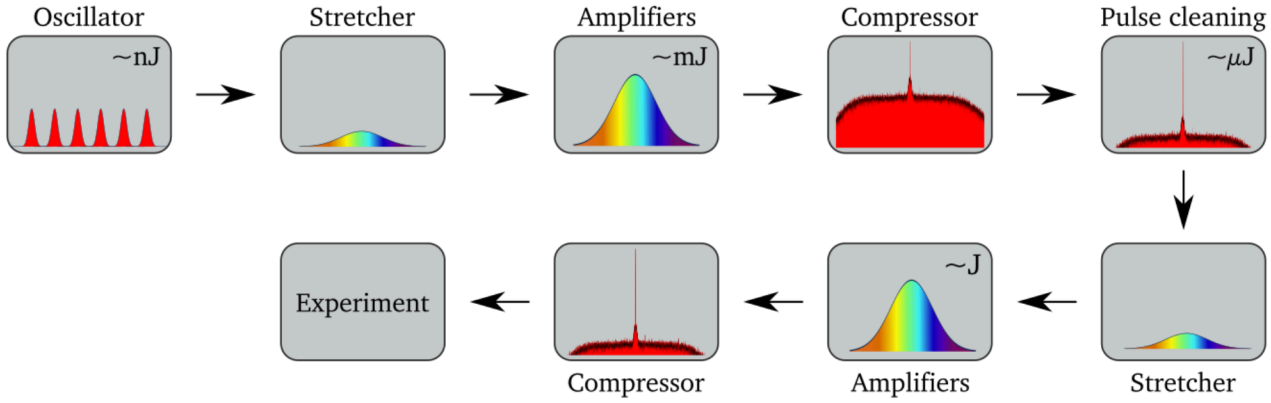


Figure 2.9.: Schematic setup of a double-CPA with the implementation of a nonlinear pulse-cleaning stage in between.

The basic principle of pulse cleaning is the creation of a pulse with significantly more energy than the oscillator can deliver but with a comparable or even improved contrast. The generated pulse is then used as the seed pulse for the main CPA. This increase in seed energy reduces the overall needed gain of the subsequent amplifiers, which in turn reduces the incoherent noise level by the same factor [56, 62]. Also, for regenerative amplifiers, the reduced gain may result in a lowered number of roundtrips and by this in a reduction of the total accumulated B-integral. In turn, the amplitude of pre-pulses generated by post-pulses would decrease.

However, it must be noted, that the implementation of a cleaning stage can only minder the already existing contrast features, but cannot avoid the creation of new pre-pulses, ASE, PSF or the ps-pedestal in the subsequent amplification chain.

To make use of the nonlinear cleaning mechanism, this technique requires to pre-amplify the pulses, as the cleaning is typically strongly intensity-dependent and its efficiency would otherwise diminish. Hence, a second CPA system is commonly implemented. Concerning the cleaning stage itself, multiple mechanisms were proposed and tested experimentally. In general, these mechanisms exhibit a nonlinear intensity dependence, which is only efficient at the peak intensity. This effectively suppresses the low-intensity portions of the pulse and the contrast gets enhanced

- **Cross (X) Polarized Wave Generation (XPW)** is a widely applied mechanism to clean the pulses. This method relies on a **F**our-**W**ave **M**ixing (FWM) process and therefore on the third-order nonlinearity of the material [102, 103]. As a result of the FWM, the linearly polarized input pulse is partially rotated to a perpendicular polarization (hence the name XPW). With the efficiency being dependent on the local cubic intensity, the rotated pulse dramatically increases its contrast. Another positive side-effect for short-pulse laser systems is a spectral-broadening effect, which however strongly depends on the residual quadratic spectral phase of the pulse [104].

  To effectively use the obtained high contrast level of the generated cross-polarized pulse, it must be separated from the residual input pulse. For this, the XPW crystal is contained in a set of crossed polarizers, such that non-rotated light is blocked, and rotated light transmits. This however limits the maximum obtainable contrast enhancement to the extinction ratio of polarizers, which is in a range of three to five orders of magnitude [102, 105, 106]. To maximize the efficiency of the process it is necessary to reach an intensity of approximately $\approx 10^{12}\,\mathrm{W/cm^2}$ [106, 107], which is however also the drawback of the method. The reason for this is twofold. First, to minimize nonlinear interaction apart from the XPW-generation, the setup is dependent on vacuum [106,107], increasing the complexity of the system. Second, the necessity of a high intensity to achieve high efficiency often leads to damage to the crystal, which may either result from a direct surface or bulk damage or darkening of the crystal [106, 107].

  Nonetheless, with this method, the incoherent-noise level could be lowered by roughly three orders of magnitude [105, 106] and contrast levels exceeding twelve orders of magnitude were demonstrated [37].

- **Nonlinear Ellipse Rotation (NER)** resides on similar mechanics as the XPW-process, as it is also using the polarization-rotating effect of nonlinear FWM, which depends on the cubic intensity and broadens the spectrum. Contrary to the previously mentioned method, NER uses pulses with an elliptic instead of linear polarization. Another difference becomes apparent in its applicability, which is not limited to crystal-based setups [108], but also allows the use of gaseous media. This enables its usage in setups based on gas-filled hollow-core fibers [109] and multi-pass cells [110, 111] and thus avoids the problem of laser-induced damage to the medium. However, since this method also relies on the separation of the fundamental and cleaned pulse via polarizers, its contrast enhancement is limited to the extinction ratio of the polarizers and therefore also to the quality of the quarter-WP [112], which is used to create and nullify the elliptically polarized light. Yet, an improvement of about 3.5 orders of magnitude could be realized with this technique, resulting in an incoherent-noise contrast of eleven orders of magnitude [113].

- **Self-Phase Modulation (SPM)** of short pulses can also be used to enhance the temporal contrast. To achieve this, it was proposed to significantly broaden the spectrum of a low-contrast pulse and filter out the fundamental spectrum, such that only the SPM induced spectrum remains [114]. As SPM is also a third-order nonlinear effect, mainly the peak intensity contributes to the generation of the spectral wings, which therefore feature an increased contrast. Via separation of the fundamental spectrum, the low-contrast portions of the pulse are removed. Since the use of this method shifts the

spectrum of the laser, a two-stage implementation must be considered to re-position the broadened spectrum back to the initial central wavelength. With this method, a contrast enhancement of seven orders of magnitude to a contrast level of nine orders of magnitude was demonstrated [114].

- **Self Diffraction (SD)** is also a FWM process, which has been implemented to clean the temporal contrast [115]. Instead of creating a collinear clean pulse that is separable by its state of polarization or spectrum as in XPW, NER or SPM, this method creates a spatially separated pulse, avoiding the use of polarizers. To spatially separate the pulses, a self-generated transient grating is used. This grating is created by crossing two pulses, whose interference pattern is intense enough to vary the refractive index quasi-instantaneously via the Kerr effect [116]. Due to the quasi-instantaneous variation of the refractive index, only the most intense parts of the pulse are diffracted, which effectively enhances the contrast. Although not limited through the finite extinction ratio of polarizers, this method's contrast limit is bound to scattered light on the surface and in the bulk of optics into the direction of the diffracted pulse [115]. Furthermore, the nonlinear diffraction in the Kerr-induced grating is accompanied by angular dispersion, which must be compensated. By this, an incoherent-noise contrast of almost ten orders of magnitude was achieved with an improvement of four orders of magnitude [117]

- **Low-gain, degenerate Optical Parametric Amplification (OPA)** as a method of pulse cleaning differs from most of the previously mentioned methods, as it is utilizing a second-order nonlinear effect. However, due to the pump-generation for this process by frequency doubling of the signal and a low gain, the pulse intensity resulting from the **D**ifference-**F**requency **G**eneration (DFG) of pump and signal is effectively proportional to the cubic of the signal intensity [118]. Since this process uses degenerate OPA, it must be applied in a non-collinear setup, to enable the separation of the generated clean pulse. However, this necessity also results in an angularly dispersed beam, especially for broadband pulses. With this method, an incoherent-noise contrast of ten orders of magnitude with an improvement of two orders of magnitude was realized [118].

- **Saturable absorbers** are another possibility to enhance the contrast between two CPA stages [119, 120]. This technique is well-known and commonly used in short-pulse oscillators [121, 122] to favor the build-up of intense pulses by suppressing fields with low intensity. This technique makes use of an intensity-dependent absorption coefficient, which for fast-recovery absorbers can be defined as $\alpha = \alpha_0/(1 + I/I_{sat})$ [123]. Here, $\alpha_0$ is the medium-dependent absorption coefficient, $I$ the intensity and $I_{sat}$ the saturation intensity. To effectively dampen the low-contrast features, these parameters must be chosen precisely. Specifically, the saturation intensity must be significantly greater than the intensity of the pre-pulses or the incoherent noise and ideally significantly smaller than the main-peak intensity to effectively dampen the unwanted signals. With this technique, an improvement of the incoherent-noise contrast by two orders of magnitude to a contrast level of twelve orders of magnitude has been demonstrated [120].

- **NonLinear Fourier Filtering (NLFF)** is a method that has been proposed and implemented for the ultra-violet spectrum [124] but claims to be scalable to other spectral regions such as near-infrared [125]. The foundation for this method lies in a selective nonlinear phase shift in the focal plane due to the plasma generation in noble gases, which induces a directional modulation of the beam [124]. The beam propagates through a set of conjugate filters, which completely block the beam if no nonlinear phase shift is induced. However, for a sufficiently intense pulse, the most intense spots in the focal plane undergo a nonlinear-induced phase shift of ideally $\pi$, which modifies the output distribution of the beam and increases the transmission through the conjugate filters [125]. Due to the low intensity of the incoherent noise, pre-pulses and to some

extent the ps-pedestal, barely any nonlinear phase-shift is introduced, causing them to be blocked at the second filter. By using a gaseous nonlinear medium, no regular replacements are necessary. With NLFF, a contrast enhancement of five orders of magnitude with an energy efficiency of 40 % has been realized in the UV [125] but has yet to be demonstrated for short-pulse lasers in the near-infrared.

### 2.4.4. Direct amplification of the short pulse

Opposed to the pulse-cleaning methods, we find the idea of a temporally clean and direct amplification of the short pulse without the need for subsequent nonlinear cleaning. Although the nonlinear cleaning methods presented in section 2.4.3 are applied worldwide in several high-intensity laser systems, their implementation has the drawback of increasing complexity due to the necessity of an additional stretcher-compressor pair. This is especially relevant for narrowband lasers whose stretcher and compressor setups are large compared to broadband lasers. Furthermore, avoiding contrast degradation instead of removing it with limited efficiency seems to be an elegant solution.

Direct amplification of the short laser pulse to relevant pulse energies of a few hundred microjoules or even millijoules was demonstrated [126]. However, this type of amplification is prone to the generation of ASE, depends on the seed energy and therefore severely limits the achievable temporal contrast [127]. Additionally, the need to transmit through an active medium multiple times to achieve high-gain levels increases the risk of pulse-replica generation.

However, parametric amplification, although plagued by PSF, offers a solution. This method, also called **u**ltrafast **O**ptical **P**arametric **A**mplification (uOPA) or ps-OPA, was proposed as a high-gain pre-amplifier [128] for high-intensity laser facilities. A schematic setup of the resulting signal-amplification chain is shown in Fig. 2.10.

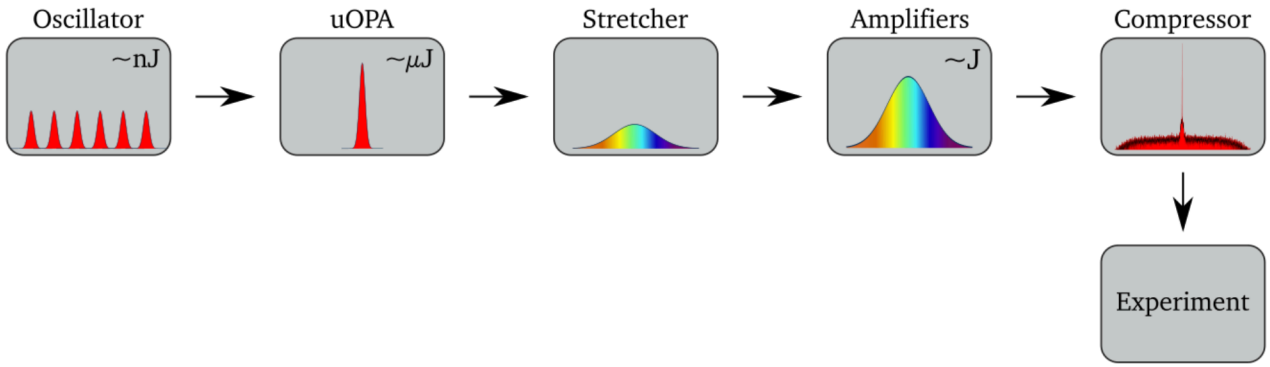


Figure 2.10.: Schematic setup of a uOPA implementation in a high-intensity laser amplification chain.

A direct comparison to the setup of a double-CPA (comp. Fig. 2.9), shows a clear decrease in complexity within the context of the signal-propagation and handling, as the additional stretcher and compressor are removed. Of course, a pump setup is needed, which however does not exhibit the same requirements concerning the temporal quality as the signal. However, since the pump-pulse acts as the noise source of the OPA as described in section 2.1.3.2, a stringent requirement to mitigate contrast degradation via PSF is the reduction of the pump-pulse duration to a similar pulse duration as that of the signal. If this requirement is fulfilled and PSF is generated, it is confined to approximately the temporal duration of the signal and therefore does not degrade the contrast on a relevant timescale. Outside this time window,

the magnitude of the contrast enhancement by this technique on the already existing contrast-degrading features is related to the overall gain of the uOPA, and therefore it is limited only by the size of the nonlinear crystal and the energy of the pump laser.

This energy scalability also makes this method interesting as it implies the capability to create millijoule-level pulses. With this output energy, a uOPA can replace millijoule-level regenerative amplifiers, and therefore may also remove pre-pulses that originate in said amplifiers while reducing the overall complexity of the laser facility instead of increasing it. Similar to the cleaning methods, it must be noted that uOPA, does not infer with the creation of the ps-pedestal, as it is implemented before stretching and does not avoid pre-pulses, which emerge in the subsequent laser chain.

### 2.4.5. Dedicated stretcher designs

I also want to mention the current research concerning the ps-pedestal in CPA lasers and how to suppress or avoid it from the beginning instead of partially suppressing it afterwards. Within the recent years, as described in section 2.1.5, the origin of this ps-pedestal could be identified as being the spectrally-dispersed beams in the stretcher and compressor of a CPA laser, which accumulate a spatially- and therefore spectrally-dependent phase shift on the non-perfect surface. Although the post-compressor cleaning mechanisms (see next section) offer a possibility to reduce this ps-pedestal, avoidance from the beginning would still be preferable. With surface irregularities being the origin of the phase noise, a logical step led to the use of super-high-quality optics which exhibit less distortion and therefore reduce the phase noise [32]. However, an indefinite increase of optical quality is neither feasible, nor does it completely suppress the ps-pedestal, but rather reduces its contrast level by a certain offset.

More recent studies show promising results by exploiting the averaging effect on the spatial noise by using a larger beam size [68] and avoiding optics in the far-field [129]. The proposed methods do however call for complete re-designs of modern stretcher systems, as these are typically folded to save space, optics, and costs or to avoid aberrations [41] and therefore use optics in the focal plane. Due to the reduced beam size on these optics, barely any averaging effect is used, causing the largest share of the total phase noise.

### 2.4.6. Cleaning of the fully amplified, compressed pulse

Contrary to the previously mentioned methods, which are used to create a high-contrast pulse to seed the CPA laser, the following methods are designed to clean the pulses after main amplification and compression of the pulse. Consequently, these methods target all contrast-degrading features. In the following list, I will briefly discuss these post-compressor pulse-cleaning methods.

- **Plasma mirrors** belong to the more widespread methods among this list. The principle of their functionality lies in a temporally precise ignition of a plasma on an AR-coated substrate, which then rapidly increases its reflectivity [130, 131]. As a result, the incoherent noise, pre-pulses and the ps-pedestal are mostly transmitted and only partially reflected due to the residual reflectivity of the AR coating, as far as their intensity is low enough to avoid a plasma ignition by themselves. The contrast increment is therefore as high as the transmission of the AR coating - in the range of two to three orders of magnitude.

  For this method to work properly, precise positioning of the mirrors is needed, such that the plasma ignites at the correct timing. Concerning nowadays laser intensities, this requires implementation in the intermediate field and therefore must avoid premature ignition, as this will otherwise not only affect the temporal contrast but also the spatial quality of the pulse [131]. Despite their usefulness

and tested applicability in high-intensity lasers, it must be noted that the implementation of such a system is generally accompanied by a large vacuum-setup, containing two off-axis reflecting mirrors to focus and re-collimate the beam, and therefore strongly increases the complexity of the laser facility. Moreover, the use of a plasma mirror results in an energy loss of about 30 % [131,132] and calls for a regular replacement of the optics, as the AR coating is destroyed, increasing the daily costs of operation. With this strategy, incoherent-noise contrast levels above 14, up to 17 orders of magnitude have been estimated [37,133,134]

- **Second-Harmonic Generation (SHG)** of the pulse in large, but thin nonlinear crystals after compression is another valid option to increase the contrast. Due to the size of the beam at the end of the amplification chain in high-intensity laser systems, the frequency conversion is applied in a collinear setup, which requires the use of multiple dichroic mirrors to separate the frequency-doubled from the fundamental wave. Similar to the plasma mirrors, the conversion to higher frequency is accompanied by a loss of energy, due to a limited conversion efficiency. Here, conversion efficiencies of 30 % [135] and 75 % (not including 70 % energy loss due to apodization to match the size of the SHG crystal) [136] were achieved. Another drawback of this method is that only view nonlinear crystals are available in the relevant aperture sizes [51]. However, with post-compression SHG, incoherent-noise contrast levels of $10^{14}$ [136] and $10^{17}$ [135] have been estimated.

- **Plasma shutters** line up together with plasma mirrors and NLFF in terms of using a plasma to manipulate the temporal contrast. Plasma shutters, however, specifically aim at reducing the ps-pedestal of the laser pulse. Note that the term "plasma shutter" sometimes also refers to plasma mirror, which, however, is not meant here. This method heavily depends on the transmissive properties of a plasma for electromagnetic waves, which is defined by its dispersion relation. In general, an electromagnetic wave can only propagate through a plasma if its frequency is above the plasma frequency, which itself depends on the electron density of the plasma and the electron mass [81]. The setup of the plasma shutter includes an additional thin target, which must be ionized by the ps-pedestal of the laser pulse. The created plasma is then ideally dense enough to reflect and absorb the ps-pedestal, while the main pulse intensity is high enough to increase the mass of the electrons by accelerating them to relativistic velocities. Accordingly, the electron mass increases relativistically, resulting in a reduced plasma frequency [137]. If the plasma frequency is sufficiently reduced to create a transparent plasma for the main pulse, the contrast after the transmission gets enhanced. This relativistic pulse-shaping was theoretically described [138] and implemented [139]. It must be noted, that exploitation of this mechanism requires accurate knowledge of the contrast [139] and is, similar to the use of plasma mirrors, a single-shot device. With this method, a transmission of 70 %-99 % was achieved but the increase of the contrast could not be quantified [139].

### 2.4.7. State of the art

Although there are plenty of mechanisms that can provide a high temporal contrast, only the most robust and mature schemes are found at high-intensity laser facilities. A comprehensive listing of mechanisms that are implemented at current laser facilities is shown in table 2.2. A more detailed overview of the laser systems and their implemented contrast-cleaning mechanisms can be found in table A.1 in appendix A.1.

The most widespread strategies to enhance the contrast at the front-ends employ XPW or short-pulse OPA systems (sub-ps to ≈20 ps). Some facilities combine these methods with saturable absorbers,

Table 2.2.: Distribution of used or planned contrast-enhancing strategies at front-ends (FE) or post-compression (PComp) at 46 high-intensity laser facilities. A detailed mapping of the strategies to the associated laser system is given in table A.1 in appendix A.1. The front-end table contains 48 entries, as two facilities use either SP-OPA or XPW, and are therefore listed for both strategies.
SP-OPA: short-pulse OPA, XPW: cross-polarized-wave generation, SHG: second harmonic generation, PM: plasma mirror, SFG: sum-frequency generation, SA: saturable absorber, LG-OPA: low-gain OPA.

| FE strategy | No. of implementations |
|---|---|
| **SP-OPA** | 12 |
| **SP-OPA + SHG/SFG** | 3 |
| **SP-OPA + LG-OPA** | 1 |
| **SP-OPA + XPW** | 5 |
| **XPW** | 18 |
| **XPW + SA** | 1 |
| **SA** | 3 |
| **None** | 5 |

| PComp strategy | No. of implementations |
|---|---|
| **PM** | 13 |
| **SHG** | 4 |
| **None** | 29 |

low-gain OPA, SHG or SFG. Among the listed systems, only three use only saturable absorbers and five systems apply no contrast-enhancement strategy at the front-end. After main amplification and post-compression, there are mainly two strategies in use, which are either plasma mirrors or SHG. However, most laser facilities do not provide any of these methods by default.

### Conclusion

The previous sections have shown that there are a variety of approaches to clean the temporal contrast or even to partially avoid contrast degradation. Within this thesis, I will lay the focus on the method of direct clean amplification via uOPA. From the pre-stretcher methods, uOPA stands out for multiple reasons.

First, it is a well-proven technique and is scalable in energy. As being developed within the PHELIX facility, the energy-scalability of uOPA is of great interest, since sufficient output energy enables to bypass one of the front-end amplifiers, which is known to be the origin of several intense pre-pulses [140]. Second, uOPA provides the elegance of directly generating a clean pulse without further need for cleaning.

Last, even though XPW is a well-proven technology and is used in lots of laser facilities, its applicability is partially restricted to ultra-short pulses ($<100\,\mathrm{fs}$), since the needed intensity can quickly result in excessively high fluence that may damage the crystal and hence, limit its energy-scalability. Furthermore, due to its energy scalability, uOPA can potentially reach higher levels of incoherent contrast, as it is not restricted to polarization-dependent extinction ratios.

The main scope of this thesis is therefore the development and setup of a versatile, millijoule-level, high-contrast module for high-intensity laser systems based on the technique of uOPA.

# 3. Design considerations for a millijoule-level uOPA

Within the previous chapter, I discussed a variety of contrast-enhancement strategies, which led me to the conclusion of using the strategy of uOPA as the foundation for a high-contrast module in front-ends of high-intensity laser systems. For this, the system will have to generate pulses with energies in the millijoule range to improve the incoherent contrast and to provide an alternative to high-gain amplifiers, such as regenerative amplifiers. As a consequence, the system may also avoid pre-pulses originating in said amplifiers.

Within this chapter, I am going to discuss the fundamentals of uOPA, the process of OPA. This includes describing the parameters which will impact the dynamics of the amplification process and the requirements for the OPA design, which originate from this. To get a clear view of the OPA-dynamics, the chapter begins with the description of the OPA fundamentals by deriving the analytical description of the process. From this description, I will detail the parameters that impact the amplification and show which parameters can be adjusted to my needs. Last, I will derive the requirements for the pump and seed of the uOPA by numerical simulation of the process with regard to the set goals of this amplifier.

## 3.1. Fundamentals of short-pulse optical parametric amplification

Before the determination of requirements for the system by numerical calculation, it is useful to get deeper insights into the theoretical description of OPA. For this purpose, the short-pulse mixing equations as well as an analytical solution of the OPA process are derived and their most important parameters with regard to short-pulse OPA are discussed in the following.

### 3.1.1. Theoretical description

OPA is a parametric process and allows to quasi-instantaneously transfer energy [66] from an intense high-frequency wave to another low-frequency wave, by utilizing the nonlinear response of optical media. As the high-frequency wave, from here on called pump, is converted to a low-frequency wave, from here on called signal, a third wave must be created to fulfill energy conservation:

$$\hbar\omega_p = \hbar\omega_s + \hbar\omega_i. \tag{3.1}$$

This wave is called idler. Here, $\omega_{p,s,i}$ is the angular frequency of the pump, signal and idler, respectively. Since the signal is not absorbed, but rather stimulates the pump wave to split into one photon at the signal- and one at the idler frequency, the signal is effectively amplified. From this point on, the idler also stimulates this process, which in turn leads again to the amplification of the idler and signal. This process is called OPA. The result of the mutual amplification of the signal and idler is an exponential growth of their field amplitudes [66]. If signal or idler experience losses during amplification, caused by e.g. absorption or parasitic processes, this can drastically reduce the exponential gain. [141, 142].

A schematic drawing of the OPA process in terms of an energy level diagram is shown in Fig. 3.1(a). The signal photon at frequency $\omega_s$ stimulates the pump photon at frequency $\omega_p$ to convert into photons

at frequencies $\omega_s$ and $\omega_p - \omega_s = \omega_i$. At this point, the same conversion can also be triggered by a photon at frequency $\omega_i$. Over the cause of the amplification process, idler and signal experience an exponential gain until the pump field depletes. Figure 3.1(b) depicts a schematic of the gain evolution of signal and idler.

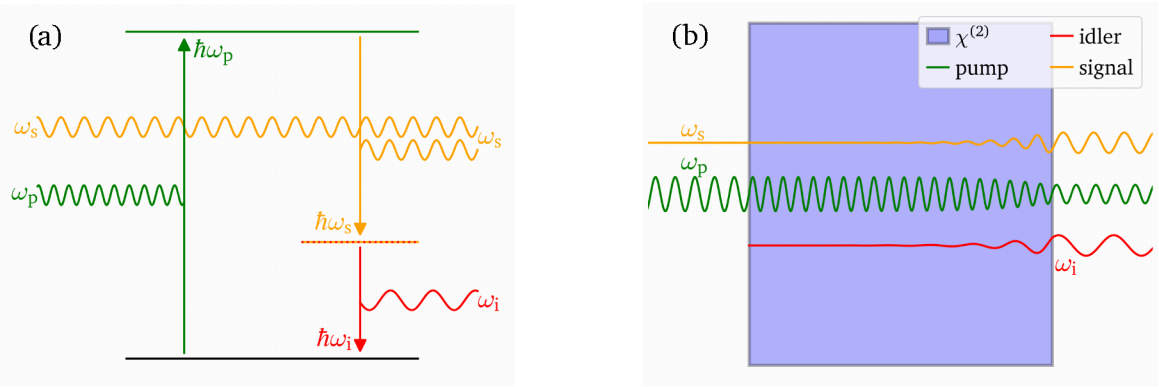


Figure 3.1.: (a) Energy level diagram of the initial **D**ifference-**F**requency **G**eneration (DFG) process. (b) Schematic of an OPA setup. Two fields at frequencies $\omega_p$ (pump) and $\omega_s$ (signal) with large and small amplitude respectively, propagate through a second-order nonlinear medium ($\chi^{(2)}$) and create a field via DFG at $\omega_i$ (idler), which is typically not present at the input. Over the propagation length of the medium, the process of OPA amplifies the fields of the idler and signal and depletes the pump field.

A theoretical description of this field evolution can be given by the coupled-wave equations, which describe the mixing of the three fields in a second-order nonlinear medium:

$$\text{signal} \quad \rightarrow \quad \left(\frac{\partial}{\partial z} + \frac{1}{v_{g,s}}\frac{\partial}{\partial t} + j\frac{GVD_s}{2}\frac{\partial^2}{\partial t^2}\right) A_s - \frac{j}{2k_s}\nabla_\perp^2 A_s = -j\sigma_s A_p A_i^* e^{-j\Delta k z} \tag{3.2}$$

$$\text{idler} \quad \rightarrow \quad \left(\frac{\partial}{\partial z} + \frac{1}{v_{g,i}}\frac{\partial}{\partial t} + j\frac{GVD_i}{2}\frac{\partial^2}{\partial t^2}\right) A_i - \frac{j}{2k_i}\nabla_\perp^2 A_i = -j\sigma_i A_p A_s^* e^{-j\Delta k z} \tag{3.3}$$

$$\text{pump} \quad \rightarrow \quad \left(\frac{\partial}{\partial z} + \frac{1}{v_{g,p}}\frac{\partial}{\partial t} + j\frac{GVD_p}{2}\frac{\partial^2}{\partial t^2}\right) A_p - \frac{j}{2k_p}\nabla_\perp^2 A_p = -j\sigma_p A_s A_i e^{j\Delta k z}., \tag{3.4}$$

$$\text{with} \quad \sigma_m = \frac{\omega_m d_{eff}}{n_m c_0}, \qquad m \in \{s, i, p\} \qquad . \tag{3.5}$$

The derivation of these equations is detailed in appendix A.3 and A.4 and follows the description of reference [66]. With $m \in \{s, i, p\}$, $A_m$ is the temporally and spatially dependent field envelope, $v_{g,m}$ the group velocity, $GVD_m$ the group-velocity dispersion, $\nabla_\perp$ the nabla operator in x and y, $k_m$ the wave number of the field's center wavelength, $d_{eff}$ the effective nonlinear coefficient, $n_m$ the refractive index, $c_0$ the vacuum speed of light, $\Delta k$ the phase mismatch and $j$ the imaginary unit. The phase mismatch is defined as

$$\Delta k = k_p - k_s - k_i, \tag{3.6}$$

and describes the phase relation between the created wave and the nonlinear polarization and is an important parameter for efficient amplification via OPA. This parameter will be further discussed in section 3.1.2.

The derived coupled-wave equations include diffractive and dispersive effects via the spatial and temporal derivatives, respectively. This allows to describe the mixing of short pulses, including beam diffraction. Solving these equations and calculating the result of the mixing needs a numerical treatment. However, for a plane, monochromatic wave and the assumption of a strong pump field that does not deplete, these equations can be solved analytically to (see appendix A.3):

$$I_s(z) = I_s(0)\left[1 + \left(\frac{\gamma}{g}\sinh(gz)\right)^2\right] = I_s(0)\cdot G_{par}(z) \tag{3.7}$$

$$I_i(z) = I_s(0)\frac{\omega_i}{\omega_s}\left(\frac{\gamma}{g}\sinh(gz)\right)^2 \tag{3.8}$$

with $$g = \sqrt{\gamma^2 - \frac{\Delta k^2}{4}} \tag{3.9}$$

and $$\gamma^2 = \frac{2\omega_s\omega_i d_{eff}^2}{c^3 n_s n_i n_p \varepsilon_0} I_p = \frac{2\omega_s\omega_i}{c^3\varepsilon_0}\zeta I_p. \tag{3.10}$$

Here, $I_{s,i,p}$ is the intensity of signal, idler and pump, $z$, the length of the nonlinear medium, $g$ is the small-signal gain, $G_{par}$ is the parametric gain and $\zeta := d_{eff}^2/(n_p n_i n_s)$ is referred to as the figure of merit of the mixing process [142]. This non-depleting pump approximation clearly describes an ideal case, because limitations, such as a finite pump pulse energy, are neglected. However, the parametric gain within this approximation can be interpreted as an upper limit for a realistic gain.

### 3.1.2. Insights from the coupled-wave equations

The equations shown in the previous section highlight the most important parameters for the mixing of short pulses. These are different group velocities and dispersion for each field, the material thickness $z$ and the small-signal gain $g$, which includes material properties via $\zeta$ as well as the phase-mismatch $\Delta k$. In the following, I will discuss the influence of these parameters.

#### 3.1.2.1. Parametric gain in the non-depleting pump approximation

The most prominent factor in eq. 3.7 is the length of the nonlinear medium $z$ and the small-signal gain $g$ for which the parametric gain $G_{par}$ scales exponentially within the non-depleting-pump regime. While the influence of $z$ is straightforward and only depends on the configuration of the setup, the small-signal gain features multiple dependencies, which are the phase mismatch $\Delta k$, the pump intensity $I_p$, the idler and signal frequencies, and material properties characterized by $\zeta$.

According to eq. 3.9, the small-signal gain is maximized when the phase mismatch is zero. This reduces the small-signal gain to $g = \gamma$, which then only depends on the previously mentioned parameters. However, for a non-zero phase mismatch $\Delta k$, $g$ and therefore $G_{par}$ reduce significantly. This also affects the gain bandwidth, as shown in Fig. 3.2(a). Here, only the center wavelengths are perfectly phase-matched and the phase mismatch grows with an increasing difference to the center wavelength. Since the phase mismatch accumulates over the propagation distance, the gain bandwidth also depends on the total propagation distance.

Furthermore, according to eq. 3.7, if the phase-mismatch is so large that the radicand in the small-signal gain becomes negative, $g$ becomes a complex value and causes oscillatory behavior, with a shorter period for a larger phase mismatch. This is depicted in Fig. 3.2(b). Initially, all waves are amplified, but the effective gain after a distance z starts to decrease for fields with a non-vanishing phase mismatch.

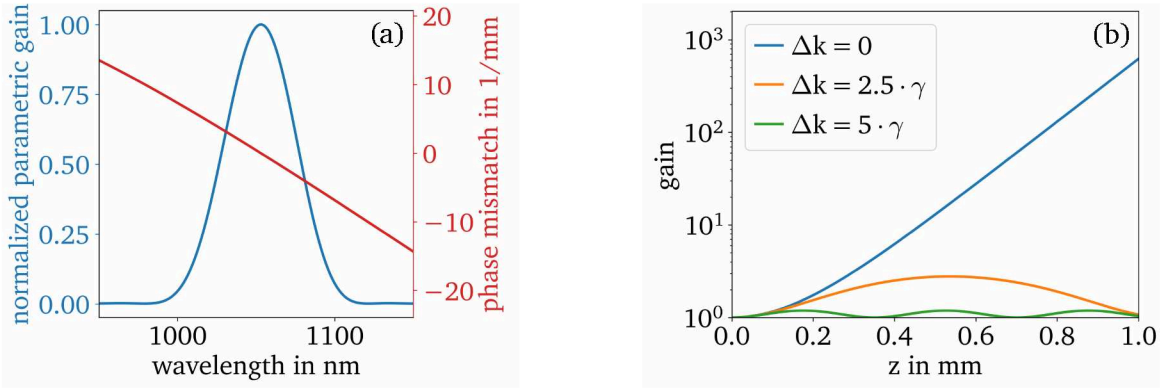


Figure 3.2.: (a) Normalized parametric gain and phase mismatch as a function of the signal wavelength with an optimized phase mismatch at 1053 nm in a 1 mm long, collinear setup. (b) Reduction of the parametric gain as a function of the phase mismatch and z. The calculations were performed for a pump with an intensity of 40 GW/cm$^2$ at 400 nm, a signal wavelength of 1053 nm and an idler wavelength of 645 nm in a common nonlinear material $\beta$-**B**arium **BO**rate (BBO).

Eventually, the fields reach a maximum and start to transfer energy back to the pump. This process is also referred to as reconversion. To increase the reconversion period aside from minimizing the phase mismatch, $\gamma$ (see eq. 3.10) can be increased by either using a higher pump intensity or a material with higher $\zeta$ might be used. However, ideally, the phase mismatch is minimized, which will be described in the next section.

#### 3.1.2.2. Phase matching

As shown before, phase matching is a condition that must be fulfilled to create a large gain via OPA and is defined by the difference of wave vectors as described in eq. 3.6. Inside media, the wave vector depends on the refractive index of the corresponding frequency and the absolute value of the wave vector takes the form $|k(\omega)| = n(\omega)\omega/c_0$, which in turn leads to the following form of the phase-matching condition:

$$\omega_p n_p = \omega_s n_s + \omega_i n_i. \tag{3.11}$$

Due to the necessity to fulfill the energy conservation (eq. 3.1) we find that the condition of eq. 3.11 would only be fulfilled, if $n_p < n_s, n_i$ which is not the case for any frequency range in a medium that exhibits normal dispersion ($dn/d\omega > 0$). Consequently, other material properties must be exploited to achieve phase matching. Well-known techniques to solve this problem are angle phase matching [143, 144], temperature phase matching [145, 146], and quasi-phase matching [147, 148], of which the technique of angle phase matching was used in this work.

Angle phase matching exploits the polarization-dependency of the refractive index in birefringent media. By choosing an angle between the propagation direction of the wave and the optical axis of the medium, the refractive index can be tuned between the ordinary index $n_o$ and the extraordinary index $n_e$. As the state of polarization is another degree of freedom in this technique, one distinguishes between phase matching of type I and II [144]. For a uniaxial crystal, which exhibits a single extraordinary axis, this angle can be calculated via [66]:

$$\frac{1}{n(\omega,\theta)^2} = \frac{\cos(\theta)^2}{n_o(\omega)^2} + \frac{\sin(\theta)^2}{n_e(\omega)^2}. \tag{3.12}$$

This equation describes an ellipse with the principal-axes radii being the extraordinary refractive index $n_e$ at $\theta = 90°$ and the ordinary refractive index $n_o$ at $\theta = 0°$. Changing the angle $\theta$ will result in a refractive index with a value between $n_e$ and $n_o$, as described by eq. 3.12. For phase-matching angles that are neither 90° nor 0°, this method also causes a birefringent, spatial walk-off due to the non-parallelism of the wave vectors and the Poynting vector [66]. Depending on $n_e$ being smaller or larger than $n_o$, the material is said to be negative or positive uniaxial [149]. As long as the desired value for the refractive index lies between the value on the ordinary and extraordinary axis for a given wavelength, a phase-matching angle can be found. Figure 3.3 shows the phase-matching angles for an exemplary setup with a pump at 400 nm in BBO as a function of the signal wavelengths for a type-I (blue, extraordinary: pump) and type-II (orange, extraordinary: pump and signal) setup.

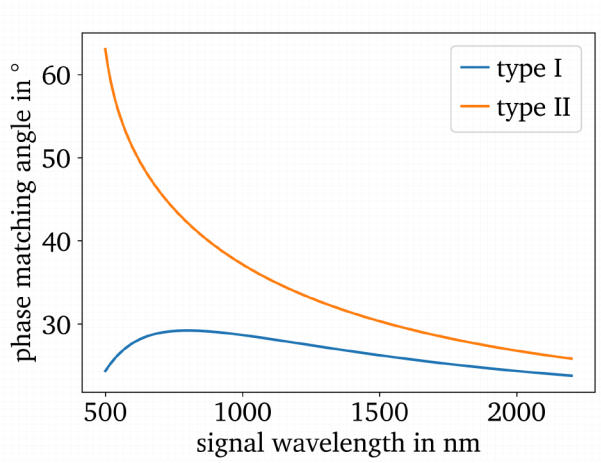


Figure 3.3.: Dependency of the type-I (blue) and type-II (orange) phase-matching angle on the signal wavelength for a pump with extraordinary polarization at 400 nm in a collinear configuration.

Figure 3.3 shows, that for a pump at 400 nm in BBO a wide spectrum of signal wavelengths can be phase matched by changing the propagation angle of the extraordinarily polarized wave accordingly. While the phase-matching angle for signal wavelengths close to degeneracy varies strongly in a type-II setup, the type-I setup exhibits only minor changes. This slow variation of the phase-matching angle dependence on the signal wavelength is a key factor for broadband amplification.

**Broadband, non-collinear phase matching**

In type-I collinear phase-matching schemes, the broadest phase-matching bandwidth is found around the degeneracy point. However, in non-collinear setups, it is possible to slightly tune the phase-matching condition, such that broader phase-matching bandwidths without degeneracy can be achieved. A schematic drawing of a non-collinear phase-matching configuration is depicted in Fig. 3.4.

Inherently different from the collinear setup, the propagation angle of the created idler frequency depends now on the frequency of the signal and the angle between signal and pump such that the phase mismatch is minimized. For a broadband signal, this will result in an idler with angular dispersion [150], as indicated in Fig. 3.4. As long as the idler is only a by-product of the signal amplification, the angular dispersion is of no concern. However, if the OPA is used to create beams in the infrared or to use the

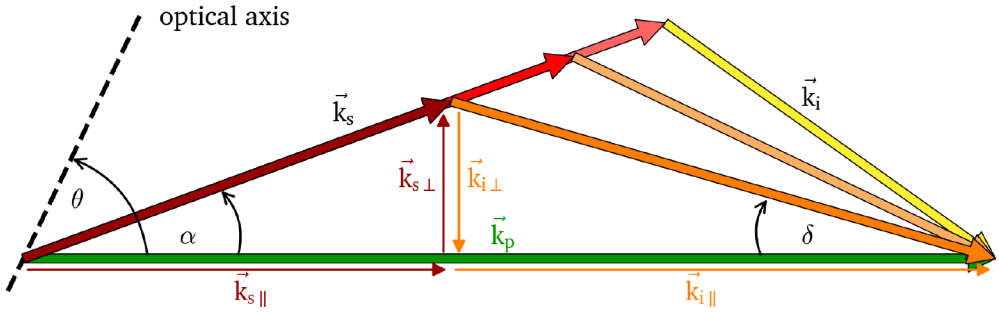


Figure 3.4.: Schematic drawing of a non-collinear phase-matching setup. The wave vectors of the idler are split into parts that are parallel and perpendicular to the pump wave vector. $\theta$ is the phase-matching angle of the pump, $\alpha$ the non-collinear angle and $\delta$ the angle between idler and pump. The colors are representative of different frequencies of signal or idler.

idler as a cleaned pulse, as described in section 2.4.3, special treatment is necessary to either remove the angular dispersion or to avoid it by using an angularly dispersed signal. In my case, the focus lies on amplifying the signal, which is why further discussion of this topic is omitted.

Figure 3.5 gives an impression of how the introduction of a non-collinear configuration and the resulting dependency of the idler propagation direction on the non-collinear angle manipulates phase-matching bandwidths. The phase-matching angle $\theta$ is plotted as a function of the signal wavelength and the non-collinear angle $\alpha$ in a type-I setup in BBO with pumps centered at 400 nm (Fig. 3.5(a)) and at 515 nm (Fig. 3.5(b)).

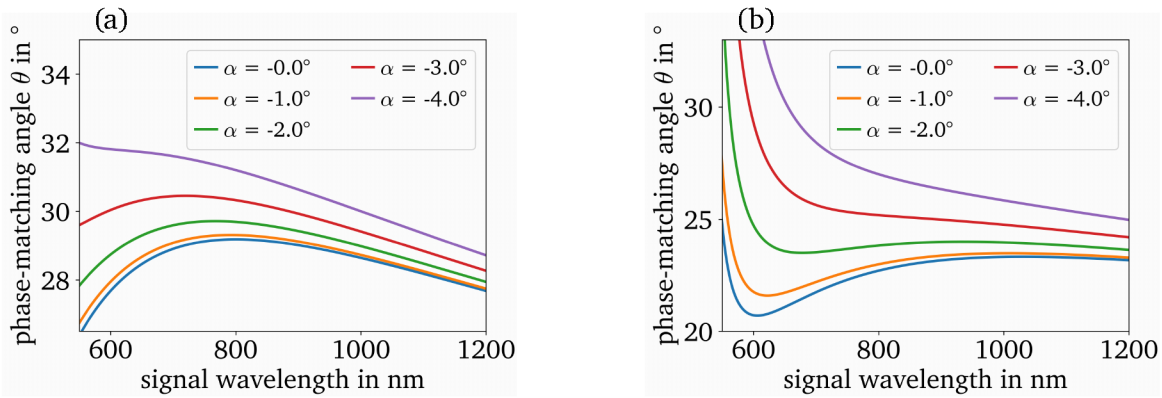


Figure 3.5.: Phase-matching angles for a non-collinear OPA configuration of type-I in BBO for a pump at 400 nm (a) and for a pump at 515 nm (b).

Figure 3.5 shows two things. First, by adjusting the non-collinear angle, the regions with a slowly-varying phase-matching angle can be shifted. For some non-collinear angles, plateau-like structures form, implying broad phase-matching bandwidths as the phase mismatch increases only slowly around a phase-matched wavelength. Second, a strong dependence on the pump wavelength can be observed.

The dependency of the phase mismatch on the non-collinear angle becomes clearer when the phase mismatch is expressed in vector form and expanded into a Taylor series around the center frequencies. Then, it can be shown (see appendix A.5) that apart from the fulfillment of phase matching for the center wavelengths (zeroth order of the Taylor series), also the first order of this series can be minimized

by choosing an appropriate non-collinear angle, which enables broader phase-matching bandwidths. The condition for the non-collinear angle reads:

$$v_{g,s} = v_{g,i} \cdot \cos(\alpha + \delta). \tag{3.13}$$

Within the context of pulse-propagation, this can be interpreted as the matching of the pulse-propagation velocities. As idler and signal have different group velocities, the pulses are expected to walk off temporally, aside from the degeneracy point.

By introducing an angle between pump and signal, the effective group velocity in direction of the signal is the projection of the idler propagation along the propagation vector of the signal. Consequently, if the angle is chosen, such that the projected idler group velocity equals the signal group velocity, the temporal overlap can be maintained.

It is to notice, that this kind of phase-matching optimization cannot be employed for a signal at any center wavelength. Since the idler group velocity must be projected onto the group velocity of the signal it is mandatory that $v_{g,i} \geq v_{g,s}$. Otherwise, no solution can be found, that fulfills the additional phase-matching condition of minimizing the first coefficient of the phase-mismatch Taylor series $\Delta k^{(1)} = 0$ perfectly.

However, this does not mean that broadband mixing is not possible, and indeed as long as the accumulated phase mismatch remains reasonably small, high efficiency can still be attained. This is pronounced in Fig. 3.5(b). Although eq. 3.13 cannot be fulfilled, a broad phase-matching plateau, ranging from 900 nm to 1200 nm for non-collinear angles around -2°, can be observed.

#### 3.1.2.3. Temporal and spatial walk-off

The previous section highlighted the importance of matching group velocities when considering pulses in order to avoid temporal walk-offs, which for signal and idler leads to a larger amplification bandwidth. With the description of the pump as a field with finite temporal and spatial extent, it immediately follows that the parametric gain, which depends on the pump intensity, also becomes a function of space and time. To obtain a uniform and non-vanishing gain, temporal and spatial separation of the fields should be avoided.

It is therefore useful to define a pulse- and beam-splitting length, which defines the propagation distance at which signal and pump separate. While the beam-splitting length $L_{BS}$ depends on the pump beam diameter $d_p$ (**F**ull **W**idth **H**alf **M**aximum (FWHM)) and the effective angle $\alpha_{eff}$ between pump and signal, including birefringent walk-off, the pulse-splitting length $L_{PS}$ depends on the pump pulse duration $t_p$ (FWHM) effective group-velocity mismatch [142], which is also dependent on the effective pump-to-signal angle. The splitting lengths can be defined as:

$$L_{PS} = \left| \frac{t_p}{\frac{1}{v_{g;s}\cos(\alpha_{eff})} - \frac{1}{v_{g;p}}} \right|, \qquad L_{BS} = \left| \frac{d_p}{\tan(\alpha_{eff})} \right|, \tag{3.14}$$

where $v_{g;p}$ and $v_{g;s}$ is the group velocity of the pump and signal. Both, $L_{PS}$ and $L_{BS}$, depend on the non-collinear angle between pump and signal and the refractive properties of the nonlinear material, which defines the group velocity and the birefringent walk-off angle.

These dependencies are visualized in Fig. 3.6, which shows $L_{PS}$ (a) and $L_{BS}$ (b) as a function of the wave-vector pump-to-signal angle and the signal wavelength. The pump is centered at 515 nm and features a pulse duration of 1 ps and a beam diameter of 2.5 mm. As there are configurations that feature no temporal or spatial walk-off, the graphic's colorbar is limited to a splitting length of 20 mm to emphasize the lower bounds.

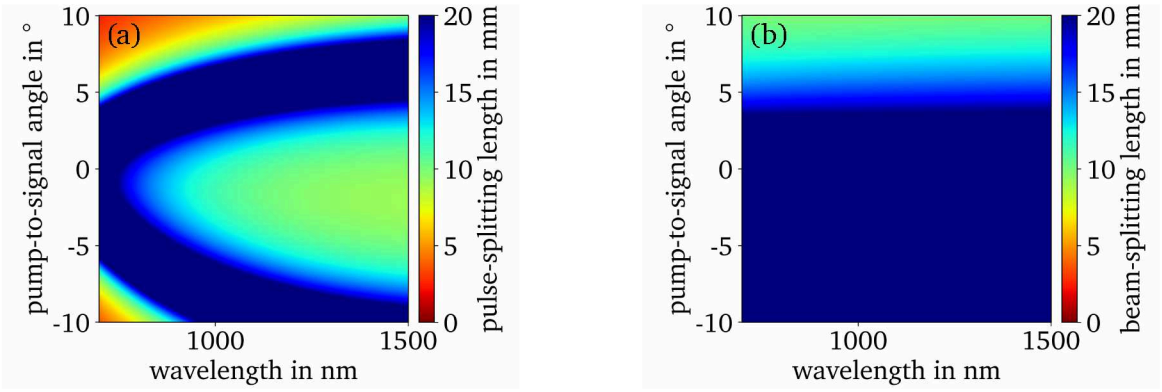


Figure 3.6.: Pulse-splitting length for a 1 ps pump (a) and beam-splitting length for a pump with a beam FWHM of 2.5 mm (b) as a function of the wave-vector pump-to-signal angle and the signal center wavelength in a type-I setup in BBO. The pump is centered at 515 nm.

In this configuration, the beam-splitting length always surpasses 9.8 mm and the pulse-splitting length is always larger than 2.5 mm for all plotted center wavelengths of the signal. Due to the positive birefringent walk-off angle in BBO, the splitting-length distributions are asymmetric, which favors the negative wave-vector pump-to-signal angles. If we restrict the non-collinear angle to a range between -7° and 6°, the splitting lengths increase to more than 14 mm and 7 mm for the beam- and pulse-splitting length, respectively. For the relevant spectral region of PHELIX and PENELOPE around 1 µm, both splitting lengths surpass 10 mm for non-collinear angles between -7° and 6°, which gives a sufficient range to optimize these parameters.

To include the effects of non-collinear propagation and birefringent walk-off into the description via the coupled-wave equations, additional terms must be added. This includes an effective walk-off term that shifts the field into walk-off direction at every calculation step. Furthermore, correction terms, which alter the diffraction and nonlinear mixing terms [151], must be added.

### Conclusion

To briefly conclude this section, I want to summarize the findings from the theoretical description of OPA via the coupled-wave equations:

- OPA is a process that allows amplifying waves by direct energy transfer without the necessity for any kind of intermediary energy storage.
- The gain of an OPA is to the first order bound to several parameters, which are the pump intensity, the nonlinear material, the length of this material and the phase mismatch.
- Phase matching is a key component for OPA as it effectively defines the efficiency and the gain bandwidth of OPA. The latter can be manipulated by choosing an appropriate non-collinear configuration.
- Further limitations of the parametric gain arise for realistic configurations with finite spatial and temporal extent of the fields. Here, the fields may separate in time due to a group-velocity mismatch and separate in space because of birefringent walk-off and non-collinear propagation angles. Moreover, the parametric gain becomes a function of space and time, which follows the shape of the pump amplitude.

### 3.1.3. Parasitic effects

In the previous sections, I discussed the most important parameters that influence the parametric gain of a uOPA. However, this did not include parasitic effects, which may cause a more rapid pump depletion that limits the total gain, or which may introduce losses to signal or idler via nonlinear conversion of these fields or via absorption. As stated before, these losses disturb the mutual amplification of signal and idler and can drastically reduce the exponential gain. In the following, I will discuss the most prominent parasitic effects, which are SHG of idler and signal, and **P**arametric **S**uper**F**luorescence (PSF).

#### 3.1.3.1. Parasitic second-harmonic generation

Aside from absorption of the signal or the idler outside the transmission window of the crystals, SHG of idler or signal can quickly build up if the phase-matching condition is fulfilled. Accordingly, these processes can be suppressed by increasing the phase mismatch of the SHG. This can be done by choosing an appropriate non-collinear pump-to-signal angle, as this must alter the propagation angle of the second harmonic with respect to the crystal optical axis if the phase-matching condition for OPA is maintained. Figure 3.7 shows the corresponding SHG phase mismatch as a function of the pump-to-signal angle and the signal wavelength.

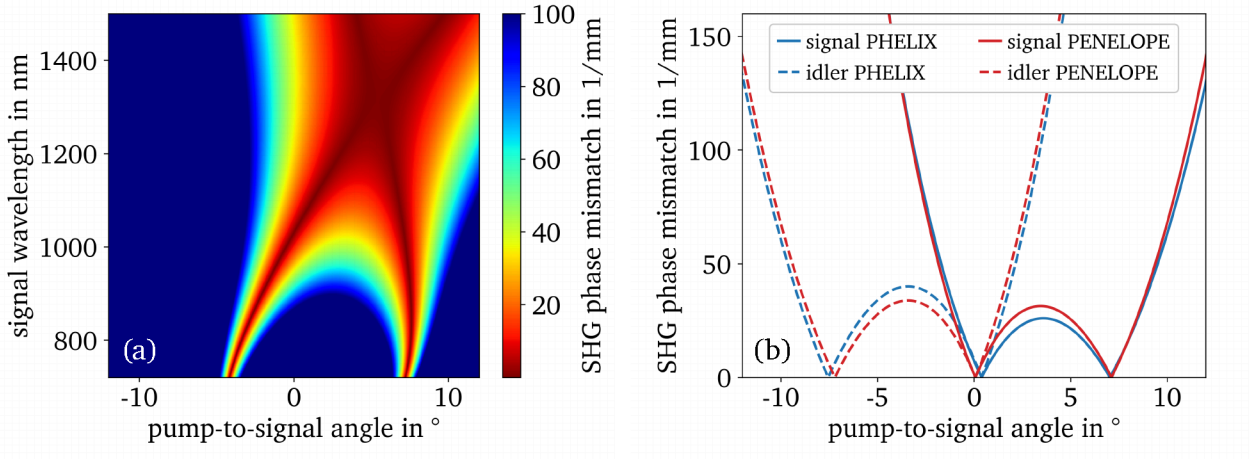


Figure 3.7.: (a) Phase mismatch of the signal SHG as a function of signal wavelength and pump-to-signal for perfectly phase-matched OPA in a BBO crystal with a pump at 515 nm. The colormap is cut off above 100 $mm^{-1}$. (b) Phase mismatch of the signal and idler SHG at the center wavelengths of PHELIX and PENELOPE.

As shown in Fig. 3.7(a), the signal SHG phase mismatch is not symmetric over the pump-to-signal angle and features areas of high and low phase-mismatch. Here, only the signal is considered, but to maximize the gain, also the idler should feature low conversion to its second harmonic. The phase mismatch for signal and idler, at the center wavelengths of PHELIX and PENELOPE as a function of the pump-to-signal angle, is shown in Fig. 3.7(b).

Since the idler-to-pump angle is negative for positive signal-to-pump angles and vice versa, its phase-mismatch shows the opposite behavior to that of the signal. Furthermore, Fig. 3.7(b) shows that the phase mismatch for the idler and signal SHG increases rapidly for non-collinear angles $|\alpha| > 10°$. However, for such large non-collinear angles, the pulse- and beam-splitting lengths become more critical, as shown in Fig. 3.6, and pulse and beam distortion can be expected. For the use of BBO, it is therefore

reasonable to use non-collinear angles around -3.4°, for which the phase mismatch of the idler SHG is maximized at the center wavelengths of PHELIX and PENELOPE.

Still, yet another trade-off between SHG phase mismatch and OPA-mixing bandwidth must be found, as the latter decreases strongly for larger non-collinear angles. By reducing the pump-to-signal angle from -3.4° to -2.25°, the mixing bandwidth roughly doubles, while the phase-mismatch for the idler SHG decreases only by 10.5 % and 8.7 % for the center idler wavelengths of PENELOPE and PHELIX, respectively.

At this non-collinear pump-to-signal angle, the phase-mismatch of the signal SHG at its center wavelength is still $\Delta k_{sig}$=64.0 mm$^{-1}$ and that of the idler $\Delta k_{idl}$=30.2 mm$^{-1}$ for PENELOPE, and $\Delta k_{sig}$=68.1 mm$^{-1}$ and $\Delta k_{idl}$=36.5 mm$^{-1}$ for PHELIX. Furthermore, the effective spatial walk-off is kept at approximately 1.1°, since the birefringent walk-off gets partially compensated.

To include the influence of parasitic SHG into the theoretical description of eq. 3.2, the corresponding mixing term for SHG, must be added. Also, a mixing equation, which describes the evolution of the SHG must be added. [152]

### 3.1.3.2. Parametric superfluorescence

In section 2.1.3, I already introduced PSF as a process that is problematic in terms of temporal contrast since it creates incoherent noise on a timescale of the pump laser. For **O**ptical **P**arametric **C**hirped **P**ulse **A**mplification (OPCPA), this can be as long as a few nanoseconds [51]. Furthermore, PSF can take up a significant portion of the output energy [153]. As the noise generation is restricted to the temporal and spatial extent of the pump, temporal contrast becomes less of an issue for uOPA since the timescale is close to the **F**ourier-**T**ransform **L**imit (FTL) of the signal. However, in OPA systems with high gain in short crystals, PSF still poses the risk of pump depletion, as phase matching will be achieved for all frequencies that can be phase-matched, due to the omnidirectional emission of PSF. Figure 3.8 shows at

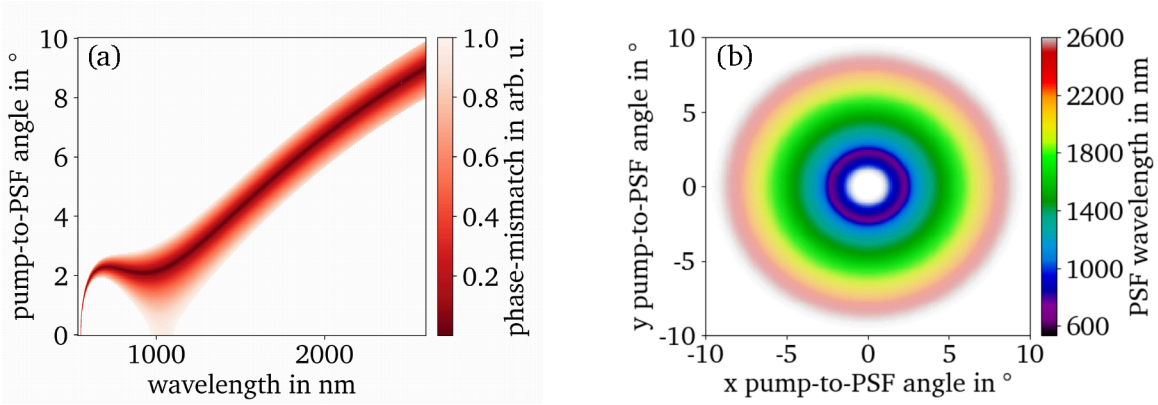


Figure 3.8.: (a) Normalized phase-mismatch (red) as a function of the non-collinear pump-to-PSF angle and the emitted wavelengths of the PSF. (b) PSF emission cone as a function of the non-collinear pump-to-PSF angle with the emission wavelength according to the colormap. The transparency is weighted by the gain. The configuration minimizes the phase-mismatch between the center wavelength of PHELIX and a 515 nm pump at a non-collinear angle of -2.25°. Only the phase-mismatch values for which the PSF does not reach reconversion are plotted for both (a) and (b). The pump intensity is chosen to reach a total gain of $10^6$ in the undepleted pump approximation and the crystal thickness 1 mm.

which non-collinear angles and PSF wavelengths the phase-mismatch is small enough, such that the wavelengths of the PSF do not reach reconversion (normalized phase-mismatch values smaller than 1 in Fig. 3.8(a)). The configuration of this calculation is described in the figure caption.

Figure 3.8 shows that PSF is phase-matchable over the whole transmission spectrum of BBO and the phase matching of the wavelengths is a function of the non-collinear angle. Accordingly, the PSF will be angularly dispersed, which results in an emission cone as shown in Fig. 3.8(b). This further mitigates the contrast issue for uOPA, as the angular dispersion of the PSF enables its removal with a spatial filter. However, the PSF can still extract energy from the pump within the crystal. Therefore, it is useful to determine the effective energy of the input noise photons. This can be done by following the description in section 2.1.3.2.

From Fig. 3.8(a), we can determine the necessary parameters. Assuming a flat-top fluence and power distribution of the pump with a duration of 1 ps and a radius of 2 mm, the input energy of the PSF is about 11 pJ. The contrast-related input noise, which remains after spatial filtering with a $\pm 1$ mrad acceptance, decreases to approximately 0.5 pJ.

These input-noise values can, however, be manipulated by the adjustment of several parameters, while keeping the parametric gain constant:

- Using a thinner crystal, with increased pump intensity will increase the effective input noise, while a thicker crystal with less pump intensity reduces it. This can be explained by a larger accumulated phase-mismatch value around the perfectly phase-matched wavelengths, resulting in reconversion of the PSF.
- Increasing the extent of the pump in time or space, while keeping a constant intensity also increases the input noise, while reducing the pump volume decreases the input noise [59].
- Splitting the amplification into two parts with reduced gain per part, but keeping the total gain constant is useful.
  - First, a gain reduction by purely decreasing the pump intensity increases the weighting of the phase mismatch compared to $\gamma$ in the small-signal gain $g$. Accordingly, the non-perfectly phase-matched portions of the PSF lose impact. Further suppression of the input noise will be applied by reducing the gain via reduction of the pump intensity and increase of the crystal thickness.
  - Second, the signal seed for the second stage will be significantly higher, rendering the impact of the input noise less meaningful, while potentially further limiting the growth of the noise due to parametric gain quenching [154, 155].

### 3.1.4. Materials for OPA

In the previous sections, it became clear that phase matching plays a dominant role in the process of OPA, especially within the use of short-pulse amplification and the mitigation of parasitic effects. Also, it was pronounced, that the nonlinear medium is a key component for phase matching since it defines the refractive indices for signal, pump and idler and therefore their wave vectors. However, the influence of the material does not end here, which is why the following section deals with explaining the material properties which are important for the OPA process and in particular for short-pulse OPA.

- The **nonlinear coefficient**, mostly described by $d_{eff}$, the effective nonlinear optical coefficient, certainly plays the most predominant role in the mixing process of OPA, as the parametric gain exponentially depends on it. Hence, a large nonlinear coefficient can be seen as one of the most

important properties of the nonlinear medium. The value of $d_{eff}$ is not only defined by the intrinsic properties of the material but also depends on the polarization of the waves and their angle to the optical axes of the crystal.

- **Refractive properties** of the material are also one of the key factors to OPA. First, the refractive indices of the mixing waves are part of the denominator of $\gamma^2$ (see eq. 3.10) and therefore influence the gain of the OPA. Second, the refractive properties define the phase-matching range of the nonlinear medium. Additionally, the refractive properties define parameters such as the spatial and temporal walk-off which are important to minimize for small-sized beams and short pulses, respectively.

- The range of **transparency** has to be large enough to support the bandwidths of not only the pump and signal but also that of the idler. In the case of absorption of either of the waves, the gain of the OPA will be reduced significantly. Also, high absorption may lead to damage to the crystal.

- **Thermal properties**, such as heat conductivity and small thermo-optic coefficients are to consider if the material should be used in systems with high average power or if it is used in environments with rather unstable temperatures.

- A high **damage threshold** is another factor to keep in mind, especially for short-pulse OPA systems, where large optical intensity is easily reached.

- The **availability** of the crystal should be ensured, which especially concerns the crystal size and optical quality.

For the most common nonlinear crystals, Table 3.1 lists the figure-of-merit $\zeta := d_{eff}^2/(n_p n_i n_s)$, which combines the nonlinear and refractive properties, the angle- and temperature tolerance of the crystal and the transparency range. The corresponding values are calculated with SNLO [156] for the signal wavelength of PHELIX and the pump wavelengths of 400 nm, 515 nm and 800 nm, which are the wavelengths of frequency-doubled Ti:Sa, frequency-doubled **Y**tter**b**ium (Yb)-doped materials and the fundamental wave of Ti:Sa.

Table 3.1.: $d_{eff}^2/(n_p n_i n_s) := \zeta$, crystal angle tilt tolerance ($\theta$ tol.), temperature tolerance (T. tol.) and transparency range for various crystals. The sub-columns, going from left to right, represent the values of the parameters at the pump wavelengths of 400 nm, 515 nm and 800 nm, respectively. If no entry is given, either no phase-matching condition could be found, the idler wavelength does not fit into the transparency range or the effective nonlinear coefficient is zero. The signal wavelength is set to 1053 nm. The tolerances and $\zeta$ were calculated via SNLO [156].

| **Crystal** | **$\zeta$ in pm$^2$/V$^2$** | | | **$\theta$ tol. in mrad·cm** | | | **T. tol. in K·cm** | | | **Transparency range in µm** | |
|---|---|---|---|---|---|---|---|---|---|---|---|
| **BBO** | 0.88 | 0.90 | 0.83 | 0.36 | 0.55 | 0.89 | 20.6 | 37.7 | 61.5 | 0.2-3.5 | [157, 158] |
| **LBO** | 0.14 | 0.17 | - | 1.56 | 3.94 | - | 9.5 | 7.0 | - | 0.16-3.2 | [159, 160] |
| **KTP** | - | 1.70 | 0.97 | - | 7.01 | 1.16 | - | 30.9 | 175 | 0.35-4.5 | [161] |
| **KTA** | - | - | 0.7 | - | - | 1.26 | - | - | 1240 | 0.35-5.2 | [162] |
| **KDP** | 0.04 | 0.04 | - | 1.41 | 2.30 | - | 9.0 | 13 | - | 0.2-1.6 | [163] |
| **DKDP** | 0.04 | 0.04 | - | 1.60 | 2.47 | - | 19.0 | 32.8 | - | 0.2-2.0 | [157, 158] |
| **$LiNbO_3$** | - | 2.04 | 1.73 | - | 6.20 | 0.94 | - | 1.0 | 3.4 | 0.4-5 | [164] |

Table 3.1 shows that KDP, DKDP and LBO exhibit rather low values for $\zeta$ compared to the other listed crystals. The highest values can be found for $LiNbO_3$ and KTP. A comparable value to that of BBO can be found for KTA, but no phase-matching conditions can be fulfilled for a signal wavelength at 1053 nm and a pump below 534 nm as calculated with **S**elect **N**on-**L**inear **O**ptics (SNLO), making this type of crystal less versatile. For the listed pump wavelengths only BBO is capable of delivering phase-matching conditions for all of them but is less performant at common pump wavelengths around 500 nm when compared to $LiNbO_3$ and KTP, which also feature a wider transmission window up to 4500 nm for KTP and up to 5500 nm for $LiNbO_3$.

Concerning the tilt tolerance of the crystals, BBO features the lowest values, while the other crystals achieve much higher tolerances for pump wavelengths of 515 nm and 400 nm. In terms of temperature tolerance, KTA is basically temperature insensitive and BBO, KTP and DKDP show moderately high and similar values around 30 K·cm. Less tolerant are LBO and KDP with around 10 K·cm, followed by $LinbO_3$ with the lowest tolerance below 4 K·cm.

Another important crystal parameter is the **L**aser-**I**nduced **D**amage **T**hreshold (LIDT) of a crystal. However, there is no clear picture for the LIDT of the materials in the literature and a variety of different values can be found. A comprehensive overview can be found in reference [165], where lots of publications have been gathered. However, since not all pulse durations at every center wavelength are covered in existent publications, and LIDTs are expected to vary from manufacturer to manufacturer, the following information should be considered only as an approximate measure.

Table 3.2.: Comparison of LIDTs in the bulk material at the wavelengths around 1000 nm and 500 nm for pulse durations around 10 ns, 1 ns and 100 ps. If not referenced, the data has been taken from [165]. If no data has been found "-" is displayed.

| | **LIDT in GW/cm², $\tau \approx$ 10 ns** | | **LIDT in GW/cm², $\tau \approx$ 1 ns** | | **LIDT in GW/cm², $\tau \approx$ 100 ps** | |
|---|---|---|---|---|---|---|
| **wavelength** | **1000 nm** | **500 nm** | **1000 nm** | **500 nm** | **1000 nm** | **500 nm** |
| **BBO** | 5-50 | >0.25-10 | 10-13 | 7 | >5-10 | >7-10 |
| **LBO** | >0.1 | >0.22 | 19 | - | 25 | >4.5 |
| **KTP** | 0.15-3.5 | 0.05-3.2 | 4.5->15 | - | - | >1.8 |
| **KTA** | >1.2 [166] | - | - | - | - | - |
| **KDP** | 0.3-0.6 | 3 | 3-20 | 3-8 | 7-23 | 14-30 |
| **DKDP** | 0.1-8 | >0.05-17 | 0.6 | >0.8 | >3 | >0.8 |
| **$LiNbO_3$** | 1.2 | - | - | - | - | - |

Table 3.2 shows various damage threshold values for different nonlinear crystals. The listed thresholds show strong fluctuations, not only for different crystals but also within the same crystal type at different pulse durations. In general, LBO, BBO and KDP seem to exhibit higher damage thresholds than the other crystals, especially for a shorter pulse duration, even though the data is sparse.

## 3.2. Demands on the pump laser for a millijoule-level, short-pulse, high-contrast OPA

In the previous sections, I discussed the most influential parameters of an OPA. In this section, I will apply the insights from the previous sections to determine the OPA configuration. Therefore, I would like to recapitulate the main goals that its implementation should fulfill. This is, providing a high-contrast pulse to seed the subsequent high-intensity laser chain, as well as representing a reasonable alternative for post-stretcher, first-stage, high-gain amplifiers, such as regenerative or multipass amplifiers. Hence, apart from an enhanced contrast, there are output parameters of the uOPA that should be comparable to that of the amplifier that should be replaced. Within these parameters are

- the **total output energy** of the amplifier. Often these range from below 1 mJ, up to a few mJ for multistage, pre-amplification systems [49, 167, 168]. The goal for the output of the uOPA is 1 mJ or above.

- the **energy stability**, which is an important parameter for a laser system to work robustly. This is especially important for laser facilities whose main amplifiers do not work in the saturated regime and initial fluctuations will not be reduced but carried to the end of the system. The goal for the output of the uOPA is a $2\sigma$ deviation of 3 % from its mean value.

- the **beam quality**, especially concerning the replacement of regenerative amplifiers, as they are generally capable of creating a close-to-perfect Gaussian beam. The goal here is to generate a highly symmetric and modulation-free beam. Ideally, close to a Gaussian beam.

- the capability to support **broadband amplification** to enable shortest pulses. The goal here is to preserve the seed bandwidth of the signal.

Here, the pump laser poses the most critical influence on these parameters. Accordingly, reasonable demands for the pump laser must be defined, such that the above-mentioned criteria can be fulfilled. For this, I conducted several simulations, which solve the coupled wave equations numerically.

In the following, I will therefore give a brief overview of available simulation software for uOPA modeling and explain which software I used within this thesis. Then, I describe the main influences of realistic pulse and beam properties within a uOPA and finally define the requirements for a high-contrast, short-pulse OPA pump system, which in turn will lay the foundation for the developed system within this PhD thesis. For this requirement derivation, I will limit the materials to only BBO, as it is a well-known material that can be produced with high homogeneity, supports sufficiently broad phase-matching bandwidths and transmission capabilities for a lot of OPA configurations and is generally listed by manufactures as a high damage-threshold material [169–173].

### 3.2.1. Simulation tools

Nowadays, there is a plethora of simulation software available for modeling the process of OPA, some of which are freely available open-source programs and some commercially available. In the following, I will therefore briefly discuss some software to numerically simulate OPA. I will limit this list to SNLO, chi2D and Miró, as they are either well-known, use interesting approaches or previously have been used by our group, respectively.

#### 3.2.1.1. SNLO

Among the freely available simulation software for modeling nonlinear optics, SNLO [156] is one of the most well-known and can be found in various publications. It features several modules to calculate parameters such as phase-matching angles, refractive indices, group-velocities, etc. for a large number of nonlinear crystals and allows modeling the three-wave mixing process in several degrees of approximations starting at effectively 1D modeling by assuming plane-waves in long pulses and ending at short pulses with 2D spatial distributions.

Here, effects like temporal walk-off and dispersion, as well as spatial walk-off, diffraction, non-collinear propagation and Kerr-nonlinearities can be applied or neglected. The solution to the mixing process is then calculated by integrating the coupled-wave equations via split-step methods.

While this software offers a broad variety of modules to simulate nonlinear processes, it also features drawbacks such as its limitation to mixing only three waves, which restricts the modeling of parasitic waves such as the second-harmonic of the input beams which could potentially influence the outcome. Furthermore, automation is not possible with the free version but can be purchased in the form of a MATLAB-based application.

#### 3.2.1.2. chi2D

A somewhat different approach to solving the coupled-wave equations is found in the free software chi2D [174]. In contrast to the "classical" way of solving the coupled-wave equations for three waves, chi2D solves a set of two coupled differential equations, which represent the fields in the two orthogonal, linear polarizations. With this treatment, all mixing products that can result from mixing three initially defined input waves can be modeled simultaneously, as long as the simulation window is large enough to contain the fields in space, time, frequency-space and spatial-frequency space. Similar to SNLO, effects like walk-off and Kerr effect can be included or neglected. Furthermore, contrarily to SNLO, chi2D includes noise terms to include effects of PSF. chi2D solves the coupled equations in the temporal and one spatial dimension, hence two dimensions.

Again, an upgrade can be purchased in the form of chi3D, which increases the number of spatial dimensions by one. Likewise to SNLO, this upgrade is also MATLAB-based and thus bound to another commercial software. However, already the 2D version can be computationally expensive, as its algorithm requires all input and generated fields to fit into a single grid in the temporal and spatial domain, but also the Fourier domain. For chirped broadband pulses and larger beam sizes in a non-collinear setup, the necessary window size as well as the resolution scales up rapidly.

#### 3.2.1.3. Miró

With Miró, we find ourselves in the field of modeling software that is capable of modeling a complete laser chain from front-end over main amplifier and compressor to the final focusing stage [175]. Within this software, there is also a module to calculate **T**hree-**W**ave **M**ixing (TWM) problems [151]. As the name indicates, this also follows the "classical" approach of solving the coupled equations for every field. Being developed for many years, this software was proven to be a powerful tool by complete modeling of large facilities such as Laser-Megajoule [176] and the **PET**awatt **A**quitaine **L**aser (PETAL) [177]. Calculations with this software have been made for our group, but being proprietary software, it is neither free to download nor to buy, which is an obvious drawback.

#### 3.2.1.4. Self-written software

While the mentioned software is, partly, readily available, it either lacks automation or demands tremendous computational resources. Therefore, a modeling script written in Python was written and used within this thesis. To combine several benefits from SNLO and chi2D, the script allows including parasitic processes by adding additional fields and mixing equations, and uses the complete refractive properties of the chosen material instead of the Taylor-coefficients of the wave-vector Taylor-expansion as in SNLO.

Also, noise terms, **S**elf-**P**hase **M**odulation (SPM) as well as cross (**X**) **P**hase **M**odulation (XPM) can be included. The code can simulate in two spatial and one temporal dimension and allows arbitrary spatial and temporal distributions. It accounts for non-collinear propagation, similar to the SNLO software. To check its validity, it was cross-checked with simulations with the above-mentioned software. As this script-based software allowed for the greatest flexibility, every following simulation result in this dissertation has been calculated with it.

### 3.2.2. Influence of temporal and spatial distribution of pump and signal

As shown in section 3.1.2.2, OPA is generally equipped to support broad bandwidths, if broad phase-matching can be achieved. This can be done via non-collinear phase-matching, a suitable choice of the pump wavelength and the nonlinear material. However, as mentioned in the conclusion in section 3.1.2.3, by using a spatially and temporally varying pump source, the parametric gain also becomes variable in space and time. This alters the evolution of the signal shape during amplification, as shown in Fig. 3.9 for the temporal domain.

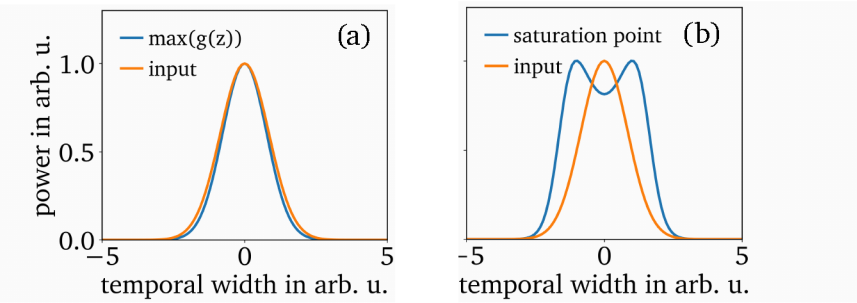


Figure 3.9.: Temporal profiles of the signal at the point of maximum gain per step (a) and at saturation (b) compared to the input distribution (orange). A pump with Gaussian shape in time and a five-fold duration compared to the signal was used for simulation.

Since the parametric gain for a Gaussian-shaped pump peaks in its center, the signal pulse duration reduces initially over the amplification distance, as can be seen in Fig. 3.9(a). If one assumes a pump pulse with infinite energy, this narrowing would continue. However, the finite pump energy leads to the onset of saturation effects and reconversion. At saturation, as shown in Fig. 3.9(b), the center part started to reconvert significantly, resulting in a distribution with a dip in the center. Since the temporal distribution is directly connected with the spectrum of the pulse, it becomes apparent that the spectral transformation via amplification is considerably different for bandwidth-limited pulses and chirped pulses. Before saturation, the spectral bandwidth of bandwidth-limited pulses will increase and that of chirped pulses will decrease, while in saturation, the bandwidth grows for chirped pulses and shrinks for bandwidth-limited pulses.

Similar to the influence of the temporal pump-pulse shape, its beam shape and distribution impact the output beam shape of the signal. The signal reshapes according to the input pump-beam distribution until saturation sets on. Consequently, to achieve a high beam quality with a Gaussian-shaped signal output, the pump must already exhibit a Gaussian shape with high beam quality and full saturation should not be reached to maintain that shape.

In general, the working point of the OPA must be chosen thoughtfully, since the reshaping takes place in both time and space. Especially for nonuniform shapes and saturated amplification, this can result in strong **S**patio-**T**emporal **C**oupling (STC). In this case, the approximation of independent spatial and temporal field properties becomes questionable, as, for example, different pulse durations are found at different spatial coordinates of the beam or different beam shapes at distinct points in time. While there are use-cases of STC, e.g., angular-dispersion in stretcher and compressor of a **C**hirped **P**ulse **A**mplification (CPA) system to handle the dispersion [16, 17, 178], in principle, these are unwanted effects and to be avoided, as they require complex setups to be measured and are difficult or even impossible to compensate for. Especially for ultra-short laser pulses, STC will result in effectively reduced peak intensity by increasing either the mean pulse duration, focus distribution or both [179, 180].

### 3.2.3. Requirements on the energy stability

Before defining the parameters to achieve a specific output energy, it is important to discuss how a specific output energy can be reached with sufficient stability. The output stability depends on the input energy stability of the signal and the gain stability of the amplifier. Obviously, the input energy stability is not influenced by the uOPA, but by the short-pulse oscillator, which is why this aspect is not discussed any further. Accordingly, the stability of the uOPA system is determined by the stability of its gain. Therefore, it is useful to isolate all parameters, that can potentially lead to unstable parametric gain.

#### 3.2.3.1. Pointing and temperature fluctuation

Equation 3.9 shows that the local gain in the undepleted-pump approximation is a function of the phase mismatch and $\gamma$, which in turn depends on the signal and idler frequencies, the nonlinear susceptibility, the refractive indices and the pump intensity (compare eq. 3.10). Some of these parameters are fixed, such as the idler and signal frequency, but others depend on the stability of the pump and signal. For instance, the extraordinary refractive index and the effective nonlinear susceptibility are functions of the internal crystal propagation angle and are therefore affected by pointing fluctuations.

In addition, the refractive index generally depends on temperature, causing the phase-matching condition to be temperature sensitive as well. Accordingly, it is reasonable to set an upper limit for the pointing and temperature fluctuations. With respect to the phase mismatch, a temperature- and angle acceptance can be defined. By assuming that the small-signal gain $g$ is dominated by the phase mismatch, the parametric gain $G_{par}$ (eq. 3.7) can be approximated by [181]

$$G_{par} \approx \mathrm{sinc}\left(\frac{\Delta k(\theta, T)L}{2}\right)^2, \tag{3.15}$$

where $\Delta k(\theta, T)$ is the angle- and temperature-dependent phase mismatch and $L$ the propagation distance. Following this approximation, the maximum tolerable fluctuation is often defined as the phase mismatch that reduces the parametric gain to half of its maximum value at $\Delta k = 0$ for $T = T_0$ and $\theta = \theta_0$ [182]. For a pump at 515 nm and signal at 1053 nm in BBO, with a -2.25° pump-to-signal angle, the tolerable angular fluctuation calculates to approximately $\pm$0.23 mrad· cm for a phase-matching angle of $\theta_0 = 24.05°$. It must be noted that the tolerance is completely dominated by the influence of

the pump fluctuations, because of its angle-dependent refractive index. For the same configuration, a temperature tolerance of about $\pm 16\,°C \cdot$ cm is found.

To define an upper limit for the fluctuations it is necessary to validate whether the modification of the phase mismatch or the modification of $\gamma$ will have a bigger impact on the parametric gain. For a pump intensity of 80 GW/cm$^2$, a 2 mm long crystal, the same pump and signal wavelengths as before and with the assumption of fluctuations of the order 1.2 mrad and 85 °C, the modification of the parametric gain by the phase mismatch is about 20 times larger than that of $\gamma$. Hence, the gain fluctuations are dominated by the fluctuation of the phase mismatch.

If we allow the temperature to fluctuate by 2 °C and request a maximum gain reduction of 0.5 %, the pointing fluctuation should be at maximum 0.26 mrad·mm.

#### 3.2.3.2. Pump-intensity fluctuation

Lastly, the stability of the pump intensity must be addressed, which boils down to the energy stability of the pump. In principle, the process of saturation and reconversion can be utilized to compensate over- or undershooting pump pulses, where even higher stability compared to the pump laser can be reached [183]. This would reduce the demands on the pump-energy stability. However, as described before, the spatial and temporal profiles of the signal are redistributed massively between the unsaturated and the saturated domain. Therefore, it is to be expected that the spatial and temporal profiles will fluctuate depending on the degree of saturation and a trade-off between energy stability and formation of STC must be made.

Guardalben et al. [184] minimized this trade-off by using temporal and spatial super-Gaussian shapes of the pump for nanosecond-long pulses in an OPCPA system to maintain an approximately equal gain at every spatial and temporal coordinate of the pump. If the pump intensity is high compared to the signal intensity, the point of saturation is reached at roughly the same propagation distance for all spatial and temporal slices of the signal and thus the deformation and STC can be mitigated.

Although the use of a temporally and spatially super-Gaussian pump is an elegant solution to reduce the impact of its energy fluctuations and at the same time to avoid most of the STC in the signal, the implementation of this method in the context of a uOPA increases the system's complexity enormously. For example, a super-Gaussian temporal shape for nanosecond pulses can be realized with fast electro- and acousto-optical devices [185, 186], that pre-compensate temporal-gain saturation of subsequent amplifiers by modulating the temporal profile. Within the domain of picosecond-long pulses, electro- and acousto-optical devices are not fast enough anymore to correctly modulate the pulse profiles in a direct manner.

To realize flat-top pulses in the few picosecond range, temporal shapes can be modified by pulse-stackers, which create a bunch of pulse replicas, that are coherently stacked in time and emulate a flat-top profile. This can, for example, be realized via multiple birefringent, temperature-controlled filters [187]. Other methods manipulate within the spectral domain by applying amplitude masks by using spatial-light modulators and creating sinc-like spectra [188] or by dispersion via acousto-optic programmable dispersive filter [42]. However, for these methods to work, the bandwidth of the pulses must be significantly increased since the shortest temporal features are inversely related to the total bandwidth. Moreover, the methods are mostly limited by the input pulse energy and have to be applied before amplification, which increases the amplifier requirements in terms of bandwidth maintainability.

Concerning the shaping to spatial flat-tops, commercial solutions do exist but are limited in pulse energy due to the damage threshold and fixed input beam diameters. Furthermore, an implementation of a beam shaper either requires its positioning close to the OPA crystal or relay-imaging of the beam is needed because flat-top distributions are not self-similar and quickly diffract. Although imaging of the

beam is generally not a major impediment, vacuum constructions are necessary to prevent air plasma ignition at the focus of the imaging telescope when pump-pulse energies are too high. As a consequence, this spatial and temporal pulse-shaping path is not followed within the scope of this thesis but may be reconsidered as a future upgrade to the system.

From omitting the idea of flat-top field shapes follows that a particularly high energy stability of the pumping system is necessary since the amplification should be non-saturated to mitigate STC. If we allow the signal output energy to fluctuate by ±3 % around its average value ($2\sigma$) over the whole amplification process, a pump-energy stability of ±0.4 % ($2\sigma$) is necessary, as depicted by the signal fluctuation (red shaded area) in Fig. 3.10.

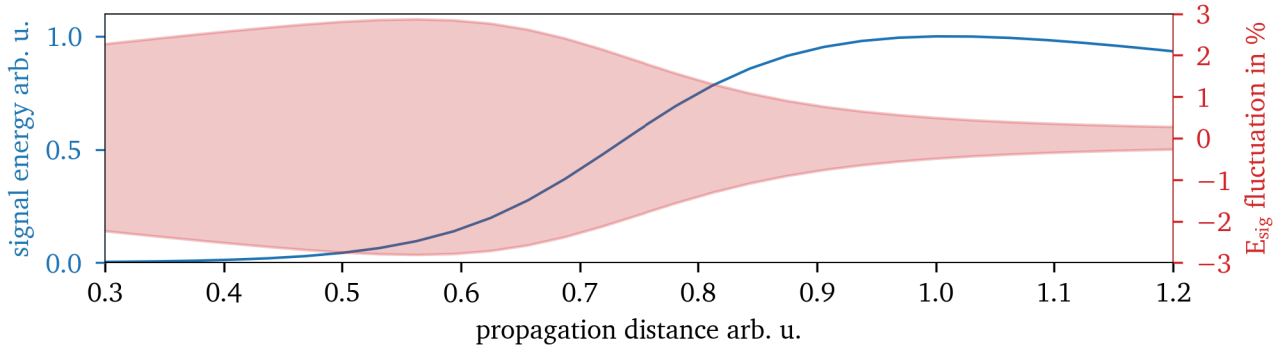


Figure 3.10.: Simulation of the signal energy fluctuation for a pump with a Gaussian shape in space and time in a two-stage setup with a maximum total gain of $3{\cdot}10^6$ and equal gain per stage. The signal energy (blue line) and its energy fluctuation (red shaded area) for a pump with relative energy stability of ± 0.4 % ($2\sigma$) are shown. The distance is normalized to the point of maximum energy at mean pump energy and the signal energy is normalized to the maximum energy at mean pump energy. Maximum fluctuation in the first stage is assumed to estimate the worst-case fluctuation of the second stage.

Figure 3.10 shows that the signal energy fluctuates at maximum 3 %, if the pump energy fluctuates by 0.4 %. Furthermore, the stability increases towards the point of saturation and beyond. Nevertheless, in contrast to the method presented by Guardalben et al. [184], a "truly" stable operation point after saturation is not found for spatially and temporally Gaussian-shaped pump pulses.

### Conclusion

Concluding this section, a set of requirements for the pump-amplifier system concerning its energy stability can be specified. Since the gain of OPA exhibits exponential behavior at non-saturated operating points, it is necessary to demand a particularly high pump-energy stability. The energy stability for the pump system I want to achieve is a $2\sigma$ deviation of 0.4 % from its average output or less. Furthermore, I aim at a pump-pointing stability of 260 µrad·mm

With such a demanded stability, the choice of available active media for the pump laser is limited to those that feature an absorption band, which can be pumped by highly stable laser diodes and an emission band that provides sufficient bandwidth to generate pulses in the 1-2 ps range. A material suitable for generating such pulses is Yb, which will be discussed in more detail later in section 4.1.1.

### 3.2.4. Pump energy requirements

The previous section emphasized the need for a high pump-energy stability to mitigate energy fluctuations in the signal, especially when operating in the unsaturated regime. However, it must still be determined how much pump energy is needed to amplify signal pulses of an oscillator from the nanojoule to the 1 mJ-level while maintaining a high spatial quality and conserving the spectral bandwidth of the signal. In the next sections, I will therefore discuss which parameters can be adjusted to achieve the desired energy of 1 mJ or more with sufficient spatial and spectral quality.

In the following, I will briefly discuss which parameters should be adjusted to reach the desired output in terms of energy and spatial and temporal quality. After this, I will apply the found optimizations to set up a parameter scan to find the minimum pump energy that is needed.

To get the most realistic estimation for the needed pump energy, the signal's characteristics are modeled with the pulse properties of the short-pulse oscillator (FLINT, Light Conversion), which is used for the development of the uOPA system. Accordingly, the signal features a center wavelength of 1034 nm with about 24 nm spectral bandwidth (FWHM), which corresponds to a bandwidth-limited pulse duration of 66 fs. The signal pulse energy is in the low-nanojoule range. I will further limit this section to BBO-based OPA systems and restrict the pump center wavelength to 515 nm, which is in the range of most common Yb-doped materials (see section 4.1.1).

#### 3.2.4.1. Determination of the uOPA working parameters

An important property of a system that should seed a high-intensity laser facility is its maintainability and robustness. For this, it is reasonable to minimize the complexity of the setup, which is why a single-stage uOPA was used in a previous implementation of the uOPA at PHELIX [36]. Because of the simplicity of the design, this setup seems attractive. However, a single-stage design encounters several limitations when scaling up the energy. In section 3.1.3 I discussed the influence of parasitic effects and suggested a non-collinear phase-matching configuration and a multi-stage amplification to suppress parasitic SHG and mitigate PSF, respectively.

Other parameters that influence the output energy of the uOPA are the spatial and temporal overlap of signal and pump. In order to increase the gain, the overlap should be maximized. In the spatial domain, this can be done via magnification telescopes. In the temporal domain, however, this requires stretching of the pulse, for example, via a stretcher or chirped mirrors.

To find the parameters for the seed duration and the pump energy that enable a high-quality output at 1 mJ or more, I conducted a set of simulations. For this parameter scan, I set the non-collinear angle to -2.25°, which still allows for a broad gain bandwidth while increasing the phase mismatch for parasitic SHG as well as reducing the effective walk-off angle to approximately 1.1°. As a reasonable estimation for the pump parameters, the pump duration is set to 1.5 ps FWHM and its beam size to 2.5 mm FWHM, such that a 10 mm aperture crystal can be used without excessive clipping. Also, a pre-amplification to 1 µJ in an additional uOPA stage is assumed for this parameter scan.

With these input parameters, I simulated a parameter set of five different pump energies and five different pulse durations of the signal. The pump energy varies from 10 mJ to 40 mJ in steps of 7.5 mJ and the signal duration is varied from its FTL at 66 fs to 852 fs by adding a quadratic spectral phase starting at 0 $fs^2$ and ending at 20000 $fs^2$ in steps of 5000 $fs^2$. Figure 3.11(a) and (b) show the simulation results in form of temporally-integrated fluence-outlines in the non-collinear plane and spatially-integrated power, respectively.

For the injection of a bandwidth-limited seed with a pulse duration of 66 fs, 1 mJ of output energy is only reached at pump-pulse energies of 40 mJ. Yet, the output quality of the pulse visibly suffers, as the energy is only reached after considerable saturation. Although the pump is tilted with a non-collinear

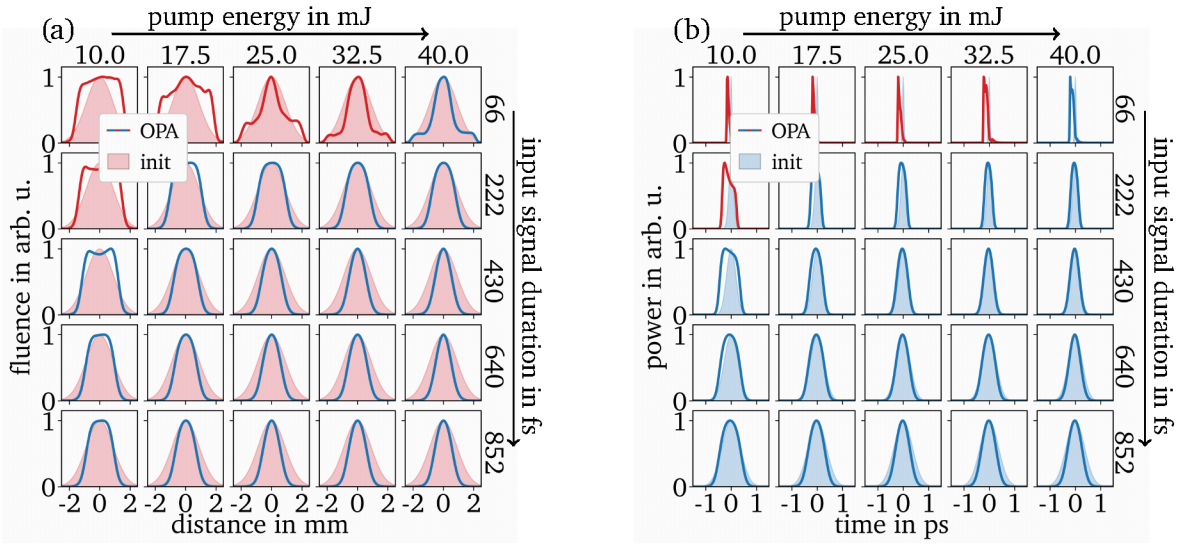


Figure 3.11.: Simulated, normalized fluence lineouts (a) and normalized, spatially integrated power (b) of the signal after uOPA at an output energy of 1 mJ (solid lines, referred to as 'OPA' in the legend) and of the input distribution (red (a) and blue (b) shaded area, referred to as 'init' in the legend). Blue lines indicate that 1 mJ of output energy was achievable in this setup. If this was not the case, red lines represent the distribution after the maximum propagation distance of 1.5 mm. The input parameters for this simulation are a 1.5 mm thick BBO-crystal, a pump-to-signal angle of -2.25° and a seed energy of 1 µJ. The pump energy and signal duration has been varied according to the titles on the top and right, respectively. The input beam size of the signal is $w = 1.8$ mm and that of the pump is $w = 2.14$ mm.

angle such that birefringent walk-off is mostly compensated, slight asymmetry in the walk-off direction can still be observed, especially at lower pump energies, since the amplification up to 1 mJ then requires a more saturated scheme and slightly longer crystals.

Less saturated output beam profiles are generated when the signal duration and the pump energy is increased. The differences in the spatial output of the signal start to diminish for chirps greater or equal to 10000 $fs^2$, corresponding to 430 fs and upwards, and pump energies of 25 mJ or more. Figure 3.11 (b) allows validating, whether these thresholds for the chirp and the pump energy also hold to maintain a high temporal quality.

Similar to the spatial profile, the resulting temporal shapes of the pulse rule out the lowest pump energies, as well as the shortest signal pulse duration, due to strong deformation because of saturated amplification and temporal walk-off. Also, at signal pulse durations between 430 fs and 640 fs, with pump energies in the range of 25 mJ to 32.5 mJ, the temporal envelope mostly maintains its initial shape, meaning that its spectral bandwidth is conserved. However, in contrast to the observation in the spatial domain, a loss of bandwidth manifests if the pump energy or the chirp is further increased. This defines an upper limit for the chirp of about 15000 $fs^2$.

Figure 3.12 shows that this chirp limit also applies if the output energy is increased to 2 mJ. At 2 mJ of output, a stretched signal pulse duration of 640 fs at pump energies of 25 mJ to 32.5 mJ works equally well in terms of spectral bandwidth preservation, compared to 1 mJ output energy. At this point, the spatial distribution slightly deforms to a more super-Gaussian-like distribution. Yet, the beam

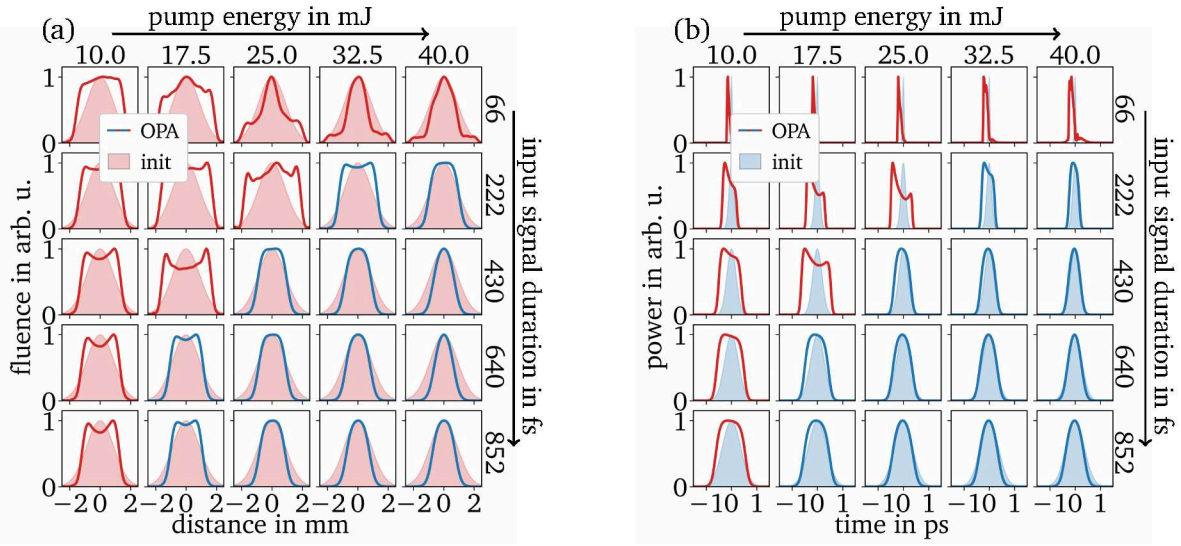


Figure 3.12.: Same simulation parameters as in Fig. 3.11, but the normalized fluence lineouts (a) and normalized, spatially integrated power (b) of the signal after uOPA are shown for an output energy of 2 mJ. The same color convention applies as in Fig. 3.11.

deformation is still in an acceptable range. For lower pump energies or pulse durations below 430 fs, either the pulse or the beam deformation is too strong. Also similar to Fig. 3.11, stretching above 640 fs results in a loss of bandwidth.

### Conclusion

To conclude this section and summarize the findings, several requirements can be specified to ensure an output energy of 1 mJ with overall high quality. Concerning the uOPA setup, it is beneficial to slightly increase the complexity by setting up two instead of a single stage. This enables operation using lower pump energy while mitigating the PSF.

Furthermore, it should be considered to stretch the signal to a pulse duration of some hundreds of femtoseconds to increase the temporal overlap with the pump and enhance the efficiency of the uOPA. For a pump pulse duration of 1.5 ps, stretching the signal to a duration of 400 fs to 700 fs is reasonable, as shown in the simulation results in Fig. 3.11 and Fig. 3.12. Also, it is advisable to set a larger pump-to-signal angle to suppress parasitic SHG. This is especially important for the second stage, in which the signal reaches an intensity that easily suffices to initiate the process of frequency doubling. For the advised pump energy and signal duration, a pump-to-signal angle of -2.25° suffices to suppress the parasitic SHG to below 5 µJ, while providing sufficient gain bandwidth and partially compensating the birefringent walk-off.

At this angle, according to the simulations, a pump energy of 25 mJ to 32.5 mJ with a pulse duration of 1.5 ps is sufficient to create a high-quality uOPA output up to 2 mJ. However, since the pump impacts the output of the uOPA in many aspects, its requirements are stringent.

First, the pump should feature a high beam quality, referring to a high similarity with a Gaussian beam. Second, the pump laser must exhibit a high energy stability since the use of Gaussian beams calls for amplification in the domain before saturation to mitigate strong STC. The targeted pump-energy stability is 0.4 % ($2\sigma$) around its average energy. Third, the pointing fluctuations should stay below 0.26 mrad·mm and last, the pump-pulse duration should lie in the vicinity of 1.5 ps.

# 4. Development of a millijoule-level uOPA system as seed for high-intensity lasers

Summarizing the last findings in the previous section, to build a millijoule-level uOPA, several parameters must be considered. This includes the optimization of the temporal overlap between signal and pump, the reduction of parasitic processes, and the implementation of a two-stage setup which mitigates the risk of pump depletion by PSF and reduces the needed total pump energy. However, the most critical point of the system is the generation of the pump pulses as they need to exhibit a pulse energy in the range of 30 mJ and feature an energy stability of 0.4 % ($2\sigma$) around its average energy. Furthermore, the pump must maintain a high beam quality and provide sufficient spectral bandwidth to create a pulse with a duration in the vicinity of 1.5 ps.

Although direct amplification to create pico- or sub-picosecond long pump pulses is possible [126, 189], this method is limited in energy, due to laser-induced damage thresholds, and therefore not ideal for the targeted pump energy. For higher output energies, it is reasonable to use the CPA technique, which in turn requires the implementation of a pulse stretcher and compressor. The basic layout of the complete uOPA follows the schematic shown in Fig. 4.1 and will be detailed in the next sections.

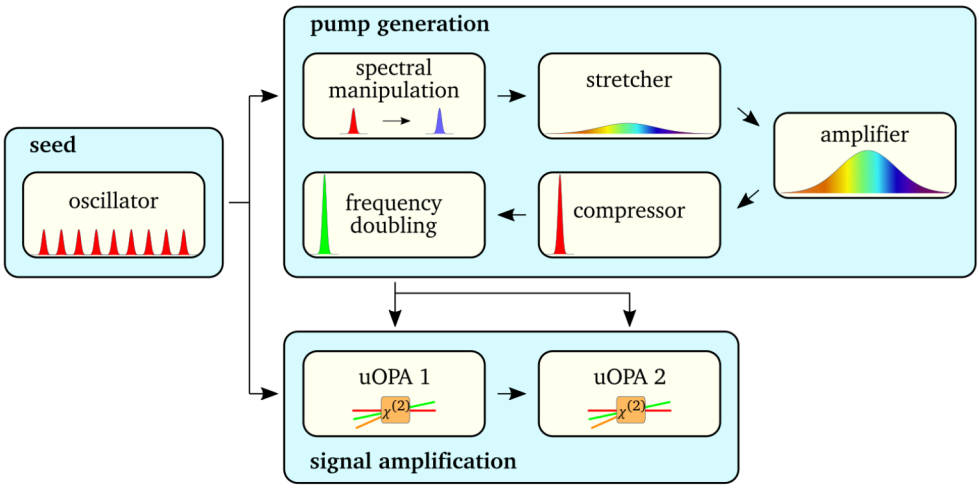


Figure 4.1.: Fundamental layout of the proposed uOPA system, which is split into two parts: the signal amplification, consisting of two uOPA stages, and the pump pulse generation, consisting of a spectral-manipulation stage, an amplification system between a pulse stretcher and compressor and a subsequent frequency-doubling stage.

Both, the signal and the pump of the uOPA originate from the same short-pulse oscillator to ensure a first-order temporal synchronization, which is indispensable for a stable amplification in a uOPA. The uOPA signal is directly sent to the uOPA stages, whereas the pump pulse is amplified in a CPA setup and subsequently frequency doubled before being split and sent to the two uOPA stages. To broaden the applicability of the pump system to a set of short-pulse oscillators with spectra around 1 µm, a

spectral-manipulation stage is employed. Specifically, compatibility with the Nd:glass-based laser facility PHELIX and the Yb:$CaF_2$-based laser facility PENELOPE must be ensured since the developed uOPA system will be used in both facilities.

In the previous sections, the targeted pump-energy output was set to 32.5 mJ, which, however, refers to the frequency-doubled pump pulse. Accordingly, to define a requirement on the uncompressed, fundamental pulse energy of the pump, the efficiency of the SHG and the compressor must be taken into account. For example, the SHG efficiency of a pump pulse generated in Yb:YAG or Yb:KGW is in the range of 50 %-70 % [36, 190, 191]. The transmission efficiency of the compressor is mainly limited by the diffraction efficiency of the used gratings since these are hit four times in a standard compressor setup. With the use of **M**ultilayer **D**ielectric (MLD) gratings, the diffraction efficiency per grating is close to 100 % [192], which reduces the losses in the compressor. However, for a lower bound estimation of the required uncompressed pump-pulse energy, a diffraction efficiency of 95 %, corresponding to a total transmission of about 80 % and an SHG efficiency of 50 % may be assumed. The corresponding pulse energy before compression and frequency doubling is then approximately 80 mJ. To plan for an energy budget that ensures that the amplifier does not use 100 % of its capacity, the final target is set to 100 mJ output energy.

Concerning the repetition rate of the amplifier, my aim clearly lies in designing an amplifier that is compact and easy to maintain rather than trying to reach the highest average output power. Although a tendency to higher repetition rates in ultra-short, high-energy lasers in the 100 J class is observable, most high-repetition rate high-energy systems perform in the range of 1 Hz to one shot every few minutes. Therefore, the presented system is not designed to work in the kHz range, but in the range of 10 Hz. This repetition rate ensures compatibility with the timing system at PHELIX.

In the next sections, I will provide a detailed view of the amplifier design and the performance of the uOPA as well as its pump system. In the first subsection, I will describe the setup of the pump amplifier and proceed to go into detail regarding its performance. After this, I will detail the setup of the uOPA and discuss its output parameters. Last, its implementation and the influence on the temporal contrast at the PHELIX laser, as well as potential upgrades to the system will be discussed.

## 4.1. Pump-amplifier architecture

The pump-amplifier architecture is a key factor to meet the described requirements. As for the general layout, setting up the amplifier in a CPA-based configuration is useful to reach the required energy and keep nonlinear interaction at a minimum. Concerning the specific type of amplifier, the most prominent configurations that provide a high gain and can operate at this energy level are either a geometric multi-pass or a regenerative amplifier.

Both of these amplifiers feature different advantages and drawbacks compared to the other one but share an overall high gain and high energy stability as long as their operational point is set at saturation. Yet, in terms of output energy, multi-pass amplifiers tend to outperform regenerative amplifiers, because their losses are not bound to an intrinsic mode formation. This reduces the difficulty of seeding these amplifiers since no mode-matching is necessary. Opposed to the advantage of reduced coupling losses, the setup complexity increases with each pass, as the beams have to be separable and are typically relay-imaged in each pass to preserve the beam quality [193].

Contrary to the geometric multi-pass design, the regenerative amplifier employs multiple passes by coupling the pulse into an optical cavity via optical switching with a **P**ockels **C**ell (PC). If designed correctly, this cavity supports only its fundamental mode, which for a cavity with spherical end mirrors is a Gaussian mode [194]. Therefore, high beam quality is theoretically given per design by its intrinsic

mode selection. Although more prone to losses due to its mode selectivity and therefore more challenging to operate at higher energies, this type of amplifier reduces the setup complexity and maintainability compared to the geometric multi-pass amplifier and reduces the number of needed optics.

Given that the beam quality of a uOPA pump is a key factor for a high-quality output beam after parametric amplification, the regenerative amplifier is my amplifier type of choice for the pump laser. However, as a total gain of about $10^8$ is needed to boost the oscillator output from the nanojoule-level to 100 mJ, a split into pre- and main amplifiers is useful. This reduces the risk of wasting pump energy by the generation of ASE and creates a more robust amplification configuration.

Because of the robust handling of low seed power, a fiber amplifier is a reasonable choice for a pre-amplification stage. Additionally, fiber amplifiers are destined to create large gains over a few meters of distance, which reduces amplification time. Also, they generate high-quality beams [195] with a fundamental mode similar to a Gaussian, which reduces the coupling losses into the mode-selective regenerative cavity.

The main aspects of the design of the pump laser are covered in a manuscript, which we published before [1]. In the next sections, I will elaborate on the architecture of the pump amplifier in more detail, beginning with the choice of gain material, followed by the description of the spectral-manipulation stage, the stretcher and the fiber pre-amplifier. After that, I will provide a detailed view of the regenerative main amplifier and conclude with the setup of the compressor and the frequency-doubling stage.

### 4.1.1. Gain material

The choice of the active medium for the pump amplifier is as crucial as its architecture since it decides the center wavelength and the output bandwidth of the pulse, but also how efficiently energy can be extracted. A first narrowing down of the available amount of active media can be done by selecting the pumping method. In section 3.2.3 it was already concluded that laser-diode-based pumping is the method of choice.

The reason for this is, first, that laser diodes can create a highly power-stable output, which is linearly proportional to the applied current [196]. Second, laser diodes tend to be significantly more efficient in terms of emitted versus absorbed power compared to, for example, flashlamps, since they produce a narrowband output in the range of a few nanometers. Also, their intrinsic electrical-to-optical efficiency can be as high as 50 % to 60 %, even for kW of output [197, 198]. Also, if the material features absorption bands, which match the emission characteristics of the diode, the heat generation is minimized as most of the light is used to pump the laser transition.

**Y**tter**b**ium (Yb)-doped gain media fall into this category with pump bands in the spectral region of 940 nm - 980 nm, which is covered by InGaAs laser diodes [199]. Furthermore, Yb-doped materials exhibit long fluorescence lifetimes (see table 4.1) compared to, for example, Nd-doped media. This is extremely helpful for the combined use with laser diodes, as these produce rather low peak power and therefore a longer pump-pulse duration is needed to deliver sufficient energy per pulse to create a reasonable population inversion. Table 4.1 summarizes the parameters of common Yb-doped host materials.

As shown in table 4.1, lots of host materials for Yb exist and aside from YVO or CALGO they exhibit quite a long fluorescence lifetime in the range of 1 ms or above, making them preferable to be pumped by a laser diode. Another important parameter to take into account, apart from the fluorescence lifetime, is the saturation fluence of the material. This parameter determines the fluence which is needed to extract the majority of the stored fluence of the medium and is directly related to small-signal gain. Consequently, choosing a material with high saturation fluence needs high input fluences to reach a high gain, which for the cases of Yb-doped glass or $CaF_2$ may even surpass the damage threshold.

Table 4.1.: Properties of various Yb-dopable host materials. $\tau_{fl}$ is the fluorescence lifetime, $F_{sat}$ the saturation fluence, $\lambda_{abs}$ the peak absorption wavelength and $\lambda_{em}$ the peak emission wavelength. The $\pm$ refers to the bandwidth (FWHM) of the emission- and absorption cross-sections. $N_m$, $\pi$ and $\sigma$ refer to the propagation axis through the crystal in the case of birefringent crystals.

| **Host material** | $\tau_{\mathrm{fl}}$ **in ms** | $\mathrm{F_{sat}}$ **in J/cm$^2$** | $\lambda_{\mathrm{abs}}$ **in nm** | $\lambda_{\mathrm{em}}$ **in nm** |
|---|---|---|---|---|
| **glass (silica)** [200] | 0.8 | 30 | 976 $\pm$ 1.7 | 1030 $\pm$ 25 |
| **YAG** [201] | 0.94 | 8.2 | 940 $\pm$ 9.4 | 1030 $\pm$ 4.4 |
| **YVO** [202] | 0.25 | 140 | 984 $\pm$ 5 | 1008 $\pm$ 10 |
| **KGW ($\mathrm{N_m}$)** [203] | 0.6 | 5.3 | 981 $\pm$ 2 | 1025 $\pm$ 10 |
| **YLF** ($\pi$) [204] | 2.2 | 22.4 | 959 $\pm$ 5 | 1019 $\pm$ 13 |
| **$CaF_2$** [201, 205] | 1.9-2.4 | 80 | 980 $\pm$ 11 | 1049 $\pm$ 30 |
| **CALGO ($\sigma$)** [206] | 0.45 | 25 | 980 $\pm$ 4 | 1025 $\pm$ 35 |

Furthermore, as the saturation fluence is inversely correlated with the stimulated emission cross-section, a high $F_{sat}$ is also associated with a low gain. To counteract this problem, a valid strategy is to increase the number of passes through the medium.

Additionally, the bandwidth of the emission and absorption is of particular interest. Concerning the former, all listed materials offer sufficient bandwidth for the creation of pulses with duration in the low picosecond range. However, a larger absorption band is also useful as it eases the requirements of the laser diode. Here, especially YAG and $CaF_2$ stand out, providing the broadest pump bands with approximately 19 nm and 22 nm, respectively.

For the pre-amplifier, Yb:glass is a valid choice as it is easy to integrate into a fiber-pre-amplifier system and provides the required spectroscopic properties to support ps-pulses. Concerning the pump bands, the requirements are not as stringent as for the regenerative amplifier, as the needed pump power is in the range of a few Watts instead of kW. At these power levels, narrowband laser diodes, whose emission band matches the absorption band of Yb:glass, are widely available. Furthermore, the applicability of a fiber pre-amplifier was already proven within the context of the previous uOPA pump system at PHELIX [36, 207].

For the main amplifier of the pump laser, YAG is my material of choice. Yb:YAG features comparably low saturation fluence, which reduces the number of potential passes through the medium. This reduces the amplification time, which is beneficial for the temporal synchronization of the signal and pump pulse of uOPA. Additionally, Yb:YAG features sufficiently broad pump and emission bands to support efficient pumping and short pulses. Also, its fluorescence lifetime is long enough to be pumped by nowadays laser diodes, which can provide up to several joules per pulse within this time frame.

However, it must be noticed that Yb:YAG, as most of the other mentioned materials, is a quasi-three-level system at room temperature [201]. This means that the lower laser level is partially populated and the signal is expected to be absorbed. For such a material, the emission and absorption cross-sections are altered at different temperatures. Figure 4.2 shows the cross-sections of Yb:YAG at four distinct temperatures.

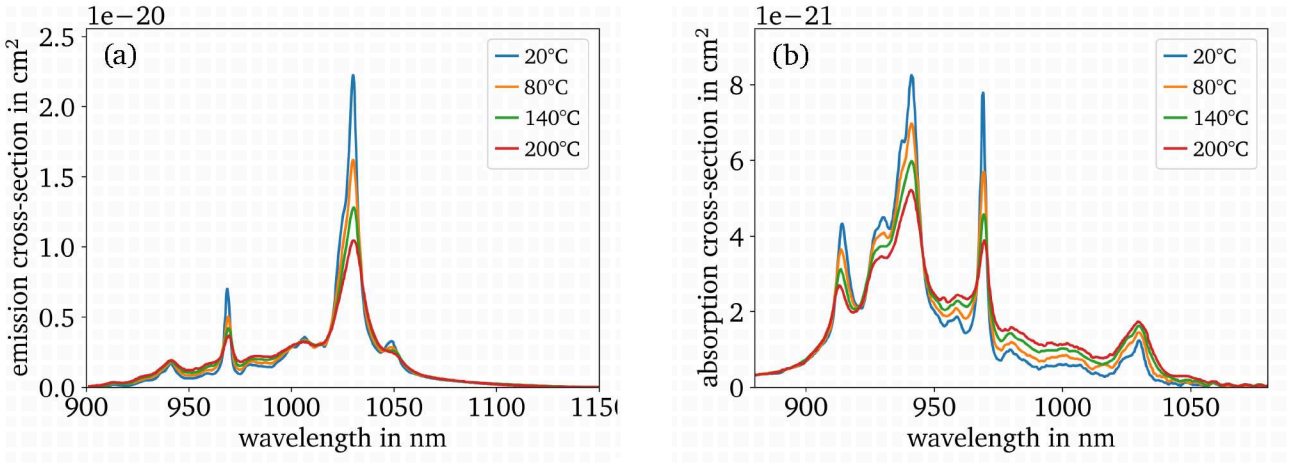


Figure 4.2.: Emission cross-section (a) and absorption cross-section (b) of Yb:YAG as a function of the wavelength at four different temperatures. The data was extracted from Koerner et al. [201].

Both the absorption and emission cross-sections of Yb:YAG benefit from lower temperatures. If the temperature rises, the cross-sections at the peak-absorption- and peak-emission wavelengths decrease. Furthermore, a rise in temperature increases the absorption at the emission band of Yb:YAG. To achieve the highest gain for the signal and absorption of the pump it is, therefore, useful to actively cool the material and stabilize its temperature. Furthermore, as shown in Fig. 4.2, not only the peak values of the cross-sections change but also the shape of the bands. For higher temperatures, the emission cross-section slightly broadens and shrinks for lower temperatures, which will influence the gain narrowing and therefore the spectral bandwidth of the pulse after amplification. At room temperature and with a total gain of $10^8$, which is the needed gain without pre-amplifier, the achievable bandwidth for Yb:YAG is about 1.1 nm and yields a FTL of approximately 1.2 ps. Thus, the pulse duration requirement of 1.5 ps is already met and gets even further relaxed by implementing a fiber pre-amplifier with a broad gain bandwidth.

The details of the fiber pre-amplifier, including the stretcher and spectral manipulation of the pump seed, are discussed in the next section.

### 4.1.2. Pump-seed generation, stretching and pre-amplification

The origin for both, the signal- and pump-amplification chain of the uOPA is the short-pulse oscillator, as shown in Fig. 4.1. Concerning the pump seed, the first step within the pump chain consists in ensuring its compatibility with different types of oscillators. While there are oscillators, whose pulse spectra overlap with the gain bandwidth of Yb:glass and Yb:YAG, for most oscillators, extra measures must be taken if the pump system should be versatile and not be limited to a small subset of oscillators.

This versatility can be achieved by spectral broadening of the seed pulses to bridge spectral gaps between the oscillator spectrum and Yb:YAG, which is centered around 1030 nm. This spectral broadening is realized via **S**elf-**P**hase **M**odulation (SPM) in a standard polarization-maintaining-fused-silica fiber (Corning, PANDA PM980) with a mode field diameter of 6.6 µm. Since the short oscillator pulses are not stretched before they are coupled into the fiber, the intensity inside the fiber is as high as a few ten GW/cm$^2$, even for pulse energies of around one nanojoule and a pulse duration of 100 fs. Consequently, the nonlinear Kerr effect dominates the propagation inside the fiber and manifests through a broadened

spectrum within the first centimeters inside the fiber. Simulations with fiberdesk [208] showed, that most of the broadening manifests within the first 10 cm (for a 100 fs long pulse with 1 nJ energy) and flattens out after 50 cm of propagation. However, to facilitate the implementation, a fiber in the meter scale can be used, as this only causes further stretching of the pulse and barely affects the spectral bandwidth.

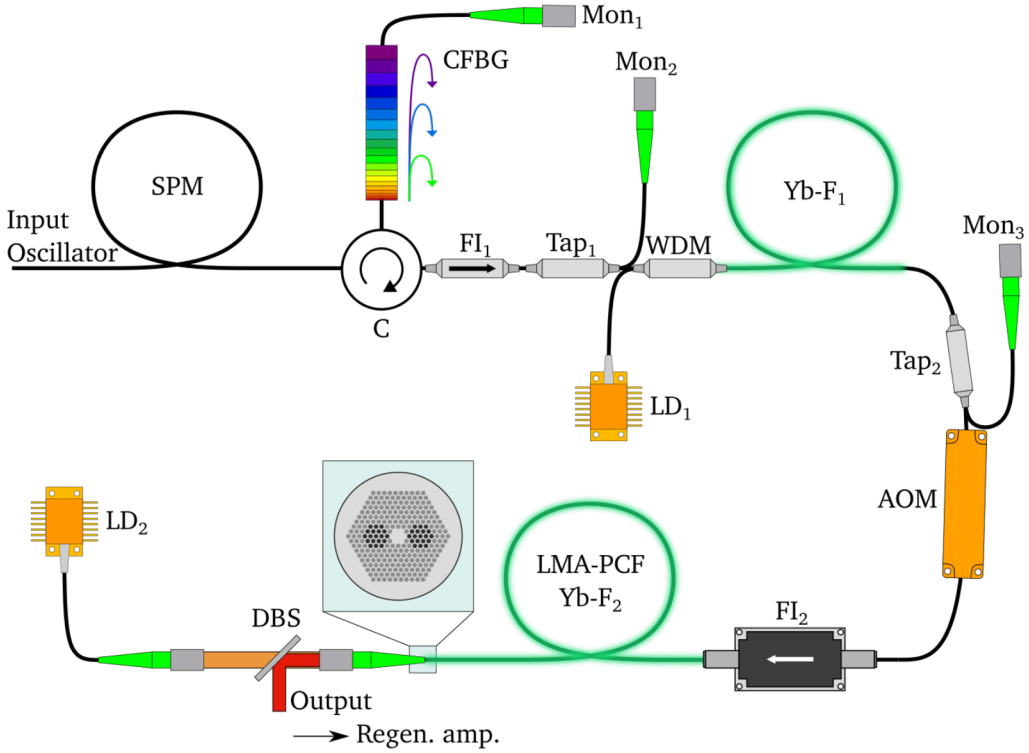


| | | | |
|---|---|---|---|
| SPM: | Self-Phase-Modulation | Yb-F: | Yttberium doped fiber |
| C: | Circulator | LD: | Laser Diode |
| CFBG: | Chirped Fiber Bragg Grating | AOM: | Acousto-Optic Modulator |
| Mon: | Monitor Output | LMA: | Large Mode Area |
| FI: | Faraday Isolator | PCF: | Photonic Crystal Fiber |
| Tap: | Tap/Coupler | DBS: | Dichroic Beam Splitter |
| WDM: | Wavelength Division Multiplexer | | |

Figure 4.3.: Schematic drawing of the fiber stage. This stage combines the spectral broadening of the seed, the stretcher and the pre-amplifier of the CPA in an "all-fiber" system. The amplification is done in laser-diode pumped Yb-doped fibers, split into two consecutive stages, which are coupled via **A**cousto-**O**ptic **M**odulator (AOM). To counteract the Kerr effect at high pulse energies, the second stage exhibits a large-mode-area, photonic-crystal fiber.

The spectrally broadened pulses are then fed into the stretcher of the pump-CPA. To reduce energy instabilities, it is useful to incorporate all components into an 'all-fiber' setup, since fiber splices are more robust and reduce the coupling losses compared to free-space couplings between fibers. The integration of all components into an 'all-fiber' setup is made possible with the use of a fiber-based stretcher, a **C**hirped-**F**iber **B**ragg **G**rating (CFBG) (TeraXion, PowerSpectrum HPSR). To stretch the pulse, a CFBG features an aperiodic refractive-index modulation along the fiber-propagation axis. This aperiodic index

modulation acts as a grating with position-dependent fulfillment of the Bragg condition for each spectral component, which results in the reflection of the respective wavelength [209]. Accordingly, different parts of the spectrum pass different amounts of optical pathways, which can be manipulated to stretch the pulse by inscribing a tailored grating modulation and thereby introducing a tailored spectral phase. Figure 4.3 shows the full setup of the fiber system.

The pulses are coupled into the SPM fiber in which they are spectrally broadened to overlap with the emission band of Yb:YAG at 1030 nm. Then, they traverse a circulator (AFR, HPMCIR-03-0.3-S-S-Q-C(SR13739B)) to couple into the CFBG, which reflects a bandwidth of 3.75 nm centered around 1030 nm and stretches the pulse to a duration of 1.2 ns. This is sufficient to mitigate nonlinear effects in the pre-amplifier, which may otherwise reduce the compressibility of the pulse.

However, accounting for the targeted output energy 100 mJ of the main amplifier and the expected gain-narrowing of Yb:YAG to about 1.1 nm, the peak power reaches approximately 0.28 GW. Accordingly, a reduction of the peak power by using a larger stretching factor would be beneficial. Yet, drastically increasing this factor would result in a bulky or complex compressor design, as the required output energy calls for a free-space grating compressor to handle the intense pulses. Therefore, the stretching factor of 320 ps/nm was chosen as it represents a compromise between partially mitigating nonlinear effects in the main amplifier and keeping the footprint of the compressor at a reasonable size.

After stretching, the pulses are coupled into the actual pre-amplifier of the pump system from the third port of the circulator with an effective seed power in the low mW range, corresponding to few tens of pJ. The fiber pre-amplifier is an upgraded version of the fiber amplifier that was developed within my master's thesis [207] and was used in the previous uOPA system at PHELIX. The first of the two consecutive amplification stages consists of a Yb-doped, single-mode, single-cladding and polarization-maintaining fiber (Coherent, PM-YSF-HI-HP, Yb-$F_1$) with a length of 1.3 m, and a continuous wave, single-mode pump laser diode (3SPTechnologies, RLS/976NM-750MW, $LD_1$) at 976 nm with up to 750 mW of power. The combining of these two beams is realized via wavelength-division multiplexing (AFR, PMFWDM-9703-N-B-Q, WDM) in a co-propagating fashion. Here, an output power of a few hundred mW is targeted, corresponding to a few nanojoules per pulse.

To protect the oscillator from potential backward propagating light, a Faraday isolator (AFR, HPMI-03-A-0.1-N-B-Q-F-1-C, $FI_1$) is installed. Following that amplification stage, a fiber-coupled AOM (G&H, FiberQ T-M300-0.1C2G-3-F2P) is set up as a pulse picker to reduce the repetition rate from about 80 MHz to 100 kHz in the second fiber stage. As the repetition rate decreases, the available pump power distributes over a reduced number of pulses, which allows the energy of the individual pulses to be increased. Hence, the AOM enables to adjust the output pulse energy of the pre-amplifier without adjustment of the pump-diode power. To avoid too large amplification factors and mitigate the risk of damage, the repetition rate should remain in the 100 kHz range.

After the pulse picking, the pulses pass another Faraday isolator (AFR, HPMI-03-A-10-N-B-Q-F-1-P, $FI_2$) and are then seeded into the second fiber-amplifier stage. Since pulse energies up to several microjoules are expected inside this stage, a fiber with a larger mode-field diameter of 15 µm is used to reduce the intensity. This photonic-crystal fiber (NKT-Photonics, DC-135/14-PM-Yb, Yb-$F_2$) has a length of 1.55 m and a second multi-mode cladding with a large numerical aperture. Accordingly, a low beam quality, but high-power (7 W) laser diode (PhotonTec, M976$\pm$0.5-7-F105/22-G4T, $LD_2$) can be used and still be efficiently coupled into the fiber. Contrary to the first fiber stage, the pump is counter-propagating and coupled into the fiber from free space. This is necessary since no wavelength-division multiplexers at this power level and connectors to a **P**hotonic **C**rystal **F**iber (PCF) were available. The splitting of the signal and the pump is done via a dichroic beam splitter (DBS).

### 4.1.3. Pump main-amplification

Following the fiber-pre-amplifier, the regenerative main amplifier is set up to boost the energy from the microjoule- to the 100 mJ level. To keep the cavity design as simple and maintainable as possible, as well as capable of delivering pulse energies in the range of 100 mJ, the number of optics should be minimized while the mode-forming optics should be selected to create a reasonably large mode. With only two curved mirrors, set up in a 0°-configuration, the cavity avoids induced aberrations and modal deformations through the off-axis use of curved mirrors.

By choosing a set of two curved end mirrors with radii of curvature of -20 m and +15 m and a cavity length of approximately 1.7 m, a stable cavity is formed with a slowly varying mode-radius from a minimum of 1.6 mm to a maximum of 1.8 mm. Here, the convex mirror allows to shorten the cavity length, while creating the same transversal mode as a 4.5 m long cavity with a -20 m mirror radius of curvature and a plane end mirror. For this, the convex mirror is positioned where its radius matches with the radius of the mode of the long cavity with plane end mirror.

This simple manipulation of the cavity reduces the total time inside the cavity by approximately a factor of 2.5, while preserving the large mode size. This is beneficial in the context of a uOPA since thermally induced delays between pump and signal are reduced, creating a more robust amplification system.

However, in operation, the mode of the cavity differs from the theoretical mode evolution of an empty cavity with spherical mirrors. To estimate the modal behavior of the cavity during operation, the influences of thermal lenses, induced by heat deposition of the pump, and the influence of nonlinear lenses due to the Kerr effect must be taken into account, which will be discussed in the next sections.

#### 4.1.3.1. Thermal lens estimation

To estimate the influence of the thermal lens, the heat deposition in the laser crystal must be calculated, which depends on the pump power. The modeled geometry of the crystal is disk-like, as this is beneficial for the reduction of the nonlinear Kerr effect. Also, the crystal is pumped from the front in its center with a pump spot diameter of 2.4 mm. Cooling is applied only on the edge of the disk since this allows the application of simpler cooling designs. The heat deposition and diffusion are then calculated via the heat equation [210]:

$$\frac{\partial u(x,y)}{\partial t} = \alpha \cdot \Delta u(x,y) = \alpha \left( \frac{\partial^2 u(x,y)}{\partial x^2} + \frac{\partial^2 u(x,y)}{\partial y^2} \right) \tag{4.1}$$

To simplify the problem, only the transversal dimensions are used since the active medium is assumed disk-like in shape. Here, $\alpha \approx 5\,\mathrm{mm}^2/\mathrm{s}$ is the thermal diffusivity of Yb:YAG corresponding to a thermal conductivity of 0.014 W/(mm·K), a specific heat of 0.59 J·/(gK) and a density of $4.56{\cdot}10^{-3}$ g/mm$^3$ [211]. $u(x,y)$ represents the temperature distribution. The initial temperature of the crystal was set to 20.5°C and the border is assumed to remain at that temperature. The heat deposition is modeled by a successive temperature increment during the pump duration of 1 ms, defined by the pump power, the temporal step size, and the fractional heat of YAG, which is defined as the fraction of the absorbed pump power that is converted into heat [212], was set to 0.1 [212, 213]. After the pump-pulse duration, the heat diffuses for the amount of off-time in between the pump cycles. This procedure is repeated until a dynamic equilibrium is reached. The estimated thermal-focal lengths and the maximum temperature of the crystal over a set of pump energies are shown in Fig. 4.4.

The maximum temperature in the crystal depends linearly on the input pump energy, or more precisely, the input average pump power. Here, the temperature increases up to 45 °C for the highest

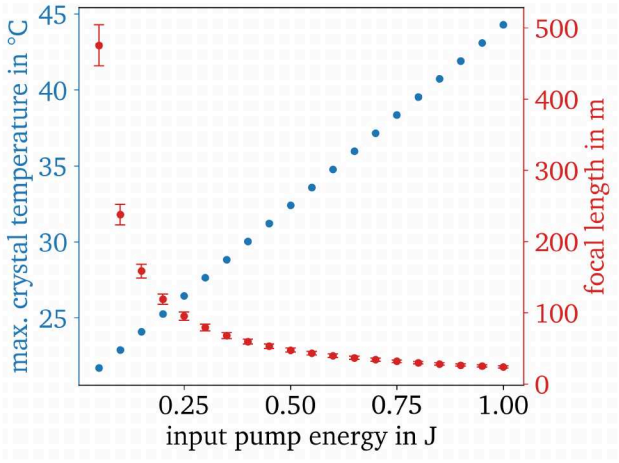


Figure 4.4.: Thermal-lens simulation via the heat-equation. The blue dots show the maximum temperature in the crystal and the red dots show the estimated focal length of the thermal lens.

pump energies, which decreases the emission cross-section at 1030 nm by 11 % and increases the absorption cross-section by 6 % (interpolated from data shown in Fig. 4.2). This will impact the overall efficiency of the amplifier if pump energies at this level are needed.

Additionally, Fig. 4.4 shows that even at 10 Hz repetition rate, which corresponds to a maximum average pump power of 10 W, the thermal lens needs to be taken into account. For sufficiently high pump power, the focal length is in the range of a few tens of meters, which is comparable to the focal lengths of the curved cavity mirrors.

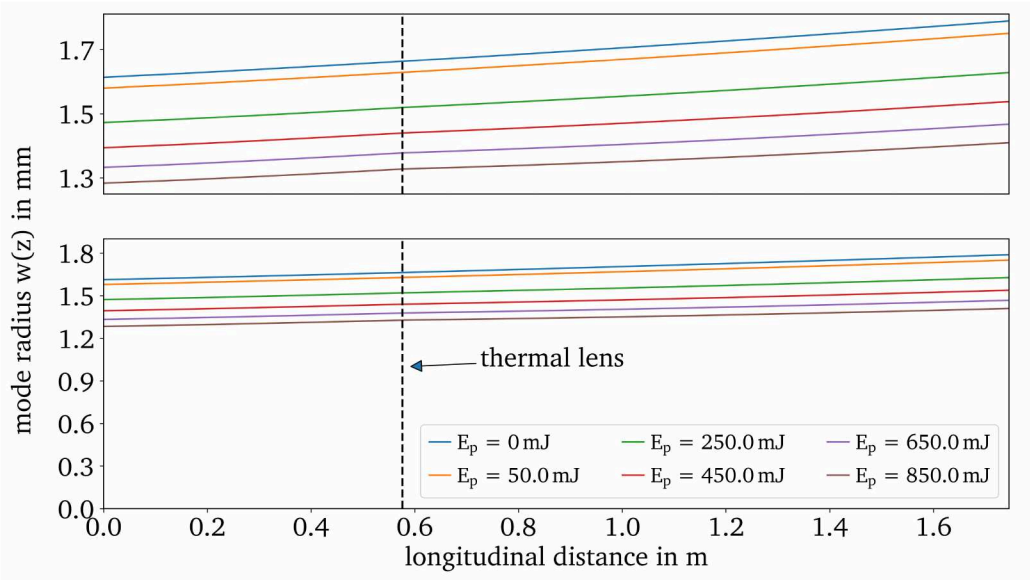


Figure 4.5.: Impact of the thermal lens on the mode radius w(z) of the cavity at 10 Hz for various pump energies. The -20 m radius mirror of the cavity is positioned at 0 m and the 15 m at 1.7 m. Bottom: absolute scale. Top: Zoom.

Extrapolating to higher repetition rates, this effect will increase up to a point where the cavity is

not stable anymore. However, since this system is supposed to work at 10 Hz, only its performance at this working point has to be ensured. The impact of the thermal lens at 10 Hz on the intracavity-mode evolution can be seen in Fig. 4.5.

Increasing the pump energy reduces the beam size of the cavity before and after the thermal lens. However, the general evolution of the mode is qualitatively similar to that of a non-pumped cavity (blue curve). At a pump energy of 850 mJ, the mode-radius is expected to reduce to 79 % of its original size in the non-pumped cavity. However, thermal lensing is not the only effect that reduces the mode size. With a stretch factor of 320 ps/nm and a lower estimation of 1.1 nm for the resulting bandwidth, the nonlinear Kerr effect is expected to show an influence on the mode formation inside the cavity via self-focusing inside the transmissive optics.

#### 4.1.3.2. Kerr-lens estimation

The Kerr effect introduces an intensity-dependent phase shift, which for Gaussian beams effectively acts as a lens. To deduce the influence of the Kerr-induced self-focusing effect during operation, it is necessary to include the effects of the thermal lens since this alters the spatial intensity distribution. In order to create a "worst-case" estimation at the shortest thermal focal length, I calculated the cavity mode for the pumped cavity at a pump energy of 1 J, which produces the smallest intra-cavity beam diameter. Also, a pulse duration of 320 ps is assumed, corresponding to 1 nm of bandwidth.

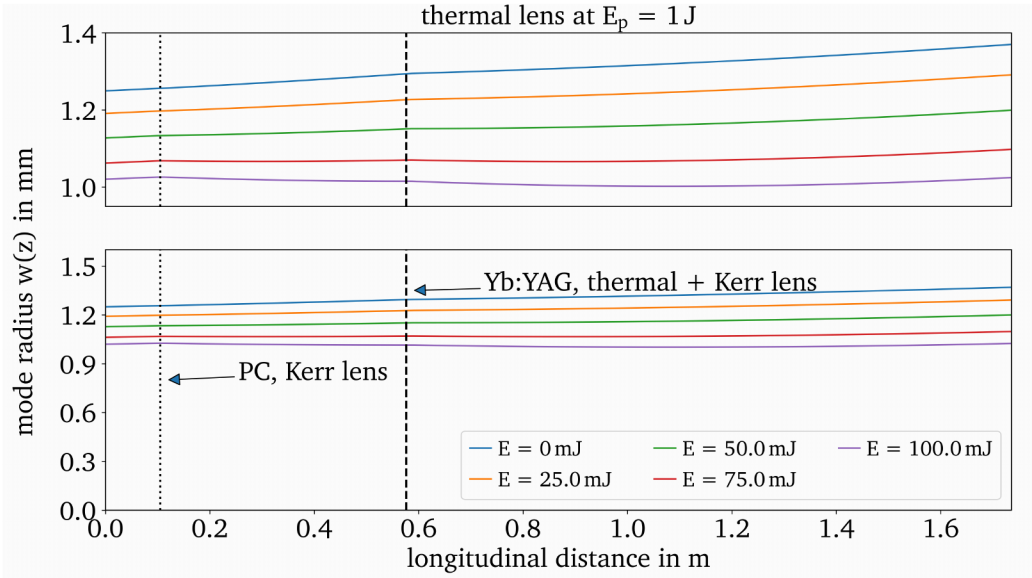


Figure 4.6.: Impact of the nonlinear Kerr effect on the mode radius w(z) for different signal energies and a thermal lens corresponding to 1 J of pump energy at 10 Hz. A pulse duration of 320 ps is assumed. The energy of the simulated beam is marked in the legend, whereas 0 mJ refers to the mode calculation without the Kerr effect. The position of the transmissive optics, namely the PC and Yb:YAG are marked with a dotted and dashed line, respectively. The **W**ave **P**late (WP) is not marked for reasons of visibility and due to its negligible influence. Bottom: Absolute scale. Top: Zoom.

For the estimation of the Kerr-lens influence, a mode distribution is numerically propagated for a whole round-trip and the phase of the thermal lens as well as the Kerr-induced phase is applied to the propagating beam within the respective transmissive elements. For a starting point of the mode

distribution, I chose the mode of the pumped cavity. The propagation step is repeated until the beam size deviation relative to the beam size of the previous roundtrip is below $10^{-8}$. When the calculation converges, the resulting distribution represents a stable mode inside this cavity for a given pulse energy and thermal lens.

Figure 4.6 shows the calculated waist of the beam as a function of the propagation distance inside the cavity for pulse energies of 25 mJ to 100 mJ in steps of 25 mJ. The mode which results if the Kerr effect is neglected is referred to as 0 mJ. The thickness of the transmissive optics in the simulation is based on standard available products, which is 20 mm for the PC, 1 mm for the Yb:YAG crystal and about 140 µm for the WP.

The first thing to notice is that the cavity design is capable of delivering a stable mode even for 100 mJ pulses with 320 ps pulse duration at the highest pump energy, and therefore the shortest thermal focal length of 24 m. Nevertheless, Fig. 4.6 shows clearly, that the Kerr effect will influence the intra-cavity beam size. A pure thermal lens (blue line) at a pump energy of 1 J, already reduces the mode size by approximately 23 %, compared to an unpumped cavity. As the thermal lens alters the cavity properties, which effectively reduces the beam size inside the transmissive optics, the influence of the Kerr effect gets enhanced due to its intensity dependence. Due to the coupling of both effects, the beam size at 100 mJ (violet line) inside the cavity is reduced by 43 %, compared to the non-pumped, Kerr-free cavity.

Comparing the focal lengths of the individual elements, we find, that the self-focusing in the PC dominates with a focal length as short as 9.5 m in the presence of the strongest simulated thermal lens. With this, the average fluence reaches 3.2 J/cm$^2$ and the peak fluence 6.3 J/cm$^2$ at the position of the smallest beam radius of 1 mm. Although these fluences are quite high, they are within the capabilities of modern optic manufacturers concerning laser-induced damage [214].

#### 4.1.3.3. Cavity setup

In the previous sections, I showed that a simple cavity design with only two curved mirrors can produce a stable mode even with the influence of the Kerr effect and a thermal lens. This design has been implemented and is schematically shown in Fig. 4.7.

As the planned output energies of the cavity are far beyond the energy-handling capacities of the fiber pre-amplifier (see section 4.1.2), safety measures must be put into place. Therefore, a set of two Faraday isolators (Coherent, Pavos series, $FI_1$ & $FI_2$) and an intermediate Faraday rotator (Coherent, Pavos series, FR) are installed to protect the fiber facets and splices of the fiber-amplifier from potential backward-propagating energetic leakage pulses. In combination with an additional polarizer and a pulse-picker PC, an extinction ratio of $10^{10}$ to $10^{11}$ is reached.

Next, a three-lens, mode-matching telescope is set up to increase the coupling efficiency between the two amplifiers. Then the pulses traverse a motorized delay stage, which is used to close the feedback loop for the uOPA pump-delay control, which stabilizes the delay between signal and pump in the uOPA. Before coupling the pulses into the regenerative main amplifier, a polarizer and a PC build the main separation unit for the incoming and outgoing pulses. The PC is configured such that the polarization rotates by 45° when there is no voltage applied and does not rotate if a voltage is applied. Accordingly, all pulses from the cavity will be reflected toward the compressor. Also, the pulse-picker PC (PC $\lambda/2$) reduces the repetition rate of the pulses to 10 Hz.

The cavity features a linear design with only two passively mode-forming curved mirrors with radii and positioning as described in the previous section. Only three transmissive optics are used: a 20 mm long DKDP PC (PC $\lambda/4$), a 140 µm thick quarter wave plate ($\lambda/4$ WP) and a 1 mm thick Yb:YAG crystal.

To facilitate the temporal overlapping of pump and signal in the uOPA, one of the end mirrors is mounted on a motorized 5 cm translation stage. For common short-pulse oscillator repetition rates

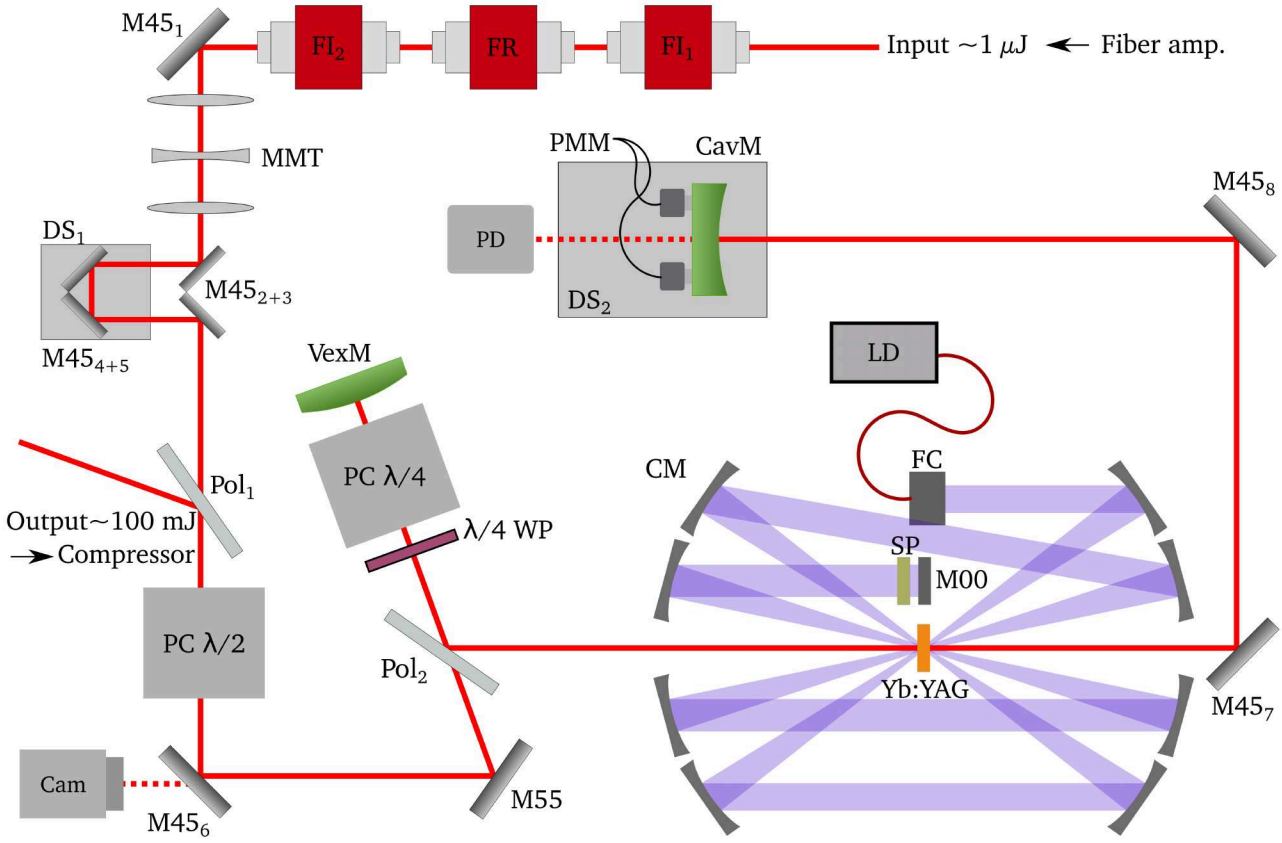


Figure 4.7.: Schematic drawing of the regenerative main amplifier and its input setup. The cavity is built around a single Yb:YAG crystal, pumped by a 12-pass pump system (for reasons of clarity only eight passes are drawn), powered by a fiber-coupled, high-power laser diode. A single PC, WP, and a pair of curved mirrors are used to set up a stable, regenerating cavity.

around 80 MHz it is often necessary to bridge temporal gaps of a few nanoseconds. This gap is easily closed here since every displacement of the motorized stage is multiplied by the number of roundtrips of the pump cavity. With this, meter-scale optical path differences can be covered by a few centimeters of mirror translation. For 50 roundtrips inside the cavity, the 5 cm travel distance of the motorized stage enables to create delays of 8.3 ns, which is sufficient to create temporal overlap at every possible delay for seed oscillators with repetition rates as low as 60 MHz. With the total intra-cavity length of about 1.7 m, the impact on the mode size by changing this length by ±2.5 cm can be neglected, as the relative mode-size change is at max 0.4 %. Lastly, a tip and tilt piezo-motorized mount for the concave end mirror is installed. This mount enables the remote alignment of the cavity during warm-up without the need to open the housed cavity.

The amplification takes place inside the 1 mm thick Yb:YAG crystal with a diameter of 12 mm and a doping concentration of 5 %. The doping concentration was selected since this is a commonly available doping concentration, which facilitates an exchange of the crystal, if necessary. The crystal thickness corresponds to the same thickness with which the Kerr and thermal lenses were estimated in the previous sections. Pumping is done via a high-power, fiber-coupled laser diode, centered around 940 nm with a maximum output power of 1.1 kW (Coherent, M1F4S22-940.3-1000Q).

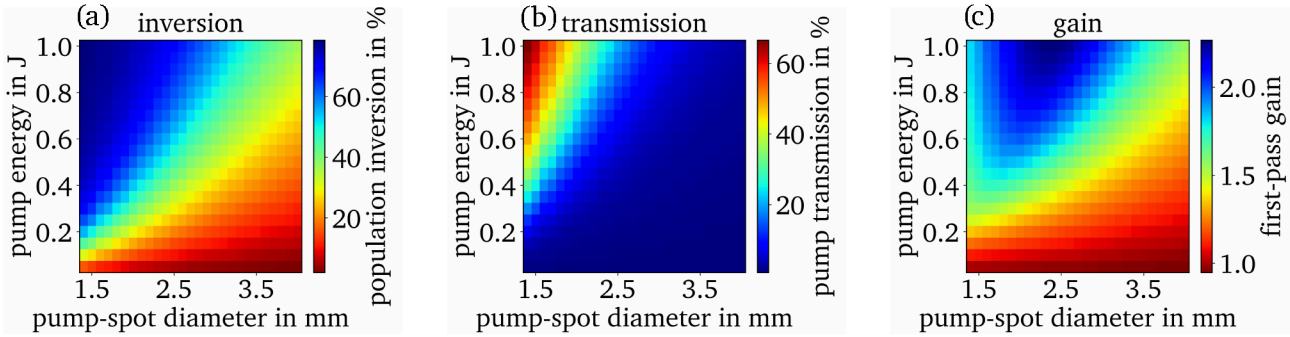


Figure 4.8.: Simulation of the pump absorption as a function of the pump-pulse energy and pump-spot-diameter for a 1 mm thick Yb:YAG crystal, with 5 % doping concentration. The pump features a center wavelength of 940 nm and a pulse duration of 1 ms. (a) Maximum population density of the laser level compared to the total doping concentration in %. (b) Transmission of the pump after twelve passes. (c) Gain of the first pass for the fundamental mode of the pumped cavity.

To enhance the pump absorption, the output of the laser diode propagates through a multi-pass module, consisting of a set of reflective 4-f telescopes. Each telescope images the fiber output of the diode onto the crystal, which allows to preserve the homogeneity of the fiber mode within the crystal. By limiting the total amount of pump passes through the crystal to twelve passes, the size of the pump module remains reasonably compact.

To determine the ideal pump spot size, I simulated the absorption of the pump for various pump-spot diameters and pump-pulse energies, including the thermal effects on the cross-sections. Figure 4.8 shows the results of the simulation. As expected, the population density of the laser level is the highest for the smallest pump-spot diameters, as shown in Fig. 4.8(a). However, Fig. 4.8(b) shows that a smaller pump spot size increases the transmission of the pump after all twelve passes, implying that the absorption saturates.

Also, a smaller pump spot size results in a stronger thermal lens, reducing the intra-cavity beam size. By calculating the mode size at the gain medium for each thermal lens and using the simulated population of the laser level, I calculated the gain of signal for the first pass, shown in Fig. 4.8(c). The highest gains are achieved for spot diameters between 1.7 mm and 3.2 mm, depending on the used pump energy. The final choice for the spot size was determined empirically, in which a pump-spot diameter of 2.4 mm performed best.

In Fig. 4.9 the corresponding pump profile at the position of the Yb:YAG crystal (a), as well as a part of the pump module (b) can be seen. To create the pump-spot diameter of 2.4 mm, the fiber output is first collimated by a collimating lens with a focal length of 2.5 cm (FC). The output profile of the 400 µm fiber is then imaged via curved mirrors with mirror radii of curvature of 30 cm onto the crystal, which results in a magnification factor of six. The spatial distribution of the pump spot is not a perfect flat-top distribution but remains symmetric.

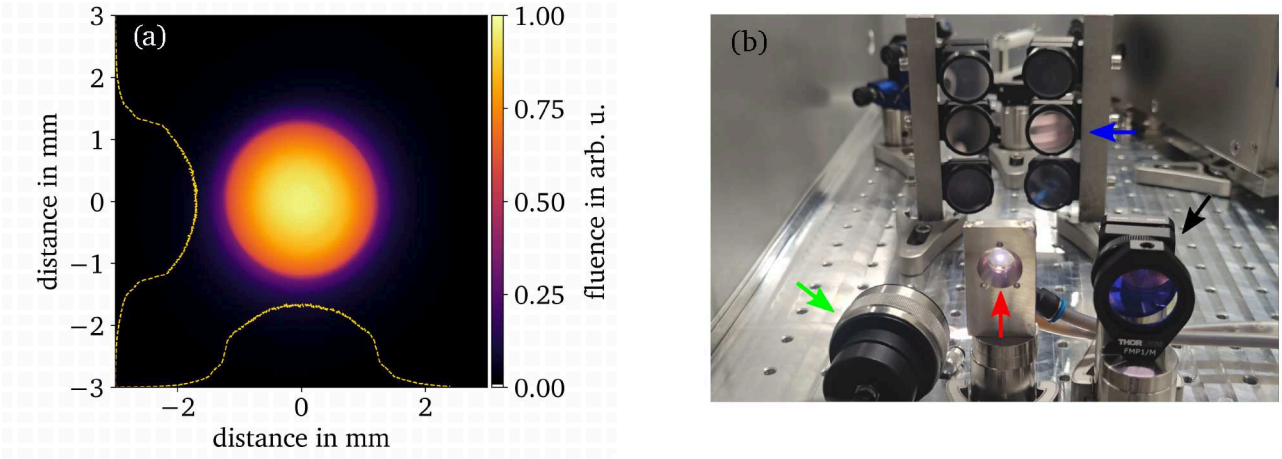


Figure 4.9.: (a) Spatial pump-distribution at position of the Yb:YAG-crystal. The lineouts are taken from the center of gravity of the spot in x and y, respectively. (b) Picture of the pump module from a view slightly above the second mirror module. The arrows mark the multipass mirrors (blue, CM), the 0°-mirror with a band-pass filter (black, M00), the fiber output (green, FC) and the Yb:YAG-crystal inside the mount (red). The bright spot in the center of the crystal is the fluorescence of the crystal at the pump spot.

The cooling configuration complies with the setup used in the simulation of the thermal lens. The crystal is mounted in between two ring-shaped copper plates. To increase the heat flow from the crystal to the copper plates, a 1 mm wide ring-shaped stripe of indium is placed on both sides of the crystal. The copper rings are screwed onto a water-cooled mount of stainless steel with thermally conductive paste, which increases heat dissipation and increases the pump absorption.

### 4.1.4. Pump compression and frequency doubling

Eventually, after amplification in the main amplifier, the pulses leave the regenerative cavity and are forwarded into the reflective-grating, folded Treacy-type compressor. Figure 4.10 depicts a schematic of the compressor setup. The beams pass a periscope (P) and are magnified by a factor of three within an afocal telescope (Tel) to reduce the fluence and intensity on the grating surface.

To reach the highest diffraction efficiencies at the pump wavelength of 1030 nm, MLD gratings with a line density of 1790 l/mm (Plymouth Grating Laboratory, PGL3751-FB, $G_1$ and $G_2$) are used. The gratings feature a clear aperture of 50 mm x 50 mm on a 60 mm x 60 mm fused-silica substrate. Since the diffraction efficiency of MLD gratings is the highest close to their Littrow angle [215], which at 1030 nm equals 67.2°, an incidence angle of 62.3° was chosen for the compressor setup. This allows to separate the incoming and outgoing beams, while staying in the vicinity of the Littrow angle.

Combined with a perpendicular grating spacing of 342.8 mm this results in a single-pass compressor length of 1.2 m for the center wavelength of 1030 nm. The dispersion by this setup exactly cancels out the dispersion of the CFBG stretcher, which has been designed to match this compressor. To eliminate the residual spectral phase which originates through dispersion inside the fiber amplifier and inside the transmissive optics of the regenerative amplifier, a manual translation stage is placed below the second grating to fine-tune the grating distance, such that the shortest possible pulses can be achieved.

To separate the incoming and outgoing pulses after the double-pass through the compressor, a retro-reflecting mirror (RR) is used, which introduces a vertical displacement of 2 cm, so that the pulse leaves

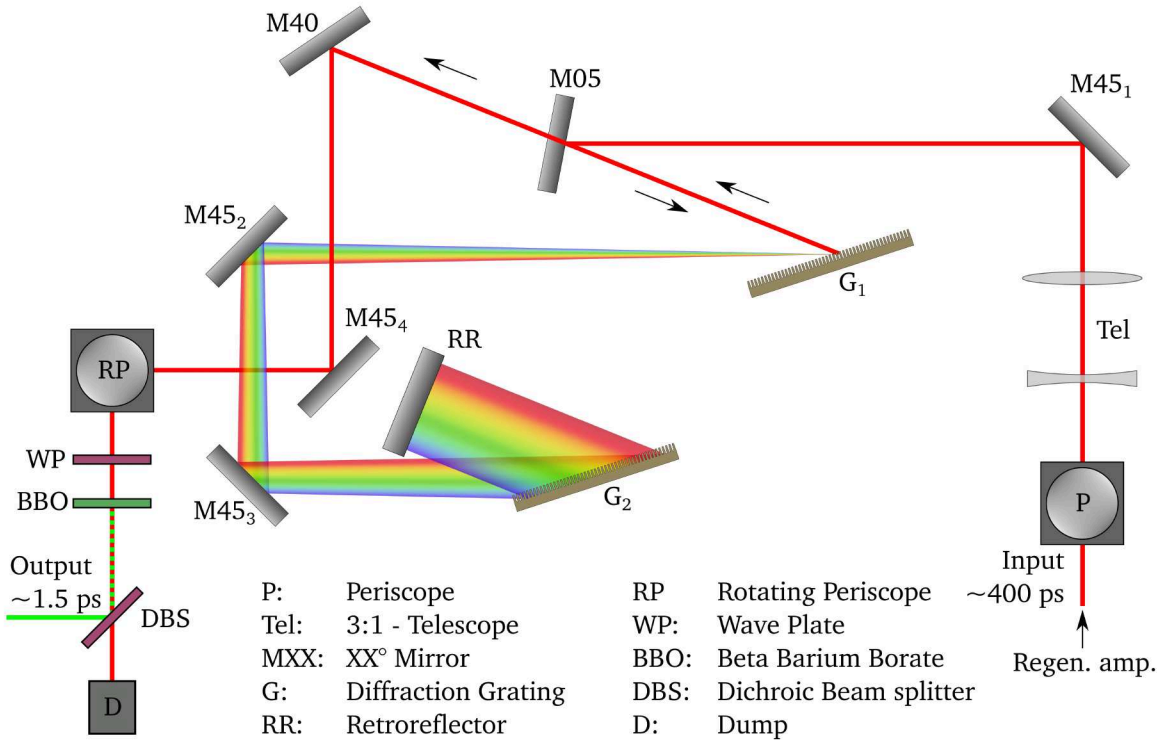


Figure 4.10.: Schematic drawing of the compressor and SHG stage. The beam is magnified and then coupled into the Treacy compressor, which is folded to increase the compactness of the system. A retroreflector enables the separation of the incoming and outgoing beams. The outgoing compressed pulses are frequency-doubled in a BBO-crystal and separated from their residual fundamental parts via a dichroic beam splitter.

slightly above the input mirror (Fig 4.10, M05). With the use of a rotating periscope (RP) the beams are displaced to their original propagation height.

Finally, before the pulse is used as the pump source for the uOPA it has to be frequency doubled. This is done inside a 10 mm diameter BBO-crystal with a clear aperture of 9 mm, which is a standard size. Assuming a pump-pulse duration of 1.5 ps (FWHM) after compression and a beam size of 2.5 mm (FWHM) the needed thickness of the SHG crystal to saturate the conversion, according to simulations, is about 0.65 mm for 25 mJ SHG output and 0.56 mm for 32.5 mJ SHG output. The thickness that was chosen for the setup is 0.6 mm. The frequency-doubled pulses then propagate to the uOPA setup and the residual, non-converted light is removed via a dichroic beam splitter and dumped.

## 4.2. Pump-laser performance

In this section, I will discuss the performance of the previously presented pump amplifier [1]. I will focus on the performance parameters of interest, which are spectral broadening, pre-amplification, main amplification, compression, and frequency doubling.

### 4.2.1. Spectral broadening of the pump seed

Following the structure of the previous sections, the first performance check involves the pump-amplifier capability to be used with different femtosecond oscillators around 1 µm. Every oscillator that covers the gain bandwidth of Yb:YAG is already compatible with the proposed setup. However, at some laser facilities, including the PHELIX laser, this is not the case. Figure 4.11 emphasizes the importance of implementing a spectral broadening stage for oscillators with insufficient spectral overlap to the gain bandwidth of Yb:YAG, by comparing the latter with the oscillator spectrum at PHELIX.

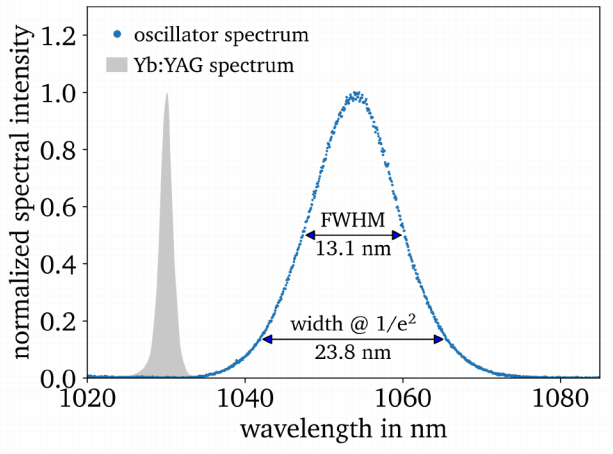


Figure 4.11.: Comparison of the oscillator spectrum at PHELIX (blue) and the bandwidth of Yb:YAG, calculated for a gain of $10^5$.

The oscillator at PHELIX exhibits a spectral bandwidth of 13.1 nm FWHM and 23.8 nm at $1/e^2$ corresponding to an FTL of about 124 fs FWHM. This however does not suffice to seed the Yb:YAG based pump-amplifier system, as clearly shown in Fig. 4.11. However, Fig. 4.12 shows that this spectral gap can be closed by the utilization of SPM in a standard fused silica fiber. In Fig. 4.12(a), the spectral broadening of the spectrum is plotted as a function of the input pulse energy in the fiber, whereas more energy results in a broader spectrum. This trend would continue when the pulse energy and therefore the intensity inside the fiber would be increased. Obviously, a limit is given by the damage threshold of the fiber.

Because of the direct input from the oscillator, the energy increase is naturally limited to the oscillator's pulse energy, which also seeds the uOPA. Therefore, it is useful to examine the actual usable energy after broadening, which corresponds to the spectral portion within the CFBG reflection or the gain bandwidth of Yb:YAG. Figure 4.12(b) shows this measured portion, expressed in average power.

This measurement emphasizes the need for a pre-amplifier. Even with 80 % of the maximum oscillator pulse energy, corresponding to a pulse energy of 2.3 nJ at PHELIX, the power in the relevant spectral domain is as low as 5 mW. At 72 MHz, the repetition rate of the oscillator, this corresponds to about 68 pJ per pulse. To reach 100 mJ of output energy in the main amplifier without pre-amplification, a gain

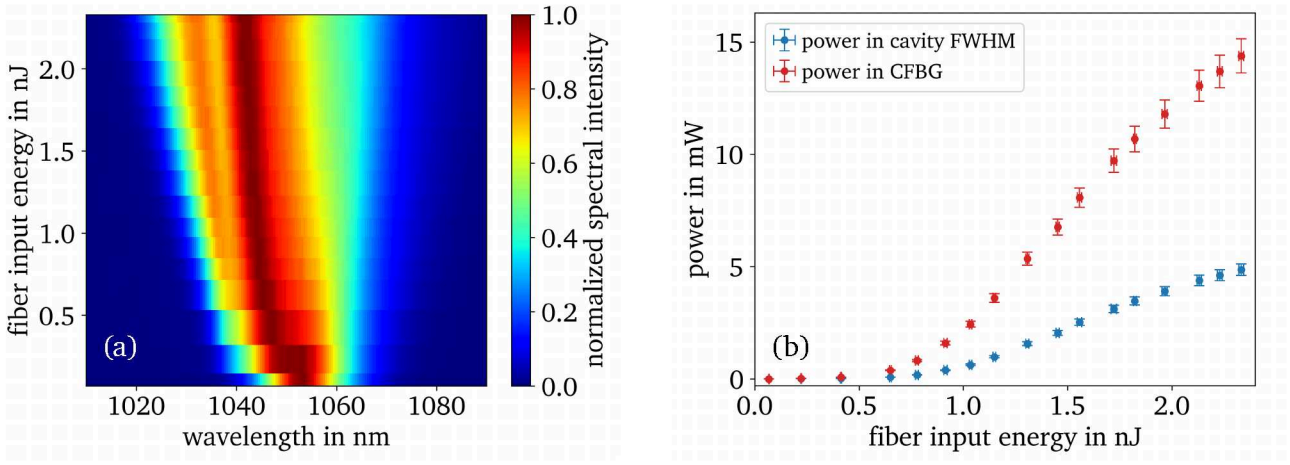


Figure 4.12.: Experimental SPM tests with a standard single-mode fiber (mode-field diameter: 6.6 µm). (a) Spectral distribution at the SPM-fiber output. Each spectral slice is normalized to its maximum amplitude. (b) Power in the correct bandwidth to seed the Yb:YAG-cavity directly (blue) and inside the reflective band of the CFBG (red).

of more than nine orders of magnitude is required. At such gain levels, the ASE may draw substantial energy from the medium and limit the amplification process, such that unreasonably high pump energy is needed. This situation may even be worse if the seed-coupling efficiency into the regenerative amplifier is not 100 %.

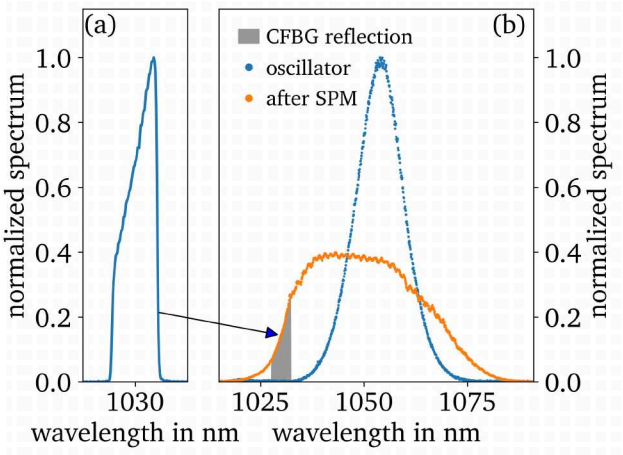


Figure 4.13.: Comparison of the input and output pulse spectra of the SPM stage at the PHELIX laser. The spectrum of the input pulse ((b), blue) is sufficiently broadened ((b), orange) to seed the fiber amplification stage. The spectra are normalized to their integral. The part of the spectrum that is stretched via CFBG is depicted in (a).

As the input for a fiber amplifier, however, this is less problematic since the whole pulse train is amplified and a total gain below $10^5$ is targeted. Then, the quasi-continuous pulse train will extract the majority of the energy in the medium, enabling operation at large gains without the risk of excessive ASE levels, as long as the average power of the pulse train is sufficient and the pulse delay is significantly smaller than the fluorescence time of the active medium. As shown in Fig. 4.12(b), the power in the

bandwidth of the CFBG is in the range of 2 mW even for input pulse energies of 1 nJ, which is already enough for such a system to dominate the amplification process [207]. The resulting output pulse spectra of the implemented SPM stage at PHELIX are shown in Fig. 4.13.

Figure 4.13(a) shows the cut-out spectrum after stretching in the CFBG. The complete, broadened spectrum is shown in Fig. 4.13(b) in orange. The spectrum is just broad enough (FWHM: 37 nm) to create a stable seed for the fiber amplifier. If necessary, the seed power is adjustable by a WP and a polarizer. In this configuration, 70 mW is sent into the SPM fiber, whereas 2 mW remains as the effective seed for the following fiber amplifier.

### 4.2.2. Pre-amplification performance

From here on, the presented data were recorded during the development of the uOPA system for the PENELOPE laser, i.e. the seed for uOPA and pump are generated in a different oscillator (Flint, Light Conversion) than the PHELIX oscillator.

After spectral broadening and stretching, the pulses are amplified over the course of two stages featuring a total gain of approximately $10^5$. By this, energies in excess of 1 µJ can be achieved. Due to its 'all-fiber' setup, the amplifier output is mainly sensitive to the input seed power but robust in terms of environmental influences. Concerning potential seed fluctuations, saturated amplification in its first stage manages to stabilize the output energy. Furthermore, the output energy can easily be regulated with the use of the AOM that couples the two fiber stages as described in section 4.1.2. Figure 4.14 shows the impact of the energy adjustment via repetition-rate tuning.

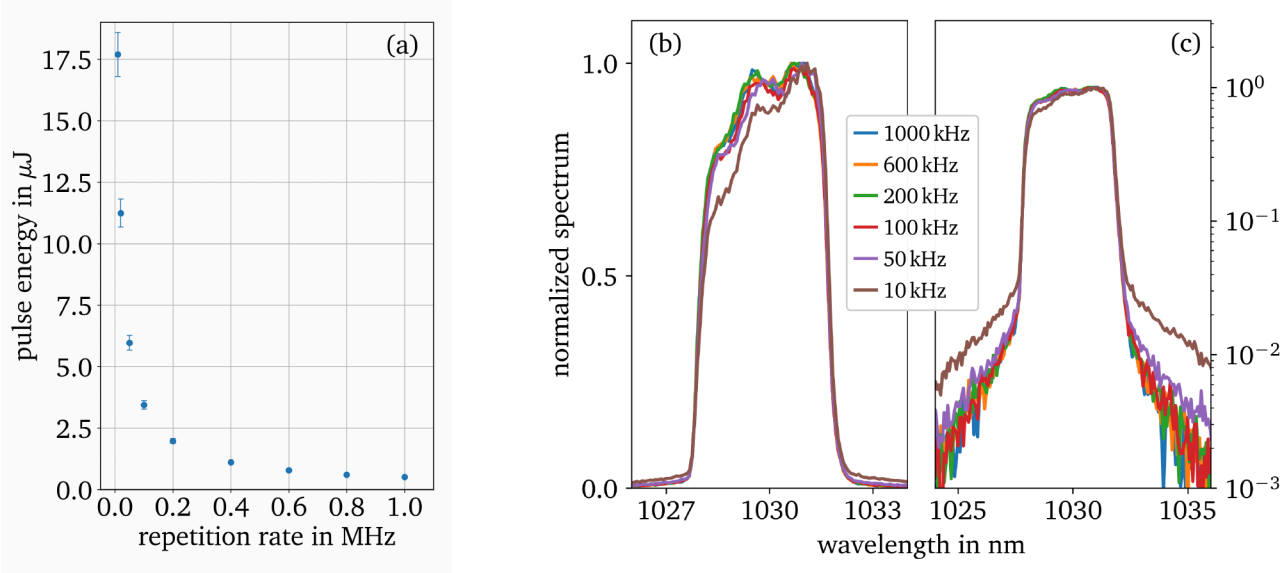


Figure 4.14.: (a) Influence of the repetition rate on the output energy of the fiber pre-amplifier via tuning of the repetition rate. The energy uncertainty is dominated by the systematic error of the power meter itself. (b)/(c) Comparison of the spectra after pre-amplification at different repetition rates. (b) linear scale, (c) log-scale.

When the repetition rate decreases, the output energy strongly increases, e.g., from 0.5 µJ at 1 MHz to 17.7 µJ at 10 kHz, corresponding to an energy-increase factor of 35. While more seed energy is indeed beneficial for the regenerative amplifier, the increase should be done thoughtfully, since the temporal Kerr effect or ASE may impact the pulse quality in the later system.

As shown in Fig. 4.14(b,c), effects on the spectrum are already observable at lower repetition rates. First, a spectral-distribution deformation begins to manifest at 50 kHz. This is most likely due to gain saturation, where the leading part of the pulse passes through regions with a slightly higher population inversion compared to the trailing part. Furthermore, there is a slight onset of ASE in the wings, which begins at 50 kHz but is most visible at 10 kHz. Finally, although not yet observable at this point, small impacts of the Kerr effect are to be expected since the nonlinear propagation length [216] is already as low as 4.5 cm (compared to 1.55 m fiber length) for pulse energies of 17.7 µJ, corresponding to an intensity of 8 GW/cm$^2$.

Consequently, to mitigate any further deterioration, the repetition rate is set to a working point of 100 kHz with an output pulse energy of (3.4 ± 0.2) µJ.

To minimize coupling losses between the pre- and main amplifier, a mode-matching telescope is constructed to match the waist size as well as the waist position of the fiber amplifier output beam and the mode of the regenerative amplifier. For this, the beam sizes of each output have been measured at the location intended for the telescope. From these measurements, the divergence of the beam and therefore the waist and its position could be determined via a fit. With the measured beam sizes and the estimated waist positions, an optimal three-lens telescope has been calculated using LaserCalc [217]. Figure 4.15 depicts the setup, the measured data, and the calculated fits.

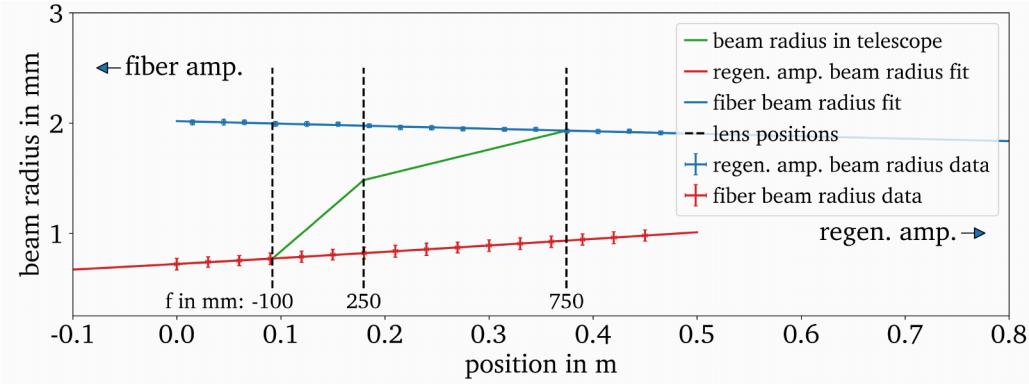


Figure 4.15.: Beam-size and waist-position manipulation via mode-matching telescope.

By restricting the lenses to standard commercial lenses within LaserCalc, a cost-effective and easy-to-implement setup is found. The lenses in use are f=-100 mm, f=250 mm and f=750 mm, which theoretically enable perfect imaging (floating point error) from one waist to the other. In reality, however, perfect mode-matching is certainly reduced by imperfections of the optics, alignment, measurement and fit errors. Nevertheless, a clear but qualitative improvement could be observed, as the number of roundtrips inside the non-pumped cavity increased significantly, indicating lower coupling losses inside the cavity.

### 4.2.3. Main-amplification performance

After pre-amplification and optimization of the coupling efficiency, the cavity was ramped up to determine its energy output capabilities. As the amplification will not only increase the energy but also alter the beam- and spectral/temporal shape, the following section will cover the characterization and control of the main amplifier. Furthermore, I will give insights into its long-term stability, temporal quality and beam quality after the compression of the pulses. Lastly, the working parameters for the uOPA will be listed.

#### 4.2.3.1. Monitoring of the output

Three monitoring systems (two cameras and one **P**hoto **D**iode (PD)) are used to ensure the stability and functionality of the amplifier. The cameras monitor both the near- and the far-field of the beam. The near-field camera is placed 65 cm after the output polarizer, behind a leakage mirror before the pulse-picker PC (compare Fig. 4.7). This camera allows tracking of the x-y position of the beam, as well as estimating the pulse energy via integration of the irradiated area.

Furthermore, the camera can detect malfunctions in the form of a disrupted beam profile. This is critical for mitigating or avoiding further damage in a running system, particularly when high fluences and high output energies are expected. Irregularities, such as circular diffraction patterns caused by dust particles or already damaged optics can cause increased local intensity and thus represent a risk for damage on successive optics. Also, deterioration of optical coatings may result in a redistributed mode shape, as shown in Fig. 4.16. The shown deformation from Fig. 4.16(a) to (b) was caused by a coating deterioration of the PC (c) and was detected during the setup of the system.

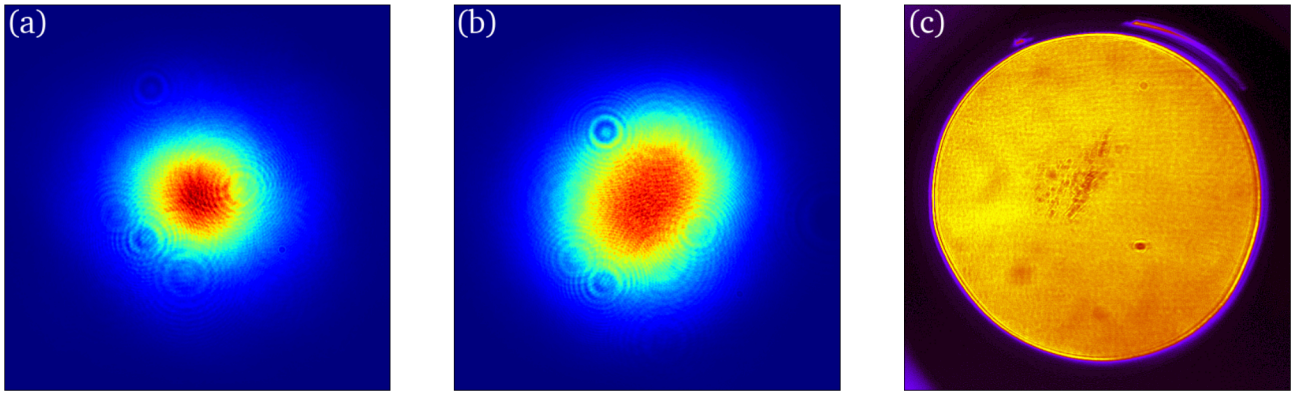


Figure 4.16.: Impact of a damaged coating on the beam profile, measured at the cavity output. (a) Beam profile before the damage, (b) beam profile after damage, (c) view through the damaged PC. The image of the PC was taken by imaging the damage onto a camera, while the cavity was not running. The violet shading around the PC aperture is due to diffraction of the used lighting. The deteriorated PC-coating induces a deformation of the beam along its diagonal, creating an asymmetric beam shape. The small diffraction patterns in (a) and (b) are due to dust on the camera filters.

Figure 4.16(a) shows the beam profile before the deterioration of the PC, Fig. 4.16(b) after the deterioration and Fig. 4.16(c) the actual cause - the damaged PC, showing a deteriorated surface close to its center. From Fig. 4.16(a) to Fig. 4.16(b) an elongation of the beam-diagonal can be observed.

Although the coating features scratch-like damages on the surface (Fig. 4.16(c)), the resulting beam profile does not feature typical diffraction patterns after propagation through such structures. While the scratch-like damage did not increase the intra-cavity losses of the cavity to a measurable level, it certainly reduces the coupling efficiency, since the mode does not match the seed anymore.

Especially as a pump for a uOPA such modifications need to be detected and removed since a change in the beam shape will impact the output of the uOPA, implying the importance of continuous monitoring of the beam profile. As mentioned before, this camera can also be used as an energy meter, but it should not be used as the exclusive device to do so.

Hence, another diagnostic device, a PD, is implemented to monitor the cavity in operation. Here, the amplitude of the pulse during the build-up time in the cavity can be observed, as shown in Fig. 4.17.

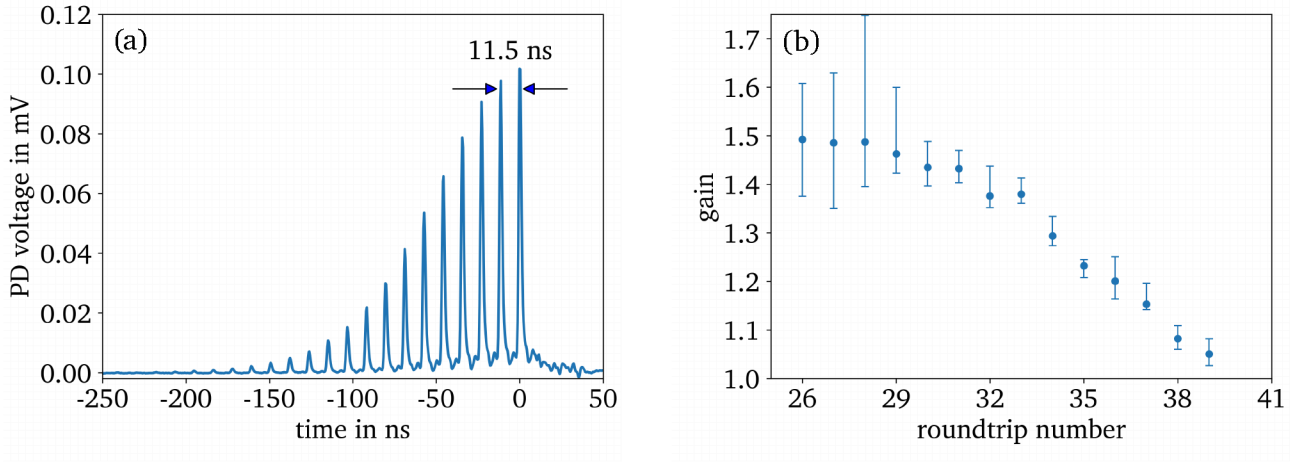


Figure 4.17.: (a) Build-up trace of the regenerative amplifier, measured via PD from leakage light at the concave end-mirror. (b) Gain per double-pass through the crystal, calculated from the PD-trace. The cavity settings for this measurement were 46 mJ output energy and an amplification time of about 448 ns.

Here, Fig. 4.17(a) shows an exemplary build-up trace of the amplifier. The parameters associated in this case correspond to an output energy of 46 mJ and an intra-cavity time of 448 ns. The pulse inside the cavity passes the active medium twice per roundtrip before hitting the mirror in front of the PD.

Consequently, as long as there is enough energy in the active medium, the pulse will be amplified and its energy increases. If the energy extraction is low compared to the stored energy, the gain of the pulse per roundtrip remains approximately constant. However, if the energy of the pulse is large enough, a sufficient amount of energy is extracted from the active medium and gain saturation can be observed.

Since only the last roundtrips are visible on the PD-trace due to its low dynamic measurement range, the gain per roundtrip, which is plotted in Fig. 4.17(b), can only be estimated close to maximum saturation. Within the last 14 roundtrips, the gain drops from about 1.5 down to 1.05 before the cavity is opened and the pulse exits the amplifier.

Aside from the gain, a PD-measurement helps to detect problems regarding the seed. If the gain of the cavity is extremely high and the seed energy generally low, a further reduction of the seed may result in excessive generation of ASE which is observable as a plateau in between the PD-peaks. Although this seems to be the case in Fig. 4.17, the plateau is, in this case, only an artifact of the slow PD response. I verified this by blocking the seed completely, which resulted in no measurable signal at all. Therefore, it can be assumed that the seed energy is sufficient.

#### 4.2.3.2. Energy output

Concerning the maximum output energy of the amplifier, a measurement of the output energy as a function of the pump energy was conducted. To account for saturated amplification, the intra-cavity time was adjusted for every pump energy to achieve maximum output energy. Figure 4.18 shows the results.

In Fig. 4.18, the output energy (blue) of the regenerative amplifier as well as the optical-to-optical efficiency (red) is depicted. As shown, the targeted energy of 100 mJ is achieved and can even be

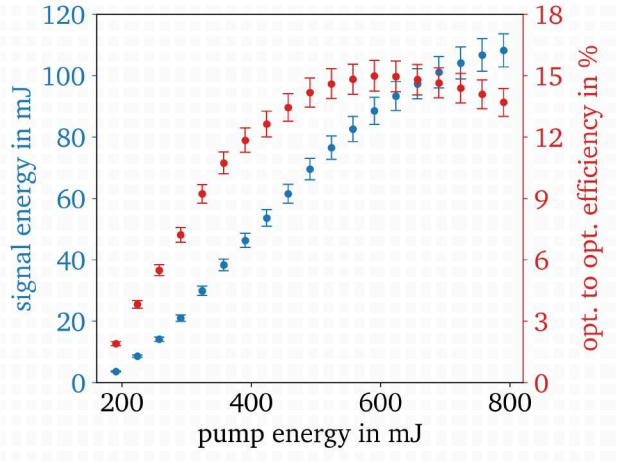


Figure 4.18.: Output energy (blue) and optical-to-optical efficiency (red) of the regenerative amplifier as a function of the pump energy.

surpassed with a maximum energy of 108 mJ. At this point, the laser diode delivered 70 % of its maximum specified output energy. Since the needed diode current to increase the output energy by 1 mJ increased to more than 2 A, the measurement was not taken any further to avoid damage to the laser diode or the optics inside the cavity.

For lower pump energies, the output of the cavity scales nearly linear with the used pump energy up to the point of maximum optical-to-optical efficiency of 15 % at an output energy of approximately 90 mJ. When further increasing the pump energy, the output energy increases, but with reduced efficiency. Despite the reduction of the efficiency, the energy goal of 100 mJ is reached with a pump energy of 690 mJ, corresponding to only 63 % of the maximum output peak power of the pump-diode. Due to the operation at a duty cycle of 1 % (10 Hz with 1 ms pulse duration), this corresponds to only 6.3 % of the maximum output average power. Accordingly, an extended lifetime of the pump diode is expected.

Nonetheless, the origins of the reduced efficiency should be discussed for potential future upgrades of the system, in which an upscaling of the energy may be desired.

#### 4.2.3.3. Limitations of the main-amplifier energy output

The limitations of the energy output arise most probably due to the onset of thermal and nonlinear effects in the cavity, which alter the spectral and spatial properties of the propagating beam during the amplification. The reasoning for this argument will be detailed in the next paragraphs.

**Thermal effects**

Concerning thermal effects, three phenomena may be observed. First, generally associated with heat deposition is thermally induced stress, resulting in depolarization and therefore increased losses. However, an inspection of the beam profiles at various pump energies does not show any signs of strong depolarization, which would otherwise result in a cross-shaped loss pattern [218]. In fact, the beam profiles remain round, even at the maximum tested energy of 108 mJ, as shown in Fig. 4.19(a).

Second, with an increase in pump energy, the temperature of the crystal increases, which reduces the absorption cross-section at the pump wavelength and the emission cross-section at the signal wavelength of Yb:YAG as shown in Fig. 4.2.

Last, the beam shrinks due to the thermal lens as described in section 4.1.3 and shown in Fig. 4.19(b)

(red data). Due to its rising influence on the mode size inside the crystal with increased pump energy, the beam will deplete the inversion faster in the center and starts to get reabsorbed sooner, whereas the inversion is depleted more uniformly for bigger beams. This finding agrees with the reduction of the optical-to-optical efficiency for higher signal energies.

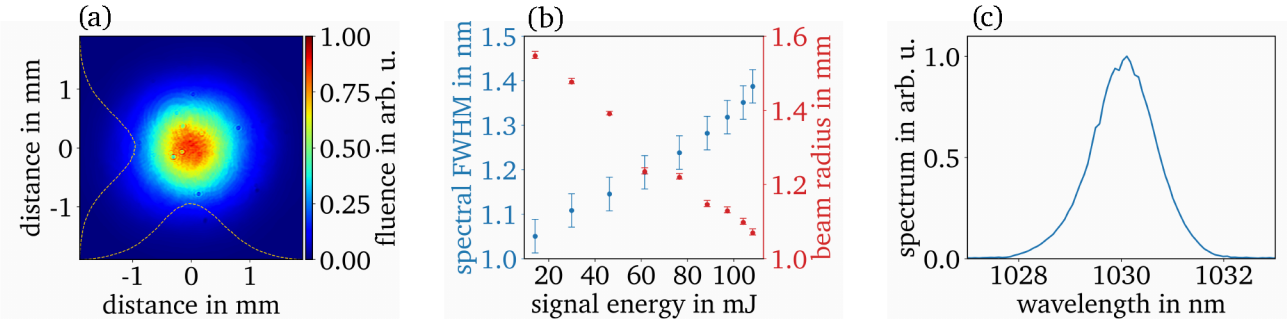


Figure 4.19.: (a) Beam profile at 108 mJ. The dashed lines represent the sum over the axes in x and y, respectively. The beam profile has been measured outside the cavity, at 65 cm distance to the cavity output. (b) Spectral FWHM and beam radius ($1/e^2$) as a function of the output energy. The y-axes are color-coded to match the represented data. (c) Pulse spectrum at 108 mJ.

Aside from the beam-size reduction, Fig 4.19(b) shows that also the spectrum (blue data) of the pulse is altered, as the signal output energy increases. The spectral bandwidth increases with increasing output energy, which may be mostly explained by the heating of Yb:YAG, which alters the shape of the emission and absorption cross-section of Yb:YAG (compare Fig. 4.2). However, this is also an indicator for the onset of the Kerr effect, which results in spectral broadening via SPM and self-focusing of the beam. This hypothesis is further corroborated by slight modulations in the spectrum, which occur at the highest energies as shown in Fig 4.19(c).

**Nonlinear effects**

To estimate the influence of the Kerr effect, I conducted a calculation of the beam size after amplification, to see whether the inclusion of the Kerr effect creates beam sizes, similar to the measured data. The simulation is set up analogously to that in section 4.1.3.1 and the results of this calculation are displayed in Figure. 4.20.

For the calculation, the actual pulse energies of the signal and the pump have been used to estimate the thermal lens and the intensity of the pulse. The red colored points represent the measured data, while the green, blue and black data points represent the simulation of the beam size by including both, thermal lensing and Kerr effect, only Kerr effect and only thermal lensing, respectively. While an exclusive thermal lens matches quite well for lower energies, the beam sizes are underestimated at higher output energies, which also holds for the simulation with exclusive Kerr-induced focusing. The closest match for the full energy-output range is given by the simulation which includes both the Kerr effect and thermal lensing. Ultimately, the Kerr lens is coupled to the thermal lens of the medium as the thermal lens reduces the beam size, which in turn enhances the influence of the Kerr lens.

Since the simulation matches the measured data reasonably well, it can be used to estimate the nonlinear focal lengths of the transmissive media by fitting the calculated nonlinear phase (phase of the thermal lens excluded) to the phase of an ideal lens. Furthermore, the B-integral of the last roundtrip can be estimated. The results are displayed in table 4.2.

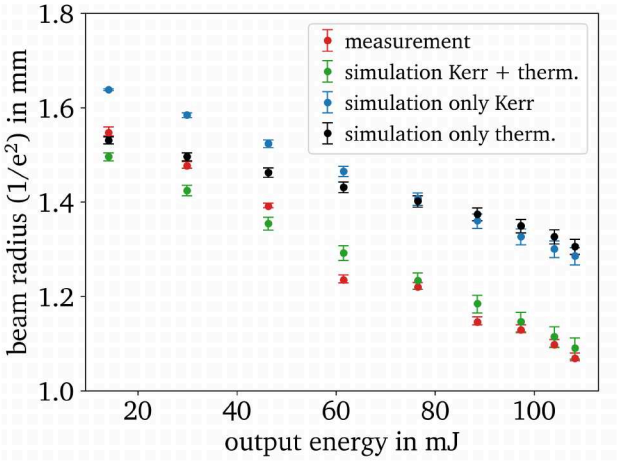


Figure 4.20.: Comparison of the measured and the simulated beam sizes at the same near-field camera position as in Fig. 4.19. The uncertainty of the values arises from measurement and fit uncertainties of the input parameters that are used in the simulation.

For each data point, I used the measured output energy and the corresponding pump energy to calculate the thermal focal lens and a measurement of the pulse duration after amplification to calculate the intensity inside the transmissive optics. As each of these parameters is associated with a measurement or fit uncertainty, they are used to calculate an upper and lower uncertainty for the values of the B-integral and the Kerr lenses.

Table 4.2.: Estimated B-integral values at the peak intensity and focal lengths of the Kerr lens for the last roundtrip inside the cavity as a function of the output energy. $f_{YAG}$ represents the Kerr-induced focal length of the 1 mm thick Yb:YAG crystal and $f_{PC}$ that of the 20 mm long PC. The uncertainty of the values arises from measurement and fit uncertainties of the input parameters that are used in the simulation.

| **Energy in mJ** | **30** | **46** | **62** | **76** | **88** | **97** | **104** | **108** |
|---|---|---|---|---|---|---|---|---|
| $\mathbf{f_{YAG}}$ **in m** | $979^{+150}_{-63}$ | $541^{+16}_{-100}$ | $434^{+70}_{-46}$ | $378^{+58}_{-22}$ | $325^{+41}_{-77}$ | $293^{+52}_{-42}$ | $236^{+73}_{-19}$ | $162^{+23}_{-87}$ |
| $\mathbf{f_{PC}}$ **in m** | $116^{+8}_{-6}$ | $65^{+4}_{-6}$ | $41^{+4}_{-2}$ | $29^{+3}_{-2}$ | $23^{+1}_{-2}$ | $19^{+1}_{-2}$ | $17^{+2}_{-2}$ | $15^{+2}_{-1}$ |
| **B in mrad** | $103^{+6}_{-7}$ | $174^{+10}_{-12}$ | $252^{+16}_{-18}$ | $338^{+22}_{-24}$ | $415^{+27}_{-31}$ | $478^{+31}_{-36}$ | $531^{+35}_{-40}$ | $568^{+38}_{-43}$ |

The table shows that the PC dominates the Kerr-induced self-focusing, as it induces Kerr-lenses whose focal lengths are in the order of ten times shorter than that of the Yb:YAG crystal and even shorter than the combined focal length of the thermal lens and the Yb:YAG Kerr lens. Although Yb:YAG features a nonlinear refractive index [219], which is approximately twice as large as that of the PC material DKDP [220], the difference in length makes up for that. This emphasizes the need to reduce the path lengths of the pulses inside transmissive media. Even for small output energies, the effective focal length of the Kerr-lens inside the PC is already about twelve times as long as the focal length of the end-mirror and reaches 1.6 times its focal length at maximum energy.

Another value that can be estimated from this simulation is the B-integral of the last roundtrip. This

shows a steady increase when incrementing the output energy, resulting in values for the B-integral ranging from approximately 100 mrad at 30 mJ up to approximately 570 mrad at 108 mJ. The latter values are rather high and may impact the compressibility of the pulse, as the nonlinear phase shift is not trivially compensated.

#### 4.2.3.4. Pump stability

Concerning the output energy, the pump laser already surpasses the demanded energy of 100 mJ. However, the pump is only useful if the requirement for energy stability is reached as well. Hence, I measured the output energy for a period of approximately 3 hours to determine the energy stability of the laser. The measurement was conducted at approximately 86 mJ output energy, which is close to the estimated needed uncompressed pump energy and also close to the point of maximum efficiency. With this setting, the build-up time to saturation takes only 288 ns, corresponding to a total roundtrip number of 25. Figure 4.21 shows the results of this measurement.

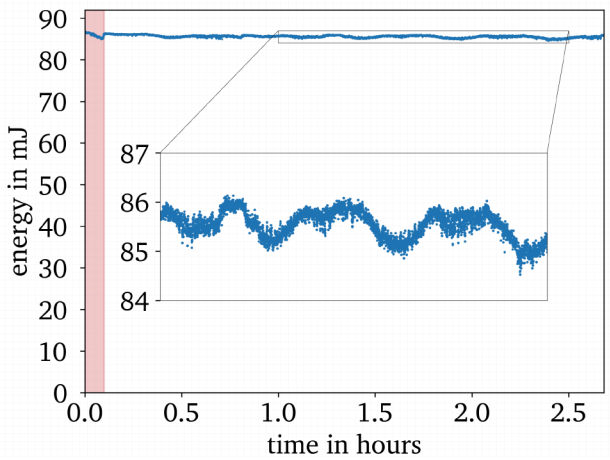


Figure 4.21.: Pulse energy of the regenerative amplifier for approximately 3 hours without interaction and 6 minutes of warm-up time (red-shaded area). The inlet shows a close-up of the energy fluctuation, most probably induced by the air conditioning system.

After a short warm-up time of 6 min (red-shaded area), the signal stabilizes and remains stable over many hours. The energy stability reaches then 0.35 % (standard deviation), mostly dominated by slow energy drifts, which are highlighted in the zoom inlet. Due to the timescale of the slow energy drifts, the most probable origin of these oscillations is the air conditioning system in the test laboratory, which is not optimized to perfectly maintain the temperature, but periodically only cools the room to a specified temperature.

To estimate the stability of the system on a more localized timescale I removed the slow variation caused by the air conditioning system by subtracting a moving-average value calculated over 60 seconds. With this, the standard deviation over the total time span is 98 µJ, corresponding to a stability with a relative standard deviation of 0.1 % and a local **P**eak-**t**o-**V**alley (PtV) fluctuation of 1.3 %. While the stability criteria is not met for the full measurement time, the stability on a one-minute timescale is about twice as good as demanded and 98.3 % of the data points fulfill the criterion.

Furthermore, I determined the pointing fluctuation by monitoring the centroid of the beam in the far-field, using a 400 mm focusing lens. I could observe the same oscillatory behavior, as the periodic cooling slightly bends the housing of the regenerative amplifier and the optical table, which results

in mostly vertical displacement of the beams. The measured standard deviations are 44 µrad in x and 90 µrad in y. However, even with this displacement, 99 % of the data points are below the defined pointing threshold (see section 3.2.3) for a 1 mm thick crystal (260 µrad), but only 81 % for a 2 mm thick crystal (130 µrad).

Nevertheless, one can argue that the oscillatory behavior is a specific property of the test laboratory and that the oscillations allow for simple counter-measures in form of a piezo-motorized pointing stabilization since the period time of about 30 min is long. This also implies a significantly higher pointing stability, which corresponds to 17 µrad in x and 12 µrad in y for a timescale of 1 min. Within this timescale, more than 99 % of the data points fulfill the requirement of the 2 mm thick crystal and all data points fulfill the requirement for the 1 mm thick crystal.

#### 4.2.3.5. Pulse compression

Apart from the output energy, it is necessary to see whether the requirement in terms of pulse duration is fulfilled and if this is the case, whether the pulse duration varies with variable pulse energy. To investigate this, I measured the temporal pulse profile with an SHG-**F**requency-**R**esolved **O**ptical **G**ating (FROG) at different output energies. I adjusted the output energy of the regenerative amplifier by increasing or decreasing the laser-diode current. This decreases the energy stability but keeps the additional dispersion during the amplification constant for every output energy since the number of roundtrips remains untouched. Like that, no realignment of the compressor has to be done for each measurement. Thus, the results remain comparable. Figure 4.22 shows a comparison of two measurements at 80 mJ (a) and 100 mJ (b).

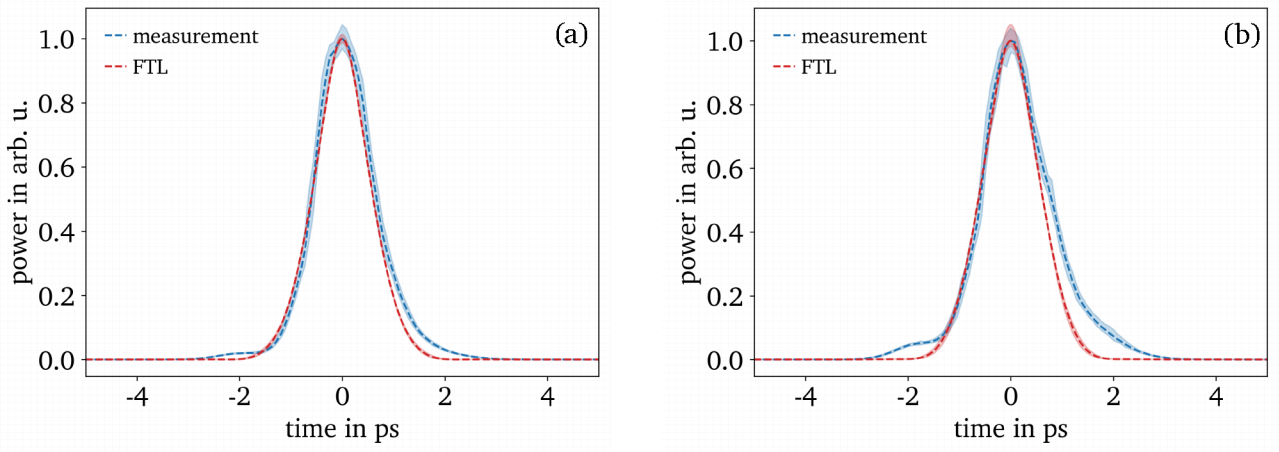


Figure 4.22.: Comparison of the compressed pulses at 80 mJ (a) and 100 mJ (b). The pulses, measured with an SHG-FROG, are depicted in blue with reconstruction errors (PtV) as blue-shaded area. The FTL, calculated numerically from the spectrum, is shown in red.

As one can see, the pulse is nicely compressible up to a certain energy. Quantitative measures like the FWHM show a near perfect compression when compared to the FTL with a measured pulse duration of $(1.27 \pm 0.03)$ ps and an FTL of $(1.21 \pm 0.01)$ ps for 80 mJ. At 100 mJ, the measured pulse duration increases to $(1.38 \pm 0.04)$ ps, but is still close to its FTL of $(1.27 \pm 0.02)$ ps.

However, when comparing the shapes of the pulses, clear differences are visible and degradation of the pulse form is observable when increasing the output energy from 80 mJ to 100 mJ. This result agrees qualitatively with the increment of the estimated values for the B-Integral in table 4.2. Because

of the reduction in compressibility with higher B-Integral, an energy increase of 25 % does not result in the same increase in peak power, but only 13 %. For the measurements below 80 mJ, no significant increase in compressibility could be observed. For either case, the pulse duration remains below 1.5 ps and is therefore in the required range.

Concerning the energy throughput of the compressor, a comparison of pulse energy before and after compression shows a transmission of $(85.6 \pm 0.8)$ %. This is lower than one would expect from the measured grating efficiency alone, which was characterized above 98 %. By careful inspection of the transmitted spectra through the compressor, I could identify spectral clipping at the second grating of the compressor as the main reason for the reduced transmission efficiency. This can be improved but does not impose problems concerning the pulse duration as the measurement shows.

#### 4.2.3.6. Beam quality

Since the spatial clipping creates sharp edges in the beam profile for some frequency components, the beam quality might suffer due to altered diffractive properties of the beam as a whole. To determine this, I conducted an $M^2$ measurement of the beam after compression, which is shown in Fig. 4.23(a) together with the focal spot distribution in Fig. 4.23(b).

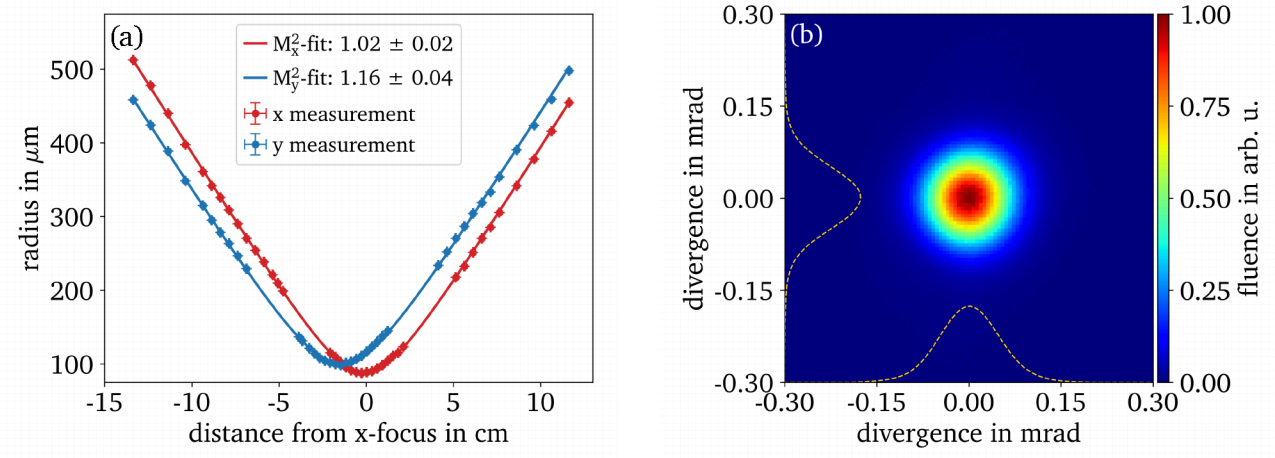


Figure 4.23.: (a) $M^2$ measurement according to ISO Standard 11146 after compression at maximum energy with a 1 m lens with $M_x^2 = 1.02 \pm 0.02$ and $M_y^2 = 1.16 \pm 0.04$. (b) Fluence distribution of the beam at the focal-spot position of the y-axis. The dashed lines represent the sum over the axes in x and y, respectively.

The measurement shows that the beam exhibits slight astigmatism and a different beam quality for the x- and y-axis. While the beam quality in the x-axis is close to the ideal with an $M_x^2 = 1.02 \pm 0.02$, the beam quality of the y-axis is in the range of $M_y^2 = 1.16 \pm 0.04$.

Obviously, $M_y^2$ is larger. Given that a rotating periscope is used after the compression, the y-axis on the camera matches the clipping axis of the second compressor grating. However, an $M^2$ measurement before compression showed the same quantitative outcome as the measurement after compression, but with a degraded beam quality in the x-axis, which excludes the clipping as a reason for the axially dependent beam quality.

A more probable cause for the discrepancy in the $M_x^2$ and $M_y^2$ lies in the trapezoidal shape of both the PCs inside and outside the regenerative cavity. As the PC crystals are wedged (0.5° wedge on each side) along the x-direction to avoid pulse replica, they cause asymmetric refraction between the two axes.

#### 4.2.3.7. Frequency doubling

The final hurdle for the pump is the efficiency of the SHG, for which the requirement is set to at least 50 %. However, Fig. 4.24 shows that this hurdle can be overcome.

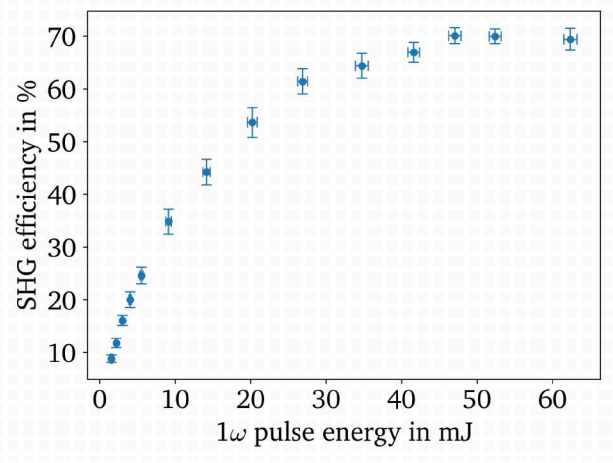


Figure 4.24.: SHG efficiency as a function of the input pulse energy after compression.

Here, the SHG efficiency is plotted as a function of the input pulse energy after compression at its fundamental frequency. The SHG efficiency starts to saturate already below 10 mJ of input energy, as the second-harmonic energy does not increase quadratically. The saturation also reflects in the energy stability of the SHG, which, depending on the degree of saturation, increases to 1.03 - 1.4 times the fundamental energy stability and thus still fulfills the energy-stability criterion.

The targeted efficiency is reached at ≈18 mJ of input energy and approaches a plateau at a maximum value of $(70.1 \pm 1.5)$ % for input energies above 50 mJ. Hence, the total required pump energy of 32.5 mJ is achieved at an input energy of about 46 mJ, corresponding to 54 mJ of pulse energy before compression. This is 50 % of the maximum deliverable energy, which allows for a large tuning range. However, the maximum frequency-doubled energy is currently limited to 43 mJ, due to damage thresholds of the crystal and self-focusing after compression. To further increase this energy, a larger beam size would be needed, which in turn would call for larger crystals and a larger second compressor grating to mitigate further clipping.

#### Conclusion

The presented design for the uOPA pump laser fulfills all the set requirements, except for the stability on a three-hour timescale. However, due to its excellent short-term stability, the pump is nonetheless regarded as suitable for a uOPA.

The generated pulses surpass the demanded energy of 100 mJ with a global long-term energy stability with a standard deviation of 0.35 % and a local stability of 0.1 %. The pulses can be compressed close to their FTL below 1.5 ps and exhibit a high beam quality of $M_x^2 = 1.02 \pm 0.02$ and $M_y^2 = 1.16 \pm 0.04$. The SHG efficiency reaches up to 70 %, which, combined with the compressor transmission, results in a transfer efficiency from uncompressed fundamental to the compressed second harmonic of 60 %.

In the next section, I will discuss the implementation and characterization of the uOPA system, which is pumped by the laser, presented in the previous sections.

## 4.3. Setup of the uOPA

The previous section detailed the design, setup and characterization of a laser that is suitable to pump a uOPA in terms of output energy, pointing- and energy stability, beam quality and pulse duration.

In this section, I will describe the experimental setup of the uOPA with emphasis on the modules required to use the pump effectively and to create robust amplification. Further, I will deal with the characterization of the uOPA module and evaluate, whether this system represents a valid alternative for first-stage regenerative amplifiers in high-intensity-laser front-ends. The results of this section were also submitted for publication and have been accepted recently [2]. Figure 4.25 shows the complete setup.

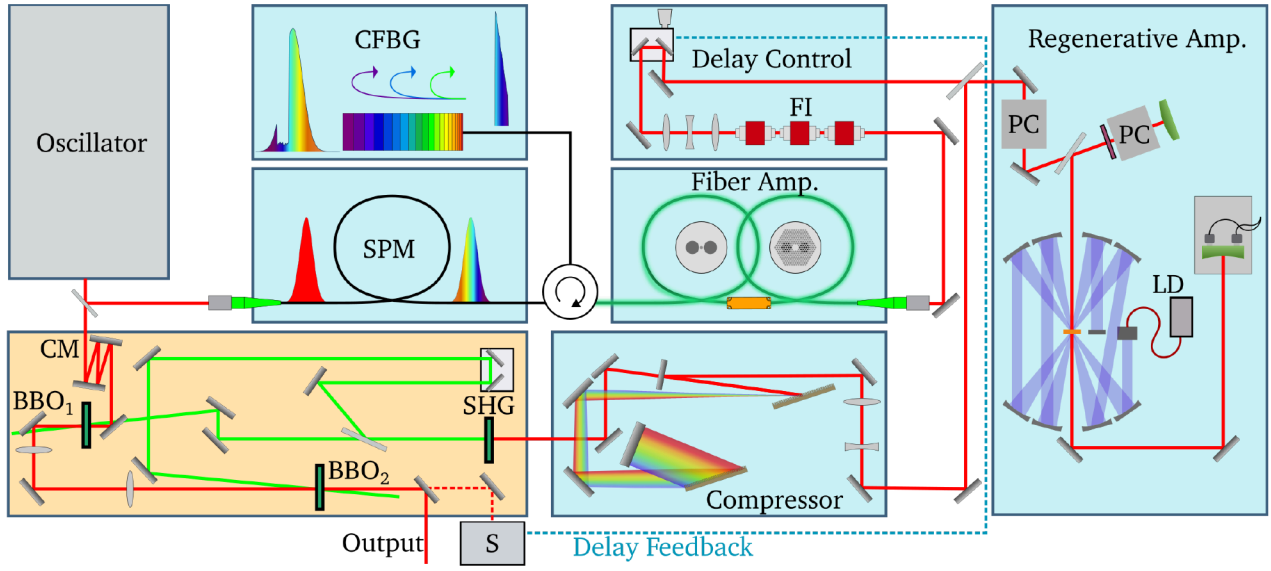


| | | | | | |
|---|---|---|---|---|---|
| SPM: | Self-Phase Modulation | S: | Spectrometer | LD: | Laser Diode |
| CFBG: | Chirped Fiber Bragg Grating | BBO: | Beta-Barium Borate | | |
| FI: | Faraday Isolator | CM: | Chirped Mirror | | |
| PC: | Pockels Cell | SHG: | Second Harmonic Generation | | |

Figure 4.25.: Schematic view of the complete uOPA system, including the oscillator (gray box), the pump laser (blue boxes) and the uOPA stages (orange boxes).

Starting from the same oscillator, the pulses are split intensity-wise to either seed the pump amplifier or the uOPA stage. On the side of the uOPA chain, the oscillator pulses pass a stretching stage consisting of two parallel setup mirrors of which one is a **G**ires-**T**ournois **I**nterferometer (GTI) mirror, also referred to as chirped mirror, to increase the temporal overlap of the signal and pump pulse as recommended by simulations, detailed in section 3.2.3. With a **G**roup-**D**elay **D**ispersion (GDD) of $(1800 \pm 100)\,\mathrm{fs}^2$ at 1035 nm, four hits account for an additional GDD of $7200\,\mathrm{fs}^2$. The pulse duration of input pulses from the FLINT oscillator consequently increases to a pulse duration of $(617 \pm 5)$ fs FWHM, measured via SHG-FROG. After stretching, the pulses seed the first of two uOPA stages.

To use the pump for both stages, it is split via a WP and polarizer into a high- and low-energy part. While the high-energy part traverses a translation stage to compensate the delay of additional signal pathways between the two stages, the low-energy part is sent directly to the first stage. To couple pump and signal into the first uOPA stage, a dichroic mirror is used to combine the pulses. Here, the pump transmits through the mirror and the signal is reflected. The beam radii in this stage are $w = (1.54 \pm 0.02)\,\mathrm{mm}$ and $w = (2.14 \pm 0.06)\,\mathrm{mm}$ for the signal and pump, respectively. This corresponds

to a beam size ratio between signal and pump of 0.72 $\pm$ 0.02.

The first stage itself consists of a 2.4 mm thick BBO crystal, in which pump and signal propagate in a close-to collinear setup. As the targeted output energies of the first stage are in the low microjoule range, parasitic SHG is less of a problem even in a close-to-collinear setup. Yet, this almost collinear setup increases the gain bandwidth of the OPA. The corresponding propagation angles inside the BBO crystal are 23.3° for the signal and 23.7° for the pump. In this stage, a pre-amplification to the microjoule level is targeted.

Because of the Gaussian shape of the beams, the associated non-uniform gain distribution and the working point of this stage in the unsaturated regime, the outgoing beam radius of the signal will be strongly reduced compared to its input radius. Hence, a magnifying telescope is implemented between the two stages to increase the beam radius by a factor of two, as well as to image the output from the first onto the second stage.

As the telescope would image not only the signal but also the residual pump and idler, a spatial filter in the focal plane is used to block the pump, idler and PSF. Imaged onto the second stage, which consists of a 1 mm thick BBO, the signal beam radius is $w = (1.80 \pm 0.09)$ mm, while the pump radius remains unchanged. This further increases the spatial overlap with a signal-to-pump ratio of 0.85 $\pm$ 0.05. To counteract parasitic SHG of idler and signal, the internal crystal angles of pump and signal inside the second stage are 24.24° and 26.61°, respectively. Furthermore, the larger pump-to-signal angle allows combining the pulses without dichroic mirrors. This is beneficial because either the high pump intensity may cause problems due to self-focusing inside the mirror or a post pulse could be created by double reflection inside the mirror, depending on which pulse is transmitted.

After amplification in the second stage, a small part of the signal pulse leaks through a 0.2 % beam splitter. This share of the signal is used to monitor the delay between pump and signal, by coupling it into a spectrometer (Ocean Insight, HR2000+). Since the signal pulse exhibits a chirp, a delay shift between pump and signal directly translates to a shift of the spectral center of the signal. A motorized linear stage, located between the fiber amplifier and the regenerative amplifier of the pump laser, can correct the delay in a closed-loop. Since the delay is caused by thermal fluctuations, only minor adjustments are required, such that the electronic timing of the pumping system, i.e. PC timing, remains unaffected. In addition, potential energy fluctuations due to the pointing jitter caused by the moving stage are minimized by the saturated operation of the regenerative amplifier.

## 4.4. Performance of the uOPA

Within this section, I want to address the performance of the system with respect to the most important parameters: spatial beam quality, spectral bandwidth conversation and energy stability. All these parameters impact the performance of high-intensity lasers and should be preserved or enhanced within this amplification scheme, as even small fluctuations in these parameters may when combined or coupled result in a significant loss of intensity [179].

### 4.4.1. Energy output

To reach 1 mJ of output energy, two uOPA stages have to be used, whereas the working point of the first one is set to moderate output energies and lower levels of optical-to-optical conversion efficiency. This ensures amplification with a barely depleting pump, hence, a minimized reconversion of the signal and an amplification scheme closer to the small-signal-gain regime, which results in less distorted spectra and beam profiles.

The corresponding output energies and optical efficiencies in dependency of the pump energy can be seen in Fig. 4.26. The pump energies have been measured with a commercial energy meter (gentec-eo, QE25LP-S-MB-D0) and adjusted via a half-wave retardation plate and the polarizer that splits the energy between the stages.

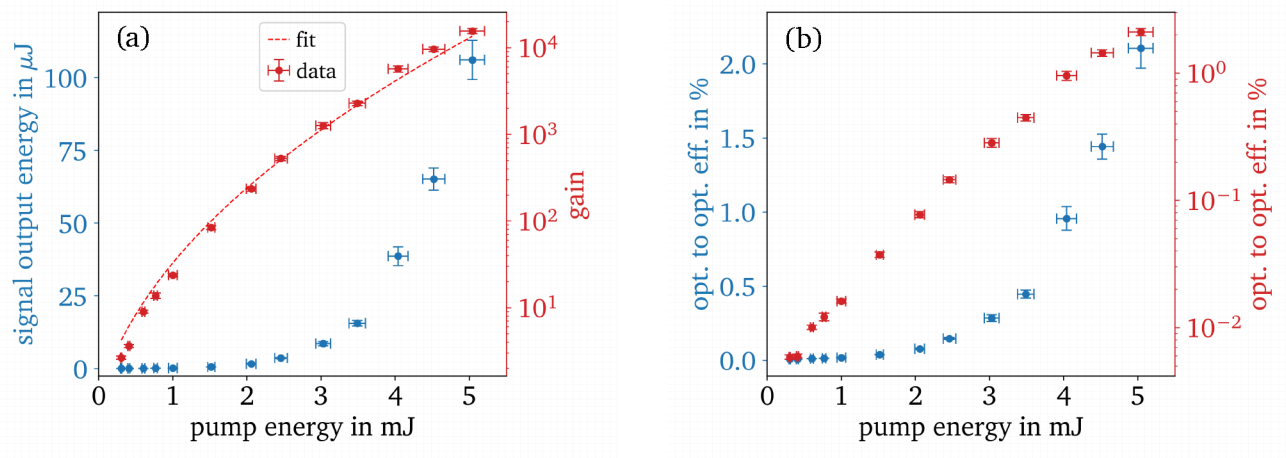


Figure 4.26.: Output energy and signal gain of the uOPA over pump energy in the first stage (a) and the optical-to-optical efficiency of the first stage (b). The error bar represents the standard deviation of the measurement.

Figure 4.26(a) depicts the output energy in linear scale (blue) and gain in the first uOPA stage in log-scale (red). A fit of the parametric gain with the theoretical scaling of an undepleted pump with perfect phase-matching (eq. 3.9 with $\gamma = g$) shows a qualitatively good agreement, indicating a non-saturated amplification. This is in agreement with the optical-to-optical efficiency, shown in Fig. 4.26(b), which only varies between 0.1 % at minimum and 2 % at maximum, corresponding to approximately 100 µJ output energy. However, since a spatial filter is implemented between the stages, the output energy should remain in the range of 10 µJ or below. Otherwise, nonlinear effects may disrupt the beam profile and the spectrum, or the ignition of an air plasma might block the beam.

The output energies and optical-to-optical efficiency of the second stage are shown in Fig. 4.27. For this measurement, I kept the pump energy of the first stage at a constant level of (2.70 ± 0.02) mJ. With this, the parametric gain of the first stage is approximately 850 and creates a seed with an energy of (5.75 ± 1.2) µJ, which, according to the conducted simulations, should suffice to reach 2 mJ of output.

In contrast to the first stage, the scaling of the output energy as a function of the pump energy differs significantly. As shown in Fig. 4.27(a), the output energy scales linearly and the efficiency starts to saturate, approaching a plateau at around (4.38 ± 0.14) %. At this point, the uOPA achieves an output energy of (1.05 ± 0.03) mJ using a pump energy of (24.0 ± 0.7) mJ. The linear growth of the signal energy indicates the existence of parasitic processes, which restrict exponential growth.

Although a pump-to-signal angle of -2.35° should suppress the generation of the second harmonics, I could observe a significant conversion for both, signal and idler, when increasing the output energy. At 24 mJ pump energy, the parasitic SHG signal approached 700 µJ, corresponding to 67 % of the achieved energy at the fundamental wave. Since the mutual amplification of idler and signal is of immense importance for the exponential amplification in the uOPA, an energy extraction through parasitic SHG results in a tremendous reduction of the gain, restricting the exponential growth. Also, a switch from a negative to a positive pump-to-signal angle by rotating the crystal did neither reduce or increase the SHG significantly. While the signal energy meets the set requirement of 1 mJ, the measured output

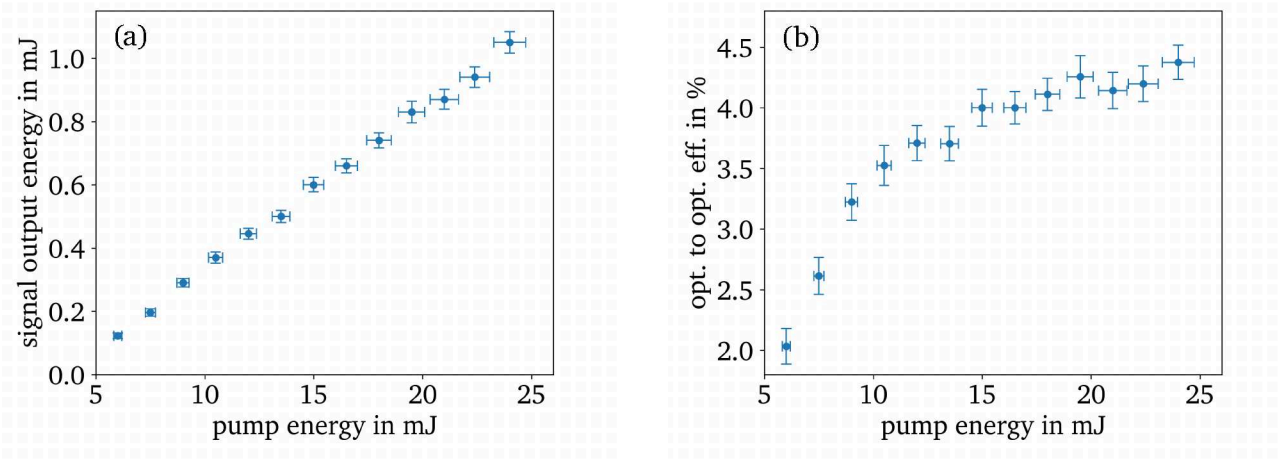


Figure 4.27.: Output energy of the uOPA over pump energy in the second stage (a) and the optical-to-optical efficiency of the second stage (b). The pump energy in the first stage is kept constant at 2.7 mJ corresponding to an input energy of (5.75 ± 1.2) µJ for the second stage.

energy does not match the expected output energy of the simulations close to or above 2 mJ and even the sum of signal and signal-SHG energy does not add up to 2 mJ. This overestimation of the output energy in the simulations is presumably due to the excessive generation of the SHG of idler and signal, which was not predicted by any simulation software and still needs further investigation.

To estimate if the efficiency is also degraded by PSF, I measured the output of the amplifier with and without seed. For this, I used a camera and integrated over all pixels. To account for the dynamic range between the measurements, two filters were used to attenuate the signal of the amplified seed by approximately a factor of $10^5$. Dividing the measurement of the system with a blocked seed by that of the seeded system, the upper limit of the energy contrast for the PSF can be estimated to be $(4 \pm 1.3) \cdot 10^{-8}$. Compared to the influence of the parasitic SHG this is negligible and can be ruled out as a limitation for the growth of the signal energy. Additionally, no cone-like PSF structures after the second stage, which may deplete the pump, were observed.

Even though the gain is limited by parasitic SHG, this does not limit the applicability of the system in a high-intensity laser as long as the target output energy of 1 mJ is achieved and the temporal and spatial quality meets the requirements. Additionally, even with a linear dependency of the pump energy, there is no onset of an energy plateau visible, indicating even higher output energies are possible when increasing the pump energy. Although this is generally possible, I avoided upscaling the energy because a further increase of the pump energy requires to expand the pump beam size to evade damage to the crystal at too high intensity, which also calls for an upscaling of the compressor gratings and SHG crystal as mentioned in section 4.2.3.7.

Furthermore, magnifying the compressed pulse is prone to beam-quality degradation due to strong self-focusing effects inside the lenses or by the off-axis use of reflective spherical telescopes, which is inherently plagued by aberrations. While off-axis, afocal parabolic telescopes would offer a theoretically feasible solution to this problem, their misalignment-sensitivity and general alignment-complexity [221] have been estimated to be too high to maintain daily. Consequently, no magnifying telescopes have been used for the sake of simplicity.

However, an energy increase can still be realized by increasing the seed energy in the second stage with only minor pump energy adjustments in the first stage, if a larger output energy is required. This,

however, has to be done with caution, due to the imaging telescope between the stages. For reasons of comparability, the following data, concerning the beam and spectral quality, has been recorded with the same seed energy as in Fig. 4.27 if not declared otherwise.

### 4.4.2. Evaluation of the spatial distribution after amplification

As a measure of the beam quality, the spatial distribution of the output beam has been monitored at different pump energy levels. To minimize the influence of any stray light from the pump beam, I conducted the measurement after approximately 3 m of propagation, such that I had to use only a minimum number of camera filters, which often create multiple reflections or introduce dust speckles and therefore distort the beam-distribution measurement. To keep the camera from saturation and remove the second harmonic of the signal, a dichroic mirror as well as a polarizer and half-wave retardation plate were used. Figure 4.28 shows the results of this measurement.

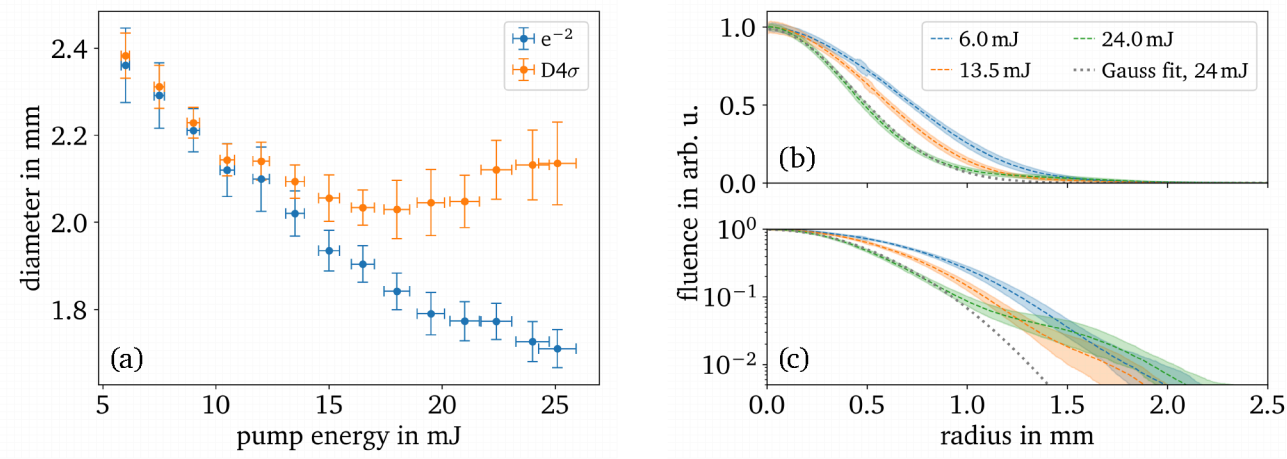


Figure 4.28.: Beam sizes after amplification in the second uOPA stage, measured at a threshold of exp(-2) (blue data) and via the second moment of the distribution (a) and exemplary radial lineouts of the beam after uOPA at different pump energies and a Gaussian fit at the highest pump energy of the second stage in linear- (b) and log-scale (c).

Figure 4.28(a) depicts the diameter of the beam at the threshold of exp(-2) in blue and the diameter measured by calculating the second moment of the beam distribution, referred to as D4$\sigma$ diameter in orange. For this, the beam distribution has been transformed to polar coordinates and the uncertainty in the beam sizes represents the standard deviation of all measurements calculated at every azimuthal angle. Similar, but not as comprehensive as an $M^2$-measurement, this gives a first impression of the deviation from a Gaussian distribution when going to higher pump energies, since the different methods should result in the same diameter if the beam distribution is Gaussian. However, above 13 mJ pump energy we can observe a clear deviation. While the diameter calculated via simple threshold evaluation decreases with increasing pump, the D4$\sigma$ diameter starts to increase again at pump energies of 17.5 mJ. This indicates that the beam diffraction shifts energy to the outer regions.

This can also be seen qualitatively in Fig. 4.28(b,c), where three radial lineouts at pump energies of 6 mJ (blue), 13.5 mJ (orange) and 24 mJ (green) are plotted in linear (b) and log-scale (c). The dotted lines represent the mean fluence and the fillings correspond to the fluctuation of the measurement. The increased fluctuation within the 6 mJ and 13.5 mJ lineout at about 0.5 mm results from a dust particle on the camera. As the pump energy increases, the beam shrinks but at the same time, the wings of the

distribution increase in amplitude. While this is not as pronounced at 13.5 mJ pump energy, at 24 mJ the wings are clearly visible, which indicates a spatial deformation towards higher-order super-Gaussian distributions at the crystal output. This agrees with the $M^2$ measurement, depicted in Fig. 4.29(b).

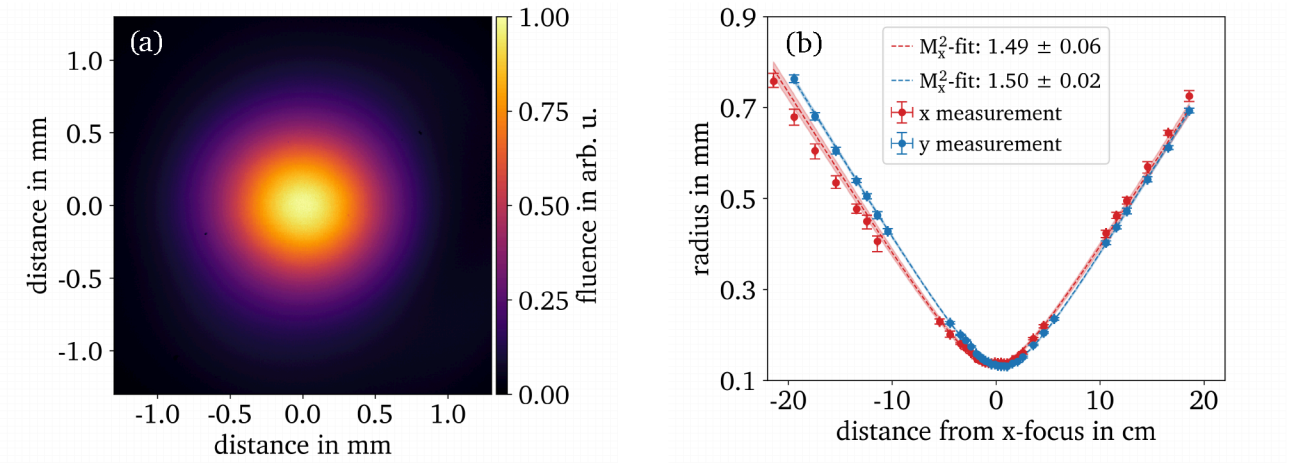


Figure 4.29.: Beam profile after the second uOPA stage (a) and $M^2$-measurement according to ISO Standard 11146 (b). Both measurements were conducted at an output energy of 1 mJ and pump energy of 24 mJ.

For the $M^2$ measurement, the output beam (see Fig. 4.29(a)) is magnified prior to the focusing lens to reduce the Rayleigh-range of the focal spot while still providing a sufficient number of illuminated pixels on the camera. Although this has a small impact on the measured $M^2$ value, it is expected to increase the value, due to the potential aberrations introduced by the telescope and therefore the measurement gives an upper bound for the actual $M^2$ of the output.

Although the beam profile in Fig. 4.29(a) seems Gaussian-like, the resulting $M_x^2$ of 1.49±0.06 and $M_y^2$ of 1.50±0.02 shows a beam-quality degradation compared to the oscillator with $M_{x,y}^2$ = 1.02±0.02 and even to the first stage with $M_x^2$ = 1.09±0.08 and $M_y^2$ = 1.09±0.09. With an $M^2$ of about 1.5, its $M^2$ is equally high to that of a fourth-order super-Gaussian distribution with perfect wavefront and its beam quality at 13.5 mJ pump energy is comparable to that of a super-Gaussian distribution of order 2.4-2.8 with an $M^2$-value of 1.20±0.02 in x and 1.28±0.03 in y.

Therefore, this degradation in the second uOPA stage can be interpreted as spatial deformation due to the onset of saturation and parasitic SHG, as well as a possible signature of spatio-temporal coupling, which cannot be completely ruled out in the presence of an even slightly saturated gain and the presence of parasitic SHG. However, even with increased $M^2$, its usability as a seed module for high-intensity lasers is still given if common beam shaping elements in the subsequent laser chain.

For example, regenerative amplifiers would reshape the beam to a near-perfect Gaussian or the use of serrated apertures cuts off the edge of the beam. In the latter case, a symmetric beam with a speckle-free distribution is of higher importance to avoid localized high intensity, which can clearly be delivered as seen in Fig. 4.29(a). Furthermore, a fit to the distribution in Fig. 4.28(b,c) (gray data) implies that the beam can still be reasonably well approximated by a Gaussian distribution up to a distance of 1 mm from its center (fit-**R**oot **M**ean **S**quare (rms)-error of 2.8 %). However, if a serrated aperture would cut off the beam at this position 23 % of the beam energy would be lost. If the fit perfectly matches the mode of a regenerative amplifier, the coupling losses are about 16 %. Another possibility to handle this is the use of diffractive beam shapers to redistribute the spatial intensity distribution. This requires custom optics but decreases the losses in the subsequent laser chain.

### 4.4.3. Energy stability and spectral output

As described in section 3.2.3, the stability of the uOPA is strongly correlated with the stability of the pump energy. However, it is not only dependent on the output energy, but on the local pump intensity with reference to the signal intensity. Accordingly, slow time drifts between pump and signal must be considered and mitigated. Since the pulses, which seed the pump- and signal chain, do not emerge from the exact same pulse, but from different pulses within the pulse train of the oscillator, their delay must be synchronized. This is done to the first order by repetition-rate locking of the oscillator to a reference clock. However, since the path lengths from the oscillator to the uOPA stages differ for pump and signal, thermal fluctuations and air circulations must be compensated for to ensure temporal synchronization. For this, a delay-control unit consisting of a motorized linear translational stage, shown in Fig. 4.25, is used that introduces small temporal shifts to the pump pulses.

To run this in a closed-loop mode, information is required from which the exact path-length difference between pump and signal can be determined. Since the signal pulses are chirped, the delay information can be obtained by measuring the signal spectrum after amplification in the second uOPA stage, which is shifted in dependency of the pump-to-signal delay. From a measurement of the spectrum and subsequent determination of the center of gravity, a delay is calculated, which is then sent to the control unit. Figure 4.30(a) shows the shift of the spectral centroid over a set of delays and Fig. 4.30(b) shows three spectra shifted by an arbitrary delay in comparison to the original oscillator spectrum.

Over a delay range of about one picosecond, the centroid shift scales approximately linear. For smaller delay shifts this approximation holds even better, which allows using the spectral shift as a measure for an additional relative delay between pump and signal. With a minimum shift of below 1 µm per micro-step of the translational stage, sufficiently fine adjustments are possible, since the pulse durations are in the range of 1 ps, corresponding to a distance of about 300 µm in air.

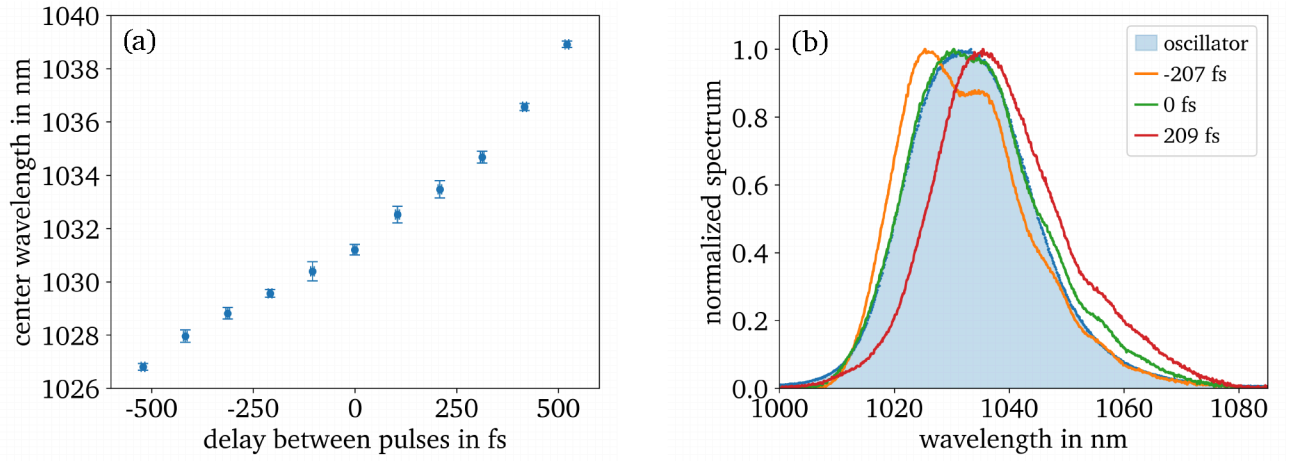


Figure 4.30.: Average shift of the spectral center of gravity as a function of the delay (a) and spectra of the uOPA output as a function of the delay between pump and seed (b). The blue-shaded region marks the original seed spectrum of the oscillator.

Figure 4.30(b), shows that, apart from the energy stability, the spectral bandwidth and spectral center is influenced by the delay, too. By freely choosing the desired spectral center of gravity, the system can be adjusted not only in terms of energy but also in terms of spectral center and bandwidth. By this, it is possible to either conserve the bandwidth of the pulse or shift it to a more desirable center for subsequent amplifiers as shown in the figure.

Noticeable when comparing the spectra are modulations, predominantly on the longer wavelengths of the spectrum, which were not observed before amplification. These seemingly come from the use of the GTI mirrors, which is indicated by the following observations:

First, I could also observe oscillations in the temporal profile, measured by an SHG-FROG, before amplification. However, the oscillations vanished when I replaced the GTI mirrors with standard high-reflectivity mirrors. Second, these types of modulations could also not be observed on the spectrum after amplification without GTI mirrors. Only small deformations near the peak were visible, but they rather indicated slightly non-uniform amplification within the uOPA process due to different group velocities of the pump and the signal and the onset of reconversion.

This leads to the assumption that the spectral modulations result from the coupling of the time-dependent gain and the time distribution of the spectral components, which in turn results from the introduced phase of the GTI mirrors, including their phase errors. While the GTI mirrors serve their purpose to reach the necessary energy and to enable temporal stabilization, overall it is reasonable to exchange them with a stretcher adapted to the rest of the laser system or to manipulate the spectral phase with a Dazzler, which both provides a smoother and more flexible tuning of the spectral phase. Another possibility for broadband pulses is the use of a glass block with high group-velocity dispersion, such as SF57. Although this method offers less flexibility, it stands out due to its simplicity.

Nevertheless, the GTI-mirror-induced phase errors do not affect the stabilization-method, since the spectral center of gravity can still be determined. Therefore, a measurement over a time span of close to three hours has been conducted, in which the energy was stabilized in a closed-loop mode. Figure 4.31 shows the results of this measurement.

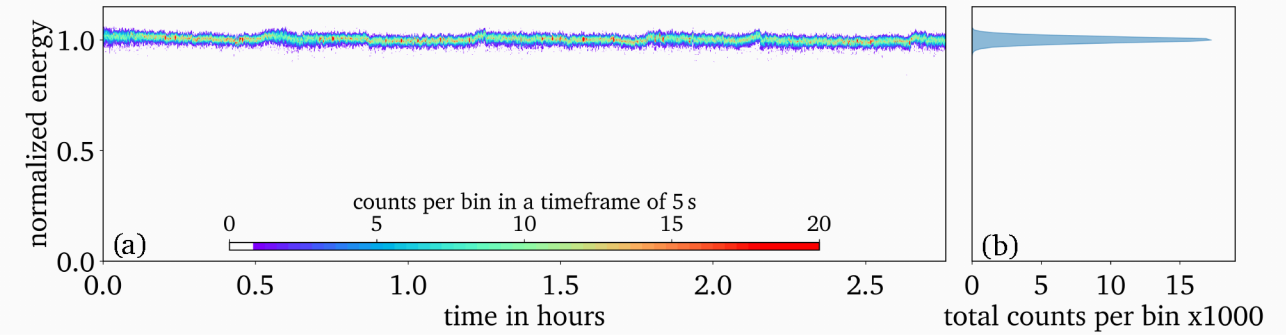


Figure 4.31.: Stability measurement of the uOPA system over approximately three hours in a test laboratory. (a) normalized energy over time. The colorbar represents the distribution of the energy over a 5 s time span to visualize the short-term stability. (b) Accumulated distribution. The mean energy of this measurement was 1.3 mJ.

Although the measurement data were taken in the same test laboratory in which the pump energy slowly fluctuated, the energy stability was found to be 1.5 % (standard deviation) including a slope of -7 µJ per hour over the full measurement window. Although, there are short-time modulations visible, even the long-term stability fulfills the set criterion. In a more temperature-stabilized environment, the stability of the uOPA energy is expected to increase.

### 4.4.4. Measurement of the stand-alone uOPA contrast

The last thing to check is the stand-alone temporal contrast of the pulses. This measurement is shown in Fig. 4.32.

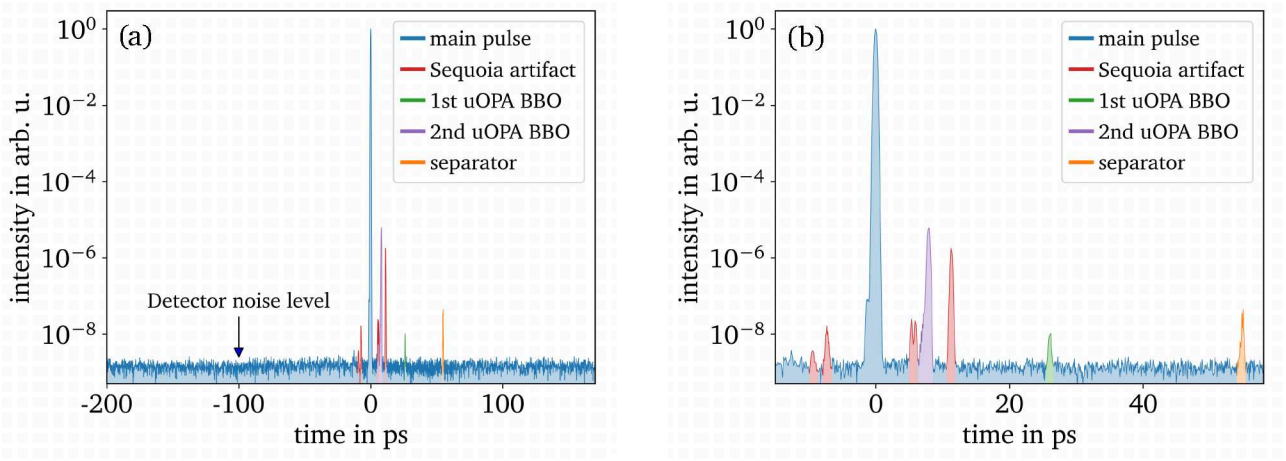


Figure 4.32.: Contrast measurement of the uOPA output at 1 mJ, measured with a commercial third-order cross-correlator (Sequoia, Amplitude). (a) Full time window from -200 ps to 170 ps. (b) zoom from -20 ps to 60 ps.

Figure 4.32(a) shows the contrast measurement on a timescale from -200 ps to 170 ps, measured with a commercial third-order cross-correlator (Sequoia, Amplitude), which is limited to a dynamic range of about nine orders of magnitude. While there are measurable pre- and post-pulses on a shorter timescale, shown with zoom in Fig. 4.32(b), the long time window is free from pre- and post-pulses above the detector noise level.

Zooming in on the measurement in Fig. 4.32(b), four origins for the pre- and post-pulses can be identified. These are the measurement device itself, the two uOPA crystals and a separator in the measurement setup. Of these four, the first and the last can be neglected, as they are existent only because of the measurement itself. The post-pulses of the BBO crystals, however, are real and will therefore also appear in the high-intensity laser system. Despite their appearance as post-pulses, it is mandatory to remove them in the long term, since the nonlinear coupling between main- and post-pulse within the stretched amplification in CPA lasers can generate pre-pulses from post-pulses as described in section 2.1.4. As the origin of these post-pulses lies in the parallelism of the crystal faces, the removal would only require the use of slightly wedged crystals and subsequent spatial filters. For example, a 1 arcmin angle will separate the beams by an angle of 1 mrad, corresponding to a 1 mm shift after 1 m of propagation.

### 4.4.5. Improvement-worthy aspects of the uOPA system

The setup and performance of the uOPA system presented in this chapter can be evaluated as successful and adequate to consider implementing the system in a high-intensity laser. However, a few improvement-worthy aspects of the system were pointed out. In this section, I will deal with components and setups within the uOPA that can be improved to further enhance the performance. Starting at the uOPA as presented in section 4.1 we can find a few things to improve, be it on the optical or more on the technical side of the implementation.

#### 4.4.5.1. Further enhancement of the spectral acceptance of the pump amplifier

The presented version of the pump amplifier employs an SPM stage to broaden the spectra of the oscillator pulses and create the needed spectral bandwidth to seed a Yb:YAG. This stage works for lasers with a center wavelength around 1 µm, but to seed the pump amplifier using Ti:Sa oscillators with pulses centered at 800 nm, further modifications are necessary.
First, the broadening fiber should be exchanged by a fiber that supports single-mode operation at this wavelength. For example, the fiber could be switched from PANDA PM980 to PANDA PM630. However, even with a reduced mode-field diameter that benefits the SPM, the energy demand to create bandwidth around 1030 nm increases to 13 nJ-15 nJ for a 100 fs long pulse centered at 800 nm according to simulations with fiberdesk [208]. Further improvements could be applied by using highly nonlinear, photonic-crystal fibers with a designable zero-dispersion wavelength [222], which benefit the SPM substantially. This will broaden the spectrum immensely, but in this case, special fiber splices will be needed, which will increase the price and reduce the maintainability of the system. Also, investigations must be conducted to estimate the actual usable energy or power within the bandwidth of Yb:YAG.

#### 4.4.5.2. Stability of the pump laser

The stability of the pump in terms of energy output and pointing was proven to be sufficient for the prototype development in the test laboratory and to be considered for the implementation at PHELIX and PENELOPE. However, as shown in Fig. 4.21 there is still room for improvement in the long-term energy stability. Targeting pulse-energy stability, an implementation of automated current adjustment for the pump laser diode could help to stabilize the output. This, however, requires a diode driver that allows fine adjustment of the current and remote control. Furthermore, a second piezo-motorized mirror mount could be implemented at the second end mirror of the cavity and again an automated correction loop has to be set up. Ideally, this would include a large- and a small-displacement piezo-actuator per mirror.

A passive and more sophisticated solution is the footprint reduction of the cavity. With a reduced footprint, a more temperature-insensitive housing with higher stiffness could be realized, which in turn calls for a redesign of the cavity with extensive folding of the beam path and size reduction of the pump module. Simultaneously, the optical pathway per pass could be reduced, which, however, would require faster PCs.

#### 4.4.5.3. Energy extraction of the pump regenerative amplifier

In Fig. 4.18 it was clear to see, that the optical-to-optical efficiency neither rises constantly, nor reaches a plateau, but peaks and drops at a specific pump energy. This implied restrictions due to beam-shrinking as a result of thermal lensing but also of the impact of the Kerr-nonlinearities in the PC.

Concerning the Kerr effect, the most straightforward solution is increasing the stretching factor of the CFBG. For this, either multiple, subsequent CFBGs are necessary or the design of the CFBG must be changed to create larger GDD. Both solutions reduce the input seed power for the fiber pre-amplifier, which requires evaluating if the seed power is still sufficient. The former solution calls for more passes through a circulator and multiple stretcher passes, which exhibit a transmission of 70 %- 85 % each. The latter is restricted due to limitations in the manufacturing process of the CFBG, which features a maximum product of bandwidth and GDD of 1.2 ns. Hence, increasing the stretching factor reduces the transportable bandwidth and therefore the seed energy for the pre-amplifier. Apart from the stretcher and pre-amplifier, one must note that this change requires a redesign of the compressor which will

either call for the use of significantly larger gratings and thus increase the total cost of the setup, or a multi-pass compressor, which reduces the transmission and increases the alignment complexity.

To mitigate the influence of the thermal lens one could increase the size of the pump spot or change the general design of the cooling housing. The first one is easy to apply but is bound to an increase in pump power to keep the pump intensity at an optimum range. The second would call for a thin-disk-like cooling, which would require a complete redesign of the pump module or the use of expensive commercial solutions.

Further enhancement of the energy extraction can be achieved with a dry-nitrogen-flooded cavity, as this would allow stronger cooling without the risk of condensing fluids on the surface of the crystal. This would increase the pump absorption- as well as the signal emission cross-section of Yb:YAG. Again, this would require air-tight housing, to avoid air turbulences that decrease the stability of the system. Last, the cavity losses could be further minimized. For this, one must use lower-loss components, mainly PCs, as these tend to be responsible for the major part of the losses. To reduce these losses artificially, a multi-pass setup for the signal per roundtrip could be set up. Yet, this increases the alignment complexity of the cavity.

#### 4.4.5.4. Enabling relay imaging of the pump

Due to the high output energy of the pump laser, all telescopes to magnify the beam after amplification are bound to be afocal, as the intensity is high enough to ignite an air plasma in the focal plane. This prevents the use of relay imaging, which would further enhance the stability of the whole system. To enable this, vacuum components are indispensable and come with a good amount of overhead to implement. Also, these can only be implemented before compression if lenses are used since Kerr-lens focusing would be dominant inside the lenses. Otherwise, reflective optics should be used. Ideally, off-axis parabolic mirrors are employed, since spherical mirrors induce aberrations if the off-axis angle is too large.

Although the integration of vacuum telescopes involves considerable effort, they have the potential to enable the implementation of a beam shaper. This would allow shaping the pump beam into a super-Gaussian prior to compression and then imaging it onto the amplifier stages through the compressor, which would increase the uOPA efficiency. Obviously, precise positioning of the telescopes to the amplification stages is needed, which may again require a redesign of the layout of the compressor and the uOPA stages. Also, the intermediary field distribution of the pump should be precisely calculated, as diffraction-induced peak fluences could increase and potentially damage the gratings.

#### 4.4.5.5. Suppression of parasitic effects

The general strategy to suppress the parasitic generation of higher harmonics in OPA is to increase the phase mismatch for these processes. This was already applied in the setup, by increasing the pump-to-signal angle. However, the measured results did not match the expectations and a significant fraction of the pulse energy was converted to its second harmonic. Further suppression could be done by increasing the already applied mitigation strategies. For example, the pump-to-signal could be increased from about 2.4° to more than 12°. However, if the angle is further increased, it is expected to impact the spatial and temporal profile and induce a spatial chirp [142], even in shorter crystals. A mitigation strategy for this could be to create a pulse-front tilt for the pump, such that the orientation of the seed and pump beam profile matches over the total propagation distance through the crystal. However, this requires a grating setup which gets bulkier for greater tilts.

Another possibility to further suppress the parasitic process is reducing the intensity of the signal, which means further stretching or using larger beams. Stretching is limited to the pump pulse duration

and the use of large beam sizes to the crystal size. Also, this would require either longer crystals or a higher pump energy to keep the gain at similar levels. In general, further investigations are needed to clarify why the parasitic processes were not suppressed sufficiently.

### Conclusion

In this chapter, I presented the experimental setup and the characterization of the uOPA system that was developed in the scope of this thesis. I detailed the design of the pump laser with regard to the requirements that were set up. Within the performance characterization, I showed that the developed pump module fulfills nearly all set requirements, except for a slight discrepancy within its long-term stability. Moreover, I described the setup of the uOPA and detailed how the findings of the previous chapter could be implemented to achieve the best possible outcome. After that, I characterized the output of the uOPA in terms of energy, energy stability, spectrum, beam distribution and contrast. Based on the results, the uOPA is well-suited to be used as a high-contrast system in a high-intensity laser. In the next section, I will describe the implementation of a prototype of the presented module at PHELIX and its impact on the temporal contrast.

## 4.5. Upgrade of the uOPA at PHELIX

Since 2012, the PHELIX facility has been using uOPA to improve the temporal contrast and has thus been able to significantly mitigate and control the problematic nature of ASE [36]. The developed high-contrast front-end was able to generate clean pulses in the range of several tens of microjoules and thus seed the PHELIX laser effectively.

A schematic of the PHELIX front-end is shown in Fig. 4.33. The starting point of the PHELIX fs-front-end is a commercial Ti:Sa oscillator (Mira Optima 900-F, Coherent), set to generate pulses centered around 1053 nm with a pulse duration of about 130 fs and a pulse energy of about 2.8 nJ.

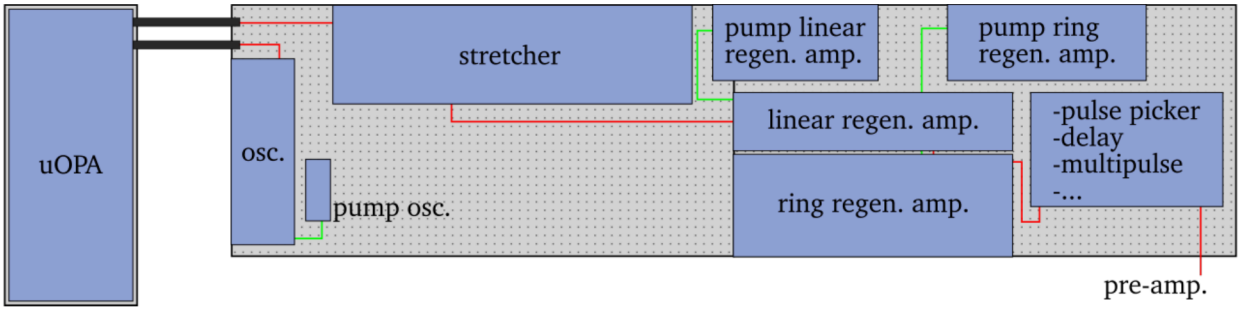


Figure 4.33.: Layout of the PHELIX fs-front-end before the implementation of the newly developed module. osc.: oscillator, regen. amp.: regenerative amplifier.

These pulses are fed into the uOPA system, where every 72000th pulse, corresponding to a repetition rate of 10 Hz, is amplified. The high-contrast pulses are then stretched to about 2 ns in the PHELIX stretcher and further amplified to the millijoule level in a linear regenerative amplifier and finally fed into a ring regenerative amplifier in which the pulses are amplified to about 20 mJ. The regenerative amplifiers are pumped by two frequency-doubled Nd:YAG lasers (Continuum, Powerlite 8000 & 9000)

Pre-amplification via uOPA reduced the amplification factor of subsequent regenerative amplifiers, and thus the ASE, by the same factor. Figure 4.34 shows a measured contrast-trace, with the old system in operation.

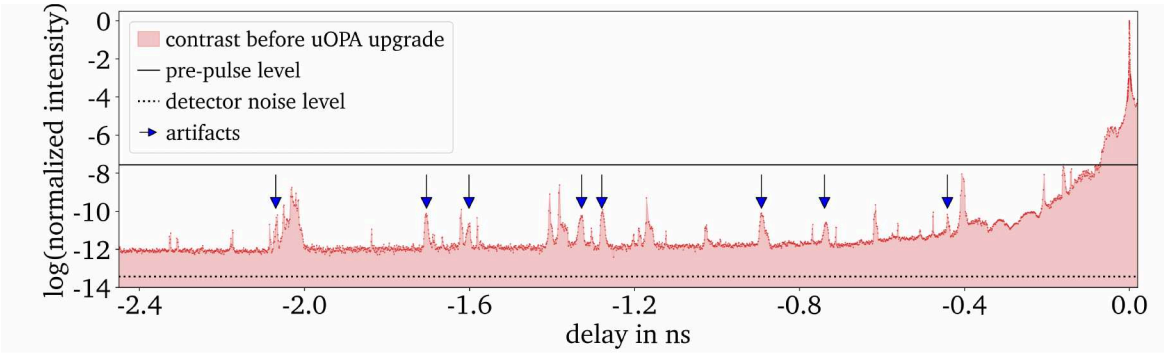


Figure 4.34.: Contrast measurement of the PHELIX laser system with the uOPA system in the old configuration.

In Fig. 4.34, the three main contrast features of PHELIX are clear to observe: the ASE-level, pre-pulses and the ps-pedestal before to the main pulse. While the ASE exhibits an intensity level that is twelve orders of magnitude below the peak intensity of the main pulse, there are several pre-pulses above this level. At least eight of them could be identified as artifacts of the measurement device itself [140] and are therefore negligible. These artifacts are marked with a blue arrow in Fig. 4.34. However, this leaves quite a number of potentially non-artificial pre-pulses and four of them are less than eight orders of magnitude below the peak intensity. At an intensity of $10^{21}\,\mathrm{W/cm^2}$, these pulses surpass $10^{13}\,\mathrm{W/cm^2}$ and are certainly above the ionization-threshold intensity as defined in section 2.2.1.

As most of these pre-pulses emerge from the linear regenerative amplifier [140], either a detailed investigation followed by an eradication of every single pre-pulse must be conducted or a bypass of the system without too much loss of seed energy for the second regenerative amplifier. Generally, identification of the exact pre-pulse origin is reasonable and may help to prevent the generation of further pre-pulses, if these are coupled to specific optical components. However, aside from the necessary tedious investigation of every optical component, it was shown, that the creation of pre-pulses is not always bound to single components, but may result from sub-cavity-like effects of multiple components and are highly sensitive to the alignment of the components themselves [140]. Hence, if possible, a complete bypass of pre-pulse-sensitive optical arrangements is a better solution.

### 4.5.1. Implementation of the developed uOPA at PHELIX

With the development presented in the previous chapters, this exact bypass of the amplifier is now possible. Therefore, the upgraded version of the uOPA was implemented at PHELIX. However, it must be noted that, due to PHELIX being a user facility, time slots for the implementation of the system into the front-end were limited.

Hence, the implementation took place before the full potential of the development, presented in the previous sections, could be realized. This is mainly due to the non-short-term availability of optical components such as dielectric gratings and low-loss PCs at the time of implementation, which limited the pump energy to a maximum of about 13 mJ after compression and SHG. In turn, this limited the uOPA output energy to only 270 µJ. Nevertheless, this was enough energy to set up a bypass of the linear regenerative amplifier and feed the uOPA output directly into the ring regenerative amplifier. Also, to make better use of the available space at the PHELIX front-end, the system was not built on an external table as before, but on the same optical table as the oscillator and the stretcher. This is shown in Fig. 4.35. With the implementation of the system onto the same optical table as the oscillator, cross-coupling of vibrations from different tables can be ruled out.

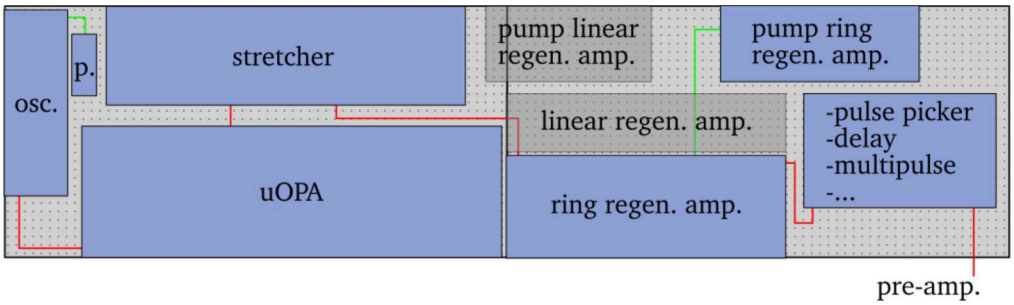


Figure 4.35.: Layout of the PHELIX fs-front-end after the implementation of the newly developed module. osc.: oscillator, regen. amp.: regenerative amplifier, p.: pump.

The bypass of the linear regenerative amplifier eliminated all of the previously mentioned particularly intense pre-pulses with a contrast level above $10^{-8}$, but the first measurement of contrast also revealed the enhancement of a previously inapparent pre-pulse. Figure 4.36 shows a close-up of this pre-pulse for the new and old configurations.

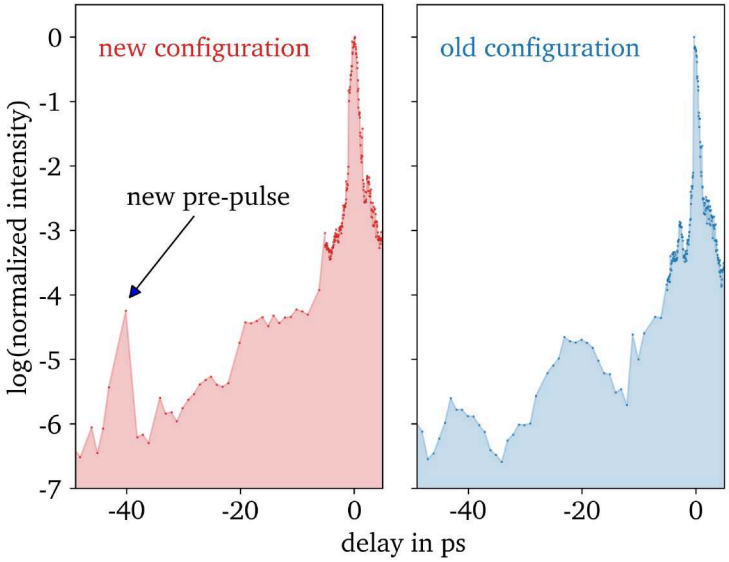


Figure 4.36.: Comparison of the new and old uOPA configurations. The bypass of the linear-regenerative amplifier in the new configuration showed an enhancement of a pre-pulse at 40 ps before the main pulse.

The pre-pulse appears approximately 40 ps prior to the main pulse with at an intensity level of only four orders of magnitude below the peak. Accordingly, the origin of this pre-pulse should be identified and removed. This delay corresponds to an optical path difference of about 12 mm, which is in the range of the thickness of optical components, suggesting a generation by a double reflection. For a material like fused silica, the thickness of the component must be approximately 4.1 mm.

Because of the bypass, there are mainly two highly probable origins, which are either the new uOPA or the ring-regenerative amplifier. However, a measurement of the uOPA contrast before the stretcher did neither show any pre-pulse nor a post-pulse with matching delay. On the contrary, we could find a post-pulse with matching delay in contrast measurements of the old configuration, which may indicate

that the pre-pulse is generated via nonlinear coupling [63] in the ring-regenerative amplifier. Since this coupling results in a pre-pulse intensity that is proportional to the post-pulse intensity and the square of the B-Integral, different gain factors inside the ring-regenerative amplifier will influence the pre-pulse intensity. This idea solidifies further by comparing older contrast measurements in which the linear regenerative amplifier was also bypassed for a test measurement. The same pre-pulse could be detected in these measurements both with and without bypass, but showing a higher intensity in the first case.

Therefore, a detailed investigation of the ring regenerative amplifier was conducted. Its schematic setup is shown in Fig. 4.37.

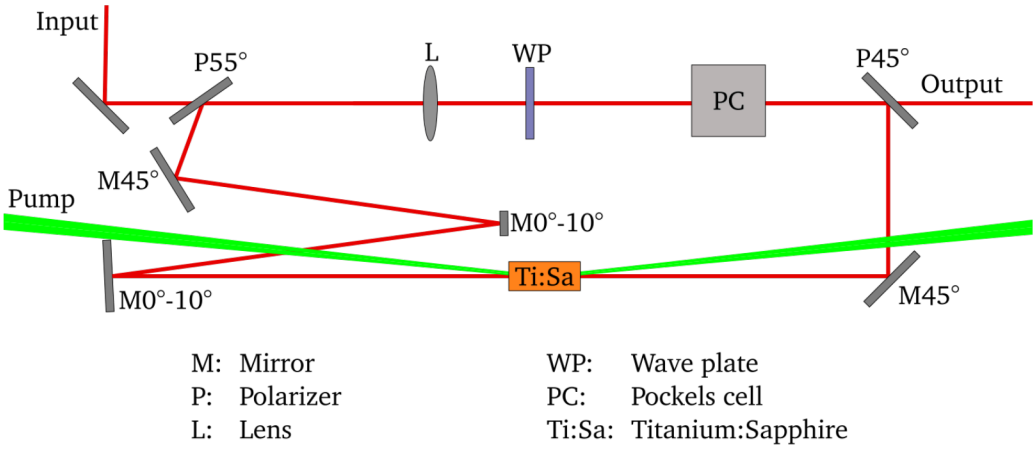


Figure 4.37.: Schematic setup of the ring regenerative amplifier of the PHELIX front-end.

The regenerative amplifier consists of a Ti:Sa crystal, which is pumped by a pulsed, frequency-doubled Nd:YAG laser, a set of HR mirrors, two polarizers, a mode-forming lens, a WP and a PC. Hence, it contains four transmissive optical components, but only the lens features an optical path length that matches the measured pre-pulse delay. Normally, a double-reflection in a lens will quickly diverge and therefore impose less of a problem in the context of post-pulses. However, the ghost focus of the lens of the regenerative amplifier exhibits a focal length that is large enough to still build a stable mode, which featured the same waist position as the original mode, for reasons of symmetry. This facilitates the optical transport of the post-pulse to the measurement device.

To test this hypothesis, we removed the lens and exchanged the first mirror after the Ti:Sa crystal (M0°-10° on the left side of Ti:Sa in Fig. 4.37) with a large-radius concave mirror. With this, we could still set up a stable resonator. A measurement revealed, that in fact, the lens caused the post-pulse, which in turn created the pre-pulse at -40 ps. The resulting contrast measurement after removal of the pre-pulse is shown in Fig. 4.38 together with the full contrast measurement of the old system as a comparison.

As shown in Fig. 4.38, the implementation of the new uOPA (blue curve) eliminated eleven pre-pulses, which were above the new pre-pulse contrast level (dashed line). With this, the pre-pulse contrast level on the nanosecond scale was reduced down to $6.2 \cdot 10^{-11} \pm 1.8 \cdot 10^{-11}$, implying an improvement of nearly three orders of magnitude. Since the implemented uOPAmodule featured a reduced energy performance, only a slight reduction of the ASE is visible. A fit to the ASE-level before and after implementation shows only a marginal enhancement from $8.6 \cdot 10^{-13} \pm 3.3 \cdot 10^{-13}$ to a new ASE level of $4.9 \cdot 10^{-13} \pm 2.1 \cdot 10^{-13}$. Compared to the energy increase of about one order of magnitude, this is less than expected. An explanation for this might be, that the coupling losses into the regenerative amplifier increased, compared to the old system. Accordingly, the total gain of the regenerative amplifier could not be reduced as much as the energy gain between the old and new uOPA.

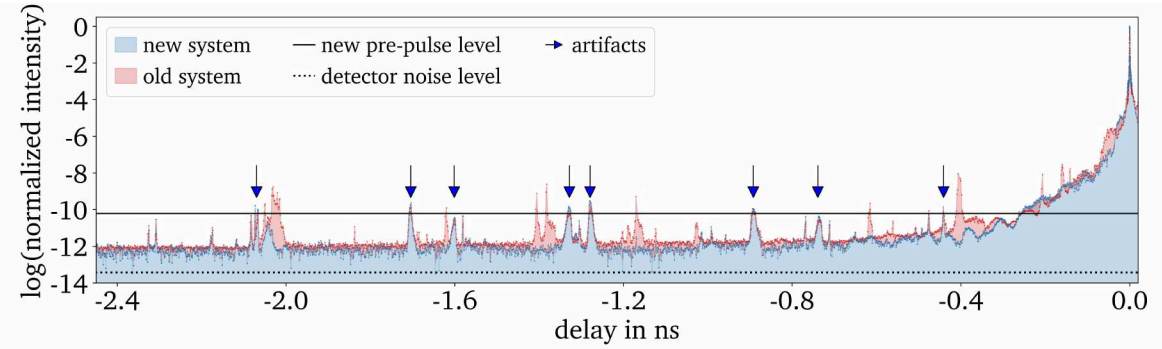


Figure 4.38.: Contrast measurement of the PHELIX laser before (red area) and after (blue area) implementation of the new uOPA. Several measurements before and after the implementation have been averaged for a clearer picture of the low-intensity levels.

The appearance of the slowly rising pedestal, however, remains almost unchanged. Starting at around -400 ps, the measurement after the implementation of the new systems reveals a similar shape, but also local improvement as well as degradation of the temporal contrast. This is not attributed to the implemented uOPA system as this is an effect that emerges from the stretcher and compressor of the system and the uOPA does not change any dynamics in this process. However, the implementation of the new uOPA required a re-alignment of the beam path into the PHELIX stretcher. As some of the optics, on which the beam is spectrally dispersed, are slightly degraded and were contaminated over time, additional phase noise and spectral modulation is generated, which degrades the ps-pedestal contrast. Accordingly, the ps-pedestal at PHELIX is very sensitive to re-alignment into the stretcher.

With another complete re-alignment of the pulses into the stretcher, avoiding the degraded areas on the optics, the ps-pedestal at PHELIX was reduced significantly. Figure 4.39 shows a comparison of the temporal contrast in the timescale of the ps-pedestal before the re-alignment.

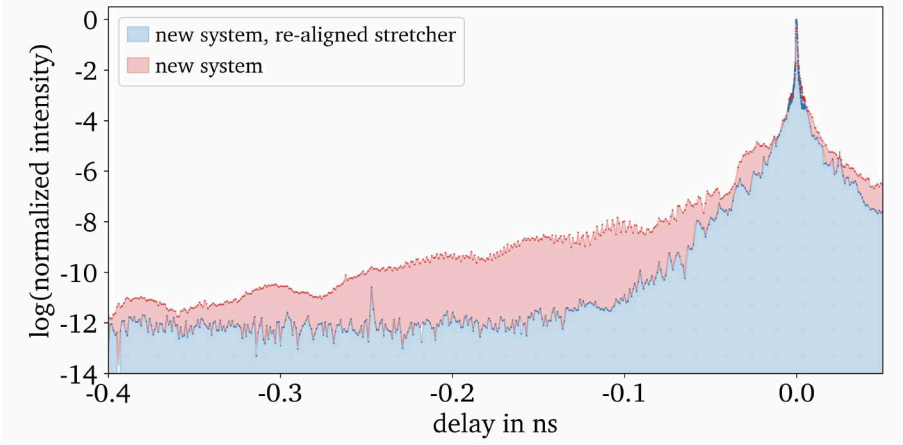


Figure 4.39.: Contrast measurement of the PHELIX laser in the range of the ps-pedestal before (red area) and after (blue area) complete re-aligning of the stretcher by Christian Brabetz.

The comparison shows, that there was indeed another pre-pulse below the pedestal at -247 ps with a contrast of $2.4 \cdot 10^{-11}$. On top of the pedestal (blue) from -100 ps to -20 ps, even more, pulse-like structures are visible. However, it is not clear if these modulations are pre-pulses, part of the pedestal or artifacts of the measurement. If we assume that all data points in this measurement represent real

intensity values and consider an ionization scaling as described in section 2.2.1 for a 100 ps timescale, we can estimate the ionization delay. For the maximum intensity of $1.4 \cdot 10^{21}$ at PHELIX [5], we find that the ionization delay is about -90 ps for a gold target. Without the stretcher re-alignment the ionization sets on at about -310 ps. In both cases, the ionization is determined by the ps-pedestal. With the old uOPA system, the pre-pulses had posed problems, which may have caused ionization at -2000 ps in a worst-case scenario but certainly at the intense pre-pulse at -400 ps.

### Conclusion

The implementation of the new developed uOPA system at the PHELIX front-end allowed to bypass the first high-gain regenerative amplifier, even with reduced energy output. The bypass of the amplifier resulted in the removal of eleven pre-pulses, increasing the pre-pulse contrast by almost three orders of magnitude to $6.2 \cdot 10^{-11} \pm 1.8 \cdot 10^{-11}$. Also, the ASE level was slightly reduced to a contrast of $4.9 \cdot 10^{-13} \pm 2.1 \cdot 10^{-13}$. Furthermore, the implementation revealed a pre-pulse that emerges from a double reflection in the mode-forming lens of the ring-regenerative amplifier. This pre-pulse was also successfully removed by exchanging the lens with a curved mirror. A re-alignment of the stretcher showed yet another pre-pulse with a contrast level of $2.4 \cdot 10^{-11}$, which was hidden below the ps-pedestal. In sum, there are 16 pre-pulses left in the measurement window, which should not be critical as they are all below the threshold, estimated in section 2.2.1. Nevertheless, determining the pre-pulse origins is useful in the long run and should be done to avoid the generation of additional pre-pulses.

# 5. Summary and Outlook

The key subject of the presented work was the development of a uOPA with output energies in the millijoule range for the improvement of the temporal contrast in high-intensity laser systems, and in particular, its implementation at the PHELIX, which was plagued by pre-pulses at contrast-levels above $10^{-8}$. The removal of these pre-pulses was achieved successfully with the implementation of the presented uOPA system

In the first chapters, I provided the theoretical background to develop a uOPA module that can deliver energy-stable pulses in the millijoule range while still providing a good beam quality and maintaining the spectral bandwidth of the seed pulses. Here, I defined the requirements for the pump laser of the uOPA.

One of the main tasks was the development of the pump laser for the uOPA, which should deliver pulses around 515 nm central wavelength with an energy of approximately 32.5 mJ and a pulse duration around 1.5 ps. For this, I developed a CPA pump system, consisting of an Yb:glass fiber pre-amplifier and Yb:YAG regenerative main amplifier. I embedded the fiber pre-amplifier in an "all-fiber" system, which combines spectral broadening, stretching and pre-amplification of the seed. The simple, yet effective spectral broadening of the seed pulses via SPM in a single-mode fiber enables broad applicability of the Yb-based pump laser at laser systems with oscillators that emit around 1 µm center wavelength. By this, seeding with the oscillator at PHELIX is possible. In the subsequent fiber amplifier, the pulses are amplified to the microjoule level and then sent into the regenerative main amplifier.

Resulting from the energy requirement of the frequency-doubled, compressed pulses of 32.5 mJ, the energy-output goal for this regenerative amplifier was set to 100 mJ. I reached this goal with a maximum measured output energy of (108±5.4) mJ. The measurements did show that the optical-to-optical efficiency peaked at lower output energies. By simulating the dynamics of the cavity, I could relate this to nonlinear and thermal effects. The generated output of the cavity features a long-term energy stability with a standard deviation of 0.35 % from its mean value (approx. three hours) and a short-term stability of 0.1 % (approx. one minute). Also, the pointing stability of the pump features a standard deviation of 44 µrad in x and 90 µrad in y in the long term and of 17 µrad in x and 12 µrad in y for a timescale of 1 min.

With the set-up MLD grating compressor, I achieved close-to bandwidth-limited compression, with $(1.27 \pm 0.03)$ ps at 80 mJ output (FTL of $(1.21 \pm 0.01)$ ps) and $(1.38 \pm 0.04)$ ps at 100 mJ output (FTL of $(1.27 \pm 0.02)$ ps). Due to the onset of nonlinear effects, a reduced compressibility at the higher energy was detected, which, however, still fulfilled the requirement of a pulse duration below 1.5 ps. The compressed pulses feature an excellent beam quality with $M_x^2 = 1.02 \pm 0.02$ and $M_y^2 = 1.16 \pm 0.04$ and were frequency doubled with an efficiency of up to 70 %.

The next task was to use the created pulses to pump the uOPA. Here, I set up a double-staged system, in which I used the first stage as a pre-amplifier to bring the pulse energy to the microjoule level. The signal of the uOPA was chirped to increase the temporal overlap with the pump. This chirp also allowed to set up a closed-loop for the delay stabilization between signal and pump, as a delay creates a shift of the signal's spectral center of gravity during amplification. With a total pump energy of approximately 27 mJ, which corresponds to less than half of the deliverable uncompressed pump energy, I realized

a uOPA output of (1.05 $\pm$ 0.03) mJ with a pump-to-signal efficiency of (4.38 $\pm$ 0.14) %. However, a strong build-up of parasitic SHG of idler and signal was observed, which limited the growth of the signal and was not expected by simulations and shall be further investigated.

The measured beam quality of the output pulses featured an $M_x^2$ of $1.49 \pm 0.06$ and $M_y^2$ of $1.50 \pm 0.02$, which showed a beam-quality degradation compared to the oscillator with $M_{x,y}^2 = 1.02 \pm 0.02$ and to the first stage with $M_x^2 = 1.09 \pm 0.08$ and $M_y^2 = 1.09 \pm 0.09$. Nevertheless, a highly symmetric and smooth beam was generated. Furthermore, the spectral bandwidth of the pulses was preserved during amplification and a long-term energy stability of the system with a standard deviation of 1.5 % was achieved. Lastly, I measured the contrast of the stand-alone uOPA output. This measurement showed, that two post-pulses from the uOPA crystals are created, which can however be easily removed by using slightly wedged crystals and a spatial filter.

In the last chapter, I presented the results from the implementation of the developed module at PHELIX. The compact setup of the uOPA allowed me to build it directly onto the optical tables of the front-end. As the implementation of the system was done before the development was complete, only 270 µJ were generated. This was nonetheless sufficient to bypass the first amplifier of the front-end. During the implementation, I identified and eliminated another pre-pulse that emerged from the subsequent front-end amplifier. As a result, with the implementation of the uOPA, I achieved an ASE contrast of $4.9 \cdot 10^{-13} \pm 2.1 \cdot 10^{-13}$ and improved the pre-pulse contrast by almost three orders of magnitude to $(6.2 \pm 1.8) \cdot 10^{-11}$, which sets the pre-pulse intensity below $10^{11}$ W/cm$^2$ even at the highest intensity that PHELIX can provide.

## Outlook

Aside from improvements of the uOPA system itself, which were already detailed in section 4.4.5, I would like to mention further projects around the uOPA system whose realization are currently ongoing or are planned/hypothesized for the near future.

### Implementation of the uOPA at PEnELOPE

The installation of the uOPA module in the front-end of the new PEnELOPE laser is not yet completed. So far, the system was built and characterized by me. Just before the completion of this thesis, the system was transported to its planned location and has to be set up again. Since the PEnELOPE laser will provide both the here developed uOPA system and a cross (**X**) **P**olarized **W**ave generation (XPW) front-end, there will be the possibility to compare the performance of both cleaning methods and to observe their influence in laser-plasma interaction experiments.

### Increasing the performance of the uOPA at the PHELIX front-end

As mentioned in section 4.5.1, the current configuration of the uOPA-upgrade still lacks in performance and a further upgrade is planned to achieve the same results as presented in section 4.4. Although this does not influence the existence of the remaining pre-pulses, their intensity might be reduced as a consequence of a decreasing B-integral in the ring-regenerative amplifier of the PHELIX front-end and a slight decrease in the ASE level can be expected.

Moreover, if a temporally clean and short 1 mJ pulse is available, the direct output of the uOPA can be measured using the full dynamic range of the **E**nhanced **I**ntensity **C**ross-correlator for **H**igh **E**nergy **L**asers (EICHEL) cross-correlator. Although a direct measurement requires moving the rather bulky cross-correlator from the laser laboratory to the front-end, this enables us to identify which pre-pulses

emerge from the front-end and which ones are artifacts of the measurement device itself. In turn, this may facilitate the identification and removal of the remaining non-artificial pre-pulses.

A more radical approach to get rid of the pre-pulses, which emerge from the last front-end amplifier, is the replacement of said amplifier by an OPCPA system. This replacement would minimize the number of transmissive optics, the B-integral and potentially reduce the incoherent noise level. However, for this to work, a powerful pump laser is mandatory.
A possible approach to the generation of such a pump pulse is an extension of the uOPA pump system by an additional amplifier stage. This would have the benefit of already being temporally synchronized to the signal pulse. Also, this amplifier can be seeded with several millijoules, as the uOPA pump provides (when upgraded) a sufficient energy budget. However, this implementation requires to increase the pump duration to at least 1 ns, which in turn requires to either use larger stretch factors in the uOPA pump or to counteract gain narrowing such that enough bandwidth is maintained and the stretch factor suffices. Obviously, this implementation is not a small task and needs thorough planning and simulation, yet it offers an elegant solution to the front-end pre-pulse problematics and replaces bulky, non-diode-pumped lasers.

### Off-Harmonic probe laser at PHELIX

The setup of the uOPA at PHELIX inspired the recent construction of an off-harmonic probe laser, SEPPL (**S**eeded **E**xperimental **P**ulsed **P**robe **L**aser (SEPPL)), which is being used in laser-plasma interaction experiments at PHELIX. The seed of this probe laser stems from leakage light of the uOPA pump laser. With the center wavelength at 1030 nm, off-harmonic probing can be realized, which allows a higher signal-to-noise ratio with respect to the scattered light from the PHELIX main pulse. A further increase of the signal-to-noise ratio can be applied by frequency-doubling the pulse, which, however, reduces the available pulse energy from 10 mJ at 1030 nm to 2 mJ at 515 nm.

Currently, the spectrum of the pump leakage is narrowed down in a Fabry-Perot setup, which generates pulses in the nanosecond range, usable for streaked shadowgraphy of the laser-plasma interaction. More variability is planned by seeding the full spectrum of the uOPA pump and setting up a compressor at the PHELIX target area to create ps pulses, which can then be used for interferometric probe setups. To make potential users aware of the availability of this kind of measurement at PHELIX, a publication is in preparation [9].

### Investigation of laser-accelerated protons with multi-ps long pulses

During this work, we conducted an experimental campaign with focus on proton acceleration via **T**arget **N**ormal **S**heath **A**cceleration (TNSA) and multi-ps long laser pulses. As the full evaluation of this experiment is still pending and would exceed the scope of this thesis, I will only give a brief outline of the concepts and the reasoning behind this study.

TNSA is one of the most robust and most investigated laser-ion acceleration mechanisms, yet, theoretical research mostly covers the pulse-duration regime of short ($<1$ ps) and ultra-short pulses ($<100$ fs) [224–226] and empirical scaling laws, which rely on experimental data, show that the available data is clustered below 1 ps and is sparse above 1 ps [227, 228]. However, in the context of inertial-confinement fusion [229], multi-ps pulses gained attention within the concept of proton-beam driven fast ignition [230]. As the laser-pulse energy needs to be in the 100 kJ-range [231], longer pulses mitigate the risk of damage on delicate optics, such as compressor gratings [232].

Therefore, to investigate laser-ion acceleration with the use of pulses with durations of 0.5 ps up to 13 ps, we conducted an experimental campaign during this work, which I planned and led. In order to

maximally isolate the influence of the varied pulse durations, we used two recent implementations at PHELIX. First, a post-compression adaptive-optics system [5] was used to keep the spatial fluctuations at a minimum. Second, the upgraded uOPA was used to enable the highest possible contrast at PHELIX and thus minimized the risk of pre-ionization. Furthermore, an **A**cousto-**O**ptic **P**rogrammable **D**ispersive **F**ilter (AOPDF) was installed and used to gain maximum control over the spectral phase. To manipulate the pulse duration on a larger scale, the length of the PHELIX stretcher was varied.

During the experiment, we varied the pulse energy and pulse duration to move along different regimes of constant laser power with 5 TW, 9 TW, 18 TW, 60 TW, 100 TW and 200 TW. At these power levels, the laser was focused onto 4 µm thick gold targets to accelerate protons via TNSA. To characterize the generated proton beams, we used two types of diagnostics: radiochromic films and a Thomson parabola. The evaluation of the data is still pending since a recalibration of the radiochromic films is necessary in order to fully characterize the generated proton beams. We believe that this dataset complements the existing ones very well and will be valuable to the plasma-physics research community as it will help to improve the accuracy of the empirical models, allowing for a better estimation of the performance of future laser systems.

# Danksagung

Zum Schluss möchte ich mich noch bei einer Menge Leute bedanken. Natürlich gibt es davon viel zu viele und um diese Arbeit nicht noch um weitere 200 Seiten zu verlängern, muss ich mich wohl oder übel auf die wichtigsten begrenzen. Ganz kurz fassen werde ich mich trotzdem nicht. Jetzt kommt es auch nicht mehr darauf an. Manche Namen werden für einige eventuell nicht direkt zuordenbar sein, aber die Angesprochenen werden wissen wen ich meine. Vielleicht.

Zuerst möchte ich mich bei **Vincent** bedanken. Wir kennen uns jetzt schon einige Jahre und ich bin froh, dich meinen Doktorvater nennen zu dürfen (oder wie die Franzosen sagen: Pápâ de doctoirée. Oder so.). Bei Fragen hattest du immer ein offenes Ohr und dir stets Zeit genommen mir zu erklären warum der Laser verdammt noch mal nicht das tut was er soll. Du konntest mir immer sagen, in welche Richtung ich gehen muss, auch wenn es manchmal ein 5 km Lauf durch den GSI-Wald war, auf den mein Herz-Kreislaufsystem definitiv nicht vorbereitet war. Ich bin wirklich froh, dass wir uns nicht nur auf einer wissenschaftlichen sondern auch auf einer freundschaftlichen Ebene verstehen und freue mich auf die kommende Zeit, die gerne mit weiteren Weinproben gespickt sein kann. Vielen Dank!

Die nächste Person in der Reihe kann keine andere als **Christian** sein. Ich habe definitiv nicht genug Finger an meinen Händen um abzuzählen, wie viele

- Überstunden du mit mir im Labor aufgebaut hast.
- Optiken wir zusammen gegrillt haben.
- Kaffees wir bei Diskussionen getrunken, gekocht oder verschüttet haben.
- OPAs wir aufgebaut haben. Halt stopp, dafür reichen die Finger zum Glück doch noch. Wenn wir die aufgebauten Regens mit dazu nehmen wird es allerdings langsam eng mit den Fingern.

Vielen Dank dass du dieses Projekt mit mir gestemmt hast. Jetzt kann ich nur noch sagen: *Muh! Der OPA läuft!*

**Dirk**, du kommst selbstverständlich nicht drum herum hier gelistet zu werden. Ich hab dich schon während meiner Bachelorarbeit an der GSI kennengelernt. Damals warst du für mich der große Kerl, der grimmig guckend ins Labor kommt, ein bisschen pöbelt und wieder geht. Was soll ich sagen, das grimmige Gesicht hast du heute noch drauf und wer dich nicht kennt, der kauft dir den grimmigen Modus vermutlich sogar ab. Ich tue es jedenfalls nicht und kann nur Danke sagen, für alles was du für mich getan hast. Ich wurde zwar manchmal von dir versklavt, aber ohne deine dubiosen Bierfass-Deals hätte mein Aufbau im Blitzlampenlabor wohl niemals eine halbwegs stabile Temperatur annehmen können und auch die Entwicklung des uOPAs im LEL (lel) hätte ohne dich wohl nie stattgefunden.

Wie sagte schon das fünfte der 10 einzig wahren Gebote: Ehre deinen Dörk und deine **Diana**. Ich weiß nicht wie, aber du bringst immer Ordnung in hereinbrechende Wellen aus Chaos und selbst Studenten wie ich, die manchmal wegen den vermutlich banalsten Dingen nerven, bringen dich nicht aus der

Fassung. Diana, ich weiß wirklich nicht was wir ohne dich machen würden, außer im kompletten Chaos der GSI-Bürokratie zu versinken. Vielen Dank, dafür!

Dann gibts da noch **Onas J. Bohland**, aber nennen wir ihn Joners. Als Bürokollegen haben wir es uns zur Aufgabe gemacht aus der heißesten, nichtklimatisierten, Eckbürosauna in der Containerübergangslösung C12 ein kleines Zuhause zu machen, in dem man entspannt Musik oder entspannt unentspannte "Musik" hören kann und dazu beim Zug am richtigen Ordner mit köklichen feierabendtauglichen Getränken versorgt wird (Sri für den langen Satz). Ich denke ich spreche die Wahrheit, wenn ich sage, dass unsere Unterhaltungen in der Regel einer äußerst gesunden Mischung aus Fachgesprächen und maximaler Gehirnfurzkernschmelze gleichen. Das tut nicht nur gut, sondern manchmal auch weh. Im Kopf. Smergol was die anderen sagen, snicer Boi dieser Joners!

Am Besten bleibe ich im gleichen Büro und bedanke mich bei **Maddin**, auch bekannt als der Mann der stets versucht mit dem Wippen seiner Beine eine Resonanzkatastrophe bei allen nicht befestigten Objekten im Büro zu provozieren. Auch wenn du zu Corona-Zeiten gerne nach Z6 geflüchtet bist möchte ich die gemeinsame Zeit nicht missen und freue mich auf die nächsten Jahre, wenn der Chaostrupp des Büros 2.008 wieder vereint ist.

Großer Dank geht natürlich auch raus an **Ohi-Johi**. Einer dieser Kerle, bei dem ich mich nicht erinnern kann, ob es eine Zeit vor ihm gab. Von nachmittaglichen Gain-Sessions, über den Aufbau diverser Frösche und mehrere bestrittene Strahlzeiten für die ich manchmal eigentlich keine Zeit hatte, war wirklich alles mit dir dabei. Zu dir konnte ich immer gehen und dir meine abstrusen Lösungsvorschläge für bisher noch nicht existente Probleme schildern. Das alles möchte ich nicht missen!

**Spondi** der alte Sponderjunge, macht das was ein Sponderjunge macht. Und das ist definitiv nicht nein zum Feierabend sagen! Was soll ich sagen, wir kommen wunderbar miteinander aus, atmen gerne mal ein paar Bier hintern Schal und meine Unterarme bedanken sich nach jeder Bouldersession mit dir. Außerdem treibst du die Meme-Schmiede ordentlich voran, das ist ja wohl das Größte!

Auch nicht zu vergessen ist das tägliche **Meeting** mit **Ohi**, **Ännigoa** und **Vicro** um 9:00 Uhr, welches am zweiten Donnerstag des Monats, also am ersten Dienstag stattfindet. Es begann lange vor meiner Zeit der Promotion und es wird hoffentlich noch lange Zeit danach bestehen. Mit ein bisschen Glück sogar mit Stückchen. Ohne euch wäre die Zeit (vor allem die vor der Promotion) an der GSI wirklich nur halb so schön gewesen.

Meine Kollegen aus dem **Home-Office 24/7** dürfen selbstverständlich nicht fehlen: **Felix**, **Markus**, **Maddin**, **Max**, **Patrick**, **Phillip** und **Sascha**. Wir kennen uns jetzt (quasi) seit Anfang des Studiums und ich weiß nicht ob ich ohne euch auch nur 1 % des Spaßes am Studium gehabt hätte, wie ich ihn mit euch hatte. Die gemeinsame Zeit ist einfach nicht zu ersetzen und definitiv unvergesslich. Naja bis auf die Abende, an die man sich halt sowieso nicht mehr erinnern kann. Ich kann wirklich nur Danke für die geile gemeinsame Zeit sagen und freue mich auf alle weiteren gemeinsamen Aktionen! (das bleibt zwar unveränderbar hier stehen, aber leute: Prag steht noch aus!1!!ELF)

Danke auch an die gesamte **PP/PHELIX Crew** mit **Abel**, **Albert**, **Bernhard**, **Dennis**, noch ein **Dennis**, **Lila**, **Sabine**, **Stefan**, **Udo** und **Zsuzsi**. Danke für eure Unterstützung in jeder Lebenslage und danke dass ihr scheinbar eine Resistenz gegenüber meinem konsistenten Fluss an Dummschwätzerei aufgebaut habt. Besser wäre es auf jeden Fall, denn los seid ihr mich ja noch nicht :D.

**Der ganze Rest der sich noch so an der GSI rumtreibt**, also **Pascal**, **Sarah**, **Haress**, **Leonard**, **Philipp** und **Marcus** verdienen sich natürlich auch ein Danke, sei es einfach nur für Diskussionen, lustige Abende oder Doktorwagenbauten. Nehmt eure Bildschirmhintergründe in acht, bald bin ich wieder regelmäßig an der GSI!

Auch vielen Dank nach Dresden an **Markus**, **Daniel** und **Mathias** für eure Unterstützung beim Aufbau des uOPA Pumplasers und auch speziell an Markus für die durchzechten Nächte in Korea.

Ein ganz besonderer Dank muss natürlich bei den Übeltätern gelassen werden, ohne die ich im wahrsten Sinne heute nicht hier wäre. **Mama**, **Papa** vielen Dank, dass ihr mich immer und bei allem unterstützt habt und auch immer noch unterstützt. Das gleiche gilt natürlich für meinen Bruder **Marcel**, auch wenn ich ihn enttäuschen muss, weil ich weder ein Lichtschwert gebaut habe, noch Bratwurstverkäufer geworden bin. Ich bin unglaublich froh euch zu haben und weiß, dass ich bei euch immer daheim bin. Ich hab euch lieb.

Offensichtlich fehlt hier noch eine letzte Person und das bis du, **Kadda**. Ich kann nur Danke sagen, für deinen Rückhalt, deinen Humor, dass du mich Kindskopf aushältst, dass du mir Mut machst, dass du mich während der Schreibphase den Schreibtisch hast zumüllen lassen, fürs Korrekturlesen, dass du mir auch mal in den Arsch trittst, dass du mich liebst. Einfach danke für alles, ich liebe dich.

# Bibliography


[1] Y. Zobus et al., Versatile, compact chirped pulse amplifier pump system for ultrafast optical parametric amplifiers, *Opt. Express*, **31**(3):5002–5015 (2023).

[2] Y. Zobus et al., Millijoule Ultrafast Optical Parametric Amplification as Replacement for High-Gain Regenerative Amplifiers, *High Power Laser Sci. Eng.*, pp. 1–13 (2023), doi: 10.1017/hpl.2023.30.

[3] T. H. Maiman, Stimulated Optical Radiation in Ruby, *Nature*, **187**(4736):493–494 (1960), doi: 10.1038/187493a0.

[4] P. A. Franken et al., Generation of optical harmonics, *Phys. Rev. Lett.*, **7**(4):118–119 (1961), doi: 10.1103/PhysRevLett.7.118.

[5] F. J. McClung and R. W. Hellwarth, Giant Optical Pulsations from Ruby, *Appl. Opt.*, **1**(S1):103 (1962), doi: 10.1364/ao.1.s1.000103.

[6] R. J. Collins et al., Coherence, narrowing, directionality, and relaxation oscillations in the light emission from ruby, *Phys. Rev. Lett.*, **5**(7):303–305 (1960), doi: 10.1103/PhysRevLett.5.303.

[7] M. DiDomenico, Small-Signal Analysis of Internal ( Coupling-Type ) Modulation of Lasers, *Appl. Phys. Lett.*, **35**(2870):1–4 (1964).

[8] L. E. Hargrove, R. L. Fork and M. A. Pollack, Locking of He-Ne laser modes induced by synchronous intracavity modulation, *Appl. Phys. Lett.*, **5**(1):4–5 (1964), doi: 10.1063/1.1754025.

[9] M. H. Crowell, Characteristics of mode-coupled lasers, *IEEE J. Quantum Electron.*, **1**(1):12–20 (1965).

[10] E. P. Ippen and C. V. Shank, Subpicosecond, kilowatt Pulses from a mode-locked CW dye laser, *IEEE J. Quantum Electron.*, **24**(373) (1974), doi: 10.1109/JQE.1974.1068270.

[11] J. A. Glaze et al., The Shiva Laser-Fusion Facility, *IEEE J. Quantum Electron.*, **17**(9):1599–1619 (1981), doi: 10.1109/JQE.1981.1071352.

[12] E. M. Campbell et al., Nova experimental facility (invited), *Rev. Sci. Instrum.*, **57**(8):2101–2106 (1986), doi: 10.1063/1.1138755.

[13] D. Strickland and G. Mourou, Compression of Amplified Chirped Optical Pulses, *Opt. Commun.*, **56**(3):219–221 (1985), doi: 10.1016/0030-4018(85)90120-8.

[14] P. Moulton, Ti-doped sapphire: tunable solid-state laser, *Opt. News*, **8**(6):9 (1982).

[15] P. F. Moulton, Spectroscopic and laser characteristics of Ti:$Al_2O_3$, *J. Opt. Soc. Am. B*, **3**(1):125 (1986), doi: 10.1364/josab.3.000125.

[16] O. E. Martinez, 3000 times grating compressor with positive group velocity dispersion: Application to fiber compensation in 1.3-1.6 $\mu$m region, *IEEE J. Quantum Electron.*, **23**(1):59–64 (1987), doi: 10.1109/JQE.1987.1073201.

[17] E. B. Treacy, Optical Pulse Compression with Diffraction Gratings, *IEEE J. Quantum Electron.*, **5**(9):454–458 (1969), doi: 10.1109/JQE.1969.1076303.

[18] P. Maine et al., Generation of Ultrahigh Peak Power Pulses by Chirped Pulse Amplification, *IEEE J. Quantum Electron.*, **24**(2):398–403 (1988), doi: 10.1109/3.137.

[19] C. Rouyer et al., Generation of 50-TW femtosecond pulses in a Ti:sapphire/Nd:glass chain, *Opt. Lett.*, **18**(3):214 (1993), doi: 10.1364/ol.18.000214.

[20] M. D. Perry et al., Petawatt laser pulses, *Opt. Lett.*, **24**(3):160 (1999), doi: 10.1364/ol.24.000160.

[21] J. J. Macklin, J. D. Kmetec and C. L. Gordon, High-order harmonic generation using intense femtosecond pulses, *Phys. Rev. Lett.*, **70**(6):766–769 (1993), doi: 10.1103/PhysRevLett.70.766.

[22] S. Augst et al., Laser ionization of noble gases by Coulomb-barrier suppression, *J. Opt. Soc. Am. B*, **8**(4):858 (1991), doi: 10.1364/josab.8.000858.

[23] P. Monot et al., Experimental demonstration of relativistic self-channeling of a multiterawatt laser pulse in an underdense plasma, *Phys. Rev. Lett.*, **74**(15):2953–2956 (1995), doi: 10.1103/PhysRevLett.74.2953.

[24] A. Modena et al., Electron acceleration from the breaking of relativistic plasma waves, *Nature*, **377**:606–608 (1995).

[25] T. Ditmire et al., High-energy ions produced in explosions of superheated atomic clusters, *Nature*, **386**:243–244 (1997), doi: 10.1038/255243a0.

[26] M. Nantel et al., Temporal contrast in Ti:sapphire lasers: Characterization and control, *IEEE J. Sel. Top. Quantum Electron.*, **4**(2):449–458 (1998), doi: 10.1109/2944.686755.

[27] C. N. Danson et al., Petawatt and exawatt class lasers worldwide, *High Power Laser Sci. Eng.*, **7**(March):1–54 (2019), doi: 10.1017/hpl.2019.36.

[28] C. Radier et al., 10 PW peak power femtosecond laser pulses at ELI-NP, *High Power Laser Sci. Eng.*, **10**:1–5 (2022), doi: 10.1017/hpl.2022.11.

[29] J. W. Yoon et al., Realization of laser intensity over $10^{23}$ W/cm$^2$, *Optica*, **8**(5):630–635 (2021), doi: 10.1364/optica.420520.

[30] H. Kiriyama et al., Enhancement of pre-pulse and picosecond pedestal contrast of the petawatt J-KAREN-P laser, *High Power Laser Sci. Eng.*, **9**(e62) (2021), doi: 10.1017/hpl.2021.51.

[31] J. W. Yoon et al., Ultra-high intensity lasers as tools for novel physics, *J. Korean Phys. Soc.*, **81**(6):562–569 (2022), doi: 10.1007/s40042-022-00411-3.

[32] L. Ranc et al., Improvement in the temporal contrast in the tens of ps range of the multi-PW Apollon laser front-end, *Opt. Lett.*, **45**(16):4599 (2020), doi: 10.1364/ol.401272.

[33] Y. Dai et al., XingGuang-Extreme Laser Facility, *Guangxue Xuebao/Acta Opt. Sin.*, **42**(17) (2022), doi: 10.3788/AOS202242.1714001.

[34] B. Shao et al., Broad-bandwidth high-temporal-contrast carrier-envelope-phase-stabilized laser seed for 100 PW lasers, *Opt. Lett.*, **45**(8):2215 (2020), doi: 10.1364/ol.390110.

[35] J. Hartmann et al., Commissioning of the laser-driven ion acceleration beamline at the Centre for Advanced Laser Applications, *Proc. SPIE 11779, Laser Accel. Electrons, Protons, Ions VI,*, p. 21 (2021), doi: 10.1117/12.2592407.

[36] F. Wagner et al., Temporal contrast control at the PHELIX petawatt laser facility by means of tunable sub-picosecond optical parametric amplification, *Appl. Phys. B Lasers Opt.*, **116**(2):429–435 (2014), doi: 10.1007/s00340-013-5714-9.

[37] T. Ziegler et al., Proton beam quality enhancement by spectral phase control of a PW-class laser system, *Sci. Rep.*, **11**(1):1–7 (2021), doi: 10.1038/s41598-021-86547-x.

[38] M. Hornung et al., 54 J pulses with 18 nm bandwidth from a diode-pumped chirped-pulse amplification laser system, *Opt. Lett.*, **41**(22):5413 (2016), doi: 10.1364/ol.41.005413.

[39] J. B. Ohland et al., Ultra-compact post-compressor on-shot wavefront measurement for beam correction at PHELIX, *High Power Laser Sci. Eng.*, **10**:1–9 (2022), doi: 10.1017/hpl.2022.9.

[40] R. W. Boyd, S. G. Lukishova and Y. R. Shen, Self-focusing: Past and Present, volume 114, Springer (2009).

[41] G. Cheriaux et al., Aberration-free stretcher design for ultrashort-pulse amplification, *Opt. Lett.*, **21**(6):414 (1996), doi: 10.1364/ol.21.000414.

[42] F. Verluise et al., Amplitude and phase control of ultrashort pulses by use of an acousto-optic programmable dispersive filter: pulse compression and shaping, *Opt. Lett.*, **25**(8):575–577 (2000), url: http://dialnet.unirioja.es/servlet/extart?codigo=4063724.

[43] C. P. J. Barty et al., Regenerative pulse shaping and amplification of ultrabroadband optical pulses, *Opt. Lett.*, **21**(3):219 (1996), doi: 10.1364/ol.21.000219.

[44] U. Schramm et al., First results with the novel petawatt laser acceleration facility in Dresden, *IPAC 2017 - Proc. 8th Int. Part. Accel. Conf.*, pp. 48–52 (2017).

[45] F. Röser et al., Millijoule pulse energy high repetition rate femtosecond fiber chirped-pulse amplification system, *Opt. Lett.*, **32**(24):3495 (2007), doi: 10.1364/ol.32.003495.

[46] H. Stark et al., 1 kW, 10 mJ, 120 fs coherently combined fiber CPA laser system, *Opt. Lett.*, **46**(5):969–972 (2021), url: https://doi.org/10.1364/OL.417032.

[47] I. Jovanovic et al., Optical parametric chirped-pulse amplifier as an alternative to Ti:sapphire regenerative amplifiers, *Appl. Opt.*, **41**(15):2923 (2002), doi: 10.1364/ao.41.002923.

[48] S. Keppler et al., Multipass amplifiers of POLARIS, *Proc. SPIE*, **8780**(87800I) (2013), doi: 10.1117/12.2019248.

[49] D. Albach et al., Performance demonstration of the PEnELOPE main amplifier HEPA I using broadband nanosecond pulses, *High Power Laser Sci. Eng.*, **7**(e1):1–9 (2019), doi: 10.1017/hpl.2018.59.

[50] J. P. Zou et al., Design and current progress of the Apollon 10 PW project, *High Power Laser Sci. Eng.*, **3**:1–4 (2015), doi: 10.1017/hpl.2014.41.

[51] M. Galletti et al., Ultra-broadband all-OPCPA petawatt facility fully based on LBO, *High Power Laser Sci. Eng.*, **8** (2020), doi: 10.1017/hpl.2020.31.

[52] W. Hong et al., Commissioning experiment of the high-contrast SILEX-II multi-petawatt laser facility, *Matter Radiat. Extrem.*, **6**(6):0–11 (2021), doi: 10.1063/5.0016019.

[53] V. Bagnoud et al., Commissioning and early experiments of the PHELIX facility, *Appl. Phys. B Lasers Opt.*, **100**(1):137–150 (2010), doi: 10.1007/s00340-009-3855-7.

[54] C. N. Danson et al., Vulcan petawatt - An ultra-high-intensity interaction facility, *Nucl. Fusion*, **44**(12) (2004), doi: 10.1088/0029-5515/44/12/S15.

[55] A. Einstein, The Quantum Theory of Radiation, *Phys. Zeitschrift*, **18**(121) (1917), doi: 10.1038/138483a0.

[56] V. V. Ivanov, A. Maksimchuk and G. Mourou, Amplified spontaneous emission in a Ti:sapphire regenerative amplifier, *Appl. Opt.*, **42**(36):7231–7234 (2003).

[57] S. Keppler et al., The generation of amplified spontaneous emission in high-power CPA laser systems, *Laser Photonics Rev.*, **10**(2):264–277 (2016), doi: 10.1002/lpor.201500186.

[58] R. Glauber and F. Haake, The initiation of superfluorescence, *Phys. Lett. A*, **68**(1):29–32 (1978), doi: 10.1016/0375-9601(78)90747-8.

[59] C. Homann and E. Riedle, Direct measurement of the effective input noise power of an optical parametric amplifier, *Laser Photonics Rev.*, **7**(4):580–588 (2013), doi: 10.1002/lpor.201200119.

[60] A. Penzkofer, A. Laubereau and W. Kaiser, High intensity Raman interactions, *Prog. Quantum Electron.*, **6**(2):55–140 (1979), doi: 10.1016/0079-6727(79)90011-9.

[61] J. B. Kinney and R. H. Staley, Applications of Photoacoustic Spectroscopy., volume 12 (1982), doi: 10.1146/annurev.ms.12.080182.001455.

[62] C. Dorrer et al., OPCPA front end and contrast optimization for the OMEGA EP kilojoule , picosecond laser, *J. Opt. (United Kingdom)*, **17** (2015), doi: 10.1088/2040-8978/17/9/094007.

[63] N. V. Didenko et al., Contrast degradation in a chirped-pulse amplifier due to generation of prepulses by postpulses, *Opt. Express*, **16**(5):3178 (2008), doi: 10.1364/oe.16.003178.

[64] H. Kiriyama et al., Experimental investigation on the temporal contrast of pre-pulses by post-pulses in a petawatt laser facility, *Opt. Lett.*, **45**(5):1100 (2020), doi: 10.1364/ol.384759.

[65] S. Keppler et al., All-reflective, highly accurate polarization rotator for high-power short-pulse laser systems, *Opt. Express*, **20**(18):20742 (2012), doi: 10.1364/oe.20.020742.

[66] R. W. Boyd, Nonlinear Optics, Academic Press, 2nd edition (2003).

[67] D. Milam and M. J. Weber, Nonlinear Refractive Index Coefficient for Nd Phosphate Laser Glasses, *IEEE J. Quantum Electron.*, **12**(8):512–513 (1976), doi: 10.1109/JQE.1976.1069197.

[68] S. Roeder et al., How the laser beam size conditions the temporal contrast in pulse stretchers of CPA lasers, *High Power Laser Sci. Eng.*, **10**(e34):7 (2022), doi: 10.1017/hpl.2022.18.

[69] V. Bagnoud and F. Salin, Influence of optical quality on chirped-pulse amplification : characterization of a 150-nm-bandwidth stretcher, *J. Opt. Soc. Am. B*, **16**(1):188–193 (1999).

[70] C. Dorrer and J. Bromage, Impact of high-frequency spectral phase modulation on the temporal profile of short optical pulses, *Opt. Express*, **16**(5):3058 (2008), doi: 10.1364/oe.16.003058.

[71] A. Mcilvenny et al., Selective Ion Acceleration by Intense Radiation Pressure, *Phys. Rev. Lett.*, **127**(19):194801 (2021), doi: 10.1103/PhysRevLett.127.194801, url: https://doi.org/10.1103/PhysRevLett.127.194801.

[72] N. Dover et al., Enhanced ion acceleration from transparency-driven foils demonstrated at two ultraintense laser facilities, *Light Sci. Appl.*, **12**(71) (2023), doi: 10.1038/s41377-023-01083-9.

[73] A. Macchi, S. Veghini and F. Pegoraro, "Light Sail" Acceleration Reexamined, *Phys. Rev. Lett.*, **103**(8):1–4 (2009), doi: 10.1103/PhysRevLett.103.085003.

[74] L. Yin et al., Monoenergetic and GeV ion acceleration from the laser breakout afterburner using ultrathin targets, *Phys. Plasmas*, **14**(5) (2007), doi: 10.1063/1.2436857.

[75] P. B. Corkum, F. Brunel and N. K. Sherman, Thermal response of metals to ultrashort-pulse laser excitation, *Phys. Rev. Lett.*, **61**(25):1846 (1988), doi: 10.1103/PhysRevLett.64.1846.

[76] J. F. Figueira and S. J. Thomas, Damage Thresholds at Metal Surfaces for Short Pulse IR Lasers, *IEEE J. Quantum Electron.*, **QE-18**(9) (1982).

[77] B. C. Stuart et al., Optical ablation by high-power short-pulse lasers, *J. Opt. Soc. Am. B*, **13**(2):459 (1996), doi: 10.1364/josab.13.000459.

[78] A. C. Tien et al., Short-pulse laser damage in transparent materials as a function of pulse duration, *Phys. Rev. Lett.*, **82**(19):3883–3886 (1999), doi: 10.1103/PhysRevLett.82.3883.

[79] B. Stuart et al., Laser-Induced Damage in Dielectrics with Nanosecond to Subpicosecond Pulses, *Phys. Rev. Lett.*, **74**(12):2248–2252 (1995).

[80] C. W. Carr, H. B. Radousky and S. G. Demos, Wavelength dependence of laser-induced damage: Determining the damage initiation mechanisms, *Phys. Rev. Lett.*, **91**(12):1–4 (2003), doi: 10.1103/PhysRevLett.91.127402.

[81] P. Mulser and D. Bauer, High Power Laser-Matter Interaction, Springer, 1st edition (2010).

[82] M. D. Perry et al., Nonresonant multiphoton ionization of noble gases: Theory and experiment, *Phys. Rev. Lett.*, **60**(13):1270–1273 (1988), doi: 10.1103/PhysRevLett.60.1270.

[83] S. Augst et al., Tunneling ionization of noble gases in a high-intensity laser field, *Phys. Rev. Lett.*, **63**(20):2212–2215 (1989), doi: 10.1103/PhysRevLett.63.2212.

[84] B. Wolff et al., Multiphoton-ionization of hydrogen atoms in intense laserfields, *Zeitschrift für Phys. D Atoms, Mol. Clust.*, **10**(1):35–43 (1988), doi: 10.1007/BF01425579.

[85] T. Brabec, Strong Field Laser Physics, volume 134, Springer (2009), url: https://books.google.com.pk/books?id=PwjSBwAAQBAJ%0Ahttp://link.springer.com/10.1007/978-0-387-34755-4.

[86] C. E. Moore, Ionization Potentials and Ionization Limits Derived from the Analysis of Optical Spectra (1970).

[87] J. Deiglmayr et al., Precision measurement of the ionization energy of Cs i, *Phys. Rev. A*, **93**(1):1–7 (2016), doi: 10.1103/PhysRevA.93.013424.

[88] P. G. Bleotu et al., Spectral broadening for multi-Joule pulse compression in the APOLLON Long Focal Area facility, *High Power Laser Sci. Eng.*, **10** (2022), doi: 10.1017/hpl.2021.61.

[89] M. Maier, W. Kaiser and J. A. Giordmaine, Intense light bursts in the stimulated Raman effect, *Phys. Rev. Lett.*, **17**(26):1275–1277 (1966), doi: 10.1103/PhysRevLett.17.1275.

[90] D. J. Kane and R. Trebino, Characterization of Arbitrary Femtosecond Pulses Using Frequency-Resolved Optical Gating, *IEEE J. Quantum Electron.*, **29**(2):571–579 (1993), doi: 10.1109/3.199311.

[91] C. Iaconis, M. E. Anderson and I. A. Walmsley, Spectral phase interferometry for direct electric field reconstruction of ultrashort optical pulses, *Springer Ser. Chem. Phys.*, **63**(10):103–105 (1998), doi: 10.1007/978-3-642-72289-9_31.

[92] T. Oksenhendler et al., Self-referenced spectral interferometry, *Appl. Phys. B Lasers Opt.*, **99**(1-2):7–12 (2010), doi: 10.1007/s00340-010-3916-y.

[93] R. Morita et al., Sub-5 fs optical pulse characterization, *Meas. Sci. Technol.*, **13**(11):1710–1720 (2002), doi: 10.1088/0957-0233/13/11/307.

[94] S. Akturk, C. D'Amico and A. Mysyrowicz, Measuring ultrashort pulses in the single-cycle regime using frequency-resolved optical gating, *J. Opt. Soc. Am. B*, **25**(6):A63 (2008), doi: 10.1364/josab.25.000a63.

[95] A. Trabattoni et al., Self-referenced spectral interferometry for single-shot measurement of sub-5-fs pulses, *Rev. Sci. Instrum.*, **86**(11) (2015), doi: 10.1063/1.4936289, url: http://dx.doi.org/10.1063/1.4936289.

[96] V. A. Schanz et al., Noise reduction in third order cross-correlation by angle optimization of the interacting beams, *Opt. Express*, **25**(8):9252 (2017), doi: 10.1364/OE.25.009252.

[97] U. Innovations, Product-Sheet: Ultra-high Contrast Third-order Autocorrelator TUNDRA.

[98] T. Oksenhendler et al., High dynamic, high resolution and wide range single shot temporal pulse contrast measurement, *Opt. Express*, **25**(11):12588–12600 (2017), url: http://arxiv.org/abs/1204.4949.

[99] P. Tournois, Acousto-optic programmable dispersive filter for adaptive compensation of group delay time dispersion in laser systems, *Opt. Commun.*, **140**(4-6):245–249 (1997), doi: 10.1016/S0030-4018(97)00153-3.

[100] A. M. Weiner et al., Programmable Shaping of Femtosecond Optical Pulses by Use of 128-Element Liquid Crystal Phase Modulator, *IEEE J. Quantum Electron.*, **28**(4):908–920 (1992), doi: 10.1109/3.135209.

[101] A. Efimov et al., Adaptive control of pulse phase in a chirped pulse amplifier, *Springer Ser. Chem. Phys.*, **63**(24):87–89 (1998), doi: 10.1007/978-3-642-72289-9_26.

[102] A. Jullien et al., $10^{10}$ Temporal Contrast for Femtosecond Ultraintense Lasers By Cross-Polarized Wave Generation, *Opt. Lett.*, **30**(8):920 – 922 (2005), doi: 10.1364/ol.30.000920.

[103] N. Minkovski et al., Nonlinear polarization rotation and orthogonal polarization generation experienced in a single-beam configuration, *J. Opt. Soc. Am. B*, **21**(9):1659 (2004), doi: 10.1364/josab.21.001659.

[104] A. Jullien et al., Spectral broadening and pulse duration reduction during cross-polarized wave generation: Influence of the quadratic spectral phase, *Appl. Phys. B Lasers Opt.*, **87**(4):595–601 (2007), doi: 10.1007/s00340-007-2685-8.

[105] L. P. Ramirez et al., High energy and efficient cross polarized wave generation for high contrast ultrashort laser sources, *Opt. InfoBase Conf. Pap.*, **19**(1):93–98 (2011), doi: 10.1364/hilas.2011.hwa6.

[106] H. Liebetrau et al., Ultra-high contrast frontend for high peak power fs-lasers at 1030 nm, *Opt. Express*, **22**(20):24776 (2014), doi: 10.1364/oe.22.024776.

[107] L. P. Ramirez et al., Compact, simple, and robust cross polarized wave generation source of few-cycle, high-contrast pulses for seeding petawatt-class laser systems, *J. Opt. Soc. Am. B*, **30**(10):2607 (2013), doi: 10.1364/josab.30.002607.

[108] A. Jullien et al., Nonlinear polarization rotation of elliptical light in cubic crystals, with application to cross-polarized wave generation, *J. Opt. Soc. Am. B*, **22**(12):2635 (2005), doi: 10.1364/josab.22.002635.

[109] N. G. Khodakovskiy et al., Generation of few-cycle laser pulses with high temporal contrast via nonlinear elliptical polarisation rotation in a hollow fibre compressor, *Laser Phys. Lett.*, **16**(9) (2019), doi: 10.1088/1612-202X/ab3852.

[110] V. Pajer and M. Kalashnikov, High temporal contrast ultrashort pulses generated by nonlinear ellipse rotation in multipass cells, *Laser Phys. Lett.*, **18**(6):1–6 (2021), doi: 10.1088/1612-202X/abff49.

[111] Y. Pfaff et al., Nonlinear pulse compression of a thin-disk amplifier and contrast enhancement via nonlinear ellipse rotation, *Opt. Express*, **30**(7):10981 (2022), doi: 10.1364/oe.455393.

[112] D. Homoelle and A. L. Gaeta, Pulse contrast enhancement of high-energy pulses by use of a gas-filled hollow waveguide, *Opt. Lett.*, **27**(18):1646–1648 (2002).

[113] J. Song et al., Temporal contrast enhancement by nonlinear elliptical polarization rotation in a multi-pass cell, *High Power Laser Sci. Eng.*, **30**(15):26297–26305 (2022), doi: 10.1017/hpl.2022.22.

[114] J. Buldt et al., Enhancement of temporal contrast by filtered SPM broadened spectra, *Opt. InfoBase Conf. Pap.*, **Part F75-A**(19):3761–3764 (2017), doi: 10.1364/ASSL.2017.JM5A.25.

[115] J. Liu and T. Kobayashi, Temporal contrast improvement of femtosecond pulses by a self-diffraction process in a Kerr bulk medium, *Opt. InfoBase Conf. Pap.*, **18**(21):22245–22254 (2011), doi: 10.1364/cleo_si.2011.ctuq4.

[116] T. Schneider et al., Rapid communication Ultrafast optical switching by instantaneous laser-induced grating formation and self-diffraction in barium fluoride, *Appl. Phys. B Lasers Opt.*, **751**:749–751 (1999).

[117] X. Z. Wang et al., A Self-Diffraction Temporal Filter for Contrast Enhancement in Femtosecond Ultra-High Intensity Laser, *Chinese Phys. Lett.*, **38**(7) (2021), doi: 10.1088/0256-307X/38/7/074202.

[118] R. C. Shah et al., High-temporal contrast using low-gain optical parametric amplification, *Opt. Lett.*, **34**(15):2273 (2009), doi: 10.1364/ol.34.002273.

[119] J. Itatani et al., Suppression of the amplified spontaneous emission in chirped-pulse-amplification lasers by clean high-energy seed-pulse injection, *Opt. Commun.*, **148**(1-3):70–74 (1998), doi: 10.1016/S0030-4018(97)00638-X.

[120] H. Kiriyama et al., Temporal contrast enhancement of petawatt-class laser pulses, *Opt. Lett.*, **37**(16):3363 (2012), doi: 10.1364/ol.37.003363.

[121] H. W. Mocker and R. J. Collins, Mode competition and self-locking effects in a q-switched ruby laser, *Appl. Phys. Lett.*, **7**(10):270–273 (1965), doi: 10.1063/1.1754253.

[122] A. J. Demaria, D. A. Stetser and H. Heynau, Self mode-locking of lasers with saturable absorbers, *Appl. Phys. Lett.*, **8**(7):174–176 (1966), doi: 10.1063/1.1754541.

[123] E. Wolf, Progress in Optics Volume 46, Elsevier Ltd., 1st edition (2004).

[124] S. Szatmári et al., Improvement of the temporal and spatial contrast of high-brightness laser beams, *Laser Phys. Lett.*, **13**(7):1–6 (2016), doi: 10.1088/1612-2011/13/7/075301.

[125] B. Gilicze et al., Improvement of the temporal and spatial contrast of the nonlinear Fourier-filter, *Laser Phys. Lett.*, **13**(7):424–429 (2016), doi: 10.1088/1612-2011/13/7/075301.

[126] M. Ueffing et al., Direct regenerative amplification of femtosecond pulses to the multimillijoule level, *Opt. Lett.*, **41**(16):3840 (2016), doi: 10.1364/OL.41.003840, url: https://www.osapublishing.org/abstract.cfm?URI=ol-41-16-3840.

[127] V. V. Ivanov et al., Study of direct amplification of ultrashort light pulses in a laser amplifier with a view to obtaining high radiation contrast, *J. Russ. Laser Res.*, **25**(4):349–360 (2004), doi: 10.1023/B:JORR.0000035717.14829.2f.

[128] C. Dorrer et al., High-contrast optical-parametric amplifier as a front end of high-power laser systems, *Opt. Lett.*, **32**(15):2143 (2007), doi: 10.1364/ol.32.002143.

[129] X. Lu et al., Suppressing Temporal Pedestal in Nd:glass Laser Systems by Avoiding Far-Field Spectral Phase Noise, *IEEE J. Sel. Top. Quantum Electron.*, **24**(5) (2018), doi: 10.1109/JSTQE.2017.2785291.

[130] H. C. Kapteyn, M. M. Murnane and A. Szoke, Prepulse energy suppression for high-energy ultrashort pulses using self-induced plasma shuttering, *Opt. Lett.*, **16**(7):490–492 (1991).

[131] B. Dromey et al., The plasma mirror - A subpicosecond optical switch for ultrahigh power lasers, *Rev. Sci. Instrum.*, **75**(3):645–649 (2004), doi: 10.1063/1.1646737.

[132] G. Doumy et al., Complete characterization of a plasma mirror for the production of high-contrast ultraintense laser pulses, *Phys. Rev. E - Stat. Nonlinear, Soft Matter Phys.*, **69**(2 2):1–12 (2004), doi: 10.1103/PhysRevE.69.026402.

[133] F. Dollar, C. Zulick and T. Matsuoka, High contrast ion acceleration at intensities exceeding $10^{21}$ W/cm$^2$, *Phys. Plasmas*, **20**(056703) (2013), doi: 10.1063/1.4803082.

[134] I. W. Choi et al., Highly efficient double plasma mirror producing ultrahigh-contrast multi-petawatt laser pulses, *Opt. Lett.*, **45**(23):6342 (2020), doi: 10.1364/ol.409749.

[135] M. Hornung et al., Generation of 25-TW femtosecond laser pulses at 515nm with extremely high temporal contrast, *Appl. Sci.*, **5**(4):1970–1979 (2015), doi: 10.3390/app5041970.

[136] D. Hillier et al., Ultrahigh contrast from a frequency-doubled chirped-pulse-amplification beamline, *Appl. Opt.*, **52**(18):4258–4263 (2013), doi: 10.1364/AO.52.004258.

[137] J. Goodman et al., Optimisation of multi-petawatt laser-driven proton acceleration in the relativistic transparency regime, *New J. Phys.*, **24**(5) (2022), doi: 10.1088/1367-2630/ac681f.

[138] V. A. Vshivkov et al., Nonlinear electrodynamics of the interaction of ultra-intense laser pulses with a thin foil, *Phys. Plasmas*, **5**(7):2727–2741 (1998), doi: 10.1063/1.872961.

[139] S. A. Reed et al., Relativistic plasma shutter for ultraintense laser pulses, *Appl. Phys. Lett.*, **94**(20):28–31 (2009), doi: 10.1063/1.3139860.

[140] V. A. Schanz et al., High dynamic range, large temporal domain laser pulse measurement, *Appl. Phys. B Lasers Opt.*, **125**(4):1–7 (2019), doi: 10.1007/s00340-019-7172-5, url: http://dx.doi.org/10.1007/s00340-019-7172-5.

[141] G. Rustad, G. Arisholm and Ø. Farsund, Effect of idler absorption in pulsed optical parametric oscillators, *Opt. Express*, **19**(3):2815 (2011), doi: 10.1364/oe.19.002815.

[142] C. Manzoni and G. Cerullo, Design criteria for ultrafast optical parametric amplifiers, *J. Opt. (United Kingdom)*, **18**(10):1–33 (2016), doi: 10.1088/2040-8978/18/10/103501.

[143] P. D. Maker et al., Effects of Dispersion and Focusing on the Production of Optical Harmonics, *Phys. Rev. Lett.*, **8**(1):21–23 (1962).

[144] J. E. Midwinter and J. Warner, The effects of phase matching method and of uniaxial crystal symmetry on the polar distribution of second-order non-linear optical polarization, *Br. J. Appl. Phys.*, **16**:1135 – 1142 (1965).

[145] M. V. Hobden and J. Warner, The Temperature Dependence of the Refractive Indices of pure Lithium Niobate, *Phys. Lett.*, **22**(3):243–244 (1966).

[146] G. D. Boyd and A. Ashkin, Theory of Parametric Oscillator Threshold with Single-Mode Optical Masers and Observation of Amplification in $LiNbO_3$, *Phys. Rev.*, **146**(1):187 – 199 (1966).

[147] J. A. Armstrong et al., Interactions between light waves in a nonlinear dielectric, *Phys. Rev.*, **127**(6):1918–1939 (1962), doi: 10.1103/PhysRev.127.1918.

[148] P. A. Franken and J. F. Ward, Optical Harmonics and Nonlinear Phenomena, **35**(1) (1963).

[149] M. Born and E. Wolf, Principles of Optics - 60th Anniversary Edition, Cambridge University Press, 7th edition (2019), url: http://journal.um-surabaya.ac.id/index.php/JKM/article/view/2203.

[150] S. A. Rezvani et al., Ultrabroadband tunable OPA design using a spectrally broadened pump source, *Opt. Lett.*, **42**(17):3367 (2017), doi: 10.1364/ol.42.003367.

[151] O. Morice, Miró: Complete modeling and software for pulse amplification and propagation in high-power laser systems, *Opt. Eng.*, **42**(6):1530 – 1541 (2003), doi: 10.1117/1.1574326.

[152] J. Bromage et al., Analysis and suppression of parasitic processes in noncollinear optical parametric amplifiers, *Opt. Express*, **19**(18):16797 (2011), doi: 10.1364/oe.19.016797.

[153] G. Cerullo et al., Few-optical-cycle light pulses with passive carrier-envelope phase, *Laser Photonics Rev.*, **5**(3) (2011), doi: 10.1002/lpor.201000013.

[154] F. Tavella, A. Marcinkevičius and F. Krausz, Investigation of the superfluorescence and signal amplification in an ultrabroadband multiterawatt optical parametric chirped pulse amplifier system, *New J. Phys.*, **8**(219) (2006), doi: 10.1088/1367-2630/8/10/219.

[155] Y. Hama et al., Control of amplified optical parametric fluorescence in hybrid chirped-pulse amplification, *Springer Ser. Opt. Sci.*, **23**(2):527–533 (2006), doi: 10.1007/978-0-387-49119-6_68.

[156] A. V. Smith, SNLO nonlinear optics code available from A. V. Smith, AS-Photonics, Albuquerque, NM.

[157] D. Eimerl et al., Optical, mechanical, and thermal properties of barium borate, *J. Appl. Phys.*, **62**(5):1968–1983 (1987), doi: 10.1063/1.339536.

[158] L. J. Bromley, A. Guy and D. C. Hanna, Synchronously pumped optical parametric oscillation in Beta-Barium-Borate, *Opt. Commun.*, **67**(4):316–320 (1988).

[159] C. Chen et al., New nonlinear optical crystal LiB3O5, *Conf. Lasers Electro-0Ptics*, **6**(4):348 (1989).

[160] K. Kato, Tunable UV Generation to 0.2325 µm in LiB3O5, *IEEE J. Quantum Electron.*, **26**(7):1173–1175 (1990), doi: 10.1109/3.59655.

[161] G. Hansson et al., Transmission measurements in KTP and isomorphic compounds, *Appl. Opt.*, **39**(27):5058 (2000), doi: 10.1364/ao.39.005058.

[162] L. Isaenko et al., Influence of growth temperature of $KTiOAsO_4$ single crystals on their physico-chemical parameters and formation of domain structures, *Quantum Electron.*, **50**(8):788–792 (2020), doi: 10.1070/qel17265.

[163] H. Yin et al., KDP single crystal growth via three-dimensional motion growth method, *Cryst. Res. Technol.*, **51**(8):491–497 (2016), doi: 10.1002/crat.201600075.

[164] G. D. Boyd, R. C. Miller and K. Nassau, $LiNbO_3$: An efficient phase matchable nonlinear optical material, *Appl. Phys. Lett.*, **5**(234):3–6 (1964).

[165] G. Dmitriev and G. G. Gurzadyan, Handbook of nonlinear optical crystals (1999).

[166] W. R. Bosenberg, L. K. Cheng and J. D. Bierlein, Optical Parametric Frequency Conversion Properties of $KTiOAsO_4$, *Opt. InfoBase Conf. Pap.*, **2765**(June):154–155 (1993), doi: 10.1364/assl.1993.nf12.

[167] V. Bagnoud and F. Wagner, Ultrahigh temporal contrast performance of the PHELIX petawatt facility, *High Power Laser Sci. Eng.*, **4**:1–8 (2016), doi: 10.1017/hpl.2016.38.

[168] S. Bock et al., Characterization of accumulated B-integral of regenerative amplifier based CPA systems, *Crystals*, **10**(9):1–12 (2020), doi: 10.3390/cryst10090847.

[169] Altechna, BBO Crystals, url: https://www.altechna.com/products/bbo-crystal/ (Accessed: 2023-03-08).

[170] Castech, $\beta$-BBO - Beta-Barium Borate, url: https://www.castech.com/product/BBO-120.html (Accessed: 2023-03-08).

[171] Laser Components, Beta-Barium Borate, url: https://www.lasercomponents.com/fileadmin/user_upload/home/Datasheets/diverse-laser-optics/laser-rods-crystals/bbo.pdf (Accessed: 2023-03-08).

[172] Edmund Opics, Nichtlineare Kristalle, url: https://www.edmundoptics.de/f/nonlinear-crystals/39487/ (Accessed: 2023-03-08).

[173] Eksma Optics, Beta Barium Borate – BBO Crystals, url: https://eksmaoptics.com/nonlinear-and-laser-crystals/nonlinear-crystals/beta-barium-borate-bbo-crystals/ (Accessed: 2023-03-08).

[174] T. Lang et al., Impact of temporal, spatial and cascaded effects on the pulse formation in ultra-broadband parametric amplifiers, *Opt. Express*, **21**(1):949 (2013), doi: 10.1364/oe.21.000949.

[175] H. Coïc et al., Modeling of the petawatt PETAL laser chain using Miró code, *Appl. Opt.*, **56**(34):9491 (2017), doi: 10.1364/ao.56.009491.

[176] V. Denis et al., The Laser Megajoule Facility: laser performances and comparison with computational simulation, *High Power Lasers Fusion Res. IV*, **10084**:100840I (2017), doi: 10.1117/12.2266675.

[177] H. Coïc et al., Modeling of the petawatt PETAL laser chain using Miró code, *Appl. Opt.*, **56**(34):9491 (2017), doi: 10.1364/ao.56.009491.

[178] O. E. Martinez, Negative group-velocity dispersion using refraction, *J. Opt. Soc. Am. A*, **1**(10):1003–1006 (1984).

[179] G. Pariente et al., Space-time characterization of ultra-intense femtosecond laser beams, *Nat. Photonics*, **10**(8):547–553 (2016), doi: 10.1038/nphoton.2016.140.

[180] C. Bourassin-Bouchet et al., Duration of ultrashort pulses in the presence of spatio-temporal coupling, *Opt. Express*, **19**(18):17357 (2011), doi: 10.1364/oe.19.017357.

[181] B. Boulanger and J. Zyss, Nonlinear optical properties, *Int. Tables Crystallogr.*, **D**:178–219 (2006), doi: 10.1107/97809553602060000634.

[182] A. V. Smith, Crystal nonlinear optics with SNLO examples, AS-Photonics, 2nd edition (2018).

[183] S. K. Zhang et al., Study of the stability of optical parametric amplification, *Opt. Commun.*, **184**(5):451–455 (2000), doi: 10.1016/S0030-4018(00)00958-5.

[184] M. Guardalben et al., Design of a highly stable, high-conversion-efficiency, optical parametric chirped-pulse amplification system with good beam quality, *Opt. Express*, **11**(20):2511 (2003), doi: 10.1364/oe.11.002511.

[185] R. A. Meijer et al., High-energy Nd:YAG laser system with arbitrary sub-nanosecond pulse shaping capability, *Opt. Lett.*, **42**(14):2758 (2017), doi: 10.1364/ol.42.002758.

[186] A. Malinowski et al., High power pulsed fiber MOPA system incorporating electro-optic modulator based adaptive pulse shaping, *Opt. Express*, **17**(23):20927 (2009), doi: 10.1364/oe.17.020927.

[187] I. Will and G. Klemz, Generation of flat-top picosecond pulses by means of a two-stage birefringent filter, *Opt. Express*, **16**(19):119–125 (2008), doi: 10.1016/j.nima.2008.06.027.

[188] A. M. Weiner, J. P. Heritage and E. M. Kirschner, High-resolution femtosecond pulse shaping, *J. Opt. Soc. Am. B*, **5**(8):1563–1571 (1988).

[189] C. Röcker et al., Direct amplification of sub-300 fs pulses in a versatile thin-disk multi-pass amplifier, *Opt. Commun.*, **460**:125159 (2020), doi: 10.1016/j.optcom.2019.125159, url: https://doi.org/10.1016/j.optcom.2019.125159https://linkinghub.elsevier.com/retrieve/pii/S0030401819311460.

[190] H. Fattahi et al., High-power, 1-ps, all-Yb:YAG thin-disk regenerative amplifier, *Opt. Lett.*, **41**(6):1126 (2016), doi: 10.1364/OL.41.001126, url: https://www.osapublishing.org/abstract.cfm?URI=ol-41-6-1126.

[191] P. Mackonis and A. M. Rodin, Laser with 1.2 ps, 20 mJ pulses at 100 Hz based on CPA with a low doping level Yb:YAG rods for seeding and pumping of OPCPA, *Opt. Express*, **28**(2):1261 (2020), doi: 10.1364/oe.380907.

[192] N. Bonod and J. Neauport, Diffraction gratings: from principles to applications in high-intensity lasers, *Adv. Opt. Photonics*, **8**(1):156 (2016), doi: 10.1364/aop.8.000156.

[193] F. Druon et al., Comparison of multi-pass and regenerative strategies for energetic high-gain amplifiers based on Yb:$CaF_2$, *Opt. Lett.*, **45**(16):4408 (2020), doi: 10.1364/ol.398612.

[194] N. Hodgson and H. Weber, Laser Resonators and Beam Propagation, Springer, 2nd edition (2005).

[195] J. Limpert et al., High Repetition Rate Gigawatt Peak Power Fiber Laser Systems: Challenges, Design, and Experiment, *IEEE J. Sel. Top. Quantum Electron.*, **15**(1):159–169 (2009), doi: 10.1109/JSTQE.2008.2010244.

[196] G. P. Agrawal, Fiber-Optic Communications Systems, John Wiley & Sons, Inc., 3rd edition (2002).

[197] M. Hübner et al., Novel high-power, high repetition rate laser diode pump modules suitable for high-energy class laser facilities, *Instruments*, **3**(3):1–13 (2019), doi: 10.3390/instruments3030034.

[198] Y. Zhao et al., High Efficiency 1.9 kW Single Diode Laser Bar Epitaxially Stacked with a Tunnel Junction, *IEEE Photonics J.*, **13**(3) (2021), doi: 10.1109/JPHOT.2021.3073732.

[199] C. Hönninger et al., Ultrafast ytterbium-doped bulk lasers and laser amplifiers, *Appl. Phys. B Lasers Opt.*, **69**(1):3–17 (1999), doi: 10.1007/s003400050762.

[200] R. Paschotta et al., Ytterbium-Doped Fibre Amplifiers, *IEEE J. Quantum Mech.*, **33**(7) (1997), doi: 10.1109/3.594865.

[201] J. Koerner et al., Measurement of temperature-dependent absorption and emission spectra of Yb:YAG, Yb:LuAG, and Yb:$CaF_2$ between 20 °C and 200 °C and predictions on their influence on laser performance, *J. Opt. Soc. Am. B*, **29**(9):2493 (2012), doi: 10.1364/josab.29.002493.

[202] Optogama, Yb:YVO, url: https://4lasers.com/en/components/crystals/laser-crystals/yb-doped-crystals/yb-yvo4-crystals (Accessed: 2023-03-20).

[203] Optogama, Yb:KGW, url: https://4lasers.com/en/components/crystals/laser-crystals/yb-doped-crystals/yb-kgw-crystals (Accessed: 2023-03-20).

[204] S. Püschel et al., Temperature-dependent radiative lifetime of Yb:YLF: refined cross sections and potential for laser cooling, *Opt. Express*, **29**(7):11106 (2021), doi: 10.1364/oe.422535.

[205] M. Siebold et al., Yb:$CaF_2$-a new old laser crystal, *Appl. Phys. B Lasers Opt.*, **97**(2):327–338 (2009), doi: 10.1007/s00340-009-3701-y.

[206] F. Pirzio et al., Sub-50-fs widely tunable Yb:$CaYAlO_4$ laser pumped by 400-mW single-mode fiber-coupled laser diode, *Opt. Express*, **23**(8):9790 (2015), doi: 10.1364/oe.23.009790.

[207] Y. Zobus, Aufbau eines doppelstufigen Faserverstaerkers als Pumpstufe eines uOPA-Systems, Master thesis, TU Darmstadt (2018).

[208] T. Schreiber, Fiberdesk (2016), url: https://www.fiberdesk.com/.

[209] D. Tosi, Review of chirped fiber bragg grating (CFBG) fiber-optic sensors and their applications, *Sensors (Switzerland)*, **18**(7) (2018), doi: 10.3390/s18072147.

[210] D. V. Vidder, The heat equation, Academic Press, 1st edition (1975).

[211] Laser Components, Yb:YAG, url: https://www.lasercomponents.com/fileadmin/user_upload/home/Datasheets/diverse-laser-optics/laser-rods-crystals/yb-yag.pdf (Accessed: 2023-03-08).

[212] T. Y. Fan, Heat generation in Nd:YAG and Yb:YAG, *IEEE J. Quantum Electron.*, **29**(6):1457–1459 (1993).

[213] Z. H. L. Lin et al., Heat generation in quasi-three-level Yb : YAG thin-disk lasers, *Opt. Soc. Am.*, **34**(8):1669–1676 (2017).

[214] Layertec, Layertec Optics and Coatings, url: https://www.layertec.de/files/catalog/2020/LAYERTEC_Optics_And_Coatings_Full_Version.pdf.

[215] Plymouth Grating Laboratory, PGL Technical Note – Diffraction Efficiency, url: https://www.plymouthgrating.com/guidance/technical-notes/fundamentals/diffraction-efficiency/ (Accessed: 2023-03-08).

[216] G. P. Agrawal, Nonlinear fiber optics, Academic Press, 3rd edition (2001), doi: 10.3367/UFNr.0160.199005k.0151.

[217] U. Eisenbarth, LaserCalc (2015), url: https://sourceforge.net/p/lasercalc/_list/git.

[218] W. Koechner, Solid-State Laser Engineering, Springer, 6th edition (2014).

[219] P. Kabaciński et al., Nonlinear refractive index measurement by SPM-induced phase regression, *Opt. Express*, **27**(8):11018 (2019), doi: 10.1364/oe.27.011018.

[220] I. A. Kulagin et al., Analysis of third-order nonlinear susceptibilities of quadratic nonlinear optical crystals, *J. Opt. Soc. Am. B*, **23**(1):75 (2006), doi: 10.1364/josab.23.000075.

[221] M. Tacca et al., Tuning of a high magnification compact parabolic telescope for centimeter-scale laser beams, *Appl. Opt.*, **55**(6):1275 (2016), doi: 10.1364/ao.55.001275.

[222] S. Zhao, R. Guo and Y. Zeng, Effects of frequency-dependent Kerr nonlinearity on higher-order soliton evolution in a photonic crystal fiber with one zero-dispersion wavelength, *Phys. Rev. A*, **106**(3):33516 (2022), doi: 10.1103/PhysRevA.106.033516, url: https://doi.org/10.1103/PhysRevA.106.033516.

[223] J. Hornung et al., Synchronized off-harmonic probe beam with variable pulse duration for laser-plasma interaction experiments at PHELIX, *in preparation*.

[224] J. Fuchs et al., Laser-driven proton scaling laws and new paths towards energy increase, *Nat. Phys.*, **2**(1):48–54 (2006), doi: 10.1038/nphys199.

[225] K. Zeil et al., The scaling of proton energies in ultrashort pulse laser plasma acceleration, *New J. Phys.*, **12** (2010), doi: 10.1088/1367-2630/12/4/045015.

[226] M. Passoni, L. Bertagna and A. Zani, Target normal sheath acceleration: Theory, comparison with experiments and future perspectives, *New J. Phys.*, **12** (2010), doi: 10.1088/1367-2630/12/4/045012.

[227] Y. Takagi et al., Multivariate scaling of maximum proton energy in intense laser driven ion acceleration, *Phys. Rev. Res.*, **3**(4):1–8 (2021), doi: 10.1103/PhysRevResearch.3.043140.

[228] M. Zimmer et al., Analysis of laser-proton acceleration experiments for development of empirical scaling laws, *Phys. Rev. E*, **104**(4):1–9 (2021), doi: 10.1103/PhysRevE.104.045210.

[229] R. E. Kidder, Energy gain of laser-compressed pellets: A simple model calculation, *Nucl. Fusion*, **16**(3):405–408 (1976), doi: 10.1088/0029-5515/16/3/003.

[230] M. Roth et al., Fast ignition by intense laser-accelerated proton beams, *Phys. Rev. Lett.*, **86**(3):436–439 (2001), doi: 10.1103/PhysRevLett.86.436.

[231] M. Temporal, J. J. Honrubia and S. Atzeni, Proton-beam driven fast ignition of inertially confined fuels: Reduction of the ignition energy by the use of two proton beams with radially shaped profiles, *Phys. Plasmas*, **15**(5) (2008), doi: 10.1063/1.2918316.

[232] M. Roth and M. Schollmeier, Ion acceleration-target normal sheath acceleration, *Proc. CAS-CERN Accel. Sch. Plasma Wake Accel.*, pp. 231–270 (2014), doi: 10.5170/CERN-2016-001.231.

[233] Lawrence Livermore National Laboratory, Jupiter Laser Facility - Titan, url: https://jlf.llnl.gov/laser-facilities/titan (Accessed: 2023-03-08).

[234] P. Rambo et al., Z-Petawatt Laser Highlights for FY21, Technical report, Sandia National Laboratories (2021), url: https://www.osti.gov/servlets/purl/1836404.

[235] Y. Wang et al., 0.85 PW laser operation at 3.3 Hz and high-contrast ultrahigh-intensity $\lambda =$ 400 nm second-harmonic beamline, *Opt. Lett.*, **42**(19):3828–3831 (2017).

[236] S. Hakimi, L. Obst-Huebl and A. Huebl, Laser–solid interaction studies enabled by the new capabilities of the iP2 BELLA PW beamline, *Phys. Plasmas*, **29**(083102) (2022), doi: 10.1063/5.0089331.

[237] K. Nakamura, H.-S. Mao and A. J. Gonsalves, Diagnostics and controls for temporal structure of the BELLA laser system, *AIP Conf. Proc.*, **1777**(110004) (2016), doi: 10.1063/1.4965693.

[238] P. Poole et al., Experimental capabilities of 0.4 PW, 1 shot/min Scarlet laser facility for high energy density science, *Appl. Opt.*, **55**(17):4713–4719 (2016).

[239] E. Gaul et al., Improved pulse contrast on the Texas Petawatt Laser, *J. Phys. Conf. Ser.*, **717**(012092) (2016), doi: 10.1088/1742-6596/717/1/012092.

[240] E. Cunningham et al., Pulse contrast enhancement via non-collinear sum-frequency generation with the signal and idler of an optical parametric amplifier, *Appl. Phys. Lett.*, **114**(22) (2019), doi: 10.1063/1.5108911.

[241] L. Bradley et al., Comparing temporal contrast measurements taken in the Vulcan front-end and target area petawatt, Technical Report 1, Central Laser Facility STFC Rutherford Appleton Laboratory (2020), url: https://www.clf.stfc.ac.uk/Gallery/35-Bradley.pdf.

[242] C. Danson, D. Neely and D. Hillier, Pulse fidelity in ultra-high-power ( petawatt class ) laser systems, *High Power Laser Sci. Eng.*, **2** (2014), doi: 10.1017/hpl.2014.39.

[243] S. Parker et al., 400 TW operation of Orion at ultra-high contrast, *High Power Laser Sci. Eng.*, **6**(e47):1–6 (2018), doi: 10.1017/hpl.2018.44.

[244] S. M. Wiggins et al., Application programmes at the Scottish Centre for the Application of Plasma-based Accelerators (SCAPA), *Proc. SPIE*, **11036**:28 (2019), doi: 10.1117/12.2520717.

[245] D. Raffestin et al., Enhanced ion acceleration using the high-energy petawatt PETAL laser, *Matter Radiat. Extrem.*, **6**(5) (2021), doi: 10.1063/5.0046679.

[246] S. Karsch, CALA - ATLAS, url: https://www.pulse.physik.uni-muenchen.de/research/high-power/atlas/index.html (Accessed: 2023-03-08).

[247] A. Kessel et al., Relativistic few-cycle pulses with high contrast from picosecond-pumped OPCPA, *Optica*, **5**(4):434 (2018), doi: 10.1364/optica.5.000434.

[248] M. Cerchez et al., ARCTURUS laser: A versatile high-contrast, high-power multi-beam laser system, *High Power Laser Sci. Eng.*, **7**(e37):1–11 (2019), doi: 10.1017/hpl.2019.21.

[249] M. Loeser, Diode-pumped high-energy laser amplifiers for ultrashort laser pulses - The PENELOPE laser system, Ph.D. thesis, Technischen Universität Dresden (2017).

[250] A. Sävert, JETi-200 Laser, url: https://www.physik.uni-jena.de/institute/institut-fuer-optik-und-quantenelektronik/arbeitsgruppen/hochfeldphysik-und-laserbeschleuniger/jeti-200 (Accessed: 2023-03-08).

[251] S. W. Jolly, Spectral Phase Manipulation of Optical Pump Pulses for mJ-Level Narrowband Terahertz Generation in PPLN, Phd, Universität Hamburg (2017).

[252] Thales, Thales Lasers ALPHA 5/XS 200TW, url: https://pdf.directindustry.com/pdf/thales/alpha-5-xs-200-tw/34770-607300.html (Accessed: 2023-03-08).

[253] L. Volpe et al., Generation of high energy laser-driven electron and proton sources with the 200 TW system VEGA 2 at the Centro de Laseres Pulsados, *High Power Laser Sci. Eng.*, **7**:2–7 (2019), doi: 10.1017/hpl.2019.10.

[254] L. A. Gizzi et al., Overview and specifications of laser and target areas at the Intense Laser Irradiation Laboratory, *High Power Laser Sci. Eng.*, **9**(e10) (2021), doi: 10.1017/hpl.2020.47.

[255] S. Simion, CETAL, url: https://cetal.inflpr.ro/newsite/pw_laser (Accessed: 2023-03-08).

[256] J. Novák et al., Dual-output kilohertz pump laser for high-energy picosecond OPCPA, *Opt. Lett.*, **47**(19):4869 (2022), doi: 10.1364/ol.472043.

[257] A. Zymakova et al., First experiments with a water-jet plasma X-ray source driven by the novel high-power-high-repetition rate L1 Allegra laser at ELI Beamlines, *J. Synchrotron Radiat.*, **28**:1778–1785 (2021), doi: 10.1107/S1600577521008729.

[258] T. Green, ELI Beamlines, L2 - Duha, url: https://www.eli-beams.eu/facility/lasers/laser-2-amos-1-pw-20-j-10-hz/ (Accessed: 2023-03-08).

[259] C. Haefner et al., High average power, diode pumped Petawatt laser systems: a new generation of lasers enabling precision science and commercial applications, *Proc. SPIE*, **10241**(June) (2017), doi: 10.1117/12.2281050.

[260] S. Borneis et al., Design, installation and commissioning of the ELI-Beamlines high-power, high-repetition rate HAPLS laser beam transport system to P3, *High Power Laser Sci. Eng.*, **9** (2021), doi: 10.1017/hpl.2021.16.

[261] F. Batysta et al., Spectral pulse shaping of a 5 Hz, multi-joule, broadband optical parametric chirped pulse amplification frontend for a 10 PW laser system, *Opt. Lett.*, **43**(16):3866 (2018), doi: 10.1364/ol.43.003866.

[262] E. Gaul et al., Hybrid OPCPA/Glass 10 PW laser at 1 shot a minute, *2018 Conf. Lasers Electro-Optics, CLEO 2018 - Proc.*, **3**:10–11 (2018).

[263] S. Gales et al., The extreme light infrastructure - Nuclear physics (ELI-NP) facility: New horizons in physics with 10 PW ultra-intense lasers and 20 MeV brilliant gamma beams, *Reports Prog. Phys.*, **81**(9) (2018), doi: 10.1088/1361-6633/aacfe8.

[264] A. Thai et al., High contrast CEP-stable OPCPA front-end for PW-class Ti : Sapphire system, *2016 Conf. Lasers Electro-Optics*, (SM1M.4):16–17 (2016).

[265] S. Kühn et al., The ELI-ALPS facility: The next generation of attosecond sources, *J. Phys. B At. Mol. Opt. Phys.*, **50**(13) (2017), doi: 10.1088/1361-6455/aa6ee8.

[266] J. Zhu et al., Analysis and construction status of SG-II 5PW laser facility, *High Power Laser Sci. Eng.*, **6**:1–13 (2018), doi: 10.1017/hpl.2018.23.

[267] Y. Chu et al., High-contrast 20 Petawatt Ti:sapphire laser system, *Opt. Express*, **21**(24):29231 (2013), doi: 10.1364/oe.21.029231.

[268] L. Yu et al., High-contrast front end based on cascaded XPWG and femtosecond OPA for 10-PW-level Ti:sapphire laser, *Opt. Express*, **26**(3):2625 (2018), doi: 10.1364/oe.26.002625.

[269] X. Zeng et al., Multi-petawatt laser facility fully based on optical parametric chirped-pulse amplification, *Opt. Lett.*, **42**(10):2014 (2017), doi: 10.1364/ol.42.002014.

[270] Q. Zhu et al., The Xingguang-III laser facility: Precise synchronization with femtosecond, picosecond and nanosecond beams, *Laser Phys. Lett.*, **15**(1) (2018), doi: 10.1088/1612-202X/aa94e9.

[271] D. Wang et al., Laser-induced damage thresholds of ultrathin targets and their constraint on laser contrast in laser-driven ion acceleration experiments, *High Power Laser Sci. Eng.*, **8**:1–7 (2020), doi: 10.1017/hpl.2020.40.

[272] Y. Arikawa et al., Ultrahigh-contrast kilojoule-class petawatt LFEX laser using a plasma mirror, *Appl. Opt.*, **55**(25):6850 (2016), doi: 10.1364/ao.55.006850.

[273] S. Fujioka et al., High-energy-density plasmas generation on GEKKO-LFEX laser facility for fast-ignition laser fusion studies and laboratory astrophysics, *Plasma Phys. Control. Fusion*, **54**(12) (2012), doi: 10.1088/0741-3335/54/12/124042.

[274] T. Yabuuchi et al., An experimental platform using high-power, high-intensity optical lasers with the hard X-ray free-electron laser at SACLA, *J. Synchrotron Radiat.*, **26**(2):585–594 (2019), doi: 10.1107/S1600577519000882.

[275] J. Bromage et al., Technology development for ultraintense all-OPCPA systems, *High Power Laser Sci. Eng.*, **7**(e4):1–11 (2019), doi: 10.1017/hpl.2018.64.

[276] J. Bromage et al., MTW-OPAL: A technology development platform for ultra-intense optical parametric chirped-pulse amplification systems, *High Power Laser Sci. Eng.*, **9**(e63) (2021), doi: 10.1017/hpl.2021.45.

[277] X. Wang et al., 13.4fs, 0.1Hz OPCPA Front End for the 100 PW-Class Laser Facility, *Guangxue Xuebao/Acta Opt. Sin.*, **42**(17) (2022), doi: 10.3788/AOS202242.1714001.

[278] B. Shao et al., Broad-bandwidth high-temporal-contrast carrier-envelope-phase-stabilized laser seed for 100 PW lasers, *Opt. Lett.*, **45**(8):2215 (2020), doi: 10.1364/ol.390110.

[279] J. C. Maxwell, A Dynamical Theory of the Electromagnetic Field, *Philos. Trans. R. Soc. London*, **155**(1865):459–512 (1865).

[280] S.-W. Huang, J. Moses and F. X. Kärtner, Broadband noncollinear optical parametric amplification without angularly dispersed idler, *Opt. Lett.*, **37**(14):2796 (2012), doi: 10.1364/ol.37.002796.

[281] B. E. Schmidt et al., Frequency domain optical parametric amplification, *Nat. Commun.*, **5**(May):1–8 (2014), doi: 10.1038/ncomms4643.

# List of abbreviations

| | |
|---|---|
| **AOM** | **A**cousto-**O**ptic **M**odulator |
| **AOPDF** | **A**cousto-**O**ptic **P**rogrammable **D**ispersive **F**ilter |
| **AR** | **A**nti-**R**eflection |
| **ASE** | **A**mplified **S**pontaneous **E**mission |
| **BBO** | $\beta$-**B**arium **BO**rate |
| **$CaF_2$** | **Ca**lcium **F**luoride |
| **CALGO** | **C**alcium **AL**uminum **G**adolinium **O**xide |
| **CFBG** | **C**hirped-**F**iber **B**ragg **G**rating |
| **CPA** | **C**hirped **P**ulse **A**mplification |
| **DFG** | **D**ifference-**F**requency **G**eneration |
| **DKDP** | **D**euterated potassium (german: **K**alium) **D**ihydrogen **P**hosphate |
| **EICHEL** | **E**nhanced **I**ntensity **C**ross-correlator for **H**igh **E**nergy **L**asers |
| **FTL** | **F**ourier-**T**ransform **L**imit |
| **FROG** | **F**requency-**R**esolved **O**ptical **G**ating |
| **FWHM** | **F**ull **W**idth **H**alf **M**aximum |
| **FWM** | **F**our-**W**ave **M**ixing |
| **GDD** | **G**roup-**D**elay **D**ispersion |
| **GTI** | **G**ires-**T**ournois **I**nterferometer |
| **HHG** | **H**igh-**H**armonic **G**eneration |
| **HR** | **H**igh **R**eflectivity |
| **KDP** | potassium (german: **K**alium) **D**ihydrogen **P**hosphate |
| **KGW** | potassium (german: **K**alium) **G**adolinium **T**ungstate (german: **W**olfram) |
| **KTP** | potassium (german: **K**alium) **T**itanyl **P**hosphate |
| **KTA** | potassium (german: **K**alium) **T**itanyl **A**rsenate |
| **LBO** | **L**ithium tri**BO**rate |
| **LIDT** | **L**aser-**I**nduced **D**amage **T**hreshold |
| **$LiNbO_3$** | **L**ithium **N**iobate |
| **MLD** | **M**ultilayer **D**ielectric |
| **MOPA** | **M**aster **O**scillator **P**ower **A**mplifier |
| **Nd** | **Neo**dymium |
| **Nd:glass** | **Neo**dymium-doped **glass** |
| **Nd:YAG** | **Neo**dymium-doped YAG |
| **NER** | **N**onlinear **E**llipse **R**otation |
| **NLFF** | **N**on**L**inear **F**ourier **F**iltering |
| **OPA** | **O**ptical **P**arametric **A**mplification |
| **OPCPA** | **O**ptical **P**arametric **C**hirped **P**ulse **A**mplification |
| **OR** | **O**ptical **R**ectification |
| **PC** | **P**ockels **C**ell |
| **PCF** | **P**hotonic **C**rystal **F**iber |

| | |
|---|---|
| **PD** | **P**hoto **D**iode |
| **PEnELOPE** | **P**etawatt **EN**ergy-**E**fficient **L**aser for **O**ptical **P**lasma **E**xperiments |
| **PETAL** | **PET**awatt **A**quitaine **L**aser |
| **PHELIX** | **P**etawatt **H**igh-**E**nergy **L**aser for heavy **I**on e**X**periments |
| **PSF** | **P**arametric **S**uper**F**luorescence |
| **PtV** | **P**eak-**t**o-**V**alley |
| **rms** | **R**oot **M**ean **S**quare |
| **SD** | **S**elf **D**iffraction |
| **SEPPL** | **S**eeded **E**xperimental **P**ulsed **P**robe **L**aser |
| **SFG** | **S**um-**F**requency **G**eneration |
| **SHG** | **S**econd-**H**armonic **G**eneration |
| **SLM** | **S**patial **L**ight **M**odulator |
| **SNLO** | **S**elect **N**on-**L**inear **O**ptics |
| **SPIDER** | **S**pectral **P**hase **I**nterferometry for **D**irect **E**lectric-field **R**econstruction |
| **SPM** | **S**elf-**P**hase **M**odulation |
| **SRSI** | **S**elf-**R**eferenced **S**pectral **I**nterferometry |
| **STC** | **S**patio-**T**emporal **C**oupling |
| **Ti:Sa** | **Ti**tanium-doped **Sa**pphire |
| **TNSA** | **T**arget **N**ormal **S**heath **A**cceleration |
| **TWM** | **T**hree-**W**ave **M**ixing |
| **uOPA** | **u**ltrafast **O**ptical **P**arametric **A**mplification |
| **WP** | **W**ave **P**late |
| **XPM** | cross (**X**) **P**hase **M**odulation |
| **XPW** | cross (**X**) **P**olarized **W**ave generation |
| **Yb** | **Y**tter**b**ium |
| **Yb:YAG** | **Y**tter**b**ium-doped **YAG** |
| **Yb:KGW** | **Y**tter**b**ium-doped **KGW** |
| **Yb:$CaF_2$** | **Y**tter**b**ium-doped **$CaF_2$** |
| **YAG** | **Y**ttrium **A**luminum **G**arnet |
| **YLF** | **Y**ttrium **L**ithium **F**luoride |
| **YVO** | **Y**ttrium **V**anadium **O**xide |

# List of publications


[1] Witold Cayzac, A. Frank, A. Ortner, V. Bagnoud, M. M. Basko, S. Bedacht, C. Bläser, A. Blažević, S. Busold, O. Deppert, J. Ding, M. Ehret, P. Fiala, S. Frydrych, D. O. Gericke, L. Hallo, J. Helfrich, D. Jahn, E. Kjartansson, A. Knetsch, D. Kraus, G. Malka, N. W. Neumann, K. Pépitone, D. Pepler, S. Sander, G. Schaumann, T. Schlegel, N. Schroeter, D. Schumacher, M. Seibert, An Tauschwitz, J. Vorberger, F. Wagner, S. Weih, **Y. Zobus** and M. Roth, Experimental discrimination of ion stopping models near the Bragg peak in highly ionized matter, *Nat. Commun.*, **8**:1–7 (2017), doi: 10.1038/ncomms15693.

[2] J. Hornung, **Y. Zobus**, P. Boller, C. Brabetz, U. Eisenbarth, J. B. Ohland, M. Zepf, B. Zielbauer and V. Bagnoud, Enhancement of the laser-driven proton source at PHELIX, *High Power Laser Sci. Eng.*, **8**(e24):1–8 (2020), doi: 10.1017/hpl.2020.23.

[3] J. B. Ohland, **Y. Zobus**, U. Eisenbarth, B. Zielbauer, D. Reemts and V. Bagnoud, Alignment procedure for off-axis-parabolic telescopes in the context of high-intensity laser beam transport, **29**(21):34378–34393 (2021).

[4] J. Hornung, **Y. Zobus**, S. Roeder, A. Kleinschmidt, D. Bertini, M. Zepf and V. Bagnoud, Time-resolved study of holeboring in realistic experimental conditions, *Nat. Commun.*, **12**(6999):1–7 (2021), doi: 10.1038/s41467-021-27363-9.

[5] J. B. Ohland, U. Eisenbarth, B. Zielbauer, **Y. Zobus**, D. Posor, J. Hornung, D. Reemts and V. Bagnoud, Ultra-compact post-compressor on-shot wavefront measurement for beam correction at PHELIX, *High Power Laser Sci. Eng.*, **10**:1–9 (2022), doi: 10.1017/hpl.2022.9.

[6] Simon Roeder, **Y. Zobus**, Christian Brabetz and Vincent Bagnoud, How the laser beam size conditions the temporal contrast in pulse stretchers of CPA lasers, *High Power Laser Sci. Eng.*, pages 1–8 (2022).

[7] **Y. Zobus**, C. Brabetz, M. Loeser, D. Albach, M. Siebold and V. Bagnoud, Versatile , compact chirped pulse amplifier pump system for ultrafast optical parametric amplifiers, *Opt. Express*, **31**(3):5002–5015 (2023).

[8] **Y. Zobus**, C. Brabetz, J. Hornung, J. B. Ohland, D. Reemts, JP Zou, M. Loeser, D. Albach, U. Schramm and V. Bagnoud, Millijoule Ultrafast Optical Parametric Amplification as Replacement for High-Gain Regenerative Amplifiers, *High Power Laser Sci. Eng. (accepted, to be publ.)* (2023), doi: 10.1017/hpl.2023.30.

[9] J. Hornung, **Y. Zobus**., H. Lorente, C. Brabetz and V. Bagnoud, Synchronized Off-Harmonic Probe Beam with Variable Pulse Duration for Laser-Plasma Interaction Experiments at PHELIX, *in preparation*.

# A. Appendix

## A.1. Contrast-enhancing strategies at various laser facilities

In this section, I intend to provide an overview of the contrast enhancement methods used in multi-TW and PW-class lasers worldwide. This is only a snapshot view of the current contrast-strategy implementations and I do not claim this overview to be exhaustive.

Table A.1.: Front-end (FE) and post main amplification and compression (PComp) contrast-enhancement strategies (CES) in various multi-TW and PW-class laser facilities and achieved ASE contrast in orders of magnitude. ASE contrast: FE only, FE & PComp. Asterisk: implementation planned/estimated contrast. Slash: CES not used simultaneously. SP-OPA: short-pulse OPA, XPW: cross-polarized-wave generation, SHG: second harmonic generation, PM: plasma mirror, SFG: sum-frequency generation, SA: saturable absorber, LG-OPA: low-gain OPA.

| Laser facility | FE CES | PComp CES | ASE Contrast |
|---|---|---|---|
| **Titan** [233] | - | SHG | 5, 10 |
| **OMEGA-EP** [62] | SP-OPA | - | 9.5 |
| **Z-Petawatt** [234] | SP-OPA | - | 10 |
| **ALEPH** [235] | - | SHG | 5.7, 12 |
| **Bella iP2** [236] | XPW | PM | 14 |
| **Bella** [237] | XPW | - | >9 |
| **Scarlet** [238] | XPW | - | >10 |
| **Hercules** [133] | XPW | PM | 11, 15 |
| **Texas PW** [239] | SP-OPA | - | 8.7 |
| **MEC** [240] | SP-OPA & SFG | - | >12 |
| **Vulcan** [241] | SP-OPA | - | 10 |
| **Astra-Gemini** [242] | - | PM | 12 |
| **Orion** [243] | SP-OPA | SHG | 9, 18 |
| **SCAPA** [244] | XPW | *PM | 10, - |
| **PETAL** [245] | - | - | 7 |
| **Apollon** [32] | XPW & SP-OPA | - | 12 |

Continued on next page

Table A.1.: Continued

| Laser facility | FE CES | PComp CES | ASE Contrast |
|---|---|---|---|
| **ATLAS 3000** [246] | XPW & SP-OPA | - | 10 |
| **PFS** [247] | XPW & SP-OPA | - | >11 |
| **Arcturus** [248] | XPW & SA | PM | 11, 13 |
| **PHELIX** [167] | SP-OPA | - | 12 |
| **POLARIS** [135] | XPW | SHG | >12, 17 |
| **PEnELOPE** [249] | *XPW/*SP-OPA | - | 9 |
| **DRACO** [37] | XPW | PM | 13, 14.5 |
| **Jeti200** [250] | XPW | PM | -, 13 |
| **ANGUS** [251, 252] | XPW | - | 10 |
| **VEGA** [253] | XPW | - | 10 |
| **ILIL** [254] | SA | - | 9 |
| **CETAL** [255] | XPW | - | 10 |
| **ELI-B, Allegra** [256, 257] | SP-OPA | - | 9 |
| **ELI-B, DUHA** [258] | SP-OPA | - | *10 |
| **ELI-B, HAPLS** [259, 260] | XPW | *PM | 9-11, n.a. |
| **ELI-B, ATON** [261, 262] | SP-OPA & LG-OPA | - | >8 |
| **ELI-NP, HPLS** [263] | XPW & SP-OPA | PM | 13, n.a. |
| **ELI-ALPS, HF-PW** [264, 265] | SP-OPA & SHG | - | >12 |
| **SG-II** [266] | - | - | >6 |
| **Qiangguang** [267] | XPW | - | 11 |
| **SULF** [268] | XPW & SP-OPA | - | >11 |
| **CAEP-PW /Silex-II** [269] | SP-OPA | - | 10 |
| **XG-III** [270] | XPW/SP-OPA | - | 9/8 |
| **CLAPA** [271] | XPW | - | >11 |
| **LFEX** [272, 273] | SA | PM | 9, 11 |
| **J-KAREN** [30] | SA | *PM | 12, n.a. |
| **SACLA** [274] | XPW | - | >11 |
| **CoReLS** [31, 134] | XPW | PM | 12, 17 |
| **MTW OPAL** [275, 276] | SP-OPA | PM | >10*, n.a. |
| **SEL-100 PW** [277, 278] | SP-OPA & SHG | - | >10 |

## A.2. Power of amplified spontaneous emission in a multi-pass amplifier

To estimate the emitted power of **A**mplified **S**pontaneous **E**mission (ASE) in a multi-pass amplifier, the power of the spontaneously emitted fluorescence must be determined first. The spontaneous emission depends on the decay rate of the upper laser level, which is described as [218]:

$$\frac{dn}{dt} = -\frac{n(t)}{\tau}, \tag{A.1}$$

with the number of electrons in the upper laser level per unit volume $n(t)$ and the radiation lifetime $\tau$. As the change of $n(t)$ describes the number of photons that are emitted from a unit volume, the power of the emitted fluorescence can be written as:

$$P_{fl} = \frac{dE_{fl}}{dt} = -\hbar\omega\frac{dn}{dt}dV = \hbar\omega\frac{n(t)}{\tau}dV, \tag{A.2}$$

with the energy of the photon $\hbar\omega$ and the total energy of the emitted fluorescence $E_f$. Using the definition of the small-signal gain $g_0$ [57]:

$$g_0 = (1-L)e^{(\sigma_{abs}+\sigma_{em})nd}, \tag{A.3}$$

with the material thickness $d$, the emission and absorption cross-sections $\sigma_{em}$ and $\sigma_{abs}$ and potential losses $L$, the population inversion $n(t)$ in eq. A.2 can be replaced by $n$ if a timescale $t << \tau$ is considered.

Inserting $n$ into eq. A.2 and integration over the pump volume $V = d \cdot A$, with the pump area $A$, leads to:

$$P_{fl}^{(1)} = \frac{\hbar\omega}{(\sigma_{em}+\sigma_{abs})\tau}A\ln\left(\frac{g_0}{1-L}\right) = I_{sat}A\ln\left(\frac{g_0}{1-L}\right), \tag{A.4}$$

where $I_{sat}$ is the saturation intensity of the material and $P_{fl}^{(1)}$ the power of the fluorescence after the first pass [57]. To account for amplifier-specific configurations, the correction factors $K_{\Delta\omega}$, $K_p$ and $K_{\Delta\Omega}$, which describe the spectral, polarization and angular acceptance, must be included. To further simplify the description, frequency-averaged values within the accepted bandwidth for the small-signal gain $\bar{g}_0$, the saturation intensity $\bar{I}_{sat}$ and the losses $\bar{L}$ may be assumed. This results in:

$$P_{fl}^{(1)} = \bar{I}_{sat}A\ln\left(\frac{\bar{g}_0}{1-\bar{L}}\right)\cdot K_{\Delta\omega}K_pK_{\Delta\Omega}. \tag{A.5}$$

If the gain per pass in a multi-pass amplifier is assumed to be the small-signal gain $\bar{g}_0$, the total accumulated power of amplified spontaneous emission after n passes can be estimated to [56]:

$$P_{ASE} = \sum_{m=0}^{n-1}{\bar{g}_0}^m \cdot P_{fl}^{(1)} = {\bar{g}_0}^{n-1}\sum_{m=0}^{n-1}\frac{1}{{\bar{g}_0}^{n-m-1}}\cdot P_{fl}^{(1)} = {\bar{g}_0}^{n-1}\sum_{m=0}^{n-1}\frac{1}{{\bar{g}_0}^m}\cdot P_{fl}^{(1)} \tag{A.6}$$

$$\approx {\bar{g}_0}^{n-1}\cdot\frac{P_{fl}^{(1)}}{1-1/\bar{g}_0} = {\bar{g}_0}^n\cdot\frac{P_{fl}^{(1)}}{\bar{g}_0-1}. \tag{A.7}$$

In the last step, the sum was approximated by the limit of a geometric series, as ${\bar{g}_0}^{-1} < 1$ for amplification.

## A.3. Derivation of the coupled-wave equations for monochromatic waves

Here, I will derive the coupled wave equations for monochromatic, plane waves and the analytic solution for a non-depleting pump.

We start with the nonlinear response of a medium that can be described by a Taylor series of the dielectric polarization density $\mathbf{P}(t)$ with [66]

$$\mathbf{P}(t) = \varepsilon_0 \left( \chi^{(1)}\mathbf{E}(t) + \chi^{(2)}\mathbf{E}^2(t) + \chi^{(3)}\mathbf{E}^3(t) + \cdots \right) = \mathbf{P}^{(1)}(t) + \mathbf{P}^{(2)}(t) + \mathbf{P}^{(3)}(t) + \cdots = \mathbf{P}_L(t) + \mathbf{P}_{NL}(t) \tag{A.8}$$

Here, $\varepsilon_0$ is the vacuum permittivity, $\chi^{(n)}$ the electric susceptibility of the order n and $\mathbf{E}(t)$ the electric field. $P_L$ and $P_{NL}$ refer to the linear and nonlinear terms of the polarization, respectively. Of particular importance for the **O**ptical **P**arametric **A**mplification (OPA) process is the second term of the polarization Taylor series, the second-order nonlinear polarization $\chi^{(2)}$. Given a medium that solely exhibits a second-order nonlinear polarization and an electric field with two frequency components $\omega_1$ and $\omega_2$, the following fields result:

$$\begin{aligned}
\mathbf{P}(t) \quad &= 2\varepsilon_0 d_{eff}\mathbf{E}(t)^2 = \frac{\varepsilon_0}{2} d_{eff} \left( \mathbf{E_1} e^{-j\omega_1 t} + \mathbf{E_2} e^{-j\omega_2 t} + c.c. \right)^2 \\
&= \frac{\varepsilon_0}{2} d_{eff} ( \mathbf{E_1^2} e^{-2j\omega_1 t} && \rightarrow SHG \\
&\quad + \mathbf{E_2^2} e^{-2j\omega_2 t} && \rightarrow SHG \\
&\quad + 2\mathbf{E_1}\mathbf{E_2} e^{-j(\omega_1+\omega_2)t} && \rightarrow SFG \\
&\quad + 2\mathbf{E_1}\mathbf{E_2^*} e^{-j(\omega_1-\omega_2)t} && \rightarrow DFG \\
&\quad + |\mathbf{E_1}|^2 + |\mathbf{E_2}|^2 && \rightarrow OR \\
&\quad + c.c.).
\end{aligned} \tag{A.9}$$

Here, $j$ is the imaginary unit and $d_{eff}$ is an effective scalar value, which represents the second-order electric susceptibility [66]. From eq. A.9, four mixing processes can be identified: **S**econd-**H**armonic **G**eneration (SHG), **S**um-**F**requency **G**eneration (SFG), **D**ifference-**F**requency **G**eneration (DFG) and **O**ptical **R**ectification (OR) of which DFG is the basis for OPA. To create a better understanding of how this process works and which factors impact the interplay between pump, signal and idler, the next section treats the analytical description of the **T**hree-**W**ave **M**ixing (TWM) process for OPA. A reasonable starting point for this description is the scalar wave-equation [66], derived from the Maxwell equations [279], which describes the evolution of the electric field

$$\nabla^2 E(x,y,z,t) - \frac{1}{c_0^2}\frac{\partial^2}{\partial t^2}\left( E(x,y,z,t) + \frac{1}{\varepsilon_0} P^{(1)}(x,y,z,t) \right) = \mu_0 \frac{\partial^2 P^{(2)}(x,y,z,t)}{\partial t^2} \tag{A.10}$$

$$\frac{\partial^2 E(z,t)}{\partial z^2} - \frac{n^2}{c_0^2}\frac{\partial^2 E(z,t)}{\partial t^2} = \frac{2d_{eff}}{c_0^2}\frac{\partial^2 E(z,t)^2}{\partial t^2}, \tag{A.11}$$

where $\mu_0$ is the vacuum permeability, $c_0$ the vacuum speed of light and $n$ the refractive index. In general, higher orders of the nonlinear polarization can also influence the evolution, but for the sake of simplicity, these are discarded to isolate the influence of the second-order polarization.

From eq. A.10 to eq. A.11, I discarded the x- and y- dependency of the fields by assuming a plane-wave and used the relation that $1 + \chi^{(1)}(\omega) = \varepsilon^{(1)}(\omega) = n(\omega)^2$ [66]. If we insert a field, consisting of

monochromatic waves with three distinct frequency components $\omega_{p,s,i}$, that fulfill the energy conservation as in eq. 3.1 and split the field into a slowly varying amplitude over z and a rapid oscillatory part such that [142]

$$E(z,t) = \frac{1}{2}\left(\sum_{m=[p,s,i]} A_m(z)e^{j\omega_m t - jk_m z} + c.c.\right), \tag{A.12}$$

with $k_m = \omega_m n_m / c_0$ being the wave-number of the m-th frequency component, the terms on the left-hand side of eq. A.11 result in:

$$\frac{\partial^2 E(z,t)}{\partial z^2} = \frac{1}{2}\left(\sum_{m=[p,s,i]} \left[\frac{\partial^2 A_m(z)}{\partial z^2} - k_m^2 - 2jk_m\frac{\partial A_m(z)}{\partial z}\right] e^{j\omega_m t - jk_m z} + c.c.\right) \tag{A.13}$$

$$\frac{\partial^2 E(z,t)}{\partial t^2} = \frac{1}{2}\left(\sum_{m=[p,s,i]} \left[-\omega_m^2 A_m(z)\right] e^{j\omega_m t - jk_m z} + c.c.\right). \tag{A.14}$$

$$\tag{A.15}$$

The nonlinear polarization term of eq. A.10 results in a bunch of mixing products, similar to that of eq. A.9. To get a closer look into the mechanism of OPA, only the components which result in the frequencies $\omega_{p,s,i}$ are kept, which reduces the term for the second derivative of the nonlinear polarization to:

$$\begin{aligned}\frac{\partial^2 P^{(2)}(z,t)}{\partial t^2} = &-\frac{\omega_s^2 d_{eff}}{c_0^2} A_p(z)A_i^*(z)e^{j\omega_s t - j(k_p - k_i)z} \\ &-\frac{\omega_i^2 d_{eff}}{c_0^2} A_p(z)A_s^*(z)e^{j\omega_i t - j(k_p - k_s)z} \\ &-\frac{\omega_p^2 d_{eff}}{c_0^2} A_s(z)A_i(z)e^{j\omega_p t - j(k_s + k_i)z} + c.c..\end{aligned} \tag{A.16}$$

As eq. A.16 describes a source term for the electric fields, it is evident, that inside a nonlinear medium, the electric fields at the frequency of the signal are created by the nonlinear coupling of the idler and pump fields and vice versa. If we insert this and eqs. A.13 and A.14 into eq. A.11, use the slowly varying envelope approximation [147]

$$\left|\frac{\partial^2 A(z)}{\partial z^2}\right| \ll 2k\left|\frac{\partial A(z)}{\partial z}\right|, \tag{A.17}$$

which allows us to neglect the second-order derivative in z, and solve for the left part of the equation we can determine the coupled equations which describe the TWM-process for three monochromatic waves:

$$\text{signal} \quad \rightarrow \quad \frac{\partial A_s(z)}{\partial z} = -\frac{j\omega_s d_{eff}}{n_s c_0} A_p(z)A_i^*(z)e^{-j\Delta kz} \tag{A.18}$$

$$\text{idler} \quad \rightarrow \quad \frac{\partial A_i(z)}{\partial z} = -\frac{j\omega_i d_{eff}}{n_i c_0} A_p(z)A_s^*(z)e^{-j\Delta kz} \tag{A.19}$$

$$\text{pump} \quad \rightarrow \quad \frac{\partial A_p(z)}{\partial z} = -\frac{j\omega_p d_{eff}}{n_p c_0} A_s(z)A_i(z)e^{j\Delta kz}. \tag{A.20}$$

These equations describe the interplay of the mixing of three monochromatic, plane waves. Furthermore, I introduced an important parameter, which is the wave-vector mismatch, also called phase mismatch:

$$\Delta k = k_p - k_s - k_i. \tag{A.21}$$

This parameter describes the phase relation between the created wave and the nonlinear polarization. For $\Delta k = 0$ this relation stays fixed, which results in the most efficient energy transfer between the three fields. The coupled equations can simply be solved in a numerical manner. However, if we assume a large discrepancy in field strength between pump- and signal fields, which is common in OPA, we can neglect the change of the pump field, such that $A_p(z) = const. = A_p$ and therefore $\frac{\partial^2 A_p(z)}{\partial z} = 0$, and further assume that $A_i(0) = 0$, which is mostly the case for OPA, the coupled equations can be solved analytically. Applying these approximations and building the second derivative of eq. A.18 and A.19 with respect to z results in:

$$\begin{aligned} \frac{\partial^2 A_{s,i}(z)}{\partial z^2} = \gamma^2 \cdot A_{s,i}(z) - j\Delta k \frac{\partial A_{s,i}(z)}{\partial z} \qquad & \text{with} \qquad \gamma^2 = \frac{2\omega_s \omega_i d_{eff}^2}{c^3 n_s n_i n_p \varepsilon_0} I_p \\ & \text{and} \qquad I_p = \frac{1}{2} n_p c_0 \varepsilon_0 \left|A_p\right|^2, \end{aligned} \tag{A.22}$$

with $I_p$ being the intensity of the pump. This sets up a linear, homogeneous second-order differential equation, which can be solved with an exponential ansatz, such that we get the following solution for the signal and idler fields:

$$A_s(z) = A_{s,0} e^{-\frac{j\Delta k}{2} z} \left( \frac{j\Delta k}{2g} \sinh(gz) + \cosh(gz) \right) \tag{A.23}$$

$$A_i(z) = A_{s,0} A_p \cdot \frac{-j\omega_i d_{eff}}{g n_i c_0} \cdot \sinh(gz) \tag{A.24}$$

$$\text{with} \qquad g = \sqrt{\gamma^2 - \frac{\Delta k^2}{4}}. \tag{A.25}$$

Here, I introduced the parameter g, the small-signal gain of the OPA [142], and the initial condition of $A_s(z = 0) = A_{s,0}$ and $A_i(z = 0) = 0$ were used. Taking the square of the absolute value of the solution for the fields and using the definition of the intensity from eq. A.22, the intensity of the idler and signal as a function of the propagation distance z in the non-depleting-pump regime can be isolated

$$I_s(z) = I_s(0) \left[ 1 + \left( \frac{\gamma}{g} \sinh(gz) \right)^2 \right] = I_s(0) \cdot G_{par}(z) \tag{A.26}$$

$$I_i(z) = I_s(0) \frac{\omega_i}{\omega_s} \left( \frac{\gamma}{g} \sinh(gz) \right)^2. \tag{A.27}$$

where $G_{par}(z)$ is the parametric gain.

## A.4. Derivation of the coupled-wave equations for short pulses

The coupled-wave equations, derived in sec. A.3 are only valid for monochromatic and plane waves. However, if realistic pulses should be described, the equations must account for dispersive and diffractive

effects, which were neglected before. The derivation and argumentation follow the description of [66]. To include diffractive, effects, we discard the approximation of a plane wave, which allowed us to exchange the nabla operator by a simple derivative by z, and start at:

$$\nabla^2 E(x,y,z,t) - \frac{n^2}{c_0^2}\frac{\partial^2 E(x,y,z,t)}{\partial t^2} = \frac{1}{\varepsilon_0 c_0^2}\frac{\partial^2 P^{(2)}(x,y,z,t)}{\partial t^2}. \tag{A.28}$$

To account for the dispersive effects during propagation, the equations must be capable of describing broadband pulses and the amplitude must exhibit a time dependency. Accordingly, a description of the electric field via:

$$E(x,y,z,t) = \frac{1}{2}\left(A(x,y,z,t)e^{j(k_0 z-\omega_0 t)} + c.c.\right) \tag{A.29}$$

$$\tilde{E}\,(x,y,z,\omega) = \frac{1}{\sqrt{2\pi}}\int_{-\infty}^{\infty} E(x,y,z,t)e^{i\omega t}dt \tag{A.30}$$

$$\tilde{A}\ (x,y,z,\omega) = \frac{1}{\sqrt{2\pi}}\int_{-\infty}^{\infty} A(x,y,z,t)e^{i\omega t}dt \tag{A.31}$$

$$\tilde{P}\,(x,y,z,\omega) = \frac{1}{\sqrt{2\pi}}\int_{-\infty}^{\infty} P_{NL}(x,y,z,t)e^{i\omega t}dt. \tag{A.32}$$

Here, $\tilde{E}(x,y,z,\omega)$ refers to the Fourier transform of the temporal electric field, $\omega_0$ is the carrier frequency and $k_0$ is the wave number of the carrier frequency. For the sake of readability, the $c.c.$ andthe x,y,z and t or $\omega$ dependencies are dropped from here on. Transforming to the spectral Fourier domain, the wave equation results in:

$$\nabla^2\tilde{E} + \frac{n^2\omega^2}{c_0^2}\tilde{E} = \frac{\omega^2}{\varepsilon_0 c_0^2}\tilde{P}_{NL} \tag{A.33}$$

and inserting the definition for the electric field, we get:

$$\nabla_\perp^2\tilde{A} + \frac{\partial\tilde{A}}{\partial z^2}^2 + 2jk_0\frac{\partial\tilde{A}}{\partial z} + \left[k(\omega)^2 - k_0^2\right]\tilde{A} = \frac{\omega^2}{\varepsilon_0 c_0^2}\tilde{P}_{NL}e^{-jk_0 z}. \tag{A.34}$$

Here, $\nabla_\perp$ is the transversal nabla operator. By approximation of $k(\omega)$ as a Taylor series, the square of $k(\omega)$ can be approximated by:

$$k(\omega)^2 = (k_0 + k_k^{(1)}(\omega-\omega_0) + \tilde{D})^2 \tag{A.35}$$

$$\approx k_0^2 + 2k_0k^{(1)}(\omega-\omega_0) + 2k_0\tilde{D} + 2k^{(1)}\tilde{D}(\omega-\omega_0) + \left(k^{(1)}(\omega-\omega_0)\right)^2, \tag{A.36}$$

with $k^{(n)}$ being the n-th derivative of $k$ by $\omega$ and $\tilde{D}$ the Taylor series starting at n=2. In eq. A.36, the term $\tilde{D}^2$ was dropped, because it is reasonably small. Inserting eq. A.36 into eq. A.34, applying the slowly-varying envelope approximation and transforming back to the temporal domain by multiplying with $e^{-j(\omega-\omega_0)t}$ and integrating over $\omega-\omega_0$, we get:

$$\left[\nabla_\perp^2 + 2jk_0\left[\frac{\partial}{\partial z} + k^{(1)}\frac{\partial}{\partial t}\right] + 2jk^{(1)}D\frac{\partial}{\partial t} + 2k_0D\right]A = \frac{1}{\varepsilon_0 c_0^2}\frac{\partial^2 P_{NL}}{\partial t^2}e^{-j(k_0 z-\omega_0 t)} \tag{A.37}$$

Here, the differential operator $D$ is defined as:

$$D = \sum_{n=2}^{\infty} \frac{1}{n!} k^{(n)} (j\frac{\partial}{\partial t})^n. \tag{A.38}$$

By representing the nonlinear polarization terms as slowly varying amplitude, similar to eq. A.29 as:

$$P_{NL}(x,y,z,t) = p_{NL}(x,y,z,t) e^{j(k_0 z - \omega_0 t)}, \tag{A.39}$$

the second derivative results in:

$$\frac{\partial^2 P_{NL}}{\partial t^2} = \frac{\partial}{\partial t}\left(-j\omega_0 \left[\left(1 + \frac{j}{\omega_0}\frac{\partial}{\partial t}\right) p_{NL}\right] e^{j(k_0 z - \omega_0 t)}\right) = -\omega_0^2 \left[\left(1 + \frac{j}{\omega_0}\frac{\partial}{\partial t}\right)^2 p_{NL}\right] e^{j(k_0 z - \omega_0 t)}. \tag{A.40}$$

Inserting this result into eq. A.37, we get:

$$\left(\nabla_\perp^2 + 2jk_0 \left[\frac{\partial}{\partial z} + k^{(1)}\frac{\partial}{\partial t} - jD\left(1 + \frac{jk^{(1)}}{k_0}\frac{\partial}{\partial t}\right)\right]\right) A = -\frac{\omega_0^2}{\varepsilon_0 c_0^2}\left[\left(1 + \frac{j}{\omega_0}\frac{\partial}{\partial t}\right)^2 p_{NL}\right] \tag{A.41}$$

In this equation, the terms within the parenthesis $\frac{jk^{(1)}}{k_0}\frac{\partial}{\partial t}$ and $\frac{j}{\omega_0}\frac{\partial}{\partial t}$ are especially relevant, if pulses in the single-cycle regime are discussed, which also means, that the pulses feature large spectral bandwidths. For such pulses, these terms are relevant, as they describe effects like self-steepening and the different diffractive properties of each frequency component. However, regarding pulses that are not close to the single-cycle regime, these terms are typically neglected, as they are small compared to unity. Using this approximation, as well as discarding all terms of $D$, except for n=2 and identifying $k^{(1)}$ as the group velocity $v_g^{-1}$ and $k^{(2)}$ as the group-velocity dispersion $GVD$, this further simplifies eq. A.41 to:

$$\left(\nabla_\perp^2 + 2jk_0\left[\frac{\partial}{\partial z} + \frac{1}{v_g}\frac{\partial}{\partial t} + \frac{j\cdot GVD}{2}\frac{\partial^2}{\partial t^2}\right]\right) A = -\frac{\omega_0^2}{\varepsilon_0 c_0^2} p_{NL} \tag{A.42}$$

Finally, if we insert an electric field, consisting of signal, idler and pump, and sort the equation, such that the center frequencies of the mixing products match with those of the inserted fields, the coupled wave-mixing equations are:

$$\text{signal} \quad \rightarrow \quad \left(\frac{\partial}{\partial z} + \frac{1}{v_{g,s}}\frac{\partial}{\partial t} + j\frac{GVD_s}{2}\frac{\partial^2}{\partial t^2}\right) A_s - \frac{j}{2k_s}\nabla_\perp^2 A_s \quad = -j\sigma_s A_p A_i^* e^{-j\Delta k z} \tag{A.43}$$

$$\text{idler} \quad \rightarrow \quad \left(\frac{\partial}{\partial z} + \frac{1}{v_{g,i}}\frac{\partial}{\partial t} + j\frac{GVD_i}{2}\frac{\partial^2}{\partial t^2}\right) A_i - \frac{j}{2k_i}\nabla_\perp^2 A_i \quad = -j\sigma_i A_p A_s^* e^{-j\Delta k z} \tag{A.44}$$

$$\text{pump} \quad \rightarrow \quad \left(\frac{\partial}{\partial z} + \frac{1}{v_{g,p}}\frac{\partial}{\partial t} + j\frac{GVD_p}{2}\frac{\partial^2}{\partial t^2}\right) A_p - \frac{j}{2k_p}\nabla_\perp^2 A_p \quad = -j\sigma_p A_s A_i e^{j\Delta k z}., \tag{A.45}$$

$$\text{with} \qquad \sigma_{s,i,p} = \frac{\omega_{s,i,p} d_{eff}}{n_{s,i,p} c_0} \qquad . \tag{A.46}$$

If the fields feature a Gaussian beam shape and the propagation distance z is significantly smaller than the Rayleigh length of the beam, the diffraction term $\nabla_\perp$ can usually be neglected.

## A.5. Derivation of the broadband phase-matching condition

Here, I will derive the condition to achieve broad-band phase matching in a non-collinear OPA setup.

Starting from the phase mismatch in vector form:

$$\Delta\vec{k} = \vec{k}_p - \vec{k}_s - \vec{k}_i = \Delta\vec{k}_{\parallel} + \Delta\vec{k}_{\perp} \tag{A.47}$$

$$\Delta\vec{k}_{\parallel} = \vec{k}_p - \vec{k}_{s\parallel} - \vec{k}_{i\parallel} \tag{A.48}$$

$$\Delta\vec{k}_{\perp} = \vec{k}_{s\perp} + \vec{k}_{i\perp}. \tag{A.49}$$

where $k_{p,s,i} = |\vec{k}_{p,s,i}|$. The phase mismatch is split up into parts, which are parallel and perpendicular to the propagation direction of the pump. These parts can be represented as scalars:

$$\Delta k_{\parallel} = k_p - k_s\cos(\alpha) - k_i\cos(\delta) \tag{A.50}$$

$$\Delta k_{\perp} = k_s\sin(\alpha) - k_i\sin(\delta). \tag{A.51}$$

Similar to the collinear configuration, a phase-matching angle, that minimizes $\Delta k$, can be found. To see how the phase mismatch varies in a frequency domain in which the center frequency is perfectly phase-matched, it is reasonable to expand the phase mismatch into a Taylor series [142]:

$$\Delta k(\omega) = \Delta k^{(0)} + \Delta k^{(1)}(\omega-\omega_0) + \frac{1}{2}\Delta k^{(2)}(\omega-\omega_0)^2 + \cdots \tag{A.52}$$

$$= \Delta k^{(0)} + \frac{\partial\Delta k}{\partial\omega}(\omega-\omega_0) + \frac{1}{2}\frac{\partial^2\Delta k}{\partial\omega^2}(\omega-\omega_0)^2 + \cdots. \tag{A.53}$$

This expansion emphasizes, that even if phase matching is achieved at $\omega = \omega_0$, it is generally not for the surrounding frequencies. In order to achieve broader phase matching the Taylor coefficients have to be minimized. This can be done by adding an additional degree of freedom, for example, the non-collinear angle $\alpha$. Calculating the first derivative of eq. A.50 and A.51 and set them to zero results in:

$$0 \stackrel{!}{=} \Delta k_{\parallel}^{(1)} = \frac{\partial k_p}{\partial\omega} - \cos(\alpha)\frac{\partial k_s}{\partial\omega} - \cos(\delta)\frac{\partial k_i}{\partial\omega} + \sin(\delta)k_i\frac{\partial\delta}{\partial\omega} \tag{A.54}$$

$$0 \stackrel{!}{=} \Delta k_{\perp}^{(1)} = \qquad \sin(\alpha)\frac{\partial k_s}{\partial\omega} - \sin(\delta)\frac{\partial k_i}{\partial\omega} - \cos(\delta)k_i\frac{\partial\delta}{\partial\omega}. \tag{A.55}$$

Combining these equations by addition, whereas eq. A.54 is multiplied by $\cos(\delta)$ and eq. A.55 by $\sin(\delta)$, the angle-derivatives vanish:

$$0 \stackrel{!}{=} \Delta k_{\parallel}^{(1)}\cos(\delta) + \Delta k_{\perp}^{(1)}\sin(\delta) \tag{A.56}$$

$$= \frac{\partial k_s}{\partial\omega}\left[\sin(\alpha)\sin(\delta) - \cos(\alpha)\cos(\delta)\right] - \frac{\partial k_i}{\partial\omega}\left[\sin(\delta)^2 + \cos(\delta)^2\right] \tag{A.57}$$

$$= \frac{\partial k_s}{\partial\omega}\cos(\alpha+\delta) - \frac{\partial k_i}{\partial\omega}. \tag{A.58}$$

The partial derivatives of k by $\omega$ can be identified as the group velocity $v_g$ of the propagating pulse and also the sum of angles $\alpha + \delta$ which is the angle between idler and signal. This is shown in eq. A.59:

$$v_{g,s} = v_{g,i} \cdot \cos(\alpha + \delta). \tag{A.59}$$

However, as the angle between idler and signal is rather difficult to set up, since the idler is typically not present before amplification, it is reasonable to express the ideal group-velocity projection as a function of the pump-to-signal angle. Using eq.3.13, the revelation between the wave vectors expressed via the law of sines and the law of cosines, as well as the identity $\cos(x)^2 + \sin(x)^2 = 1$, the signal-to-pump angle to match the group velocities of idler and signal, can be expressed as:

$$\sin(\alpha) = \pm \sqrt{\frac{1 - \frac{v_{g,s}^2}{v_{g,i}^2}}{1 + 2\frac{k_s v_{g,s}}{k_i v_{g,i}} + \frac{k_s^2}{k_i^2}}}. \tag{A.60}$$

If further enhancement of the broadband capabilities of OPA is necessary, another degree of freedom must be added to minimize the phase mismatch. One solution to overcome this phase mismatch is to "swap" the role of idler and signal by introducing an angular dispersion to the signal to mitigate this angular dispersion in the generation of the idler [280]. Ideally, this angular dispersion is set, such that there is perfect phase matching for every wavelength at the same pump-to-crystal angle $\theta$. Another solution to this is the so-called "frequency domain optical parametric amplification" [281] in which the individual frequency components are split and amplified in distinct nonlinear crystals at different angles. Shifting the manipulation from the side of the signal to that of the pump, yet another method would be to use a broadband, chirped pump and split the amplification not in space, but in time such that a single crystal can be used [150]. While all these solutions offer a broader amplification bandwidth, the complexity of the experimental implementation rises quickly and has to be considered in the whole scheme and goal of the amplification setup.